The Nature of the tectonic shortening in Central Andes

Michaël Pons

Kumulative Dissertation

zur Erlangung des akademischen Grades

"doctor rerum naturalium"

(Dr. rer. nat.)

in der Wissenschaftsdisziplin "Geophysik"

eingereicht an der

Mathematisch-Naturwissenschaftlichen Fakultät

Institut für Geowissenschaften

der Universität Potsdam

und

Sektion 2.5: Geodynamische Modellierung

Deutsches GeoForschungsZentrum Potsdam

Ort und Tag der Disputation: Potsdam, 17/03/2023

First supervisor
Prof. Dr. Stephan Sobolev, GFZ Potsdam, Universität Potsdam

Second supervisor
Prof. Dr. Frank Krüger, Universität Potsdam

Reviewers
1. Prof. Dr. Stephan Sobolev, GFZ Potsdam, Universität Potsdam
2. Prof. Dr. Hanna Čížková, Charles University Prague
3. Prof. Dr. Eline le Breton, Freie Universität Berlin

Published online on the
Publication Server of the University of Potsdam:
https://doi.org/10.25932/publishup-60089
https://nbn-resolving.org/urn:nbn:de:kobv:517-opus4-600892

Declaration of Autorship

I hereby declare that this dissertation has not been previously submitted to any other university and that this dissertation has been prepared independently by the author, Michaël Pons without the use of any other means than the specified resources. This work has only been submitted at the university Potsdam.

Abstract

The Andean Cordillera is a mountain range located at the western South American margin and is part of the Eastern- Circum-Pacific orogenic Belt. The ~7000 km long mountain range is one of the longest on Earth and hosts the second largest orogenic plateau in the world, the Altiplano-Puna plateau. The Andes are known as a non-collisional subduction-type orogen which developed as a result of the interaction between the subducted oceanic Nazca plate and the South American continental plate. The different Andean segments exhibit along-strike variations of morphotectonic provinces characterized by different elevations, volcanic activity, deformation styles, crustal thickness, shortening magnitude and oceanic plate geometry. Most of the present-day elevation can be explained by crustal shortening in the last ~50 Ma, with the shortening magnitude decreasing from ~300 km in the central (15°S-30°S) segment to less than half that in the southern part (30°S-40°S). Several factors were proposed that might control the magnitude and acceleration of shortening of the Central Andes in the last 15 Ma. One important factor is likely the slab geometry. At 27-33°S, the slab dips horizontally at ~100 km depth due to the subduction of the buoyant Juan Fernandez Ridge, forming the Pampean flat-slab. This horizontal subduction is thought to influence the thermo-mechanical state of the Sierras Pampeanas foreland, for instance, by strengthening the lithosphere and promoting the thick-skinned propagation of deformation to the east, resulting in the uplift of the Sierras Pampeanas basement blocks. The flat-slab has migrated southwards from the Altiplano latitude at ~30 Ma to its present-day position and the processes and consequences associated to its passage on the contemporaneous acceleration of the shortening rate in Central Andes remain unclear. Although the passage of the flat-slab could offer an explanation to the acceleration of the shortening, the timing does not explain the two pulses of shortening at about 15 Ma and 4 Ma that are suggested from geological observations. I hypothesize that deformation in the Central Andes is controlled by a complex interaction between the subduction dynamics of the Nazca plate and the dynamic strengthening and weakening of the South American plate due to several upper plate processes. To test this hypothesis, a detailed investigation into the role of the flat-slab, the structural inheritance of the continental plate, and the subduction dynamics in the Andes is needed. Therefore, I have built two classes of numerical thermo-mechanical models: (i) The first class of models are a series of generic E-W-oriented high-resolution 2D subduction models thatinclude flat subduction in order to investigate the role of the subduction dynamics on the temporal variability of the shortening rate in the Central Andes at Altiplano latitudes (~21°S). The shortening rate from the models was then validated with the observed tectonic shortening rate in the Central Andes. (ii) The second class of models are a series of 3D data-driven models of the present-day Pampean flat-slab configuration and the Sierras Pampeanas (26-42°S). The models aim to investigate the relative contribution of the present-day flat subduction and inherited structures in the continental lithosphere on the strain localization. Both model classes were built using the advanced finite element geodynamic code ASPECT.

The first main finding of this work is to suggest that the temporal variability of shortening in the Central Andes is primarily controlled by the subduction dynamics of the Nazca plate while it penetrates into the mantle

transition zone. These dynamics depends on the westward velocity of the South American plate that provides the main crustal shortening force to the Andes and forces the trench to retreat. When the subducting plate reaches the lower mantle, it buckles on it-self until the forced trench retreat causes the slab to steepen in the upper mantle in contrast with the classical slab-anchoring model. The steepening of the slab hinders the trench causing it to resist the advancing South American plate, resulting in the pulsatile shortening. This buckling and steepening subduction regime could have been initiated because of the overall decrease in the westwards velocity of the South American plate. In addition, the passage of the flat-slab is required to promote the shortening of the continental plate because flat subduction scrapes the mantle lithosphere, thus weakening the continental plate. This process contributes to the efficient shortening when the trench is hindered, followed by mantle lithosphere delamination at ~20 Ma. Finally, the underthrusting of the Brazilian cratonic shield beneath the orogen occurs at ~11 Ma due to the mechanical weakening of the thick sediments covered the shield margin, and due to the decreasing resistance of the weakened lithosphere of the orogen.

The second main finding of this work is to suggest that the cold flat-slab strengthens the overriding continental lithosphere and prevents strain localization. Therefore, the deformation is transmitted to the eastern front of the flat-slab segment by the shear stress operating at the subduction interface, thus the flat-slab acts like an indenter that “bulldozes” the mantle-keel of the continental lithosphere. The offset in the propagation of deformation to the east between the flat and steeper slab segments in the south causes the formation of a transpressive dextral shear zone. Here, inherited faults of past tectonic events are reactivated and further localize the deformation in an en-echelon strike-slip shear zone, through a mechanism that I refer to as “flat-slab conveyor”. Specifically, the shallowing of the flat-slab causes the lateral deformation, which explains the timing of multiple geological events preceding the arrival of the flat-slab at 33°S. These include the onset of the compression and of the transition between thin to thick-skinned deformation styles resulting from the crustal contraction of the crust in the Sierras Pampeanas some 10 and 6 Myr before the Juan Fernandez Ridge collision at that latitude, respectively.

Zusammenfassung

Die Andenkordillere ist ein Gebirgszug am westlichen Rand Südamerikas und Teil des östlichen zirkumpazifischen Gebirgsgürtels. Der ~7000 km lange Gebirgszug ist einer der längsten der Erde und beherbergt mit dem Altiplano-Puna-Plateau das zweitgrößte orogenetische Plateau der Welt. Die Anden sind als nicht-kollisionsbedingtes Subduktionsgebirge bekannt, das durch die Wechselwirkung zwischen der subduzierten ozeanischen Nazca-Platte und der südamerikanischen Kontinentalplatte entstanden ist. Entlang des Höhenzugs der Anden lassen sich Segmente unterschiedlicher morphotektonischer Provinzen ausmachen, die durch Variationen in topographischer Höhe, vulkanischer Aktivität, Deformationsform, Krustendicke, Krustenverkürzung und ozeanischer Plattengeometrie gekennzeichnet sind. Der größte Teil der heutigen Hebung lässt sich durch die Krustenverkürzung der letzten 50 Mio. Jahre erklären, wobei das Ausmaß der Verkürzung von ca. 300 km im zentralen Segment (15°S-30°S) auf weniger als die Hälfte im südlichen Teil (30°S-40°S) abnimmt. Es wurden mehrere Faktoren vorgeschlagen, die das Ausmaß und die Beschleunigung der Verkürzung der zentralen Anden in den letzten 15 Mio. Jahren beeinflusst haben könnten. Ein wichtiger Faktor ist wahrscheinlich die Plattengeometrie. Durch die Subduktion des Juan-Fernandez-Rückens und dessen hohe Auftriebskraft fällt die Platte bei 27-33°S in ~100 km Tiefe horizontal ein und bildet den pampeanischen *flat-slab*. Es wird angenommen, dass die horizontale Subduktion den thermomechanischen Zustand des Sierras-Pampeanas-Vorlandes beeinflusst, indem sie beispielsweise die Lithosphäre stärkt und die dickschalige Verlagerung der Deformation nach Osten sowie die Hebung der kristallinen Basis der Sierras-Pampeanas fördert. Vor etwa 30 Mio. Jahren verschob sich der *flat-slab* von der geographischen Breite des Altiplano zu seiner heutigen Position nach Süden. Die mit der Positionsverlagerung verbundenen Prozesse und Folgen für die gleichzeitige Beschleunigung der Verkürzungsraten in den zentralen Anden sind noch immer unklar. Obwohl die Passage des *flat-slab* eine Erklärung für dafür sein könnte, erklärt ihr Zeitpunkt nicht die beiden aus der Geologie abgeleiteten Verkürzungsimpulse vor etwa 15 und 4 Mio. Jahren. Ich stelle die Hypothese auf, dass die Deformation in den zentralen Anden durch eine komplexe Wechselwirkung zwischen der Subduktionsdynamik der Nazca-Platte und der dynamischen Materialschwächung der südamerikanischen Platte aufgrund einer Reihe von Prozessen in der oberen Platte gesteuert wird. Um diese Hypothese zu prüfen, ist eine detaillierte Untersuchung der Rolle des *flat-slab*, sowie der strukturellen Vererbung der Kontinentalplatte und der Subduktionsdynamik in den Anden erforderlich. Daher habe ich zwei Klassen von numerischen thermomechanischen Modellen erstellt: (i) Die erste Klasse von Modellen umfasst eine Reihe von generischen E-W-orientierten 2D-Subduktionsmodellen mit hoher Auflösung. Diese beinhalten subhorizontalen Subduktion um die Rolle der Subduktionsdynamik auf die zeitliche Variabilität der Verkürzungsrate in den zentralen Anden auf dem Altiplano (~21°S) zu untersuchen. Die modellierte Verkürzungsrate wurde mit der beobachteten tektonischen Verkürzungsrate in den zentralen Anden validiert. (ii) Die zweite Klasse von Modellen besteht aus einer Reihe von datengesteuerten 3D-Modellen der heutigen pampeanischen *flat-slab*-Konfiguration und der Sierras Pampeanas (26-42°S). Diese Modelle zielen darauf ab,

den relativen Beitrag der heutigen subhorizontalen Subduktion und der ererbten Strukturen in der kontinentalen Lithosphäre zur Dehnungslokalisierung zu untersuchen. Beide Modellklassen wurden mit Hilfe des fortschrittlichen geodynamischen Finite-Elemente-Codes ASPECT erstellt.

Das erste Hauptergebnis dieser Arbeit ist die Vermutung, dass zeitliche Änderungen der Verkürzung in den Zentralanden in erster Linie durch die Subduktionsdynamik der Nazca-Platte gesteuert werden, während diese in die Mantelübergangszone eindringt. Die Dynamik hängt von der westwärts gerichteten Geschwindigkeit der südamerikanischen Platte ab, die die Hauptantriebskraft für die Krustenverkürzung in den Anden darstellt und den Subduktionsgraben zum Zurückziehen zwingt. Wenn die subduzierende Platte den unteren Erdmantel erreicht, wölbt sie sich auf, bis der erzwungene Rückzug des Grabens dazu führt, dass auch die Platte im oberen Erdmantel steiler wird. Die aufgesteilte Platte behindert wiederum den Graben, der sich der vorrückenden südamerikanischen Platte widersetzt, was eine pulsierende Verkürzung zur Folge hat. Dieses Subduktionsregime, bestehend aus Aufwölbung und Aufsteilung, könnte durch die allgemeine westwärts gerichtete Geschwindigkeitsabnahme der südamerikanischen Platte ausgelöst worden sein. Der Durchgang des *flat-slab* ist zudem eine notwendige Bedingung, um die Verkürzung der Kontinentalplatte voran zu treiben, da subhorizontale Subduktion Teile der Mantellithosphäre abträgt und so die Kontinentalplatte schwächt. Dieser Prozess trägt somit zur effizienten Verkürzung bei während der Graben behindert wird und ist gefolgt von der Ablösung der Mantellithosphäre vor etwa 20 Mio. Jahren. Das Subduzieren des brasilianischen kratonischen Schildes unter das Orogen erfolgte schließlich vor etwa 11 Mio. Jahren aufgrund der mechanischen Schwächung der dicken Sedimentschicht, die den Schildrand bedeckte, sowie wegen des abnehmenden Widerstands der geschwächten Gebirgslithosphäre.

Das zweite Hauptergebnis dieser Arbeit ist die Vermutung, dass der kalte *flat-slab* die darüber liegende kontinentale Lithosphäre stärkt und damit verhindert, dass sich Verformungen lokalisieren können. Daher wird die Deformation durch die an der Subduktionsfläche wirkende Scherspannung auf die östliche Front des *flat-slab*-Segments übertragen. Der *flat-slab* wirkt wie ein Eindringling, der die unter *mantle-keel* bekannte Anhäufung von abgelöstem Mantelmaterial beiseite schiebt. Der Versatz in der ostwärts gerichteten Deformationsausbreitung der flachen und der steileren Plattensegmenten im Süden führt zur Bildung einer transpressiven dextralen Scherungszone. Hier werden ererbte Verwerfungen vergangener tektonischer Ereignisse reaktiviert und helfen bei der Lokalisierung neuer Deformation in einer en-echelon-artigen Scherungszone. Dies geschieht durch einen Mechanismus, den ich als "*flat-slab-Conveyor*" bezeichne. Das laterale Zusammenschieben wird besonders durch das Flacherwerden des *flat-slab* beeinflusst, welches den Zeitpunkt mehrerer geologischer Ereignisse erklärt, die der Ankunft des *flat-slab* bei 33°S vorangehen. Dazu gehören der Beginn der Kompression und der Übergang von dünn- zu dickschaliger Deformation, die sich aus der Krustenkontraktion in den Sierras Pampeanas etwa 10 bzw. 6 Mio. Jahre vor der Kollision mit dem Juan-Fernandez-Rücken auf diesem Breitengrad ergaben.

Table of Contents

List of Figures

Figures in the main text

Figures in the Appendices

List of Tables

Tables in the main text

Tables in the Appendices

Declaration of authors

This thesis consists of 3 chapters as well as an introduction, a discussion and a conclusion. Each chapter corresponds to a study that has been published or will be submitted soon. Michael Pons is the first author of these studies. The format of these studies has been redesigned for ease of reading. Additional figures and bibliographic references for each study have been placed at the end of the thesis in the appendix.

Chapter 2 is based on the study *"Hindered trench migration due to slab steepening controls the formation of the Central Andes"* published in the Journal of Geophysical Research: Solid Earth (*DOI : 10.1029/2022JB025229*). And is co-authored by Michael Pons, Stephan V. Sobolev, Sibiao Liu and Derek Neuharth. MP and SS have design the study and the model and their interpretation. D.N contributed to the coupling between ASPECT and FASTSCAPE that handle the mesh deformation MP performed the numerical simulations of subduction under the supervision of SS. MP, SS, SL and DN have participated to the reviewing and the editing of the manuscript.

Chapter 3 is entitled *"Controls of the dip geometry and plate strength on the localization of the deformation in the Sierras Pampeanas"* is accepted in the journal Tectonics. It is co-authored by Michaël Pons, Constanza Rodriguez Piceda, Stephan V. Sobolev, Magdalena Scheck-Wenderoth, Manfred Strecker. MP and CRP participated equally in the design of the study. MP performed the numerical simulation based on the Sierras Pampeanas lithosphere model published from previous CRP studies. MP, CRP, MSW, and MS participated in the interpretation of the results, revision and editing of the manuscript.

Chapter 4 is entitled *"Conveyor effect from precursory crustal contraction foreshadows the arrival of the Pampean flat-slab "*, builds on the study in Chapter 3. It is co-authored by Michaël Pons, Constanza Rodriguez Piceda, Stephan V. Sobolev, Magdalena Scheck-Wenderoth, Manfred Strecker. MP and CRP participated equally in the design, interpretation of results, and writing of the study. SL and MSW supervised the work. All co-authors contributed to the revision and editing of the manuscript.

List of Symbols and Abbreviations

Parameter	Symbol	Unit
	ASPECT	
	Thermal parameters	
Thermal expansivity	α	K^{-1}
Thermal diffusivity	κ	$m^2\ s^{-1}$
Thermal conductivity	k	$W\ m^{-1}\ K^{-1}$
Heat capacity	C_p	$J\ kg^{-1}\ K^{-1}$
Heat production	H	$W\ m^{-3}$
	Rheological parameters : plasticity	
Cohesion	C	Pa
Internal friction angle	ϕ	◦
Plastic strain weakening factor	ϕ_{wf}	-
	Rheological parameters : viscosity	
Stress exponent (dislocation)	n	-
Constant prefactor (dislocation)	A_{dis}	$Pa^{-n}\ s^{-1}$
Activation energy (dislocation)	E_{dis}	$J\ mol^{-1}$
Activation volume (dislocation)	V_{dis}	$m^3\ mol^{-1}$
Constant prefactor (diffusion)	A_{diff}	$Pa^{-1}\ s^{-1}$
Activation energy (diffusion)	E_{diff}	$J\ mol^{-1}$
Activation volume (diffusion)	V_{diff}	$m^3\ mol^{-1}$
Grain size (diffusion)	d	m
Grain size exponent (diffusion)	m	-
	Additional parameters	
Gas constant	R	$J\ K^{-1}\ mol^{-1}$
gravity	$\boldsymbol{g}$	$m\ s^{-2}$
velocity	$\boldsymbol{u}$	$m\ yr^{-1}$
Strain rate tensor	$\dot{\varepsilon}$	s^{-1}
Temperature	T	K
Viscosity	η	Pa s
Effective viscosity	η_{eff}	Pa s
Pressure	P	Pa
Density	ρ	$kg\ m^{-3}$
Reference density at room temperature	$\bar{\rho}$	$kg\ m^{-3}$
Time	t	yr
Compositional field	c_i	-
Reaction rate	q_i	-
Temperature of the phase transition	T_{tr}	K
Pressure of the phase transition	P_{tr}	Pa
Pressure width of the phase transition	Pw	Pa
Clapeyron slope	λ *or* γ	Pa/K
	FastScape	
Drainage area exponent	m	-
Slope exponent	n	-
Bedrock/sediment diffusivity	K_c	m^2/yr
Bedrock/sediment erodibility	K_f	$m^{0.2}/yr$
Bedrock/sediment deposition coefficient	G	-
Topographic elevation	h	m
Drainage area	A	m^2

ABBREVIATION	EXPLANATION
AFTB	Aconcagua Fold-Thrust Belt
ASPECT	Advanced Solver for Problems in Earth's ConvecTion
CB	Cuyo Basin
CC	Coastal Cordillera
CP	Cerrilladas Pedemontanas
EAB	Extra-Andean basins
ESP	Eastern Sierras Pampeanas
FA	Forearc
FC	Frontal Cordillera
GPE	Gravitational Potential Energy
JFR	Juan Fernandez Ridge
LAB	Lithosphere Asthenosphere Boundary
LC	Lower Crust
LRFTB	La Ramada Fold-Thrust Belt
MC	Middle Crust
MFTB	Malargüe fold-thust belt
NB	Neuquén basin
OP	Overriding plate
P	Payenia
PC	Principal Cordillera
PRC	Precordillera
SA	South America
SR	San Rafael Bloc
TRB	Triassic basins
UC	Upper Crust
VSR	Velocity of shortneing (= Shortening rate)
VTR	Velocity of trench retreat (Trench retreat rate)
VTR	Velocity of the overriding plate
WSP	Western Sierras Pampeanas.

Chapter 1 Introduction

1.1 General background of the Andes and main problematic

Mountain ranges related to compressive orogenic belts are the result of significant crustal shortening and they form at the edge of continental plates (Figure 1.1). We can distinguish two types of compressive orogenic belts: the "Tethyan belt type", which results from the collision between two continental plates (e.g., the Alps, the Carpathians, the Himalayas), and the “Andean belt type,” or non-collisional orogens that often form in subduction zones where an oceanic plate sinks beneath a continental plate (e.g., the Andes or the North American Cordillera that is located along the the eastern side of the Circum-Pacific zone). Although the formation of mountain ranges resulting from continental collision is more intuitive, the mechanism of the plate interactions responsible for the formation of non-collisional orogens remains unclear. Moreover, in this latter type mountain range formation can be related to subduction zones with flat-slab segments (e.g., Sierras Pampeanas in Argentina and the Rocky Mountains in North-America; Jordan & Allmendinger, 1986), which increases the complexity in determining their origin. The eastern Pacific margin is, or was, occupied by multiple present-day or past flat subduction segments (Figure 1.1) that are thought to play an important role in the formation of the Central Andes (e.g. Barazangi & Isacks, 1976, 1979; Sobolev et al., 2006; Ramos, 2009; Horton & Folguera, 2022).

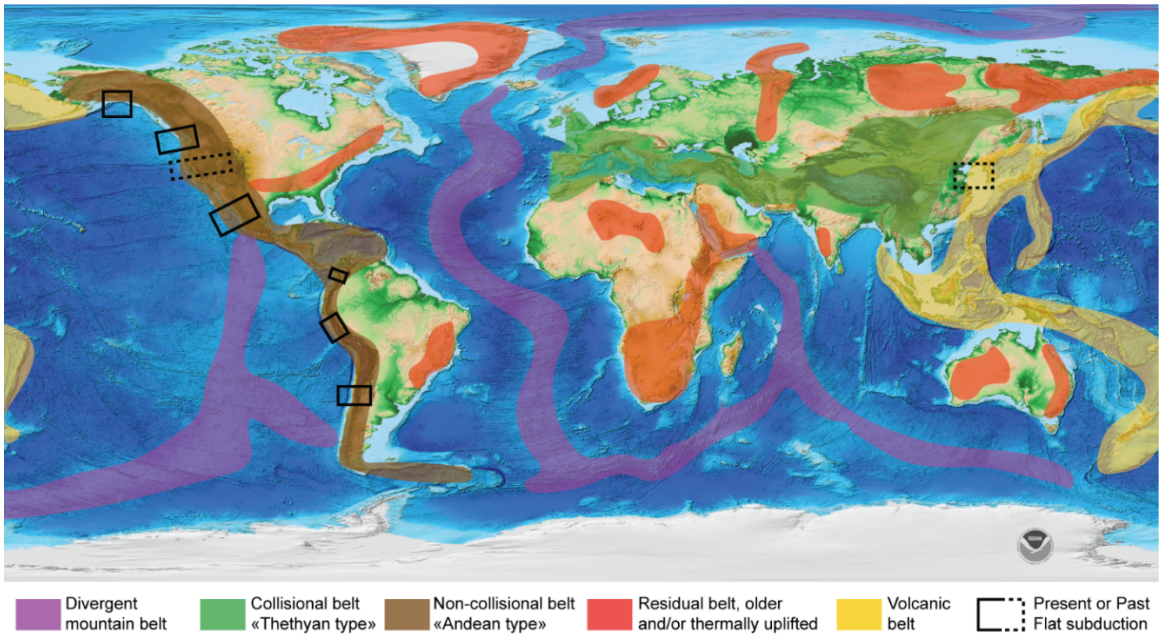

Figure 1.1 Main mountain belts. Green and brown stands for the Thetyan and East-Pacific (i.e., Andean belt type) compressive orogenic belt, respectively. Purple stands for mountains belts formed at divergent plate boundaries, red are mountain belts that are either from Mesozoic or older orogenic events, and/or "thermally uplifted" reliefs. Yellow indicates volcanic belts. Continuous and dashed rectangles indicate areas of present and proposed past flat-slabs, respectively. Topographic map is based on ETOPO1 (Amante & Enkins., 2009).

The Andes form the longest mountain range in the world (~7000 km N-S) and are located on the western margin of South America. It is also the second highest mountain range on Earth (~4000 km) and is up to ~300 km wide (E-W). The Andes are a non-collisional orogeny that formed above the Chilean subduction zone, where the Nazca oceanic plate subducts eastward beneath the South American continental plate (Jordan et al., 1983). Although the westward motion of the South American plate is likely the primary driving force behind the formation of the Andes (Russo & Silver, 1994; Silver et al., 1998; Sobolev & Babeyko, 2005; Martinod et al., 2010; Husson et al., 2012), the orogen exhibits a high variability in the elevation (Figure 1.2-1.3) and in the magnitude of shortening along strike of the subduction zone, which the motion of the South American plate alone cannot explain. Many hypotheses have been proposed to explain this spatial variability, involving different degrees of climatic, tectonic and geodynamic interactions (Chapter 1.3). In order to elucidate the causal mechanisms and key factors in the significant shortening of the Central Andes, in this thesis I address the cause of the temporal variability in shortening. I also examine the role of the present-day flat subduction style on the localization of the deformation in the Southern Central Andes.

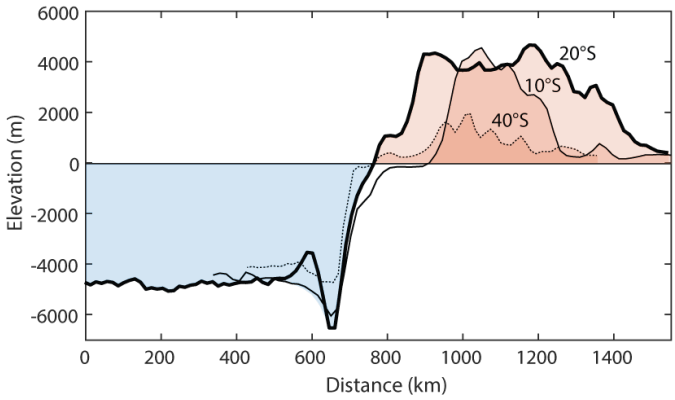

Figure 1.2 Topographic cross section of the Andes taken at 10, 20 and 40°S illustrating the significant variation of the encountered relief.

1.2 Tectonic segmentation of the Andes

The Chilean subduction zone has been active since at least the Mesozoic (>200 Ma; Burchfiel et al., 1976). We can distinguish 3 segments showing different physical and morphological characteristics, and the transition between these segments roughly corresponds to the latitudes at which the Nazca Ridge at ~18°S and the Juan Fernandez Ridge at 33°S subduct (Figure 1.2):

- The **northern Andean segment** (0-15°S) is characterized by a high (~4000m) and narrow (~200km) mountain range (Figure 1.2). The curvature of the trench is convex toward the ocean. The trench is filled with a thick sedimentary layer (>500m, Lamb & Davis, 2003). Where the oceanic plate has the flat-slab segment, the orogen is volcanically inactive (James & Sacks, 1999). In the north, where the Nazca ridge subducts, the narrow foreland shows thick-skinned deformation and that uplifts the crystalline foreland basement (Kley, 1998). In the south, a foreland fold-and-thrust belt developed by thin-skinned deformation of the sedimentary cover. The oceanic plate age at the trench varies from ~30 Ma in the North to 40 Ma in the south (Figure 1.3, Sdrolias & Müller, 2006; Capitanio et al., 2011). At these latitudes, the shortening is up to ~100km (Key and Monaldi, 1998; Arriagada et al., 2008) and the crustal thickness is ~45 km (Aranda & Assumpção, 2013).
- The **Central Andean segment** (15-33°S) is characterized by a high (~4000m) and wide (~700km) mountain range (Figure 1.2). The curvature of the trench in concave toward the trench forming the Arica bend. The ~8-km deep trench contains almost no sediments (Figure 1.3, Lamb & Davis, 2003). The central Andes is volcanically active at present-day. The flat reliefs of the Central Andes are typical of the orogenic Altiplano-Puna plateau. The shortening of the Altiplano reaches ~300km or more, whereas it significantly decreases to ~150km in the Puna (Key & Monaldi, 1998; Oncken et al., 2006; Arriagada et al., 2008). This difference in the total shortening is attributed to a different tectonic deformation style in the foreland (Allmendinger & Gubbells, 1996; Babeyko et al., 2005; Sobolev et al., 2006; Liu et al., 2020). At Altiplano latitudes (15-

24°S), the Chaco-Parana foreland develops into thin-skinned deformation, forming the Sierras Subandinas. Whereas at Puna latitudes (24-30°S), the foreland shows thick-skinned deformation in the Santa-Barbara System (Allmendinger & Gubbels, 1996). Uplift of the Altiplano-Puna plateau only took place in the last 15 Ma (Garzione et al., 2017). The crustal thickness at this latitude can reach ~75-80 km (20°S; Kley and Monaldi, 1998; Beck et al., 2002; Yuan et al, 2002). The sublithopheric mantle is mostly delaminated under the plateau (Kay & Kay, 1993; Gao et al., 2021). The surface heat flow is relatively high on top of the plateau (up to 200 mW/m²; Hamza et al., 2005).

- The **Southern Andean segment** (33-46°S) is characterized by low (~2000m) and narrow (~200km) mountain ranges (Figure 1.2). The volcanic activity is null between 29-34°S in an area known as the Pampean flat-slab (James & Sacks, 1999). South of this area, the thickness of the orogen crust is ~45 km (Aranda & Assumpção, 2013). Sediments at the trench are 1.5 to 2 km thick on the southern side of the Juan Fernandez Ridge (Lamb & Davis, 2003). Palaeozoic basement blocks are uplifted in the Sierras Pampeanas foreland, representing an end member of thick-skinned deformation (Jordan & Allmendinger, 1986). At 36°S -40°S the shortening is less than 100km, and the cumulated shortening can reach ~70km (Giambagi et al., 2022).

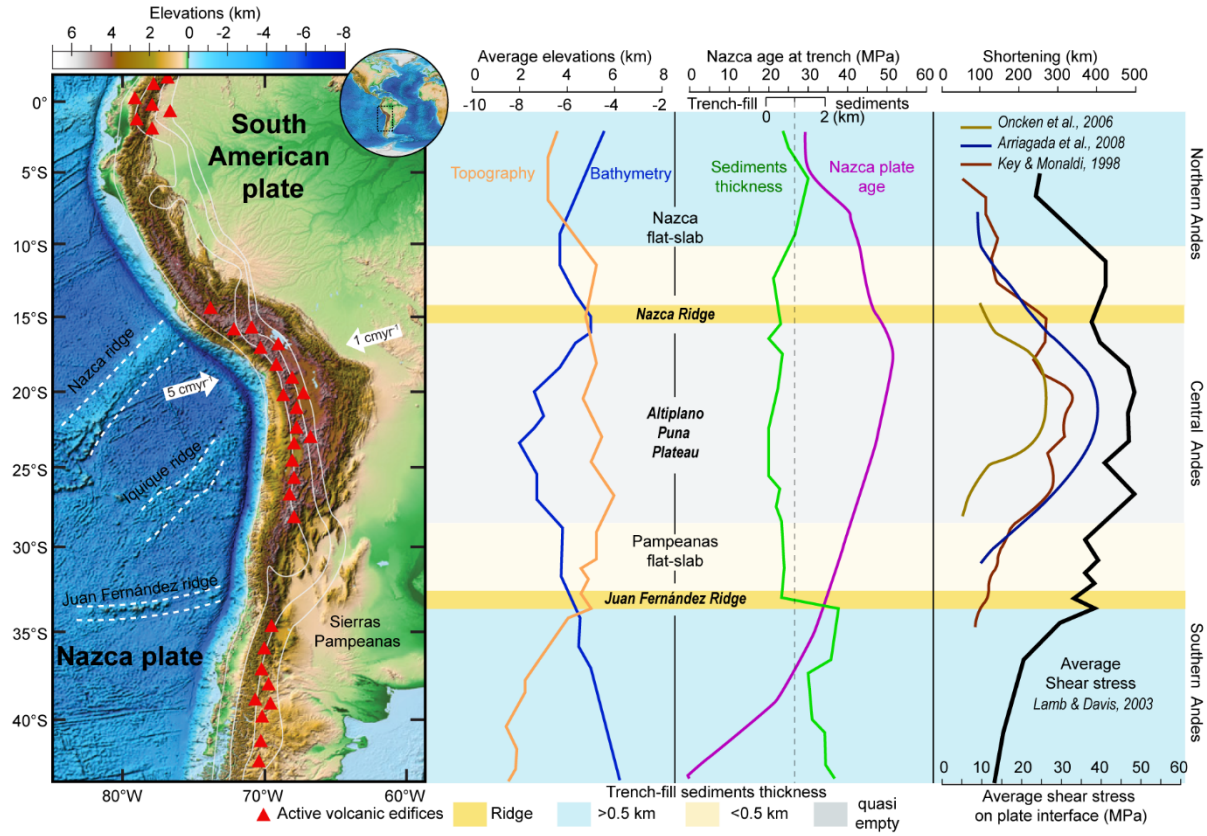

Figure 1.3 Andean Segments. Composite diagram of the latitudinal variations along the extent of the Chilean Margin (modified from Lamb & Davis, 2003; Hu et al., 2011; Capitanio et al., 2011). The figure illustrates the average topography and bathymetry (ETOPO 1, Amante & Eakins, 2009), the thickness of

the sediments in the trench (Lamb & Davis, 2003), the age of the Nazca plate (Capitanio et al., 2011), the shortening magnitude and the average shear stress at the subduction interface (Lamb & Davis, 2003). Red triangles show the zones where volcanism is active. The white isolines show the depth to the top of the slab which are taken every 50 km between the surface and 200km depth (Portner et al., 2020).

1.3 Hypothesis for the segmentation of the Andes

Most of the current central Andes elevation can be explained by crustal shortening (Arriagada et al., 2008). Multiple studies have addressed the cause of the difference in magnitude of shortening between Andean segments, but there is no clear consensus. In the following sections, I summarize these hypotheses.

1.3.1 Hypotheses related to the lower-plate processes

A first type of studies proposes that the difference of shortening within the Andes is caused by differences in the interplate coupling strength that is caused by climatic variations in the different segments (Montgomery, 2001; Lamb & Davis, 2003; Hu et al., 2021). In the Central Andes, because of the arid climate, erosion is less efficient and less sediments are transported to the trench (Figure 1.3). The sediments carry fluids that reduce the friction of the subduction interface due to an increase in the pore fluid pressure. A lack of sediments referred to as trench starvation, therefore increase the interplate coupling, as estimated by the increasing shear stress (Figure 1.3, Lamb & Davis, 2003). Alternatively, other authors have considered the effect of the ridges, which act as bathymetric barriers for the along-strike transportation of sediments along the trench (Völker et al., 2013; Hu et al., 2022).

A second type of studies proposes that kinematic changes, such as the plate convergence velocity, can also increase the shear stress transmitted from the oceanic plate to the continental plate and thus affect the magnitude of upper plate tectonic shortening (Silver et al., 1998; Quiero et al., 2022; Sdrolias & Muller, 2006). However, it is clear that convergence rates do not change much along the Andean trench, so it is unlikely to be the reason for large spatial variations in the magnitude of tectonic shortening.

A third type of studies proposes that the dynamics of the subducting oceanic plate explains the magnitude of shortening in the Andes. When the oceanic plate sinks into the mantle, the previously subducted segment tends to cause the hinge to roll-back in order to accommodate the plate bending, thus causing the trench to retreat (Garfunkel et al., 1986; Kincaid and Olson, 1987; Conrad and Hager, 1999; Capitanio et al., 2007). Many authors have proposed that roll-back of the Chilean subduction zone is not homogeneous, but occurs faster in the north and in the south where toroidal flow within the asthenospheric mantle is faster than in the centre of the slab (Russo & Silver 1994, 1996; Schellart et al., 2007). The westward moving continental plate therefore “collides” with the slower trench. Reconstructions of the paleo-position of the trench relative to the mantle frame shows that the trench retreat, indeed, slowed down over the last 50 Ma (Faccenna et al., 2017; Becker et al., 2015). Schepers et al (2017) demonstrates that most of the trench retreat is not

induced by slab roll-back, but that the trench is forced to retreat by the westward motion of the South American plate. The high interplate friction slows the sinking slab, preventing it to roll back and the trench to retreat (Buiter et al., 2001). Additionally, the upper plate, due to its thickness and size, could also resist the dragging from slab roll back (Holt et al., 2015; Hertgen et al., 2020). The along-strike age (Figure 1.3) and thickness of the oceanic plate can also contribute to a higher shear stress in the Central Andes, and to decrease the subduction velocity (Figure 1.3; Capitanio et al., 2011). Alternatively, Faccenna et al (2017) propose another mechanism to explain the decreasing velocity of trench retreat in the Central Andes. In their model, they show that the slab anchoring into the high-viscosity lower mantle could slow down the retreat of the trench and cause an additional increase of horizontal stress in the upper plate, which could potentially explain the timing of the extensive tectonic shortening in the Central Andes (Oncken et al., 2006; Oncken et al., 2012). In their "slab suction" model, they also propose that the penetration of the slab in the lower mantle can produce additional drag force of the continental plate towards the trench by producing a larger asthenosphere convection cell (Faccena et al., 2017; Faccenna et al., 2021; Husson et al., 2013). Other alternative models (Lee & King, 2011; Gibert et al., 2012) propose that the interaction between the slab and the more viscous lower mantle, can cause the slab to buckle in the mantle transition zone, potentially explaining the ~30 My cycles of plate convergence. Finally, Cerpa et al., (2014) propose that the oblique convergence of the Nazca plate with slab folding could partially explain the segmentation of the Andes. In this thesis, I investigate in detail the effect of slab folding in the context of the Central Andes. Specifically, I investigate whether this mechanism could produce pulsatile shortening phases that are similar in timing and in magnitude to the shortening rate inferred from the compilation of geological data (Oncken et al., 2006-2012).

1.3.2 Hypotheses related to upper plate processes

A fourth type of studies proposes that the difference in the magnitude of the shortening rate in Central Andes is caused by a latitudinal strength difference within the continental plate (Sobolev et al., 2006; Babeyko et al., 2006; Gerbaut et al., 2009). The variation in shortening magnitude spatially correlates with a change of foreland deformation style, which is controlled by the strength of the foreland (Ramos et al., 2004; Sobolev et al., 2006; Babeyko et al., 2006; Giambiagi et al., 2015, 2022; Mescua et al., 2016; Ibarra et al., 2019; Barrionuevo et al., 2021; Liu et al., 2022). Allmendinger and Gubells (1996) noticed that the presence of porous sedimentary Mesozoic layers that accumulate fluids correlate with thin-skinned deformation of the foreland, and in turn higher shortening in Altiplano when compared to thick-skinned foreland deformation at Puna latitude. In Altiplano latitudes, the weaker foreland may have facilitated the underthrusting of the Brazilian cratonic shield at 11 Ma (Sobolev et al., 2006; Babeyko et al., 2006; Liu et al., 2022; Giambiagi et al., 2022). Babeyko et al., (2006) show that a strong erosion of the foreland due to the orographic barrier effect can also weaken it, so that the topographic denudation brings the deep rocks closer to the surface. This rock uplift uplifts the geotherms and favours the switch to simple-shear deformation,

which is expressed as thin-skinned at the surface. Another factor that may have decreased the Central Andes lithospheric strength and increased the shortening magnitude is the quasi-total delamination of the lithospheric mantle under the Altiplano plateau (Kay & Kay, 1993; Sobolev et al., 2006; Babeyko et al., 2006; Gao et al., 2021). Authors have suggested that delamination occurs under certain conditions (e.g., high coupling at the subduction interface; Sobolev et al., 2006) caused by the eclogitization of hydrated lower crust under high pressure (Sobolev et al., 1994; Babeyko et al., 2006) caused by the eclogitization of hydrated lower crust under high pressure (Sobolev et al., 1994; Babeyko et al., 2006), or by the scraping the continental sublithosphere mantle through the southward migration of the Pampean flat-slab through the Central Andes (Liu & Currie, 2016; Gutscher et al., 2018). In this context, the continental lithosphere is mechanically and thermally weakened as the crust becomes exposed to the warmer asthenosphere during the steepening of the flat-slab (Isacks et al., 1988). The increased basal heat flux also results in strong partial melting of the crust, therefore forming the largest magmatic body chamber in the world that produces the high surface heat flux observed in the Central Andes (De Silva & Kay, 2018). The higher temperature can also lead to intra-crustal convection at the base of the crust, further contributing to the lithospheric weakening (Babeyko et al., 2002; Babeyko et al., 2006). In this thesis, I have investigated the role of some of these processe (e.g eclogitization and delamination, weakening of the foreland sediments, passage and steepening of the flat-slab) in the context of the Central Andes. I have built a model able to dynamically simulate the weakening of the upper plate that results from the interaction between the Nazca and South American plate.

1.3.3 Hypotheses related to the flat-slab subduction and associated problems

The Juan Fernandez Ridge (JFR) has been migrated southwards from Altiplano latitudes at ~30 Ma to Sierras Pampeanas latitudes (33°S) at present-day. This migration was followed by an acceleration in the shortening rate seen in the Central Andes (Ramos et al., 2004; Oncken et al., 2006-2012; Giambagi et al., 2022). Early on, authors thought that the collision of the high-relief topographic features from the JFR subducting beneath the South American plate could explain the Andean segmentation (Pilger et al., 1981-1984; Ramos et al., 2002; Von Huene et al., 1997). These topographic features are produced by the Juan Fernandez hotspot and are comprised of thicker oceanic crust that contains ~1 to 2km high submarines volcanoes. At present-day, the oceanic crust of the JFR is ~10-15 km thick (Yañez et al 2001; Gans et al 2011), whereas the crust of the Nazca Ridge is ~20 km thick (Woods & Okal, 1994) and produce an average ~2km high topography relative to the surrounding sea floor (Figure 1.3). The subduction of the thicker Nazca ridge is correlated with significantly less shortening (Hindle et al., 2002) than from subduction of the JFR, thus indicating no strong link between the thickness of the crust, topography of the ridge, and the shortening intensity.

Additionally, at present-day, the subduction of the JFR is also associated with the propagation of deformation from the trench to the broken foreland of the Sierras Pampeanas, where Paleozoic blocks from

the crystalline crust of the basement have been uplifted indicating a classical “thick-skinned” deformation style (Jordan & Allmendinger, 1986; Babeyko & Sobolev, 2005; Liu et al., 2022). Where the Nazca ridge subducts, however, the foreland deformation mostly affects the sedimentary cover of the fold-and-thrust belt, typical of a “thin-skinned” deformation style (Jordan & Allmendinger, 1996; Babeyko & Sobolev, 2005; Liu et al., 2022). In this context, many authors have addressed the questions of "why does the deformation front propagate eastward in the flat-slab regions?" and "why is thick-skinned deformation produced in the case of JFR subduction in the Sierras Pampeanas?". Barazangi & Isacks (1976, 1979) suggest that this issue could be related to the Nazca and Pampean flat-slabs in the North and in the South, respectively, as shown by the gaps in the volcanic activity. It has also been proposed that slab flattening is caused by the subduction of buoyant ridges or oceanic plateaus (Gutscher et al., 2000; Espurt et al., 2008), however more recent modelling work suggests that the buoyancy from the present day thickness of the crust of oceanic ridges is not sufficient to sustain the flat-slab (Schellart et al., 2020, 2021). Other authors have proposed that a decreased slab pull force related to a shorter slab (~300 km long), possibly resulted from slab break-off (Gao et al., 2022), together with the late eclogotization of the oceanic crust could lead to flat subduction (Van Hunen et al., 2002; Gerya et al., 2009; Liu & Currie, 2016; Dai et al., 2020). Alternatively, Schellart et al., (2021) suggest that a short slab segment is not necessary to produce a flat-slab if the subduction has been going on for a sufficiently long time. Thus, the long history of subduction in the region (>200 Ma) and, what is possibly of more importance, the westward drifting of the South American plate could have contributed to a shallower slab dip (Sobolev et al, 2006; Schellart et al., 2021) as well as to hydrating the mantle wedge, causing a suction effect that flattens the slab (Manea & Gurnis, 2007). Slab shallowing explains the eastward migration of the volcanic activity anddeformation (Ramos et al., 2002). The shear stress is transmitted to the east by the flat slab segment which bulldozes the continental lithosphere mantle-keel (Martinod et al., 2010; Gutscher et al., 2018). However, although this transmission of shear stress is suggested for both the Nazca and Pampean flat-slab, only the Sierras Pampeanas are characterized by a thick-skinned deformation style with the uplift of large basement blocks (Figure 1.4), which suggests additional contributing factors. Dávila & Lithgow-Bertelloni (2008, 2013) propose that the subduction of the Nazca and Pampean flat-slab leads to a dynamic uplift on top of the flat segment and dynamic subsidence at its front. Nevertheless, to explain the differences in foreland tectonic styles, other authors have suggested contributions from the reactivation of weaker and older inherited structures, such as terrane sutures, or the inversion of cretaceous pre-existing rifting normal faults (Cristallini & Ramos, 2000; Kley & Monaldi, 1998; Mescua et al., 2014; Giambiagi et al., 2014; Martino et al., 2016; Lossada et al., 2017). The onset of compressive deformation in the Sierras Pampeanas happens 10 Ma before the arrival of the flat slab (Yáñez et al., 2001; Ramos et al., 2009). In this context, it was proposed that the flat slab alone cannot explain the propagation of deformation to the east, the reactivation of pre-existing faults and the uplift of basement blocks (Figure 1.4). Zapata et al., (2022) suggest that a combination between slab anchoring and the reactivation of inherited structures is sufficient to explain the deformation in Southern Andes. Based on the above, the role of the flat subduction versus the

role of the inherited structures in the Sierras Pampeanas (Figure 1.4) is a central problem in our understanding of plate interactions. Assessing the effect of inheritance within a natural system is indeed a complex task. Inheritance can be geometric, structural, stratigraphic, compositional or thermal (Rodriguez Piceda et al., 2021, Ibarra et al., 2018; Horton & Folguera, 2022 ; Ramos et al., 2010). This topic is addressed in chapter 4 and 5, where I propose a new mechanism associated to the passage of the flat slab that reconciles the propagation of deformation to the east, the change in the foreland tectonic style of deformation and the timing of the onset of the deformation, in a single scenario supported by a 3D data-driven geodynamic model.

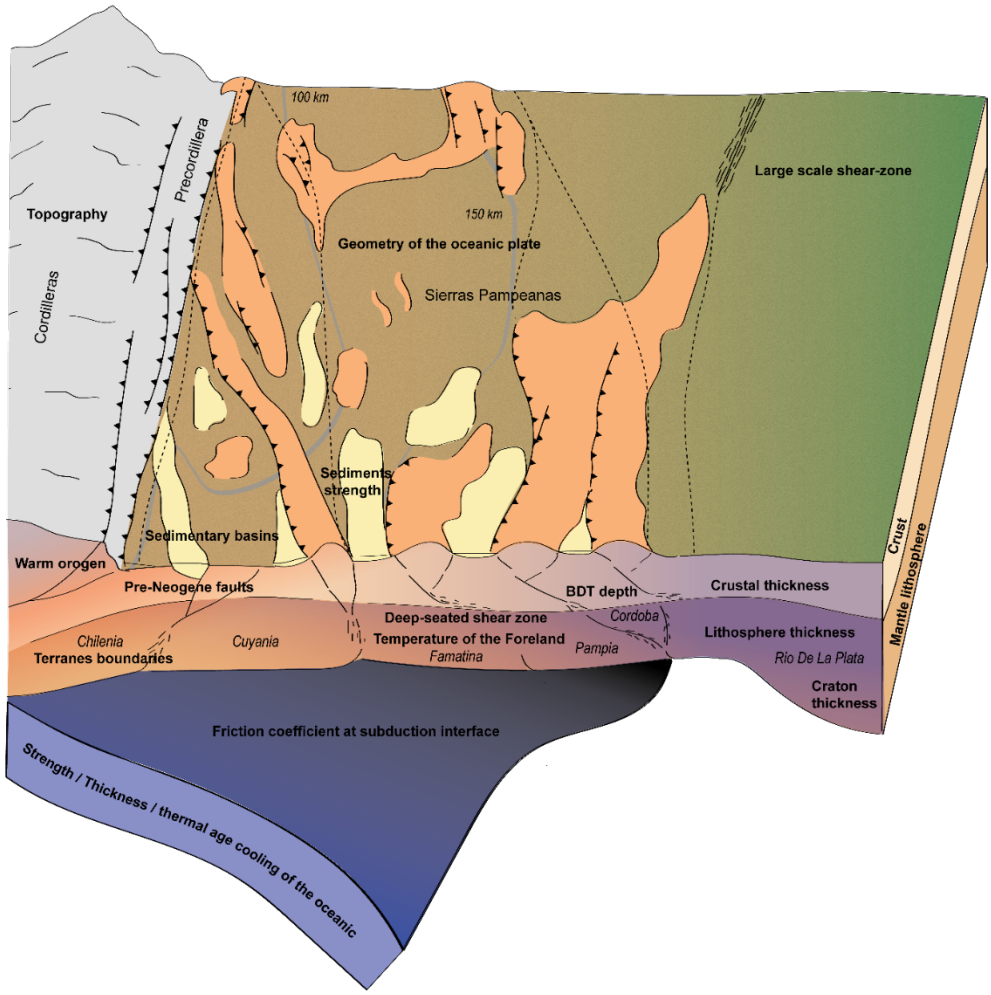

Figure 1.4 Lithosphere inheritance. List of the possible processes and inherited structures that can affect strain localization and the tectonic foreland deformation style of the Sierras Pampeanas. BDT is for Brittle Ductile Transition.

1.4 What are the main driving and resistive forces in a subduction zone?

Insights on the mechanisms behind the formation of the Andes require understanding the forces involved in a subduction zone. While oceanic plates are generated at ridges, subduction zones are convergent

boundaries where the plate is recycled into the asthenospheric mantle (Christensen & Hofmann, 1994). The subduction of an oceanic plate beneath a continental plate involves multiple forces. In general, we can distinguish the main driving forces from the resistive forces (Figure 1.5; Turcotte & Schubert, 2002; Billen et al., 2008; Wolf et al., 2018; Zoltan et al., 2021).

Ridge push force (F_{RP}) is a driving force that occurs when topography builds up at ridges as a result of the thermal expansion of the asthenosphere mantle. The gravitational forces caused by the difference of elevation with the oceanic floor produces the sliding of the plate (eq. 1 ; Turcotte & Schubert, 2002; McKenzie, 1968-1969). Ridge push force is ~3.10^{12}N/m. Additionally, at ridges the mantle decompression leads to partial melting, depletion, and the formation of new oceanic crust. When the oceanic plate gets thicker and colder as a function of its thermal age, the plate becomes denser and the gravitational body forces increase. As the plate sinks into the asthenosphere, the negative buoyancy of the downgoing slab causes a slab pull force (F_{SP}; eq. 2, left term; Turcotte & Schubert, 2014). The slab Pull force is generally considered to be the primary driving force of subduction, with a magnitude of ~5.10^{13}N/m. The slab pull force is magnified by density jumps related to phase transitions within the mantle and oceanic crust (eq. 2, right term; Turcotte & Schubert, 2014). For the olivine-spinel transition, the density jump can generate a force in the order of ~$1.5.10^{13}$N/m. Additional to the ridge push and slab pull forces, the underlying convective mantlegenerates a viscous basal traction or drag force (F_{DF}, eq. 3,) beneath the lithosphere (Turcotte & Schubert, 2014). Depending on the direction of the mantle flow, this force can be a driving or a resistive force and can be on the same order of magnitude as slab pull forces.

Alternatively, resistive forces are also applied against a subducting oceanic plate, such as the shear resistance of the interface, which can be approximated by the integrated frictional strength (F_{IF}, eq. 4, Wolf et al., 2018) and the length of the interface, or the viscous bending of the slab which depends on its curvature radius (F_{BD}, eq. 5, Erdős et al., 2021). Both forces are in the order of ~10^{12}N/m. In a flat subduction zone where thick and young oceanic ridge subducts, it is thought that slab pull force is not the dominant driving force (Cerpa et al., 2014).

$$F_{RP} = \alpha \rho_m g T_m \kappa \left(1 + \frac{2\rho_m \alpha T_m}{\pi(\rho_m - \rho_w)}\right) t\,, \tag{1.1}$$

$$F_{SP} = \left[2\alpha \rho_m g l T_m \sqrt{\frac{\kappa t}{\pi}}\right] + \left[\frac{2T_m \gamma \rho_{Tr}}{\rho_0} \sqrt{\frac{\kappa t}{\pi}}\right], \tag{1.2}$$

$$F_{DF} = \eta_{asth} * \frac{\Delta v}{h} L\,, \tag{1.3}$$

$$F_{IF} = \frac{1}{2} \rho g z_{SI} sin\Phi + C z_{SI} cos\Phi\,, \tag{1.4}$$

$$F_{BD} = v_{conv}\, \eta_{slab} * \frac{H_{slab}}{r^3}\,, \qquad (1.5)$$

Where, α is the mantle thermal expansivity, ρ_m and ρ_w are the mantle and water densities, κ is the thermal diffusivity, t is the age of the lithosphere, l is the slab length, γ is the clapeyron slope, $\rho_{Tr}$is of the density jump. $\eta_{asth}$is the asthenosphere viscosity, Δv is the difference of velocity between the plate and the underlying asthenosphere mantle flow, h is the thickness from Couette flow of the viscous layer beneath the plate, z_{SI} is the depth at the subduction interface. v_{conv} , η_{slab}, H_{slab} are the velocity of convergence between the plates, the effective viscosity and the thickness of the slab, r is the radius of curvature of the oceanic plate.

In general, two major subduction zone styles are recognized: advancing and retreating subduction zones, where the style Depends on the ability of the trench and the overriding plate to move or not, respectively (Heuret et al., 2007; Xue & Strake, 2022; Stegman et al., 2010). In the advancing style, the slab can roll-over on it-self, whereas in the retreating style the slab is rolled backwards, which leads to additional forces playing a role in the evolution of a subduction zone. For example, suction forces can take place in the context of significant slab roll-back and are associated with convective thinning processes and back-arc spreading (Erdős et al., 2021). The asthenospheric mantle underneath the oceanic plate can escape the roll-back of the slab by either poloidal or toroidal flow, depending on whether it is at the edge or the middle of the downgoing plate (Schellart et al., 2007). Other forces can also resist the effect of the trench motion and the style of deformation. For instance, in a subduction type orogen, differences in the gravitational potential energy related to the forearc and foreland can also resist the slab and inhibit the advance of a trench (Becker & O'Connell, 2001).

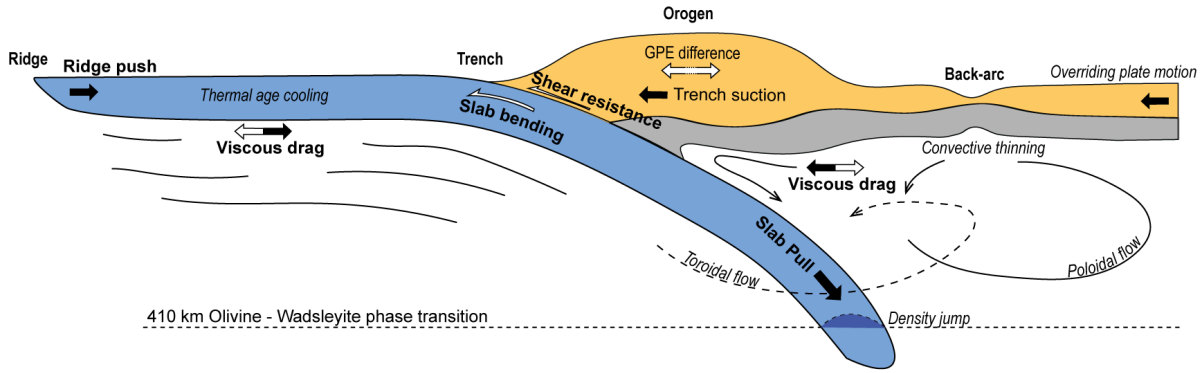

Figure 1.5 Summary of plate-driving forces. Simplified overview of the different forces in a subduction zone. Black filled and white filled arrows indicate the main driving and resistive forces. GPE is for Gravitational Potential Energy.

1.5 Method

1.5.1 Governing equations

We use the geodynamic finite element code ASPECT (Advanced Solver for Problems in Earth's ConvecTion, Bangerth et al., 2021; Kronbichler et al., 2012; Heister et al., 2017; Rose et al., 2017) to setup 2D (Chapter 2) and 3D (Chapter 3-4) subduction models. The models solve three conservation equations for the momentum (1.6), mass (1.7) and energy (1.8), as well as the advection and reaction equations (1.9) for the different compositional fields. The energy equation includes the radiogenic heating, shear heating, and adiabatic heating.

$$-\nabla \cdot (2\eta\dot{\varepsilon}) + \nabla p = \rho g\,, \tag{1.6}$$

$$\nabla \cdot \boldsymbol{u} = 0\,, \tag{1.7}$$

$$\rho Cp\left(\frac{\partial T}{\partial t} + \boldsymbol{u} \cdot \nabla T\right) - \nabla \cdot k\nabla T = \rho H + (2\eta\dot{\varepsilon}) : \dot{\varepsilon} - \alpha T\, \boldsymbol{u} \cdot g\,, \tag{1.8}$$

$$\frac{\partial ci}{\partial t} + \boldsymbol{u} \cdot \nabla ci = qi\,, \tag{1.9}$$

with the deviatoric strain rate tensor $\dot{\varepsilon} = \frac{1}{2}(\nabla \boldsymbol{u} + (\nabla \boldsymbol{u})^T$, the velocity field $\boldsymbol{u} = u(\vec{x}, t)$, the pressure $p = p(\vec{x}, t)$, the temperature $T = T(\vec{x}, t)$, Cp the heat capacity, ρ the density, ρ the reference density, k the conductivity, α the thermal expansivity, H the radiogenic heat production, η the viscosity, t the time, ci the composition, and qi the reaction rate. Note, that for the 3D data-driven model (Chapter 3-4), the energy equation (1.8) does not include the radiogenic heating term because it is already included in the initial thermal model (Rodriguez Piceda et al., 2022), but it does include the shear and the adiabatic heating terms.

The conservation equations are solved assuming a continuous medium. Therefore, rather than discrete fault structures, highly deformed areas consist of shear zones that potentially represent highly "faulted areas".

Although the models are incompressible, we adopt the equation of state of Murnaghan (1.10) (Murnaghan, 1944) to simulate realistic phase transformations that require a temperature and pressure dependent compressible density formulation. Previous studies have shown compressibility to have a small effect on mass conservation for subduction models, suggesting that it can likely be neglected (Fraters, 2014).

$$\rho f = \rho refi \left(1 + \left(P - \left(\frac{\alpha i}{\beta i}\right)(T - Tref)\right) ki\beta i\right)^{\frac{1}{ki}}, \quad (1.10)$$

Where ρf is the final density and $\rho refi$ is the reference density for each composition at surface pressures and a surface temperature of 20°C (Tref). Where αi is the thermal expansivity, βi is the isothermal compressibility, and ki is the isothermal bulk modulus pressure derivatives.

1.5.2 Rheology

Material in the model uses a visco-plastic rheology (Glerum et al., 2018). The viscous regime is handled using a harmonic average of the dislocation and diffusion creep (1.11), whereas the plastic regime uses the Drucker-Prager criterion when the viscous stress exceeds the yield stress (1.12-1.13).

$$\eta_{\mathrm{diff|disl}} = 0.5\, A_{\mathrm{diff|disl}}^{\left(-\frac{1}{\mathrm{n}}\right)} d^{m} \dot{\varepsilon}_{\mathrm{e}}^{\frac{1.-\mathrm{n}}{\mathrm{n}}} \exp\left(\frac{Q_{\mathrm{diff|disl}} + P.V_{\mathrm{diff|disl}}}{nRT}\right), \quad (1.11)$$

A is the prefactor rescaled from uniaxial experiment, n is the stress exponent, d and m are the grain size and grain size exponent, $\dot{\varepsilon}_e$ is the square root of of the second invariant of the strain rate, Q is the Energy of activation, V is the volume of activation, P the pressure, R the gas constant and T the temperature. Here n=1 for the diffusion creep case and m=0 for the dislocation creep case. The yield stress σy is defined by Drucker-Prager law.

$$in\ 2D: \sigma y = C.cos(\Phi) + P.sin(\Phi), \quad (1.12)$$

$$in\ 3D: \sigma y = \frac{6C.cos\Phi}{\sqrt{3(3-sin\Phi)}} + \frac{6P.sin\Phi}{\sqrt{3(3-sin\Phi)}}, \quad (1.13)$$

Where C is the Cohesion, P the effective pressure and Φ the internal friction angle in radian. We also included plastic strain softening of the friction and cohesion that depends on the accumulated plastic strain through time. For example, in model M1 (Chapter 2, Table A.S1), the internal friction angle of the upper crust decreases linearly from 30° to 6° between an accumulated plastic strain weakening interval of 0 to 1.5, while the weak foreland sediments decrease from 30° to 3° between 0 to 0.5.

The effective plastic viscosity is then calculated by

$$\eta = \frac{\sigma y}{2\dot{\varepsilon}}, \quad (1.14)$$

1.5.3 Technical challenges

Geodynamic numerical modelling is a useful tool to simulate the interactions of forces involved in subduction dynamics in a physically consistent manner. This thesis relies on this approach and presents two primary original aspects. The first one, which is related to the first part of the thesis, concerns the development of a 2D high-resolution model to study the interaction between overriding plate deformation and subduction dynamics using the geodynamic code ASPECT (Advanced Solver for Problems in Earth's ConvecTion, Kronbichler et al., 2012; Rose et al., 2017; Heister et al., 2017; Bangerth et al., 2021). The 2D high-resolution subduction model (chapter 2) builds upon the model of Sobolev et al (2005), and incorporates self-consistent, buoyancy-driven, subduction while allowing the overriding plate to dynamically weaken and deform. For that aim, I have extended the model deeper and incorporated the Mantle Transition Zone and lower mantle, which are necessary to simulate the subduction dynamics. The slab sinking velocity is controlled by the buoyancy of the subducting plate, which depends on its density contrast with the asthenosphere as well as on the tambient mantle viscosity, often referred to as the Stokes velocity (Quinteros et al., 2010; Booma et al., 2019, Ribe et al., 2010; Goes et al., 2011; Capitanio et al., 2007). An innovating aspect of this study was the ability to reproduce the shortening phases of the central Andes in a self-consistent subduction model. This was possible by incorporating realistic phase changes for the oceanic mantle lithosphere and asthenosphere (olivine-ringwoodite-bringdmanite-spinel) and for the oceanic crust and lower crust (gabbro-eclogite-stishovite). The drawback with this approach is that more complex models are computationally expensive. Thus, a second challenge was to develop multiple new modules that utilize the Adaptative Mesh Refinement function (AMR) of ASPECT to track and refine the deforming overriding plate, the subduction interface and the subducting plate at high resolutions while maintaining a relatively short computation time. The third challenge was to develop an efficient postprocessing workflow that extracts the relevant model information (e.g., plate velocities, slab dip, trench velocity, and topography) to compare them to geological and geophysical observations.

The second original aspect similarly utilizes the ASPECT code to construct a 3D geodynamic data-driven model. This model includes the geometry of the oceanic Nazca plate and the lithospheric structures of the South American plate to investigate the effect of the flat slab and the inherited structures on the localization of deformation. The 3D data-driven model described in chapter 3 and 4 is inspired by the work of Dr. Sibiao Liu and Dr. Federico Ibarra (both PhD students from the StRATEgy training group). They developed a 3D data-driven model of the Central Andes foreland (Chaco–Paraná basin and Santa Barbara system) and demonstrated the importance of weak foreland sediments and orogenic crustal thickness on the foreland deformation style (e.g thick versus thin-skinned; Ibarra et al., 2019: Liu et al., 2022). Using a similar approach, I incorporate the structural and thermal lithospheric models of the Southern Central Andes, published by the

former StRATEGy II PhD student Constanza Rodriguez Piceda et al. (2021,2022), into a large-scale, dynamic, 3D model. Additionally, I integrate geometries that correspond to the present-day subduction of the Nazca plate, as well as the Pampean flat slab, to discuss the relative effects, and importance of, of continental inheritance and the oceanic plate geometry (Chapters 3-4).

1.6 Problematics and structure of the thesis

Overall, the main question addressed in this thesis is, "what is the nature of the tectonic shortening in the Central Andes? " According to previous work mentioned in earlier sections, the shortening of the Andes involved complex interactions between the oceanic Nazca and South American continental plates. Therefore, I have subdivided the main question into three questions that are addressed in different chapters:

(I) What controls the variability of the shortening rate in Central Andes?

(II) What is the effect of inherited structures within the continent on strain localization?

(III) What is/was the role of the Pampean flat-slab on strain localization and in the formation of the Andes?

Chapter 2 is based on a paper submitted to the Journal of Geophysical Research: Solid Earth. It investigates how the variability in shortening rate in the central Andes (Oncken et al., 2006-2012), as well as other geologic events such as the timing of topographic growth (Garzione et al., 2017) or volcanic activities (Trumbull et al., 2006), are related to plate interactions and subduction dynamics associated with the Nazca oceanic plate. To do so I built high-resolution, buoyancy driven 2D geodynamic subduction models in which I've incorporated the key factors proposed in previous studies (section 1.5-1.8) that are relevant for the dynamic weakening of the upper plate (e.g., absolute westward motion of the South American plate, eclogitization of the lower crust, rapid foreland sediment weakening, high friction at the subduction interface, etc.). I tracked the upper plate shortening rate and compared it to geological data. After defining a reference model, I ran multiple simulations to assess the relative effects of these key factors on the shortening rate and subduction dynamics. Based on these models, I proposed a new mechanism explaining the pulsatile deformation of the Central Andes in the last 15Ma, which is steepening and buckling of the subducted plate.

Chapter 3 introduces a 3D thermomechanical data-driven geodynamic model of the Southern Central Andes, including the Pampean flat slab and the Sierras Pampeanas, based on the lithospheric structural model and thermal model of Rodriguez Piceda et al (2021, 2022). In this study, I utilized short time simulations where I assess the relative contribution of the material properties, the surface topography, the strength of the subduction interface, and the velocities of the plates on surficial strain localization on top of the flat- and steeper- slab segments. With this approach, I was able to quantify the effect of inherited structures and plate geometry on strain localization.

Chapter 4, uses the results of the 3D thermomechanical data-driven geodynamic model of the southern Andes (chapter 3) to propose a new mechanism that reconciles multiple geological events in the southern Central Andes, including the onset of the deformation and the uplift of the basement blocks of the Sierras Pampeanas. I also revised the geological interpretation of the switch of the foreland deformation style. Further, I examine whether this interpretation is applicable in explaining the uplift of the Rocky Mountains during the Laramide orogeny and the passage Farallon flat-slab. In the last part of the chapter, I integrated the results from previous chapters in order to discuss a "big picture" of the interaction between the Nazca plate and the South American plate in the Central and Southern Central Andes.

Chapter 5 discusses the results of the previous chapters and particularly, discusses how they contribute to answering the three questions posed in this introduction, as well as the main question of this work. Finally, I propose targets of future subduction modelling work of the Andes.

Chapter 6 presents a summary of the most important results of this thesis.

Chapter 2 Hindered trench migration due to slab steepening controls the formation of the Central Andes

2.1 Abstract

The formation of the Central Andes dates back to ~50 Ma, but its most pronounced episode, including the growth of the Altiplano-Puna Plateau and pulsatile tectonic shortening phases, occurred within the last 25 Ma. The reason for this evolution remains unexplained. Using geodynamic numerical modelling we infer that the primary cause of the pulses of tectonic shortening and growth of the Central Andes is the changing geometry of the subducted Nazca plate, and particularly the steepening of the mid-mantle slab segment which results in a slowing down of the trench retreat and subsequent increase in shortening of the advancing South America plate. This steepening first happens after the end of the flat-slab episode at ~25 Ma, and later during the buckling and stagnation of the slab in the mantle transition zone. Processes that mechanically weaken the lithosphere of the South America plate, as suggested in previous studies, enhance the intensity of the shortening events. These processes include delamination of the mantle lithosphere and weakening of foreland sediments. Our new modelling results are consistent with the timing and amplitude of the deformation from geological data in the Central Andes at the Altiplano latitude.

2.2 Introduction

The Central Andes is a natural laboratory to study tectonics and geodynamics processes. Although the subduction of the Nazca oceanic plate below the South American plate has been ongoing since at least ~200 Ma, most of the Andean orogen formed in the last ~15 Ma (Oncken et al., 2006, 2012). This unusually short growth time is recorded by shortening rates using various geological methods that constrained fault activities (Oncken et al., 2006, 2012 ; Anderson et al., 2018). The Central Andes hosts the second largest plateau in the world, the Altiplano-Puna plateau, which is on average ~4 km high and extends over an area of 500,000 km² (Figure 2.1a-b). A few different mechanisms are thought to have contributed to the shortening of the Central Andes at the Altiplano latitude (~21°S):

- The *westward absolute motion of the South American plate* (~2 cm/yr) provides the main shortening force (Silver et al., 1998; Sobolev & Babeyko, 2005; Martinod et al., 2010; Husson et al., 2012), where the relative velocity between the trench and the plate determines the tectonic stress regime (Lallemand et al., 2005; Funiciello et al., 2008; Lallemand et al., 2008; Holt et al., 2015). Slower trench migration as a consequence of the slab anchoring in the lower mantle over the last ~40 Ma (Faccenna et al., 2017; Schepers et al., 2017) is argued to have initiated the shortening in the Central Andes.
- A *high interplate friction coefficient* of ~0.05-0.07 due to the low supply of sediments at the trench promotes the stress transfer from the slab to the overriding plate, accelerating the shortening (e.g., Lamb

& Davis, 2003; Sobolev & Babeyko, 2005; Sobolev et al., 2006; Gerbault et al., 2009; Heuret et al., 2012; Tan et al., 2012; Cosentino et al., 2018; Horton 2018; Muldashev & Sobolev, 2020; Brizzi et al., 2020).

- W*eakening of the continental lithosphere* that results from the eclogitization of the mafic lower crust (Sobolev & Babeyko, 1994; Babeyko et al., 2006) and the delamination of the lithospheric mantle (Kay & Mahlburg Kay, 1993 ; Beck & Zandt, 2002 ; Babeyko & Sobolev, 2005; Sobolev & Babeyko, 2005; Beck et al., 2015) helps strain localization and thereby increases the amount of shortening. The crust is eventually exposed to the hotter asthenosphere, leading to an increased basal heat flow. This increased heat flow could lead to strong partial melting of the thermally weakened crust (up to ~20%, Haberland et al., 2003; Schurr et al., 2003; Hamza et al., 2005), which may weaken it further.
- *Weak sediments in the foreland* help initiate simple shear shortening characterized by underthrusting of the Brazilian Cratonic shield (Allmendinger & Gubbels, 1996; Allmendinger et al., 1997; Kley, 1999; Babeyko & Sobolev, 2005; Gao et al., 2021; Liu et al., 2022; Gimbiagi et al., 2022).
- *The passage of the flat-slab* at ~30-35 Ma (~21°S; Yáñez et al., 2001; Bello-González et al., 2018) may have contributed to the weakening of the continental lithosphere and the acceleration of Andean shortening by scraping and bulldozing the continental sublithospheric mantle. (Jordan, 1984; Ramos & Folguera, 2009; Liu & Currie, 2016; Horton, 2018; Gutscher, 2018).

Despite the multitude of proposed shortening mechanisms, none adequately explains the evolution and variability of the deformation in the Central Andes during the last ~35 Ma (Figure 2.1c). However, the resolution of the shortening rate compilation (< 5 Ma) from Oncken et al (2006-2012, Figure 2.1c) offers a solid base to investigate this problem through geodynamic models. Although the data may carry intrinsic uncertainties from using different measurement methods, it shows a systematic consistency in shortening amplitudes across time and latitude.

Shortening rates along the Altiplano section at 21°S are the most temporally resolved and suggest four different phases of deformation in the last ~50 Ma (Figure 2.1c). Between ~50 to 33 Ma (*Phase 1*), the shortening rate linearly increased from 0 to ~3.5 mm/yr before escalating at ~33 Ma to ~8 mm/yr. From ~33 to 15 Ma (*Phase 2*), the shortening rate stagnates in a range between ~4 and ~7 mm/yr. From ~15 to 7 Ma (*Phase 3*) the shortening rate pulsed, reaching a maximum of ~11 mm/yr before dropping to ~5 mm/yr. Following this, a second pulse occurred from ~7 Ma to present (*Phase 4*) that reached a maximum value of ~16 mm/yr before dropping to the ~8 mm/yr seen from present day GPS velocities (Bevis et al., 2001; Klotz et al., 2006) .

Utilizing high-resolution geodynamic models, with buoyancy-driven subduction, and validating them through geological shortening data from the Central Andes, this study proposes a new mechanism associated with slab steepening due to buckling events. This mechanism provides an explanation for the variability of the shortening rate. The models additionally address the decline in deformation intensity between 7 and 4

Ma to present-day levels. Our results suggest that a complex interaction between the oceanic and continental plates controls the timing and variability of the deformation in the Central Andes since the Oligocene.

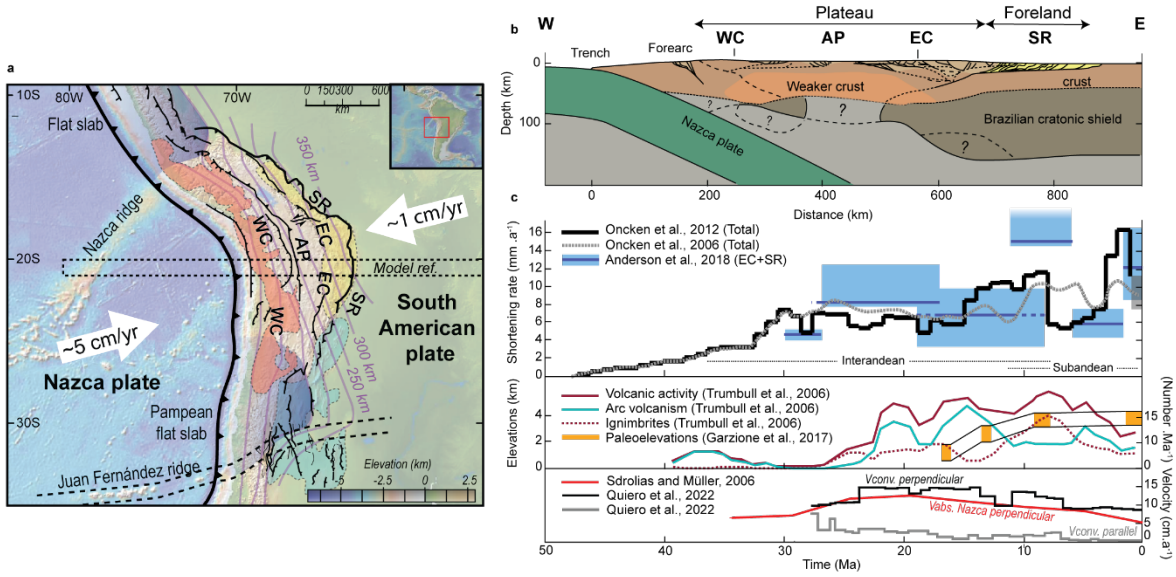

Figure 2.1 Structural map and cross section of the Central Andes. **a** Structural map of the Central Andes (modified from Oncken et al., 2006), overlain with the extent of the active magmatic arc (red) and the foreland areas with thin-skinned (yellow) and thick-skinned (light-blue) deformation. Blue shaded areas indicate the neighbouring flat-slab regions. White arrows show the present day absolute plate velocity (Becker et al., 2015). **b** Schematic tectonics of the Altiplano transect at 21°S (dashed rectangle in a), modified from Oncken et al. (2006) and Armijo et al. (2015). The question mark indicates an unclear presence of the lithosphere. **c** Estimated shortening rate evolution (Oncken et al., 2006-2012; Anderson et al., 2018), volcanic activity (Trumbull et al., 2006), paleoelevations (Garzione et al., 2017), absolute velocity of the Nazca plate (Sdrolias and Müller, 2006) and perpendicular and parallel convergence velocity (Quiero et al., 2022). Blue squares indicate the margin of error of the estimated retroarc shortening rate (EC+SR, Anderson et al., 2018, modified from Quiero et al., 2022). WC: Western Cordillera; AP: Altiplano Plateau; EC: Eastern Cordillera; SR: Subandean Ranges.

2.3 Numerical model set up

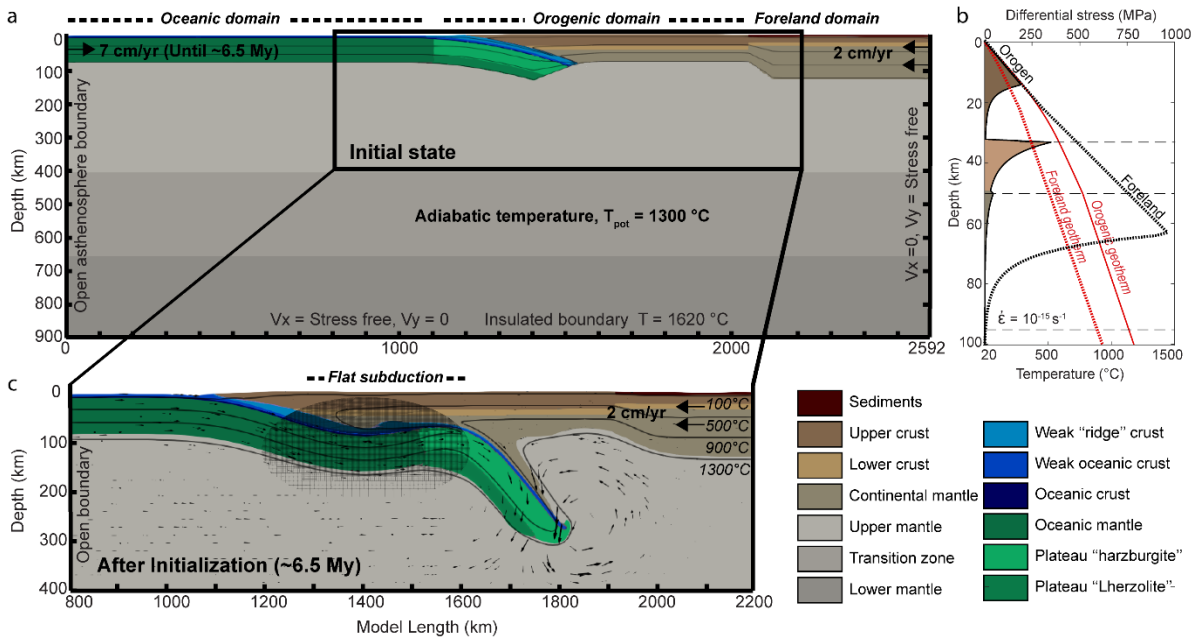

Figure 2.2 Model setup (Chapter 2). Tpot is the mantle potential temperature. **a** Shows the initial state of the model. **b** shows the initial temperature (red lines) and yield strength envelops (dark lines) of the orogenic (solid lines) and foreland (dotted lines) domain. **c** is a zoom-in on the area of plate interface during the initial flat-slab subduction stage for all models at the beginning of the free subduction at ~ 6.5 My.

We split the model box into 2 sub-boxes; a 96 km thick (in depth) box that represents the lithosphere, and an 804 km thick box that represents the sublithosphere mantle. This allows us to set more flexible independent side boundary conditions for each sub-box. For example, during the initialization we prescribe horizontal velocity to the lithosphere, the vertical velocity is stress free, whereas the initial lithostatic pressure is used to simulate an open side boundary in the sublithosphere mantle. The left border is fully open after initialisation. The entire box is 2592 x 900 km, which gives an aspect ratio of ~1:3 while the cells are square (Gerya et al., 2019). The adaptive mesh is refined based on the compositional fields and the magnitude of the strain rate. The asthenosphere mantle and the oceanic lithosphere mantle have a fixed resolution of 32 and 4 km, respectively. Surface topography is calculated using the ASPECT-Fastscape coupling (Braun & Willet, 2013; Bovy, 2021; Neuharth et al., 2021a; 2021b) using a very low diffusion coefficient (~1e-6 m^2/year) simulating sluggish surface erosion in the central Andes.

In order to convert the model time (t_{mod}) to a real time (t_{real}) we assume that t_{real} (Ma)= 38-t_{mod}(My). As such, after the initial flat-slab stage (~6.5 My) the model starting time corresponds to a t_{real} value of 31.5 Ma (Figure 2.5). Subduction in the model is initiated by prescribing an oceanic plate velocity of 7 cm/yr in the first 6.5 My, which represents the plate velocity between 35-30 Ma (Sdrolias and Müller, 2006). After this no oceanic plate velocity is prescribed, and the oceanic plate freely sinks through the mantle due to slab pull. The trenchward velocity of the continental plate is set to 2 cm/yr, corresponding to the average overriding plate velocity during the last 40 Ma. As gaps in the Andean volcanic activity at ~30-35 Ma suggest a phase of

flat-slab subduction (Barazangi & Isacks, 1976; Isacks, 1988; James and Sacks, 1999; Ramos et al., 2002; Ramos & Folguera, 2009), we initialized the model with a flat-subduction stage (Figure 2.2a, A.2). After initialization (Figure 2.2c), the flat-slab segment is ~250 km long at ~100 km depth, similar to the current Pampean flat-slab (Marot et al., 2014). This initialization (A.2) is required in a 2D model to simulate change of buoyancy of the oceanic plate in the Central Andes linked to the southwards migration of the flat-slab at ~25 Ma (Yañez et al., 2001; Bello et al., 2018). Note, that alternative conceptual models also exist. For instance, Kay and Coira (2009) indicate that slab steepening could have occurred at ~16 Ma between ~21 and 24°S based on the timing of the volcanic activity reconstructed from the ignimbrite volume record. O´Driscoll et al. (2012) and Martinod et al. (2020) consider 2 episodic horizontal subduction events at ~35 Ma and ~15 Ma, respectively.

The geometry of the continental plate is based on structural reconstructions and crustal balance estimations during the Oligocene (Hindle et al., 2005; Sobolev et al., 2006; Armijo et al., 2015). For the shortening analysis, we differentiated two continental domains: the orogenic and the foreland with the thicker lithosphere of the Brazilian Shield margin. We used an oceanic lithospheric thickness consistent with a 40 My old (Maloney et al., 2013) plate near the trench (Turcotte et al., 2002). We assumed a conductive geotherm for the lithosphere and an adiabatic temperature profile for the asthenosphere (Figure 2.2b) and let the temperature re-equilibrates during the initialization phase.

2.4 Modelling results

We have tried to incorporate the most important ingredients found in the literature to simulate the deformation of the Central Andes. In summary, five key ingredients are used to simulate plate interaction in Model 1 (reference model). First, a high-resolution (1 km) visco-plastic subduction interface with a low effective friction coefficient (0.05) enables the brittle-ductile transition to occur at ~45 km depth. Second, the simulate o the main phase transitions, Olivine-Wadsleyite-Ringwoodite-Post Spinel transitions for the asthenosphere and lithospheric mantle (Arredondo & Billen, 2016, 2017; Faccenda & Dal Zilio, 2017) and Gabbro-Eclogite-Stishovite phase transitions for the oceanic crust and continental lower crust to simulate eclogitization (e.g. green colour gradient, Figure 2.4 and Figure 2.6) and delamination. Third, the rapid weakening of foreland sediments (see Method for details) to allow a transition from a thick-skinned to thin-skinned deformation style, and to initiate underthrusting of the Brazilian cratonic shield (Sobolev et al., 2006; Liu et al., 2022). Fourth, the prescribed trench-ward motion of the overriding plate velocity, which provides the main driving force for building the Andes (Silver et al., 1998; Sobolev & Babeyko, 2005; Martinod et al., 2010; Husson et al., 2012). Fifth, the flat-slab subduction which helps to initiate the thermomechanical weakening of the overriding plate through scrapping of the sublithospheric mantle and its removal, exposing the continental crust to the warmer asthenosphere after steepening of the flat-slab (Isacks, 1988; Liu & Currie, 2016). We ran 9 alternative simulations to Model M1 (Table A.S2) : (i) three models with variable

interplate friction coefficient (0.015, 0.035, 0.06; model M2a-c, Figure 2.4b-d, A.1 movie S3-S5); (ii) one model without eclogitization of the lower crust to illustrate its importance for weakening of the overriding plate and strain localization (model M3, Figure 2.4e, A.1 movie S6); (iii) one model to evaluate the importance of higher heat flow and lower crustal viscosity related to partial melting (model M4; Figure 2.4f, A.1 movie S7); (iv) two models demonstrating the role of weak foreland sediments (model M5a-b; Figure 2.4gh, A.1 movie S8-9); and (v) two models to illustrate the role of the overriding plate velocity (model M6a-b; Figure 2.4ij, A.1 movie S10-S11). In addition, we provide a model without flat subduction (Figure SA.10, A.1 movie S12, A.3) where we illustrate its role, in this context we also discuss the resulting subduction velocity. In all models, we measured the balance between the rate of trench retreat (V_{tr}), which is positive when the trench migrates westwards, and the overriding plate shortening rate (V_{sr}), which includes the orogenic shortening rate (V_{os}) and the rate of underthrusting of the Brazilian cratonic shield (V_{und}; Table A.S3). The orogenic shortening and the underthrusting rate are equivalent to the Interandean and Subandean shortening rate (Oncken et al., 2006; 2012, Figure 2.1c). All of these components contribute to accommodating the westward velocity of the overriding plate ($V_{op} = V_{os}+V_{und}+V_{tr}$). When the trench retreat rate is less than the overriding plate velocity, the shortening rate increases to maintain the balance. In this context, we refer to the trench as hindered or blocked.

2.4.1 Reference model (M1)

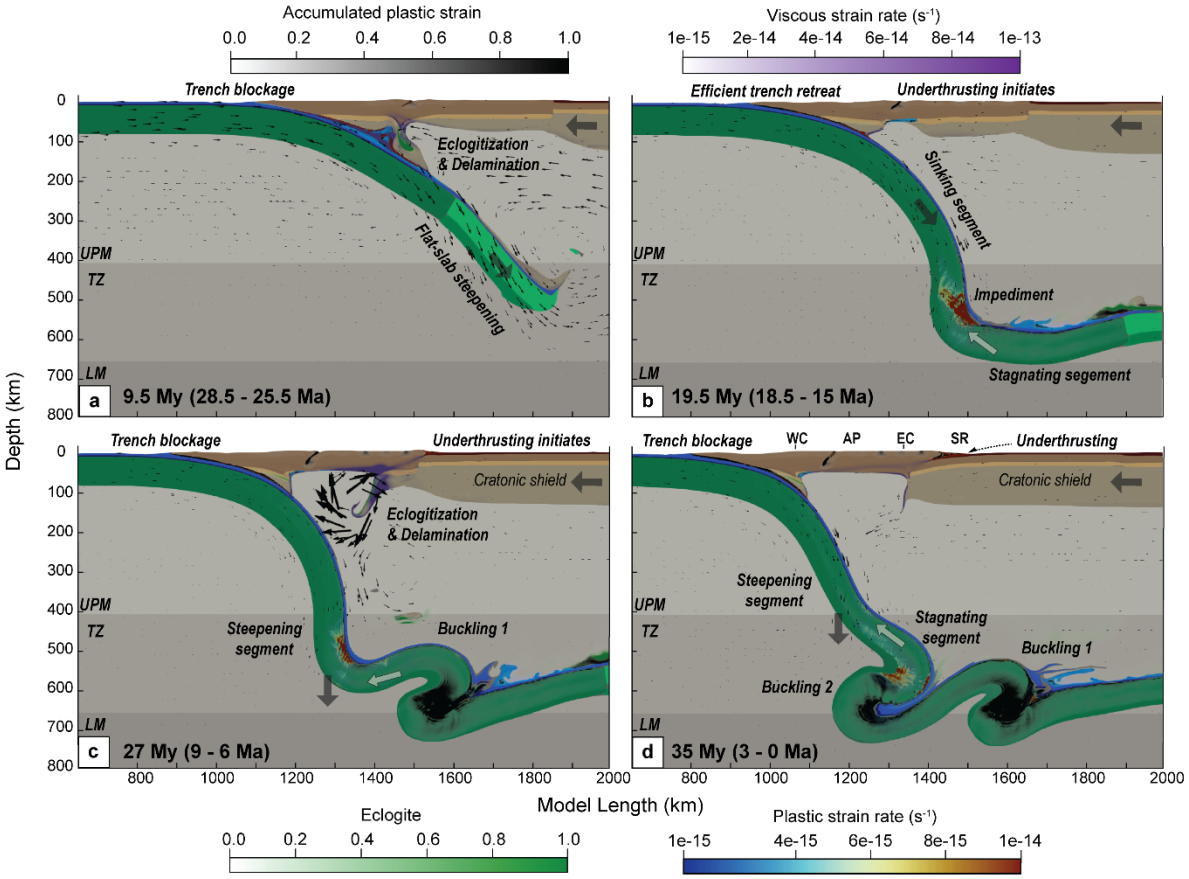

Figure 2.3 Evolution of the reference Model. Evolution of the subduction model M1. UPM, TZ and LM are the upper mantle, transition zone and lower mantle, respectively. Other acronyms defined in Figure 2.1. The small dark arrows indicate the direction of the velocity vectors. Bold arrows indicate the direction of the plate motion and white arrows indicate the direction of the main resistive forces due to slab stagnation in the transition zone. **a** The steepening of the slab is associated with the continental lithospheric mantle removal. **b** The slab freely sinks and flattens at lower mantle transition. **c** The slab buckles, the continent delaminates, the deformation migrates eastward and the foreland underthrusts. **d** The slab buckles a second time and the foreland underthrusts. We also present evolution of the viscosity field in the model (Figure SA.11).

After the initialization stage, subduction evolved dynamically from 7 to 11 My (Figure 2.3a). The slab steepens and accelerates, slowing down the seaward migrating trench as it retreats. Part of the continental mantle starts delaminating when plastic strain localizes over a main thrust fault in the top of the continental crust. During this period, the topographic uplift is limited to the central area or the orogenic domain (equivalent to the Altiplano plateau). At ~10 My, the block of continental lithosphere consisting of eclogitized lower crust and mantle delaminates and sinks with the slab. At ~10.5 My, the subduction velocity decreases as trench retreat reinitiates.

From ~11 to ~20 My (Figure 2.3b), relatively fast slab rollback continues as the slab sinks into the transition zone. At ~18 My, the slab reaches the lower mantle but does not immediately penetrate into it, instead it is deflected and slowly traverses horizontally along the 660-km phase transition boundary. At ~20 My, the slab buckles by folding twice to the west and to the east at the transition zone as the trench continues to retreat.

At ~23.5 My, the slab segment in the upper mantle steepens and halts trench retreat such that the trench no longer moves relative to the mantle. Simultaneously, subduction velocity increases, the previous thrust fault is reactivated, the strain localizes in the eastern orogenic domain, and the lithospheric mantle successively delaminates in the east as the deformation intensifies and migrates east towards the foreland (Figure 2.3c). Underthrusting of the cratonic shield initiates at ~26 My during the delamination period. The eastern domain uplifts from ~20 to 24 My, then slightly subsides at ~24 Ma.

From ~25 to ~31 My the topography significantly uplifts and approximately reaches elevations of the present day (Figure 2.1c and Figure 2.6). At ~29 My, active deformation in the foreland decreases and trench retreat reinitiates as the new slab segment reaches the lower mantle transition trenchward of the older and stalled slab segment. After this time, topography no longer significantly changes (Figure 2.5). At ~30 My, the slab buckles a second time followed by another stage of hindered trench motion at ~35 My (Figure 2.3d) as the slab steepens and accelerates. By ~33.5 My, the cratonic shield has re-initiates underthrusting beneath the orogenic domain. At ~37.5 My foreland deformation becomes less efficient and the mantle wedge starts to delaminate as trench retreat reinitiates. Overall, after 38 My the trench retreats ~330 km, the orogen shortens ~195km. Because of underthrusting the foreland shortens by ~105 km (Table A.S3, Figure 9a-b, A.1 movie S2).

2.4.2 Models with variable interplate frictions (M2a-c)

We ran 3 variations of the reference model M1 that has a friction coefficient at the subduction interface of 0.05 (Figure 2.4b-d, A.1 movie S3-5) where we varied the friction: 0.015 (model M2a), 0.035 (model M2b), 0.06 (model M2c). The friction used in model M2a is thought to be similar to the Southern Andes (Sobolev et al., 2006), although the slab geometry and structure of the upper plate may vary latitudinally. Shortening in model M2a is ~100 km, with most of the deformation being accommodated within the orogen. No underthrusting occurs in that model, suggesting that the deformation did not reach the foreland. With a friction of 0.035 (model M2b) the orogenic shortening increases (~170km), but once the deformation has migrated to the foreland, the shield underthrusts by ~90km at ~29 My. Finally, with a higher friction (0.06) at the interface in model M2c, underthrusting of the shield occurs sooner ~25 My and reaches ~105 km. Initially, most of the shortening is accommodated by the orogen before it quickly migrates to the foreland. The models also suggest that lower friction at the interface results in higher oceanic plate velocities (Figure SA.2).

2.4.3 No Eclogitization Model (M3)

We ran one model (Figure 2.4e, A.S7, A.1 movie S6) without eclogitalization of the lower crust to illustrate the importance of this process. As in the reference model, in the model without eclogitization the slab steepens after the flat subduction stage, however, only a small block of the continental mantle is delaminated. Deformation does not efficiently localize as the plastic strain becomes distributed within the orogen. At ~27.5 My, after the first buckling of the slab, the slab steepens, the orogen shortens, and deformation migrates to the foreland. Shortly after, the shield starts underthrusting as a result of the weakening of the foreland sediments Underthrusting soon becomes inefficient, but after the second slab buckling (~34 My), it reinitiates. After ~38 My, the trench has retreated ~455 km, the orogenic domain has shortened by only ~110 km, and the total underthrusting is only ~65 km.

2.4.4 High heat flow model (M4)

The Central Andes hosts the largest magmatic body in the world (Perkins et al., 2016), and as such the surface heat flux is particularly high (>110 mW/m/K; Hamza et al., 2005; Schilling et al., 2006). This is partly due to partial melting of the crust (up to 20%) as suggested by the high Vp/Vs and high seismic attenuation detected in the area (Haberland et al., 2003; Schurr et al., 2003; Hamza et al., 2005). An increase of the degree of partial melting would result in lower viscosities (McKenzie & Bickle, 1988; Dingwell et al., 1996), and stimulate intra-crustal convection (Arndt et al., 1997; Babeyko et al., 2002). To evaluate the importance of lower viscosities related to partial melt, we ran a model (Figure 2.4f, A.S7, A.1 movie S7) where we increased the thermal conductivity of the upper crust by 1000x and decreased its minimum viscosity to 2.5e18 Pas (vs. ~1e22 Pas in the reference model) when the temperature is greater than 1000 K. In this model the orogenic shortening increases (~280 km vs. ~195 km in the reference model), with the orogenic domain accommodating the majority of the shortening. Strain in the orogen strongly localizes onto a few faults and, thus, does not migrate to the foreland (Figure SA.7, A.1 movie S7). As a result, the sediments do not accumulate enough plastic strain to weaken and underthrusting does not occur. Shortening rate after the first slab buckling cycle is more efficient than in the reference model and reaches ~25 mm/yr. Compared to the reference model, the greater orogenic deformation results in a thicker orogen and higher surface heat fluxes (>120 mW/m; Figure SA.3).

2.4.5 Foreland sediments strength (M5a-b)

Foreland sediments in the reference model (M1) have an internal friction angle of ~3° and a cohesion of 1 MPa, thus an effective friction coefficient is ~0.05. We ran two models in which we increased the internal friction angle and cohesion to 10° and 20 MPa (model M5a, Figure 2.4g, A.1 movie S8) and 30° and 20 MPa (model M5b, Figure 2.4h, A.1 movie S9). In both models, the model initially evolves like the reference model,

but underthrusting is not significant, resulting in a lower accumulated shortening magnitude of ~240 km (Figure SA.8).

2.4.6 Overriding plate velocity (M6a-b)

In the reference model, the overriding plate velocity is 2 cm/yr, which represents an average absolute motion orthogonal to the trench over the last 40 Ma. We ran two alternative models where the overriding plate velocity is 1 cm/yr (model M6a, Figure 2.4i, A.1 movie S10) and 4 cm/yr (model M6b, Figure 2.4j, A.1 movie S11). The M6a model results in a total shortening of ~155 km and a retreat of the trench of ~160 km (Figure SA.9). The slab piles in the transition zone (Figure 2.4i), the orogenic domain shortens during the steepening of the flat-slab and after its delamination during the last 7 Ma. In model M6b, the slab does not deform and is anchored to the lower mantle, the amplitude of shortening is ~450 km and the trench retreat is ~810 km, most of the shortening comes from early foreland underthrusting at ~23 Ma which stops in the last ~5 Ma.

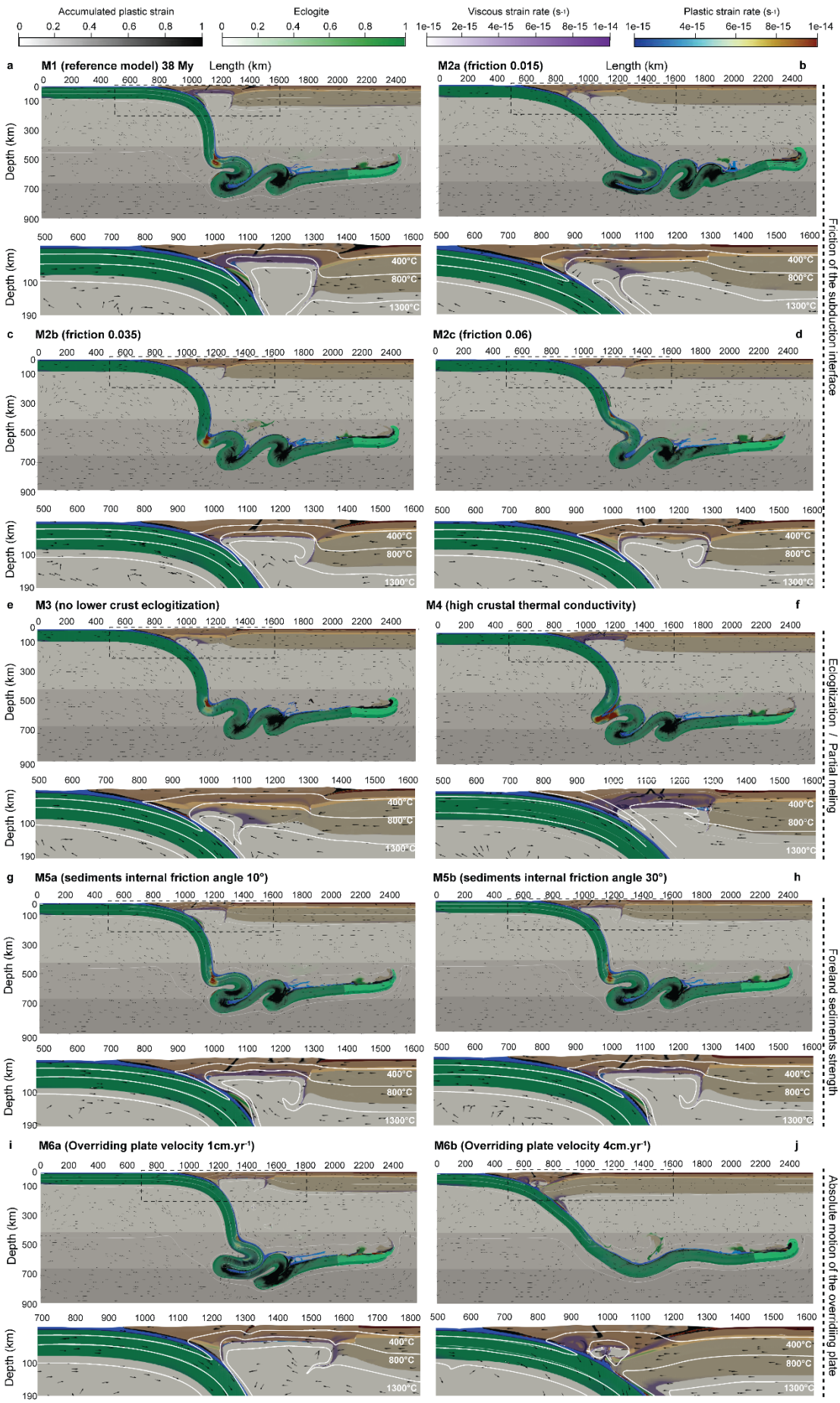
Accumulated plastic strain
0 0.2 0.4 0.6 0.8 1
Eclogite
0 0.2 0.4 0.6 0.8 1
Viscous strain rate (s-1)
1e-15 2e-15 4e-15 6e-15 8e-15 1e-14
Plastic strain rate (s-1)
1e-15 4e-15 6e-15 8e-15 1e-14
a
M1 (reference model) 38 My
Length (km)
b
M2a (friction 0.015)
Length (km)
c
M2b (friction 0.035)
d
M2c (friction 0.06)
e
M3 (no lower crust eclogitization)
f
M4 (high crustal thermal conductivity)
g
M5a (sediments internal friction angle 10°)
h
M5b (sediments internal friction angle 30°)
i
M6a (Overriding plate velocity 1cm.yr-1)
j
M6b (Overriding plate velocity 4cm.yr-1)
Depth (km)
400°C
800°C
1300°C
Friction of the subduction interface
Eclogitization / Partial melting
Foreland sediments strength
Absolute motion of the overriding plate

Figure 2.4 Final state of the model variants. Final state of the models at ~38 Ma which is supposed to be equivalent to present day. **a** M1. **b** M2a. **c** M2b. **d** M2c. **e** M3. **f** M4. **g** M5a. **h** M5b. **i** M6a. **j** M6b. White line isotherms are for 400°C, 800°C, 1300°C.

2.5 Discussion

Our results suggest that the timing of the shortening events is a direct consequence of the interaction between the buckling subducting plate and the weakened overriding plate. In the reference model, we distinguish four notable deformation phases that correspond in amplitude, timing and space to the shortening rate from the geological compilation (Onken et al., 2012). Overall, deformation migrates across the orogenic domain to the eastern foreland in 4 phases, illustrated in Figure 2.5.

Phase I : *Central orogenic domain deformation* (~6.5 to ~11 My): Plastic strain is localized in the center of the orogenic domain (e.g. Altiplano plateau) due to flat-slab steepening and removal of the lithospheric mantle.

Phase II : *Eastern Cordillera domain* deformation (~11 to ~20 My): Distributed plastic strain slowly accumulates in the east. No significant deformation is observed in the continent due to efficient trench retreat.

Phase III : *Deformation migrates from the Eastern Cordillera to the foreland domain* (~20 to ~29 My): Strain intensifies in the Eastern Cordillera domain and migrates to the foreland. The delamination follows this migration. When the Brazilian Cratonic shield starts to underthrust below the orogeny, the delamination accelerates and the underthusting becomes more effective.

Phase IV : *Foreland domain deformation* (~29 to ~38 My): Underthrusting of the shield slows down. At ~33.5 My, it re-accelerates until ~35 My before decelerating until 38 My.

The compressive stress generated by the difference of velocity between the trench and the overriding plate is accommodated in one of two ways: 1) orogenic shortening, 2) underthrusting of the foreland. The effectiveness of deformation localization depends on the strength of the overriding plate and the interplate coupling. Here, we discuss the key processes that affect the strength of the overriding plate, the subduction and deformation dynamics of the slab, and, finally, the interaction between the two plates.

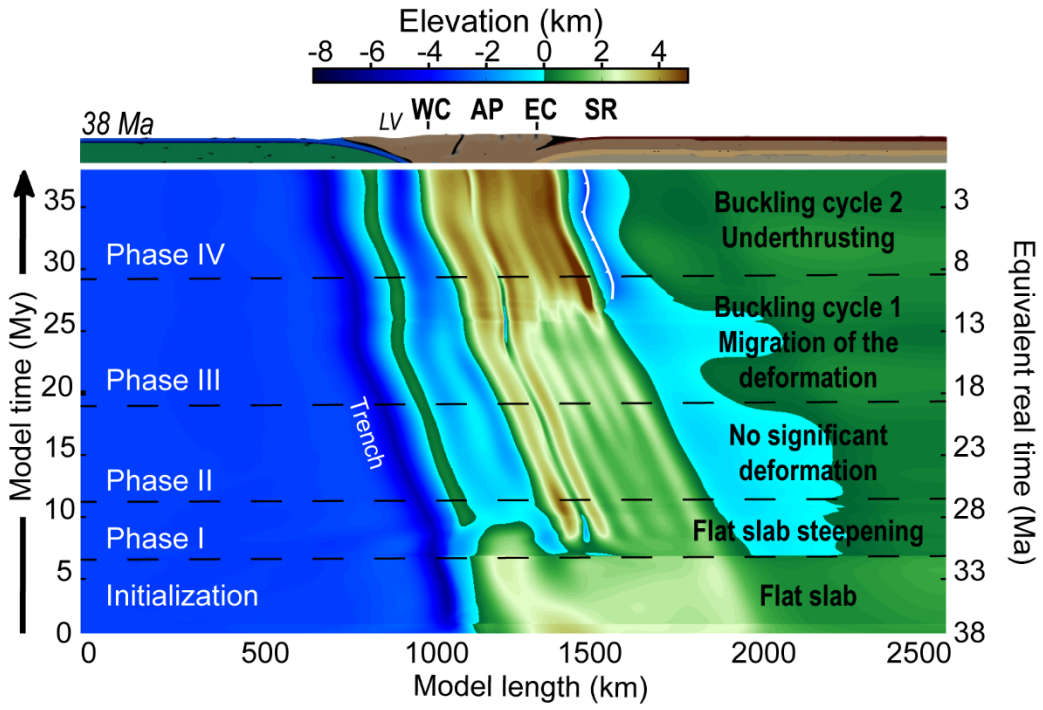

Figure 2.5 Topographic evolution of the reference model, with deformation phase timings shown using dotted black lines, and key features of each phase are written in black. LV is for Longitudinal Valley. Other acronyms defined in Figure 2.1.

2.5.1 Overriding plate

2.5.1.1 Delamination

Extensive lithospheric delamination is known to have taken place under the Altiplano-Puna plateau (Kay & Kay, 1993; Beck & Zandt, 2002; Beck et al., 2015) and contributed to present-day elevations (Garzione et al., 2006, 2008, 2017; Wang et al., 2021). This process is thought to be the result of the eclogitization of the mafic lower crust and lithospheric mantle, which is facilitated by the hydration of the sub-lithosphere from the ~200 Ma subduction history that accelerates the metamorphic reaction (Babeyko et al., 2002, 2006). Additionally,the thick (~45 km) initial crust at ~30 Maresults in a high lithostatic pressure in the lowermost crust (Hindle et al., 2005; Sobolev et al., 2006; Armijo et al., 2015). After eclogitization and delamination the crust warms up, which enhances the weakening of the overriding plate and leads to localized deformation and subsequent delamination events. Model M3 demonstrates that delamination and shortening are inhibited without eclogitization (Figure 2.4). Whereas model M4 shows that, due to the faster crustal thickening accumulated by the weak crust, eclogitization and delamination are very effective when the orogenic domain is thermally weakened. In that latter case, the migration of the deformation to the foreland is not guaranteed (Figure SA.7).

We observe two delamination stages after the first event caused by steepening of the flat-slab in Phase I. First, the initial removal exposes the crust at the western edge that is directly in contact with the asthenosphere, thereby increasing its temperature and decreasing the viscosity at its base. As a result, the lower crust delaminates faster in the west, causing it to asymmetrically drip to the east (i.e., Stage 1 in Figure 2.6a). The pure shear deformation localizes in the orogenic domain until delamination is complete. Second, when the viscous deformation of the orogen connects with the plastic deformation of its foreland at 26 My, the foreland start underthrusting beneath the orogen due to the low effective friction of sediments. This results in orogenic thickening and a switch from pure shear to simple shear shortening. Consequently, deformation migrates to the east causing delamination to accelerate (Stage 2 in Figure 2.6b). We note that our model contrasts with the previous model of Sobolev et al. (2006) where the delaminating lithospheric mantle flowed toward the subduction wedge, and coupled with the sinking plate, increasing the shortening rate.

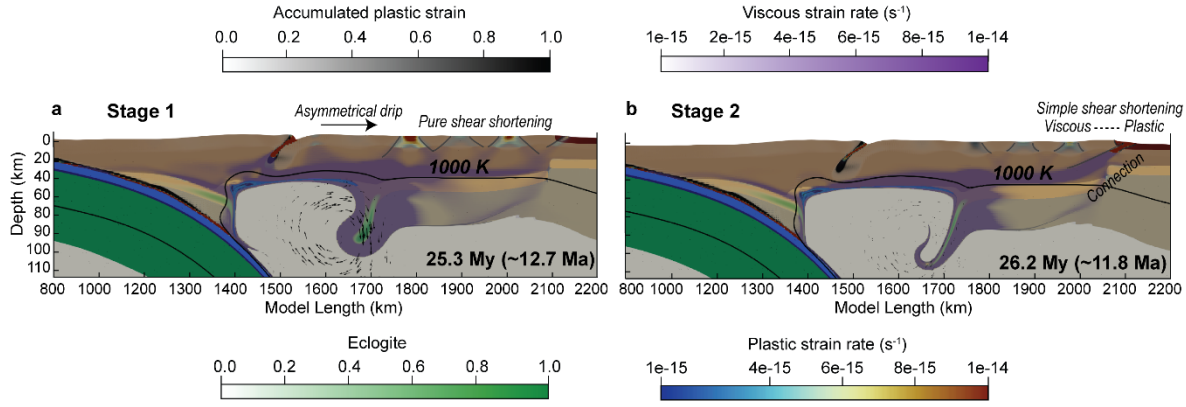

Figure 2.6 Delamination stage. Two stages of delamination associated with different modes of shortening. **a** Stage 1: Asymmetric delamination, facilitated by the heating and pure shear thickening of the continental crust. **b** Stage 2: Delamination acceleration, accompanied by migration of the deformation to the foreland and initiation of the foreland underthrusting by simple shear shortening.

2.5.1.2 Mechanical weakening of the foreland sediments.

The presence of weak foreland sediments in our model is the key factor in simulating the transition from pure shear deformation to simple shear deformation at ~10 Ma in the Atliplano. Simple-shear shortening is associated with higher strain localization over fewer faults and the formation of deep low-angle detachments. In the foreland, these faults are situated near the base of the sedimentary cover and are characteristic of the thin-skinned tectonic style. Increased fluid pressure in the Paleozoic shale layers (Allmendinger and Gubbels, 1996), likely due to rapid deposition of foreland basin strata (Uba et al., 2009), at the front of the orogen, may have resulted in transient weakening and reduction of the effective coefficient

of friction to ~0.05 or less, initiating the underthrusting of the Brazilian cratonic shield (Babeyko & Sobolev, 2005; Babeyko et al., 2006).

In the reference model, underthrusting takes place in two stages. The first stage happens during hindered trench motion at ~20.5 My, causing the deformation to migrate to the foreland. When the active brittle shear zone, from the failure of the foreland sediments, connects to the ductile shear zone accommodating the on-going delamination, underthrusting becomes more efficient. The delamination also facilitates the underthrusting of the Brazilian cratonic shield that meets less resistive forces. Underthrusting of the shield forces the middle and lower crust to flow and thicken forcing the topography to uplift, reaching present-day elevations of ~4 km at ~31 My (~7 Ma ago). A second stage of underthrusting occurs in the last ~4 My when the trench is again blocked, but the topography does not change significantly (Figure 2.5).

2.5.2 Subducting plate

While the westward motion of the South American plate provides the main force (Martinod et al., 2010; Husson et al., 2012) for the tectonic shortening, the magnitude of the compressive stress in the South American plate margin is determined by the resistance of the Nazca plate (i.e., by the ability of the trench to retreat; Lallemand et al., 2005; Funiciello et al., 2008; Lallemand et al., 2008; Holt et al., 2015). In the Central Andes, the trench has migrated west over the last ~40 Ma as a result of the rollback and subsequent sinking of the bending slab in the asthenosphere, as well as the forced trench retreat from the excess velocity of the overriding plate (Schepers et al., 2017). Recent studies have proposed that the trench velocity can also be affected by deep subduction dynamics (Faccenna et al., 2017; Briaud et al., 2020, Boutoux etal., 2021). In this section, we discuss the implications of these subduction dynamics.

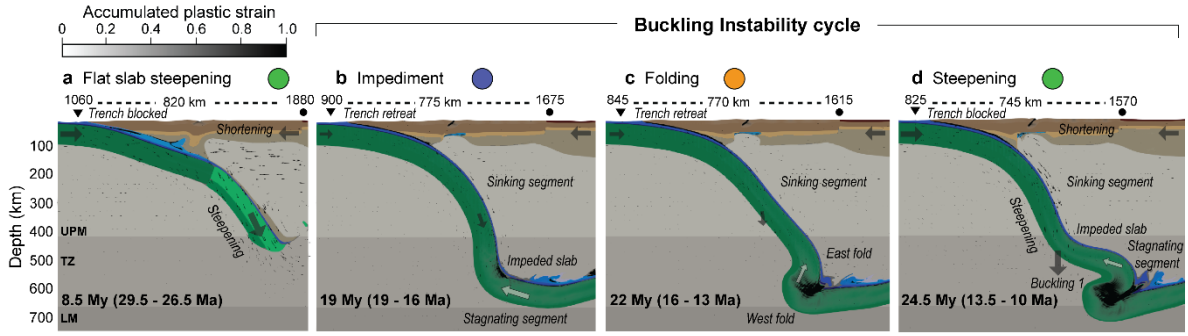

Figure 2.7 Subduction dynamics and slab buckling. Subduction dynamics. Black triangle and circle indicate the position of the trench and the foreland edge, respectively. Colored circles indicate slab evolution in Figure 2.9. The small dark arrows indicate the direction of the velocity. Bold arrows indicate the main plate motion and white arrows indicate the direction of the main resistive forces due to slab stagnation in the transition zone. **a** Steepening and sinking of the flat-slab leads to an increase of plate velocity and slows

down the trench. **b** The slab front is impeded in the viscous lower mantle transition zone. **c** The stagnant slab folds, meanwhile the trench retreats. **d** The slab folds but the lack of obstacle leads to its steepening.

2.5.2.1 Flat-slab steepening

The cause of flat subduction is still debated. It likely results from the shallowing of the slab from long lasting subduction, as well as larger buoyancy related to the Juan Fernandez ridge (Schellart, 2020; Schellart & Strak, 2021) that has migrated to the south during the last ~35 My (Figure 2.1; Yáñez et al., 2001; Bello-González et al., 2018). Others authors (Quinteros et al., 2013; Liu & Currie, 2016) suggested that slab break-off in the upper mantle could have further contributed to the slab flattening by decreasing the slab pull force. The flattening of the slab could also be caused by an increase in asthenospheric pressure due to the proximity of a thick cratonic lithosphere (Pérez-Gussinyé et al., 2008; Manea et al., 2012, 2017).Most shortening in the Central Andes occurs after the passage of the ridge (Oncken et al., 2006; 2012), so in this study we focus on processes after the flattening event. . Our models suggest that a flat-slab at ~100 km depth, analogous to the Pampean flat-slab, could scrape the base of the lithosphere. Eventually at ~7 My model time, the slab steepens and accelerates as the trench becomes blocked (Figure 2.7a). The continental mantle coupled to the flat-slab segment blocks the corner and is pulled down and thus accommodates the deformation. When the lower continental crust eclogitizes, plastic strain localizes in the top portion of the crust. Slab steepening then accelerates due to the eclogitization of the oceanic crust and parts of the lithosphere are removed. This process of delamination is similar to the mechanism of “blocking of the subduction corner” of Sobolev et al (2006) for which the increase in shortening rate results from the coupling between the delaminated lithosphere driven downward by the slab. According to our alternative model M7 (Figure SA.10) that has no flat-slab, flat-slab steepening plays a key role in triggering the initial weakening of the overriding plate, and is facilitated by lower-crustal eclogitization.

2.5.2.2 Buckling instability cycles

Slab buckling occurs when the oceanic plate subducts into the more viscous mantle transition zone or the lower mantle. The difference in velocity between the deeper slab segment relative to the new subducting segment, is accommodated by slab deformation (Ribe et al., 2007). Previous studies have suggested that the lower mantle viscosity and the dip, age, thickness and strength of the oceanic plate may affect the buckling periodicity and timing of slab stagnation in the transition zone, and additionally could be linked to periodic crustal deformation (Ribe et al., 2007; Capitanio et al., 2010; Lee & King, 2011; Quinteros et al., 2010; Capitanio et al., 2011; Quinteros & Sobolev, 2013; Cerpa et al., 2014; Marquardt & Miyagi, 2015; Lyu et al., 2019; Briaud et al., 2020, Boutoux et al., 2021). Analyzing the variety of interchangeable parameters that affect the buckling process exceeds the scope of this study. Here, we first interpret the different stages of the buckling cycles and then propose that the westward velocity of the upper plate is a primary factor in controlling the subduction dynamics regime.

We identified two buckling cycles, at ~20 My and at ~30 My. Within each cycle, three main events are distinguished that may affect the trench migration rate:

(1) Slab impediment (Figure 2.7b) takes place when the slab meets viscous resistance. This is the case when the slab is impeded by the viscous lower mantle at the beginning of a buckling cycle (~17 My and ~29.5 My), or before steepening. For instance, when the slab reaches the viscous lower mantle it does not immediately penetrate it. The first slab segment in contact with the lower mantle slows down and viscously resists the new, still sinking, segment. This difference of velocity between the two segments is accommodated through bending in the slab. During these slab impediment events the dip of the slab becomes shallower and the trench continues retreating. This mechanism differs from slab anchoring (Faccenna et al., 2017), in which the difference of velocity between the two segments is too small to cause the folding of the slab.

(2) Slab folding (Figure 2.7c) events occur when, after slab impediment, the slab dip flips in the transition zone. The now shallower slab dip enables the trench retreat, though no significant deformation is observed. Each buckling cycle consists of two folding events, each consisting of a syncline and an anticline at ~20, 21 My and ~30, 33 My, respectively.

(3) Slab steepening (Figure 2.7d) is a drastic event that occurs at the end of a buckling cycle after the second folding event, (~23.5 My and ~33.5 My). Chronologically, the sinking slab meets resistance from the last fold to the east (i.e., Impediment) and bends to the west as for the first folding event. However, the overriding plate has forced the trench to retreat during the previous events, which, prevents the slab from piling up. The slab continues to sink in the transition zone, steepens and accelerates. The trench slows down and blocks the overriding plate that shortens to accommodate the ongoing deformation. When the trench is blocked, the horizontal stress in the overriding plate can reach values of ~350 MPa (Figure SA.1, A.1 movie S1), which exceeds the maximum strength of the crust (~250 MPa, Figure 2.2) and causes it to shorten. Overall, slab shallowing is associated to periods of trench retreat related to the folding events, whereas slab steepening is associated to periods of hindered trench motion following folding events.

This chain of events occurs in a single subduction dynamics regime, primarily determined by the absolute motion of the overriding plate orthogonal to the trench. By comparing the subduction velocity to the trench velocity, we can identify 3 regimes of subduction dynamics. In the first regime, the lower velocity of the overriding plate leads to the "piling" of the slab in the transition zone (Regime 1; Model M6a, Figure 2.4i, Figure 2.8b and A.S9). In the second regime, the trench episodically blocks due to "buckling and steepening" of the slab (Regime 2; Model M1, Figure 2.4a, Figure 2.8a, and Figure 2.9). In the third regime, the "anchoring" of the slab in the lower mantle and the high forced trench retreat prevent it from buckling (Regime 3; Model M6b**,** Figure 2.4j**,** Figure 2.8c, A.S9).

In all models, flat-slab steepening occurs in a similar manner (i.e., Phase 1). However, westward migration of the trench (i.e., Phase 2) is associated with steady trench retreat for M1 and M6a, but not for M6b for which delamination began earlier. In the latter case, the velocity of the overriding plate is absorbed by the deformation of the orogenic domain, its early delamination, and the underthrusting of the foreland, as the craton no longer encounters resistance from the lithospheric mantle. The rates of shortening and of trench retreat further intensify when the slab becomes anchored in the mantle and the craton is blocked by the slab (Figure 2.8c, A.S9). Both models M1 and M6a are characterized by slab folding, but the higher trench retreat of M1 allows episodic slab steepening, resulting in trench blocking and a slight acceleration of the subduction rate. In contrast, in model M7 that we ran without a flat-slab (Figure SA.10), no deformation happens implying that buckling and steepening occur independently. Nevertheless, the initial weakening of the overriding plate caused by the passage of the flat-slab is necessary to trigger the shortening. Thus, the strength of the orogenic domain is controlled by the timing and intensity of delamination, which plays a major role in transmitting the velocity of the overriding plate to the trench, and controls the timing of underthrusting. The trench velocity ultimately determines the regime of subduction dynamics. Given that westward movement of the overriding plate has decreased from 45 Ma (~3 cm/yr) to the present day (~1 cm/yr), we suggest that the Andean subduction regime may have changed from anchoring to buckling and steepening over the last ~20 Ma.

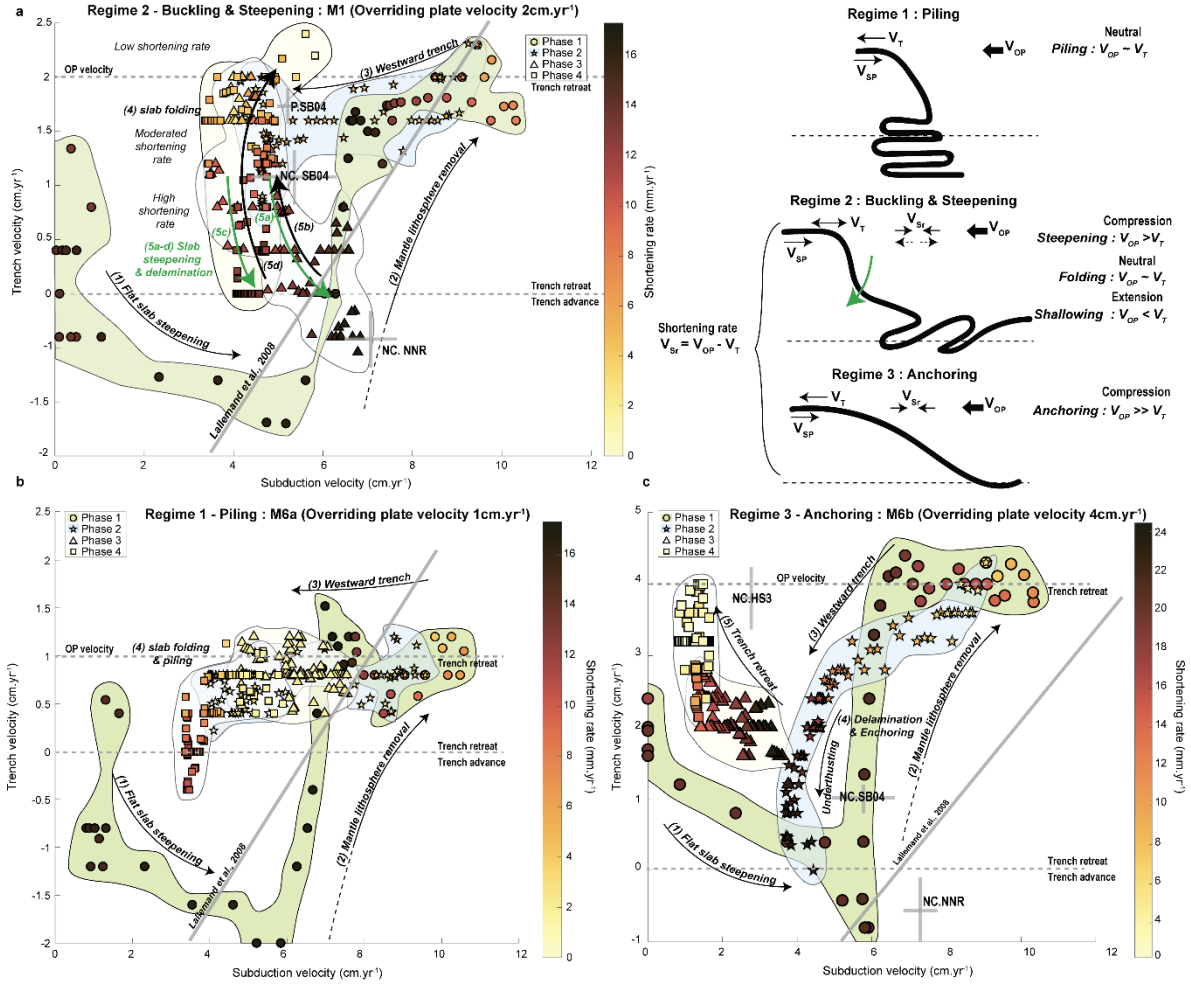

Figure 2.8 Subduction regimes. Detailed evolution of the velocity of the trench (VT) and the subduction (VSP) velocity every 500 ka for : **a** model M1 (VOP = 2cm/yr). **b** M6a (VOP = 1 cm/yr). **c** M6b (VOP = 4cm/yr). Background colors correspond to the time interval of the defined shortening phases (see Discussion for more details) also illustrated by geometric symbols. Symbols are filled by the shortening rate color gradient. Grey cross indicates the range of velocities calculated by Lallemand et al., (2008) for North Chile (NC) and Peru (P) using different reference frame NNR-NUVEL1A and HS3-NUVEL1A (NNR and HS3, Gripp & Gordon, 2002) and SB04 (Steinberger et al, 2004). The grey line is the regression (Lallemand et al., 2008) for which subduction zones at present day trend to align with using HS3.

2.5.3 Interaction between overriding and subducting plates

2.5.3.1 Interplate coupling

Our models predict that an effective friction of 0.035 to 0.05 is required in the Central Andes to obtain significant deformation that is consistent with previous estimates (Sobolev and Babeyko, 2005; Sobolev et al., 2006). Higher friction values result in slightly slower subduction velocity (Figure SA.2) but more intense pulsatile shortening phases during slab steepening (Figure SA.6). The effective friction is dependent on the

sediment thickness at the trench, which at present day may vary from ~0.5 km to ~2 km in the Central and Southern Andes, respectively (Lamb & Davis, 2003). This latitudinal variation results from the efficiency at which the surface processes supply sediments to the trench. In the last ~6 Ma, glacial erosion supplied a large amount of sediments to Southern Andes trench. Whereas in the Central Andes, the internal drainage of the Altiplano-Puna plateau is related to low erosional rates that have contributed to sediment starvation at the trench (Lamb & Davis, 2003; Melnick & Echtler, 2006; Oncken et al., 2006). Hu et al (2021) also show that the temporal variation of sediments included in subduction can lead to a temporal variation in the interplate coupling, suggesting that sediments can be a major contribution of the along-strike shortening magnitude and, thus, the onset of deformation.

2.5.3.2 Slab buckling and overriding plate interaction

The rapid growth of the Andes in the last ~10 Ma (Figure 2.1c, Garzione et al., 2017) results from a sequence of events generated by plate interactions. While subduction dynamics exerts a major control on plunging plate deformation by blocking trench migration, the overriding plate strength ultimately controls where deformation localizes and forces the trench to retreat. In model M1, when the slab does not steepen, the trench is forced to retreat at the prescribed westwards velocity of the overriding plate, ~2 cm/yr (M1, Figure 2.9c). Alternatively, in model M3 without lower crustal eclogitization, the slab steepens independently of the shortening of the stronger overriding plate and the velocity of the overriding plate is accommodated by the forced trench retreat (Figure SA.7). This latter case indicates that the steepening is mostly controlled by slab strength and the slab buoyancy rather than the shortening of the overriding plate. The upper plate strength is evolving, first, with the passage of the flat-slab that may have initially weakened the lithosphere through partial removal of the lithospheric mantle, and through thermal weakening related to crustal exposure near the hotter asthenosphere (Isacks, 1988), and second, by triggering the subsequent delamination (see previous section).

Pulsatile behavior in the deformation of the South American plate has been inferred from paleoelevation reconstructions using stable isotope (Leier et al., 2013 ; Boschman, 2021 ; Garzione et al., 2008) and the magmatic activity (Decelles et al., 2009). We suggest that buckling instabilities in a subducting plate offer a plausible explanation in the variability and timing of the Nazca plate deformation during the last ~20 Ma as well as the present-day deep seismicity distribution (Figure SA.4). We find that shortening rate pulses occur at the end of each buckling cycle when slab steepening inhibits trench retreat (Figure 9c-d), and that these pulses reproduce similar signals to what is seen in the geological data. When the slab steepens the forced trench retreat from the overriding plate is hindered and the horizontal stresses increase (Figure SA.1; A.1 movie S1), resulting in a shortening of the upper plate. Additionally, in the last ~2 Ma the geological data shows a decrease in the shortening rate, which is also predicted by our model through underthrusting. At later stages, the trench retreat resumes and underthrusting loses its efficiency, which could indicate the beginning of a new buckling cycle. More recently, based on updated high-resolution convergence rate data

orthogonal to the trench (Figure 2.1c), Quiero et al., (2002) show that there are some short-term variations over the last ~30 Ma. They attribute these variations to the delamination of the Central Andes (Quiero et al., 2022). The model M7 with no flat-slab suggests that these variations could represent pulses associated with deep subduction dynamics, causing a periodic increase in subduction velocity (Figure SA.10, A.3). Nonetheless, in this model, no deformation occurs due to the lack of weakening of the overriding plate from the absence of the flat-slab and the overriding plate remains strong, so trench retreat is therefore more effective and may delay the steepening of the slab, causing the last pulse to occur ~3 Ma later (Figure SA.10d). We also notice that the periods of steepening also correlate with flare-up of volcanic activity and greater volume of ignimbrites (Figure SA.1c, Trumbull et al., 2006). Slab steepening and lithospheric mantle delamination becomes more active when the trench is hindered, which can lead to (Figure 2.9a) an increase in the basal heat flow of the lithosphere and more intense volcanic activity (section 4.1.1, Isacks, 1988; Kay & Coira, 2009).

Previous seismic tomography studies indicate two large negative seismic anomalies near the transition zone (at depths of 600 km and 900 km) that are attributed to slab accumulations (Widiyantoro, 1997; Liu, 2003; Chen et al., 2019). The deeper accumulation may relate to a slab anchoring before (Faccenna et al., 2017, Figure SA.4), suggesting that previous accumulation cycles could have occurred before and have "avalanched" in the lower mantle (Briaud et al., 2020; Hu & Gurnis, 2020), wherein they may have become detached from the shallower slab. Indeed, the Peruvian phase from ~110 to 70 Ma consists of a rapid series of alternating compressive and extensive regimes of ~10 Ma (Mora et al., 2009; Faccenna et al., 2017) may indicate that slab buckling events have happened earlier in the northern subduction history. However, because of the absence of an efficient weakening mechanism to trigger delamination and too thin crust to facilitate eclogitization, the orogen experienced no significant deformation. Potentially, we suggest that these avalanche events may have repeated at least 3 times over the last ~90 Ma, as suggested by the 3 cycles of convergence rate recognized in Martinod et al. (2010). These events could also explain the cyclicity of the orogenic processes (Decelles et al., 2009; Haschke et al., 2002; DeCelles et al., 2014).

2.5.4 Model limitations

The main limitation of our model is its dimensionality. The use of 2D modelling is appropriate for the Central Andes, where toroidal flow affecting the edges of the Nazca plate can be neglected. However, latitudinal crustal flow is estimated to have contributed between ~10% to 30% of the present day crustal thickness of the Central Andes (Kley & Monaldi, 1998; Hindle et al., 2005). In our models the crustal thickening is mainly caused by intraplate shortening. As a result, the crustal thickness of the orogen in our models is lower than the actual thickness of the Central Andes. For example, in model M1 the final orogenic crustal thickness is ~57 km, whereas it should increase to ~62-74 km (+10 to 30 %) taking into account the latitudinal

crustal flow. In addition, shortening may also be underestimated, which could partially explain the crustal thickness deficit in the models.

In the model M2a (Figure SA.6), the final dip of the slab agrees with the seismic tomography (Figure SA.4). In this model the interplate friction is 0.015, similar to the expected friction of the southern Andes (Sobolev and Babeyko, 2005). This suggests that the current dip of the subducting plate in the central Andes is partially caused by lateral support of the shallower oceanic plate to the south. In addition, the appearance of a deeper slab pile 900 km to the east could also indicate deep mantle flow that is not accounted for in our model. Slab buckling could provide a plausible explanation for the distribution of deep seismicity (Figure SA.4).

We find that with an interplate effective friction of 0.05 (Figure SA.2), the maximum amplitude of the modeled subduction velocity is lower than the absolute normal velocity of the Nazca plate (~12.5 cm/yr at ~20 Ma, Sdrolias & Müller, 2006). This suggests that slab velocity is largely controlled by the slab interface friction southward and northward of central Andes, where effective friction is lower due to the presence of sediments. Interestingly, despite the lower subduction velocity, our model predicts a decrease in the pulsatile intensity during the last ~25 Ma to 20 Ma in accord with the observations.

2.6 Conclusion

In this study, we demonstrate that cycles of slab buckling due to dynamic slab behaviour can explain the timing and amplitude of tectonic shortening pulses observed in the Central Andes since the Late Eocene. The findings of our subduction-related Andean models, suggest that the primary cause of these pulses that contributed to the growth of the Central Andes is the evolving geometry of the subducting Nazca plate. In particular, the steepening of the slab in the upper mantle slows down the trench retreat and subsequent shortening of the advancing South American plate. This steepening first occurs after the end of the flat-slab episode at ~25 Ma. By eroding the lower part of the mantle lithosphere, this episode predisposes the margin for the next deformation phases by decreasing its strength. Later, slab steepening occurs following the buckling of the slab in the mantle transition zone. This new buckling-steepening mechanism sheds light on the causes of the rapid pulsatile growth of the Central Andes during the last ~20 Ma, and the model evolution is consistent with geological data (Oncken et al., 2012) and with the timing of uplift of the Altiplano plateau (Garzione et al., 2017). Our study also confirms the previous modelling results (Sobolev and Babeyko, 2005; Babeyko and Sobolev, 2005; Sobolev et al., 2006; Liu et al., 2022) regarding the important roles of long-term overriding by South America plate, high intraplate friction due to the lack of sediments in subduction channel, lithosphere delamination of the lithospheric mantle and weakening of the foreland sediments in the shortening evolution of Andes.

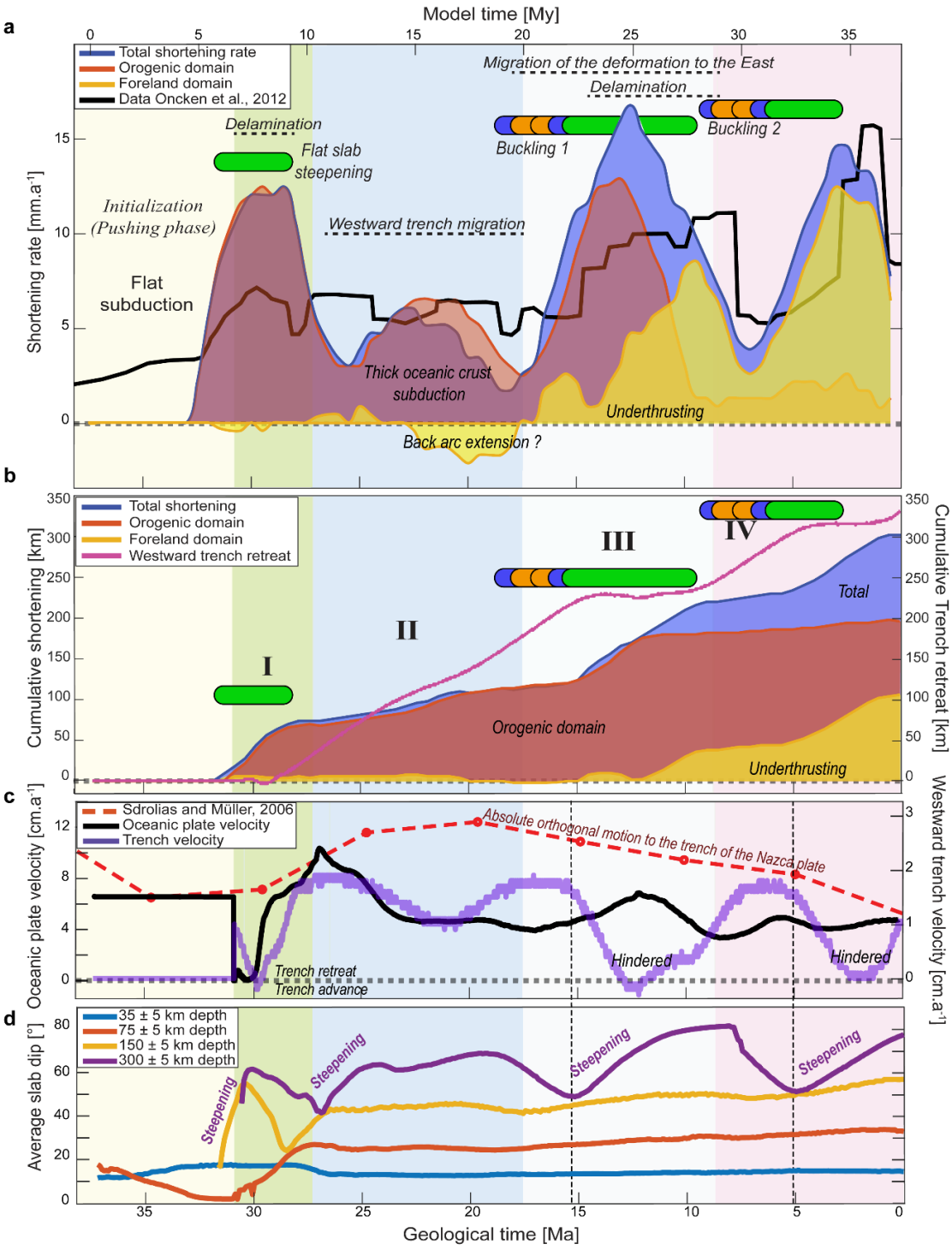

Figure 2.9 Summary of the main events of the reference model. Summary exposing the relation between continental plate deformation (**a** and **b**) and oceanic plate dynamics (**b** and **c**) for the reference model. Background colors indicate the shortening phases. Colored pills indicate the slab evolution stage as in Figure 2.7. **a** Smoothed shortening rate for the orogenic and foreland domain (see data acquisition and processing for details). **b** Cumulative shortening for the orogenic and foreland domain and cumulative trench retreat. Numbers indicate the shortening phases**. c** Velocity of the oceanic plate (black line) and trench migration rate (purple line). **d** Average slab dip for different depth intervals.

Chapter 3 Controls of the slab dip geometry and upper plate strength on the localization of the deformation in the Sierras Pampeanas

3.1 Abstract

The localization of deformation in the southern Central Andes (29°S-39°S) has been attributed to numerous factors related to the oceanic Nazca plate and the continental South American plate. However, the relative contributions to strain localization from the Pampean Flat Slab and from inherited structures of the continental lithosphere remain poorly understood. In this study, we integrated the present-day configuration of the overriding and subducting plates in a data-driven geodynamic workflow to assess their role on the strain localization. Our model predicts: (I) propagation of deformation to the east of the flat slab segment by bulldozing and pure-shear shortening in the broken foreland (27°S-31°S), and (ii) simple shear shortening in the orogenic fold and thrust belt above the steep slab segment. Between these segments, we predict a 370 km-wide area of diffuse shear where deformation transitions from pure to simple shear, resembling the transition from the thick to thin skinned foreland deformation style in the southern Sierras Pampeanas. This pattern is controlled firstly by the change in dip geometry of the oceanic plate and secondly by weak sedimentary basins related to inherited faults. Topography locally enhances strain localization at the eastern flank of the orogen. East of the Sierras Pampeanas, pre-Andean structures related to the thickening of the South American plate, such as the Transbrazilian Lineament, could affect the strain localization regionally by reducing the amount of horizontal stress transmitted to the foreland.

3.2 Introduction

Flat subduction occurs on 10% of convergent margins (M. A. Gutscher et al., 2000). The western continental margin of South America exhibits two flat subduction segments: the Nazca and the Pampean flat slab caused by the subduction of the Nazca and Juan-Fernandez Ridge (JFR) hotspots, respectively (Figure 3.1; Gutscher et al., 2000; Yáñez et al., 2001; Bello-González et al., 2018). The Pampean flat slab has migrated from the Central Andes at Altiplano latitude (~20°S) at 35 Ma to its present-day position (~32°S), which was followed by an increase of shortening magnitude in the Central Andes (Ramos et al., 2002; Oncken, 2006; 2012). Therefore, examining the interaction between the sinking plate and the upper plate along with the role of the inherited structures and plate geometry is vital in understanding the factors contributing to strain localization at a convergent margin. In this study, we explore the role of different shortening contributors in the Southern Central Andes (SCA, ~27°S-40°S) by integrating the previously constrained structural and thermal configurations of the plates (Rodriguez Piceda et al., 2021; 2022). Above the flat slab segment,

deformation extends across a broad broken foreland and localizes at the border of the uplifted crustal basement blocks of the Sierras Pampeanas (V. A. Ramos et al., 2002b), a characteristic of the thick-skinned deformation style. This style is often opposed to the thin-skinned style that occurs typically in the Fold and Thrust Belt (FTB), where the foreland sedimentary cover is primarily involved in deformation (Isacks et al., 1982; Jordan, 1984; Jordan & Allmendinger, 1986; Kay & Abbruzzi, 1996; Ramos et al., 2002b). The SCA foreland is characterized by a transition from dominantly thick-skinned (~27°S-33°S) to thin-skinned deformation (>~36°S, Manceda & Figueroa, 1995; Giambiagi et al., 2012; Fuentes, 2016). Between ~33°S and 36°S the deformation styles are mixed. The eastward propagation and localization of deformation away from the trench can be explained by 2 main mechanisms. The first is the flat slab bulldozing the continental lithosphere keel (e.g., Jordan, 1984; Ramos & Folguera, 2009; Horton, 2018; M.-A. Gutscher, 2018), where the shear stress is transmitted from the subduction interface to the eastern edge of the flat slab segment. The second mechanism involves the reactivation of inherited faults from previous extensional phases (Figure 3.1d, Kley & Monaldi, 1998; Cristallini & Ramos, 2000; Mescua et al., 2014; Giambiagi et al., 2014; Lossada et al., 2017). By investigating the relative importance of the key contributors to strain localization, we discuss the validity of each mechanism in the SCA.

We distinguish between shallow and deep contributors that affect the deformation of the crust or the whole lithosphere, respectively. At the surface, topography and the strength of the sediments are investigated. In the SCA, the sediment distribution is primarily related to the formation of depocenters that developed during Mesozoic extensional events, later the inherited normal faults were reactivated during compressional phases (Mpodozis & Kay, 1990; Uliana et al., 1995; Kley, 1999; Kley & Monaldi, 2002a; Hongn et al., 2007; Del Papa et al., 2013; Fennell et al., 2019). Low frictional strength of unconsolidated and porous sediments may favor strain localization and thin-skinned deformation (Allmendinger et al., 1997; Allmendinger & Gubbels, 1996; Kley, 1999; Babeyko & Sobolev, 2005; Liu et al., 2022). Therefore, by including them in our model we examine the role of heterogeneities at the crustal scale. At greater depths, strain localization can be affected by lithospheric-scale heterogeneities, which can be classified as inherited discrete discontinuities such as sutures that are related to the amalgamation of Paleozoic terranes (e.g. Ramos, 2010), or volumetric discontinuities associated with inherited variations in the composition and/or thickness of the layers composing the continental lithosphere (i.e., crystalline crust, lithospheric mantle), which result from the distinct tectono-magmatic evolution of different segments (Ibarra et al., 2018, 2019; Liu et al., 2022; Rodriguez Piceda et al., 2021). Overall, structural and geometric parameters can have an impact on lithospheric strength and the localization of deformation.

Using data-driven geodynamic modelling, the objective of this study is to answer the question "What is the degree of contribution of lithospheric and crustal scale heterogeneities on the localization of deformation in the SCA?" To this end, we developed a numerical modelling workflow in which data-driven three-dimensional structural, density, and thermal models (Rodriguez Piceda et al., 2021; 2022) were integrated

into a geodynamic model to simulate continental shortening of the SCA lithosphere. Ultimately, this work sheds new light on a long and contentious debate about the degree to which flat slab geometry and continental plate structural inheritance contributed to the change in foreland deformation style (Ramos & Scientific, 2002; Ramos & Folguera, 2009; Horton, 2016; Lossada et al., 2017).

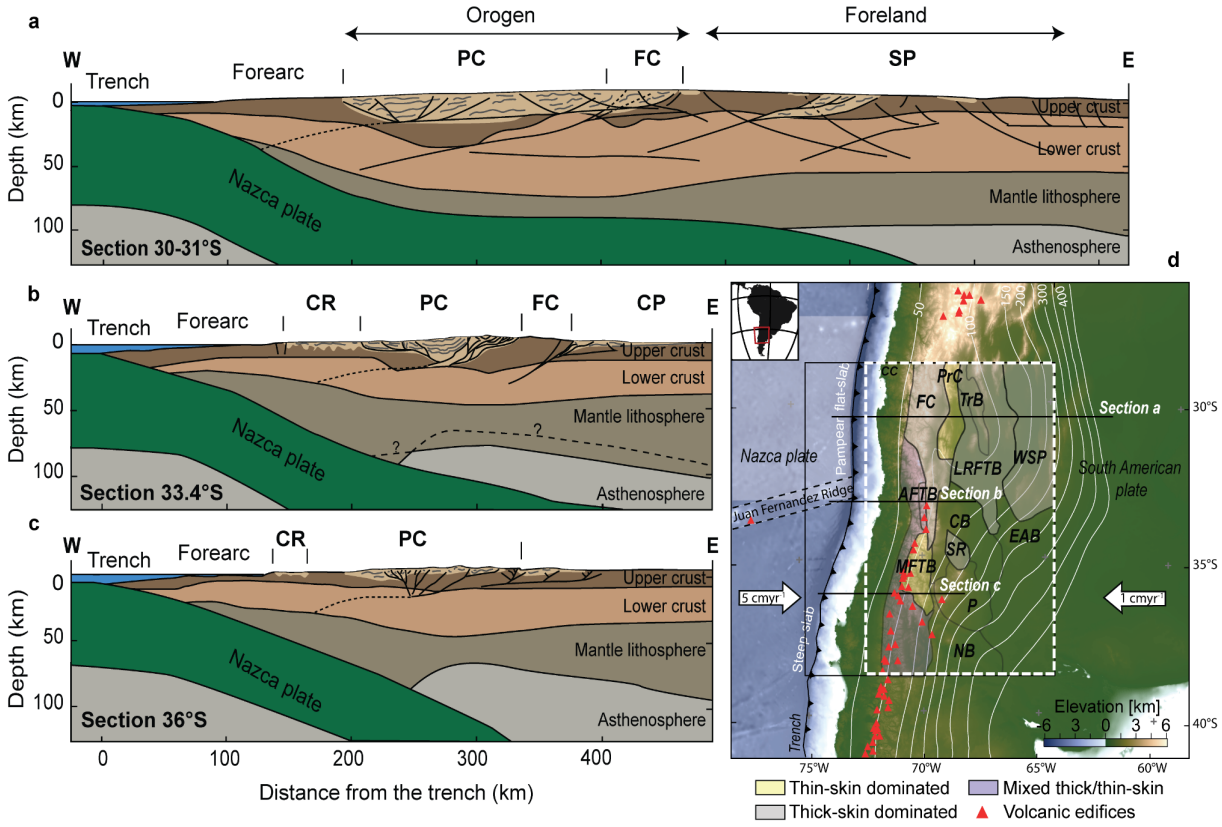

Figure 3.1 Structural cross sections and map of the Southern Central Andes. **a** Transect between 30-31°S (modified from Lossada et al., 2017, Gans et al., 2011; Stalder et al., 2020 and Ramos et al., 2002a). **b** Transect at 33.4°S (modified from Barrionuevo et al., 2021). **c** Transect at 36°S (modified from Barrionuevo et al., 2021). Light brown indicates crustal regions with intense deformation. Slab dip was extracted from crust 2.0 (Hayes et al., 2018). **d** topography and bathymetry of the model area based on ETOPO1 global relief model (Amante & Eakins, 2009), indicating the higher modelled resolved area (white rectangle) and the borders of the geomorpho-tectonic provinces (modified from Rodriguez Piceda et al., 2021) color-coded by the dominant style of deformation. The black dashed rectangle shows the extent of the gravity-constrained structural model (Rodriguez Piceda et al., 2021). Red triangles depict the volcanic edifices. Depth contours of the top slab (Hayes et al., 2018) are shown in white lines. Oceanic and continental plate velocities are shown in white arrows (Sdrolias & Müller, 2006; Becker et al., 2015). Abbreviations of main morphotectonic provinces: CB: Cuyo basin, CC: Coastal Cordillera, CP: Cerrilladas Pedemontanas, ESP: Eastern Sierras Pampeanas, NB: Neuquén basin; P: Payenia, PC: Principal Cordillera (LRFTB= La Ramada fold-

thrust belt, AFTB: Aconcagua fold-thrust belt, MFTB: Malargüe fold-thust belt), FC: Frontal Cordillera, FA: forearc, PrC: Precordillera, SR: San Rafael Block, TrB: Triassic basins, WSP: Western Sierras Pampeanas, EAB: Extra-Andean basins.

3.3 Model set up

The geometries of the lithospheric layers were adopted from the 3D structural model of Rodriguez Piceda et al. (2021). This model is built upon the integration of geophysical and geological data and models, including the gravity field, and covers a region of 700 km x 1100 km x 200 km (Figure 3.1). Eight layers composing the model were defined based on the main density contrasts in the lithosphere: (1-2) oceanic and continental sediments ('sediments', Figure 3.2a); (3) upper continental crystalline crust ('upper crust', Figure 3.2c) ; (4) lower continental crystalline crust ('lower crust', Figure 3.2d); (5) continental lithospheric mantle ('continental mantle', Figure 3.2f); (6) oceanic crust; (7) oceanic lithospheric mantle ('oceanic mantle') and (8) asthenospheric mantle. For the geodynamic simulations, two main modifications were done to the original model of Rodriguez Piceda et al. (2021). First, the model was extended 200 km in depth, 500 km in the E-W direction and 200 km in the N-S direction. The resulting box model is 1700 x 1700 x 400 km, with a central area of interest of 600 x 600 x 400 km (Figure 3.3). Second, we introduced an interface representing the lithosphere-asthenosphere boundary (LAB) in the continental part based on based on the thermal LAB model from Hamza & Vieira (2012). The main features of the model are depicted (Figure 3.2) in terms of the: (a) thickness of sediments; (b) thickness of continental crust; (c) thickness of upper crust; (d) thickness of lower crust; (e) Moho depth and (f) LAB depth.

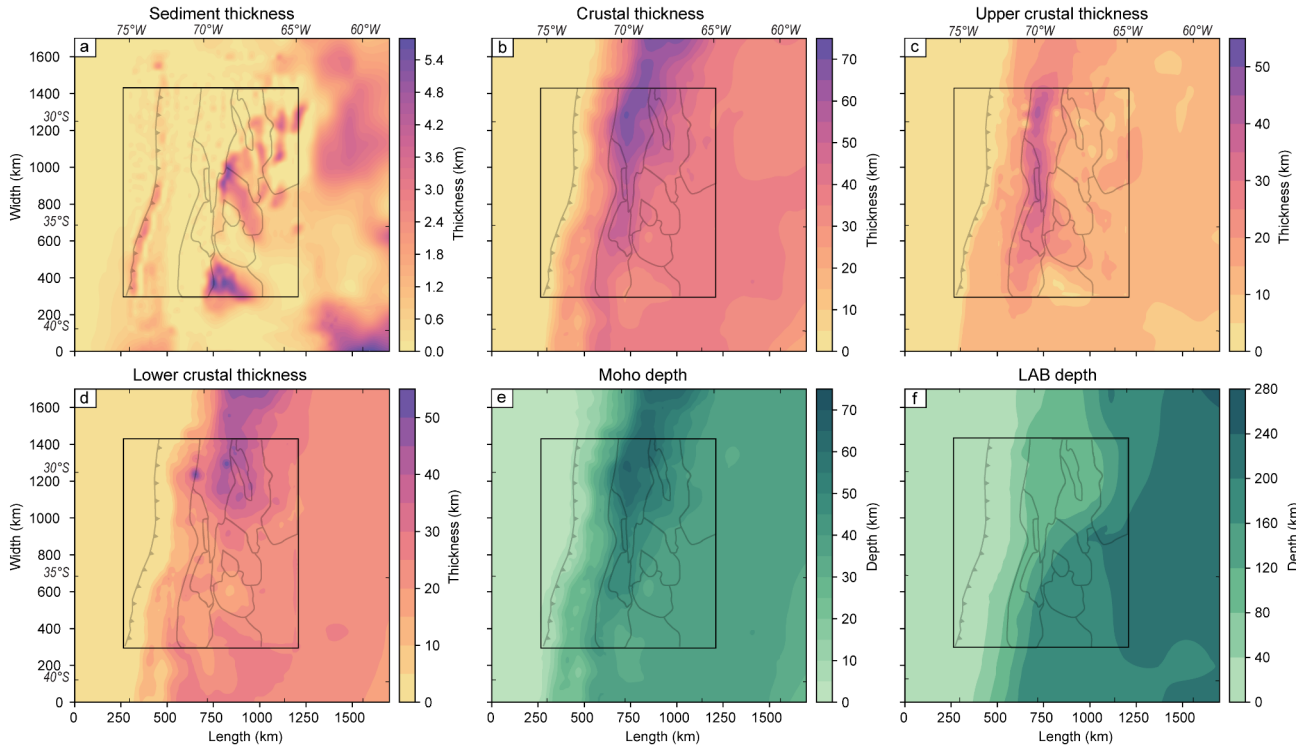

Figure 3.2 Layer thickness and depth map of the SCA. Main structural features of the SCA lithosphere from the model of Rodriguez Piceda et al. (2021). **a** Sediment thickness. **b** Total crystalline crustal thickness. **b** Upper continental crustal thickness. **c** lower continental crustal thickness. **d**. **e** Moho depth. **f** LAB depth is from Hamza and Vieira (2012). The black rectangle shows the most refined model area.

The initial temperature field is based on a 3D thermal model of the SCA (Rodriguez Piceda et al., 2022), covering the same region as the structural model of Rodriguez Piceda et al. (2021). Temperatures were derived from the conversion of S-wave tomography (Schaeffer & Lebedev, 2013) together with steady-state conductive modelling, and were additionally validated by borehole temperatures and surface heat flow data (Rodriguez Piceda et al., 2022). One caveat of this model is related to the determination of the thermal structure of the oceanic slab through the conversion of S-wave tomography to temperature The lack of seismic tomography resolution (0.5° longitudinally and 25km in depth) does not allow us to properly resolve the oceanic plate boundaries, which results in relatively high temperatures in comparison to the temperatures predicted by numerical solutions (Wada & Wang, 2009; van Keken et al., 2019). For this reason, we have assigned a conductive geotherm between 273 K and 1573 K from the top to the base of the oceanic plate.

The thermomechanical properties of each model unit were assigned according to its lithological composition (Rodriguez Piceda et al., 2021; 2022). These lithologies were inferred from the comparison between gravity-constrained densities (Rodriguez Piceda et al., 2021), and mean *P* wave velocities (Araneda et al., 2003; Contreras-Reyes et al., 2008; Pesicek et al., 2012; Marot et al., 2014; Scarfi & Barbieri, 2019), combined with rock-property compilations (Sobolev & Babeyko, 1994; Christensen & Mooney, 1995;

Brocher, 2005) and other seismic properties (Wagner et al., 2005; Gilbert et al., 2006; Alvarado et al., 2007; Ammirati et al., 2013; 2015; 2018). The reference density for each composition was recalculated so the estimated final density of each composition (i.e. after correcting for pressure and temperature, eq. 5), is in the range of the density predicted by the structural model of Rodriguez Piceda et al (2021) and the resulting topography was compared to the real one (Text B.S1 and Figure 3.1). The thermal properties used in the initial thermal field are from published average values for the lithology of each model unit (Cermak & Rybach, 1982; Hasterok & Chapman, 2011; He et al., 2008; Xu et al., 2004);

We assigned rheological properties to each composition for the viscous regime, dry olivine (Hirth & Kohlstedt, 2004, H&K2003) to the oceanic mantle (3321 kg/m³), diabase (Mackwell et al., 1998, Mck1998) to the lower crust (3129 kg/m³), wet olivine (Hirth & Kohlstedt, 2004) to the continental mantle (3388 kg/m³), wet quartzite (Gleason & Tullis, 1995, G&T1995) to the upper crust (2812 kg/m³), the oceanic and continental sedimentary layer (2300 and 2400 kg/m³) , and wet olivine (Hirth & Kohlstedt, 2004) to the upper mantle as representative of the hydrated mantle wedge.

For the oceanic crust (2857 kg/m³), we prescribed a weak quartzite rheology (Ranalli, 1997) to simulate the visco-plastic behavior of a quartz-dominated “mélange”, which is characteristic of the subduction interface (Sobolev et al., 2006; Muldashev & Sobolev, 2020) with a relatively low friction coefficient of 0.015 which produces an appropriate maximum shear stress of 20 to 40 MPa depending on the temperature and the dip of the oceanic plate (Figure SB.5; Lamb & Davis, 2003; Sobolev et al., 2006).

For the plastic regime, we set a cohesion of 40 MPa and friction angle of 30° to the mantle layers. The short model runtime prevents the layers from weakening by accumulating plastic strain, thus we assign a weak plastic rheology to the sedimentary layer (i.e. friction angle of 3° and cohesion of 2 MPa). The minimum viscosity was set to 1e19 Pas during the first 100 ka of model run, and subsequently changed to 2.5e18 Pa.s. In this study, we refer to the second invariant of the square root of the deviatoric strain rate in the plastic and viscous domains as plastic strain rate and viscous strain rate, respectively. The plastic strain represents the integrated plastic strain rate over time and allows us to see the regions of the model that have been deformed and weakened during the model run. We used adaptive mesh refinement (Figure 3.3) to resolve the central and outer domains, with a resolution of ~6km and 12.5km, respectively. We ran the model simulation for ~250 ka while applying velocities of 5 cm/yr and 1 cm/yr to the oceanic and continental plates, respectively (Sdrolias & Müller, 2006), whereas the left and right asthenosphere borders were left open. To fulfill the volume conservation constraint, we prescribed an equivalent volume outflow to the bottom boundary equal to the prescribed inflow from the plate velocity. We use the advantages of the ASPECT code by prescribing a dynamically deformable mesh in order to simulate present-day topography. In particular, the topography in the model is uplifted and advected using the ASPECT-FastScape coupling (Braun & Willett, 2013; Bovy, 2021; Neuharth et al., 2021).

		Asthenosphere (AST)	Oceanic plate			Continental plate			
	Units	Upper mantle	Weak Gabbro	Lithomantle	Oceanic sediments	Continental Sediments	UpperCrust	LowerCrust	Lithomantle
Lithology	/	Harzburgite	Gabbro +melange (serpentinite)	Moderately depleted Lherzolite	Siliclastic	Siliclastic	Diorite	Mafic Granulite	Wet olivine
Reference	/	H&K2003	Ranalli, 1997	H&K2003	G&T1995	G&T1995		Mck1998	H&K2003
Composition used in the model	/	Dry olivine	Wet quartzite	Dry olivine	Wet quartzite	Wet quartzite		Maryland diabase	Wet olivine
Grainsize	m	1e-3	1e-3	1e-3	1e-3	1e-3		1e-3	1e-3
Creep pre-exponential factor Bd / Bn	$Pa^{-ndiff/ndisl}$. s-1	1e-9 / 8.49e-15	- / 2.25e-17	2.25e-15 / 2.96e-16	- / 8.57e-28	- / 8.57e-28		- / 7.13e-18	1e-9 / 2.96e-14
Grain size exponents	mm	0	-	3	-	-		-	0
Activation energies Ed / En	kJ/mol	335 / 540	- / 154	375 / 535	- / 223	- / 223		- / 345	335 / 515
Activation volume Vd / Vn	m^3/mol	4.8e-6 / 12e-6	- / 0	10e-6 / 14e-6	- / 0	- / 0		- / 0	4.8e-6 / 14e-6
Stress exponents	n	3.5	2.3	3.5	4	4		3	3.5
Internal friction angle	degree	30	0.8594	30	30 -> 6	3	30 -> 6	30 -> 6	30
Cohesions	MPa	40	0.1	40	20 -> 10	2	20	40 -> 20	40
Plastic strain weakening interval	none	-	0 - 0.3	-	0.5 - 1.5	0 - 1.5	0.5 - 1.5	0 - 1.5	0 - 1.5
Thermal conductivity	W/K/m	3.3	2.5	3.3	2.2	2.2	2.5	2.6	3.3
Densities	kg/m^3	3347	2857	3321	2300	2400	2812	3129	3388

Table 3.1 Model parameters for each composition. G&T1995 : Gleason & Tullis, 1995. Mck1998 : Mackwell et al., 1998. H&K2003.Hirth & Kohlstedt, 2004. Lithology corresponds to the one defined in Rodriguez Piceda et al., (2020) whereas representative composition in the model are defined from deformation experiments. Prefactors (A) were scaled from uniaxial compression experiments (Dannberg et al., 2017). We applied wet olivine (Hirth & Kohlstedt, 2004) to the upper mantle as representative of the hydrated mantle wedge and mantle lithosphere caused by the long term subduction Chilean subduction (Babeyko et al., 2006).

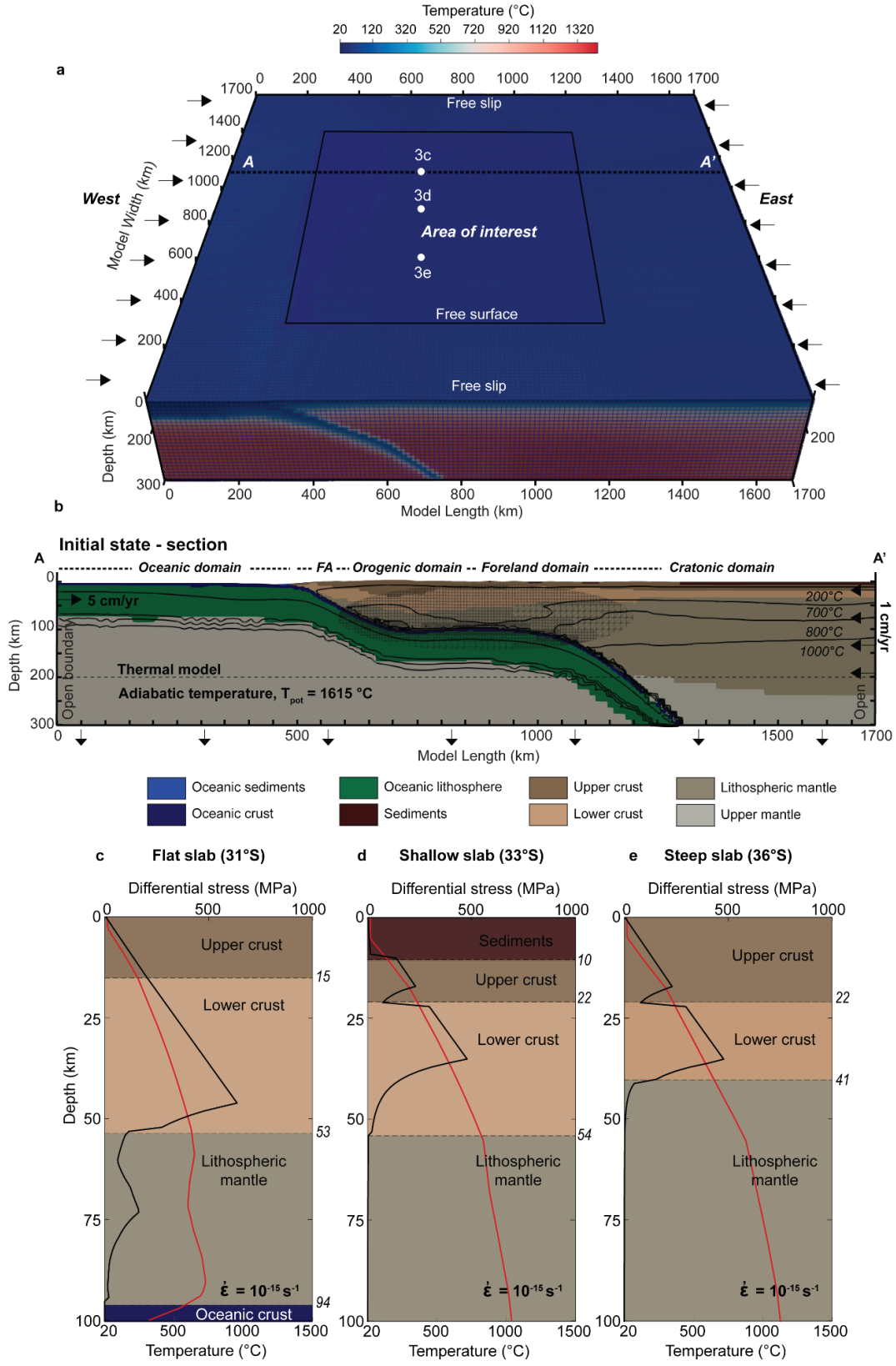

Figure 3.3 Model setup. **a** 3d model geometry, mesh refinement and temperature. **b** 2D W-E cross-section long location indicated in **a**, showing: boundary conditions, refinement of the interface, composition of the lithospheric layers and temperature. T_{pot} indicates the mantle potential temperature

and FA the forearc domain. **c-e** yield strength and temperature profiles of the upper plate at : **c** flat-slab. **d** shallow slab . **e** steep slab.

First, we have computed the reference model (S1) to best fit observations. Then, we ran a series of models (S2, S3, S4 and S5, Table. 3.2) varying multiple parameters to investigate the relative contribution of key factors on the strain localization in the upper plate.

3.4 Modelling results

3.4.1 Reference model (S1)

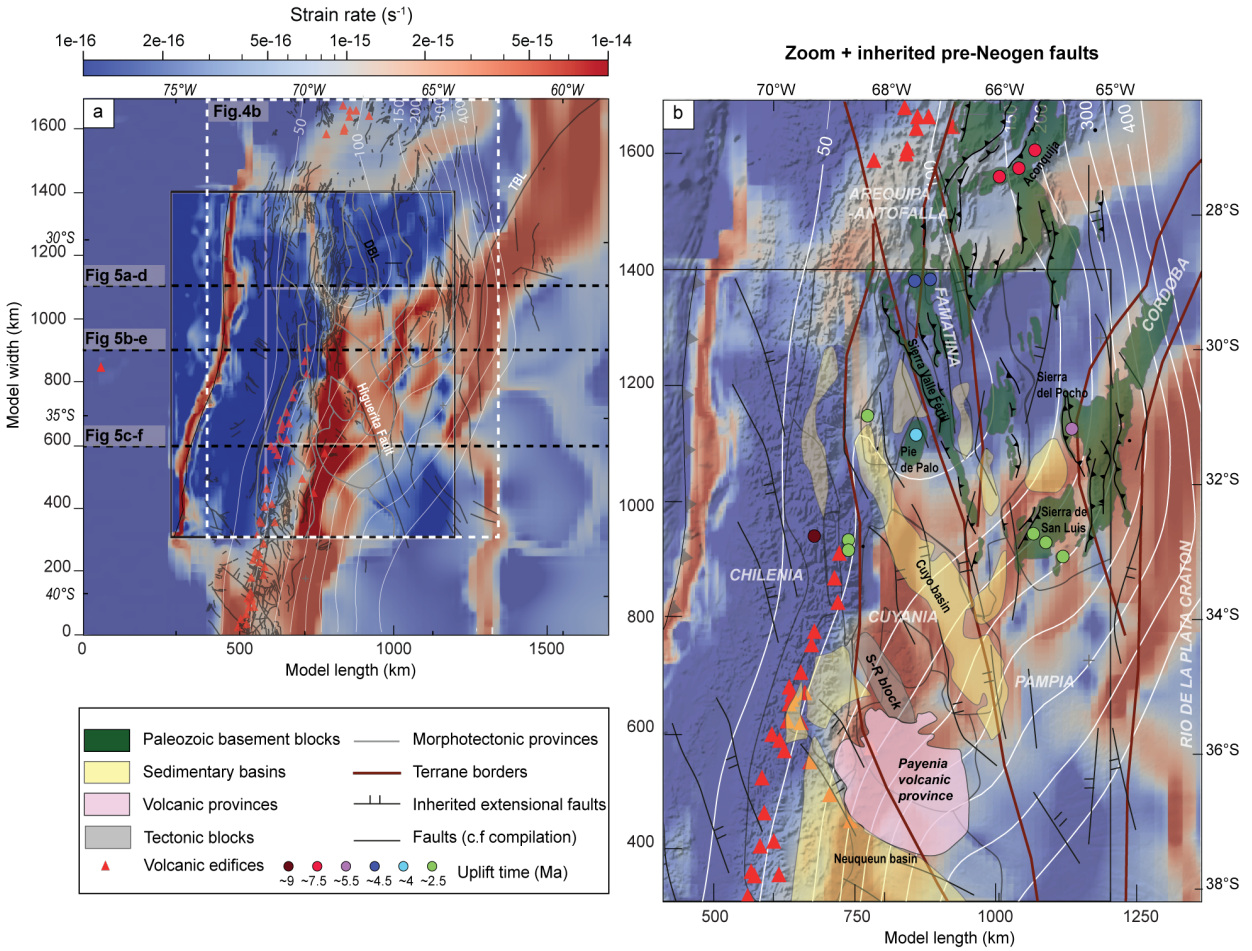

Figure 3.4 Surface strain rate of the Reference model. **a.** Strain rate overlapped by compiled faults. **b.** Close up on the Sierras Pampeanas overlapped by the major inherited extensional faults and terrane sutures in red (Ramos et al., 2002a; Wimpenny, 2022). Green structures indicate uplifted Sierras Pampeanas blocks. The time of the uplift is indicated by filled colored circles (Table B.S1). White lines are isobaths of the top of the oceanic plate. Red triangle indicates the position of known volcanic edifices. Major structures and provinces are described by different colours in the legend.

The reference model S1 is built upon the known values for the plate convergence, subduction interface coefficient, sediment strength and present day topography. From South to North, the deformation migrates

to the east (Figure 3.4 and 3.5) and the strain localizes and then is distributed over multiple faults, respectively. This shift is related to a change in the shortening mode from simple shear to pure shear. Simple shear shortening occurs when, in the strain rate snapshot, the plastic strain rate band in the upper crust connects with the viscous strain rate band in the lower crust to form a shear zone (Figure 3.5c-d), which is expressed by thin-skinned deformation style in the FTBs. Conversely, if no connection occurs between the plastic and viscous strain rate localization zones, pure shear shortening over multiple faults is favoured, leading to distributed deformation of the crystalline basement which corresponds to to thick-skinned foreland deformation style. The resulting surface strain rate field indicates 3 distinct North to South branches (Figure 3.4a) characterized by a distinct shortening mode:

(i) ***A Western branch, 75°W to 73°W*** corresponds to the trench. At the trench, both plates are decoupled by the weak subduction interface, where most of the deformation localizes. Conversely, the crust of the adjacent cold and mechanically strong forearc is almost not deformed.

(ii) ***A Central branch,* 73°*W to 70°W*** that is composed of the orogen and the adjacent foreland. Strain distribution varies from north to south. In the flat slab segment, the strain localizes in the eastern front of the orogen and intensifies towards the south. The foreland crust is almost undeformed. In the shallow slab segment, the strain distributes in the foreland over multiple obliques or 'en echelon' crustal scale structures, associated with pure shear shortening, that connect to the Eastern branch. In the steep slab segment, the strain strongly localizes in front of the orogen in the foreland by simple shear shortening.

(iii) An Eastern branch,* 60°*W to 65°W where deformation localizes in front of the flat slab by pure shear shortening, as well as along regions that spatially correlate with Pre-Andean cratonic structures that are related to the amalgamation of terranes during the formation of Gondwana in the Precambrian (e.g. Transbrazilian Lineament; Fairhead & Maus, 2003; V. Ramos, 2010). In the south, the deformation localizes within smaller structures that border the Rio de la Plata craton. The central and eastern branch connect by the intermediary of the broken foreland.

On a lithospheric scale these 3 branches spatially interact with each other. The Sierras Pampeanas appears as a large shear zone that accommodates the deformation through the development of en-echelon structures associated with the uplift of the isolated rigid basement blocks. The deformation at the borders of these blocks is accommodated by a diffuse dextral strike-slip motion (Chapter 5).

We also distinguish 3 slab segments (Figure 3.5): a flat segment (27°W to 32°W, 1000-1400 km model width-coordinates), a shallow segment (32°W to 35°W , 600-1000 km model width-coordinates) and a steep segment (35°W to 41°W , 0-600 km model width-coordinates). Above the steep segment, the upper plate is characterized by simple shear shortening at the front of the orogenic thrust wedge (Figure 3.5c). Above the shallow segment, the model predicts a mixed simple and pure shear shortening (Figure 3.5b). Whereas above

the flat-slab segment no significant deformation occurs, while a pure-shear deformation takes place at the eastern edge of the flat-slab segment (Figure 3.5a).

The E-W oriented cross-sections across the reference model (Figure 3.5) illustrate how the plastic (brittle) and viscous deformation is accommodated in the continental plate along the segments with different slab geometry (Figure 3.5a-c), and how the stress is distributed in the plates (Figure 3.5d-f). The horizontal stress is effectively transmitted from the continental plate to weak regions where the deformation localizes. In the flat-slab section (Figure 3.5a), the deformation takes place more than ~700 km away from the trench and is localized over a 200-km-wide band in the eastern Pampeanas of the broken foreland. The model predicts local plastic (equivalent to brittle in reality) deformation (Figure 3.5a) on top of the colder flat-slab segment at a 100 km depth (Figure 3.5c), which also correlates with the bending of the slab (i.e. internal shear stress, Figure 3.5a, d). High horizontal stresses of more than 200 MPa build locally in the crust and in the colder lithospheric mantle of the forearc, where the BDT is deeper, but it is not enough to cause significant deformation. The thick and warmer orogen shows no significant deformation despite being weaker, which is illustrated by the shallower BDT (Figure 3.5a). On top of the flat-slab segment, the horizontal stress is mainly provided by the subducting plate shown by the velocity vectors pointing eastwards (Figure 3.5d). The stress also builds up within the cold and strong foreland lithospheric mantle lithosphere. Despite the presence of a weak sedimentary basin at the surface, the deformation does not localize and the stress is partially transmitted eastward from the base of the upper crust to the Eastern Sierras Pampeanas. Finally, crustal shortening results in a stress drop in the Eastern Sierras Pampeanas, meanwhile the velocity field polarity switches from east to west indicating that the velocity is now coming from the overriding plate (Figure 3.5d). Shortening is distributed on multiple faults over a relatively wide area (~200 km), similar to pure shear shortening. In the shallow slab section. In the shallow slab section (Figure 3.5b), the plastic and viscous strain rates connect in front of the orogen (at ~800 km model coordinates) to form a deep shear zone indicating simple shear shortening. In the foreland, the deformation distributes over multiple faulted areas along a wide area which are alternated by rigid crustal blocks with a shallower BDT. Similarly to the previous section the deformation terminates at the transition with the cratonic domain. That is a thick-skinned style of deformation which results from pure shear shortening. The horizontal stress also builds up locally in the cold forearc (>~200 MPa; Figure 3.5e), where high strength prevents it from breaking resulting in the stress being transmitted to the orogen. Additionally, stress builds up at shallow depth and is transmitted to the orogenic front before a stress drop occurs as the orogenic front shortens. In the steep-slab section, the deformation strongly localizes in front of the orogen (~800 km model length; Figure 3.5c). Plastic and viscous strain rates connect leading to simple shear shortening.

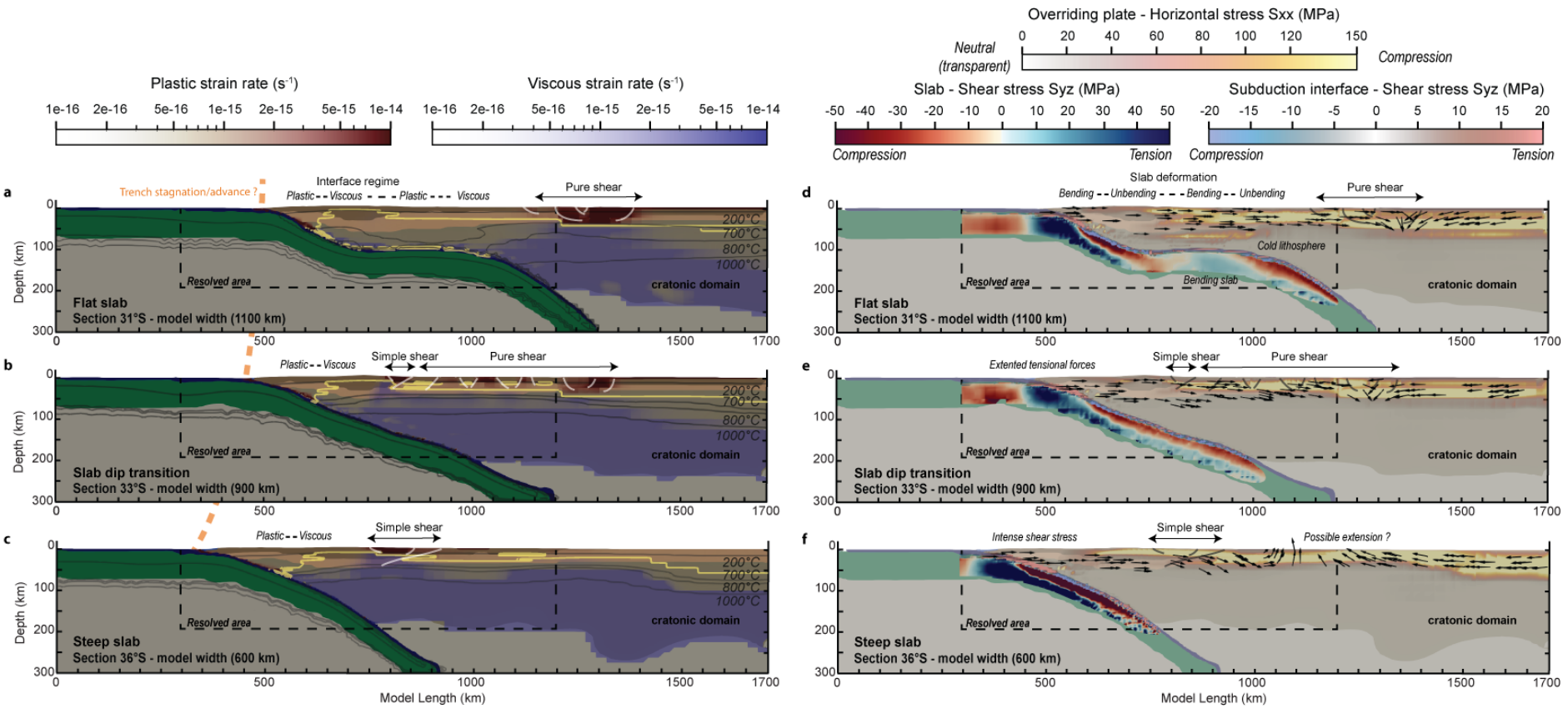

Figure 3.5 Cross-sections representative of the subduction segments for the reference model (see location in Figure 3.1): Strain rate **(a-c)** and stress (**d-f**). **a-d** Flat-slab (31°S). **b-e** Shallow slab (33°S) and **c-f** Steep slab (36°S). **a-c** white lines are interpreted faults, yellow lines show the depth of the brittle-ductile transition (BDT) and dark lines indicate the isotherms. **d-f** black lines indicate the interpreted faults and arrows indicate the sense of the velocity for the crust.

3.4.2 Model variations

In this section, we test the relative contribution of four key parameters on the resulting surface strain rate distribution: (1) the friction coefficient at the oceanic plate interface, (2) the strength of continental sediments, (3) the topography, and (4) the velocity applied to the model boundaries. The friction coefficient at the oceanic plate interface is varied between 0.005 and 0.05 (models S2a-c) in agreement with the models of the long-term evolution of the Central Andes (Sobolev et al., 2006; Sobolev & Babeyko, 2005; Chapter 2). The internal friction angle (Φ) and cohesion (C) of the sediments is varied from 3° to 30° (friction coefficient 0.05 to 0.5) and from 2 to 20 MPa, respectively (Figure 3.6, models S3a-d). In addition, we tested the effect of topography on the strain distribution by removing the topographic relief in the initial configuration with and without applied velocities at the boundaries (Figure 3.6, models S4a-d). Finally, the oceanic and continental plate velocities are varied between 0 cm/yr and 6 cm/yr, covering the range of possible velocities (Figure 3.6, models S5a-d). Table 3.2 summarizes the alternative model runs. In order to discuss the relative effect of each key parameter to the strain localization we have computed the residual surface strain rate between the model variant and the reference model (Figure SB.3). To estimate the variation in strain localization above the trench related to flat, shallow and steep subduction, we have divided the surface of each model into sub-domains. For each domain, we calculated an average of the strain rate using the root mean square. Finally, we calculated the relative change between the domains of the model variants and of the reference model. Thus, we obtained a summary of the relative percentage of contribution of each key parameter to the reference model for each domain (Figure 3.7). Note that for a similar budget of force between the reference model and the model variants, if the strain at the surface localizes further in one of the branches (section 3.1), it may decrease in another one to keep the balance, but this does not apply to the domains defined.

Group	Name	Variation
Friction coefficient of the subduction interface (μ_{int})	S2a	μ_{int} = 0.005
	S2b	μ_{int} = 0.035
	S2c	μ_{int} = 0.05
	S2d	μ_{int} = 0.07
Sediment strength (internal friction angle Φ and cohesion C)	S3a	Φ = 30° ,C = 20 MPa
	S3b	Φ = 30°, C = 2 MPa
	S3c	Φ = 15°, C = 20 MPa
	S3d	Φ = 3°, C = 20 MPa
Model with variation of the topography	S4a	no initial topography w/ boundary velocity
	S4b	no initial topography, w/o boundary velocity
	S4c	no topography w/ boundary velocity
	S4d	no topography w/ boundary velocity
Velocities of the subducting plate (SP) and the overriding plate (OP)	S5a	SP= 0 cm/yr , OP= 1 cm/yr
	S5b	SP= 5 cm/yr, OP = 0 cm/yr
	S5c	SP = 6 cm/yr, OP = 0 cm/yr
	S5d	SP = 0 cm/yr, OP = 6 cm/yr

Table 3.2 Model variations with respect to the reference model.

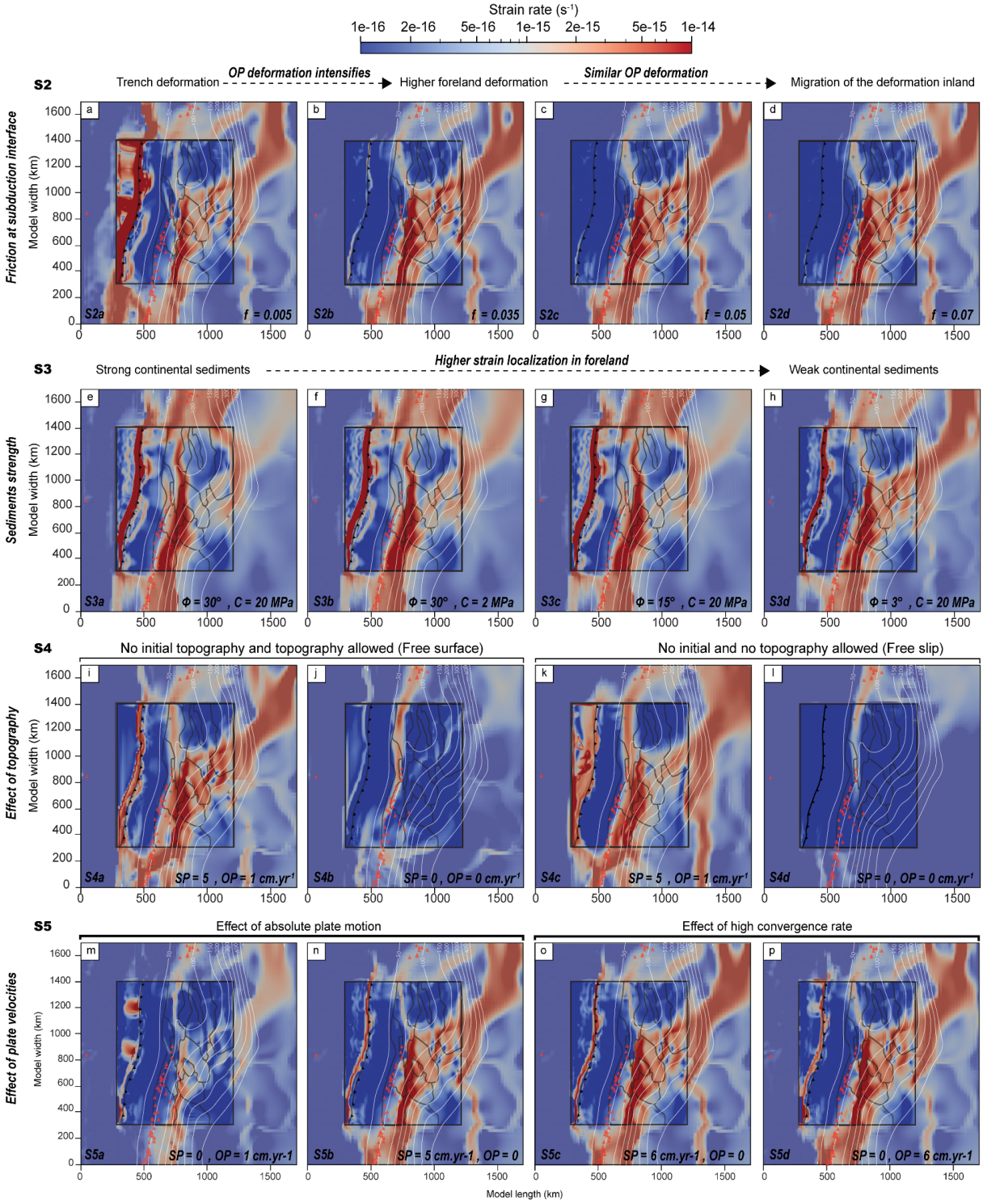

Figure 3.6 Strain rate distribution in various models. **a-d** Models with variable friction coefficients (f) at the subduction interface: **a** S2a, f 0.005. **b** S2b, f 0.035. **c** S2c, f 0.05. **d** S2d, f 0.07. **e-h** Models with alternative strength (Φ internal friction angle, and C cohesion) of the sedimentary layer. **e** S3a, Φ = 30° C = 20 MPa. **f** S3b, Φ = 30° C= 2 MPa. **g** S3c, Φ = 15° C= 20 MPa. **h** S3d Φ =3° C=20 MPa. **i-l** Models without prescribing initial topography. **i-j** Free surface with advection of the topography

allowed. **k-l** Free-slip, no advection of topography allowed. **I,k** models with plate velocity, SP = 5 cmyr-1 and OP =1 cmyr-1 . **j,l** models without velocity, SP and OP = 0 cmyr-1. For abbreviations of plate velocities, see table 3.2. **m-p** Models with variations of prescribed plate velocity. **m** Absolute overriding plate velocity orthogonal to the trench, no subducting plate velocity. **n** Absolute subducting plate velocity orthogonal to the trench, no overriding plate velocity. **o** Convergence velocity, applied only to the subducting plate. **p** Convergence velocity, applied only to the overriding plate. Black rectangle is the resolved area Dark line indicates the boundaries of the morphotectonic provinces and red triangles, the position of the volcanic domes.

3.4.2.1 Models with variable slab interface friction (S2a-d)

The greatest differences between the reference and alternative models related to the slab interface friction occurs along the trench (Figure 3.6). With low slab interface friction (S2a; Figure 3.6a), the strain strongly localizes more at the trench (x18 or +994%, Figure 3.7). Less strain localizes within the overriding plate (-27 to -54%), including the orogen and the back-arc. Conversely, higher interplate friction (S2b-c; Figure 3.6b-d) translate into 2x lower strain localization in the trench (-92 to 97%), and slightly higher overriding plate deformation (+6%). Therefore, for these short simulations the increase of friction at the interface results in similar intensity of upper plate deformation with respect to the reference model S1.

3.4.2.2 Continental sediment strength (S3a-d)

Changing the sediment strength results in a significant change in strain rate distribution. Weaker sediments lead to higher strain localization adjacent to the orogen and the foreland basins (S3a-d, Figure 3.6e-h). A decrease in the internal friction angle (S3c and S3d, Figure 3.6f and h) decreases the strength significantly more than a decrease of cohesion (S3b and S1, Figure 3.6g and Figure 3.4), promoting the tectonic activation of foreland structures. With a high friction and cohesion (S3a, Figure 3.6e), the strain rate in the in the foreland appears to be more diffuse and less localized (Figure 3.7. -35 and -40%), causing strain to localize closer to the orogen and the trench (+220%) than in the reference model. With weaker continental sediments, the major component of deformation switches from the orogen interior to its front. Overall, stronger sediments result in more active deformation superficially near the trench and in the orogeny above the flat slab (S3a, 423%), and less active deformation in the foreland above the shallower and steeper domains (~-40%).

3.4.2.3 Models with topography variations (S4a-d)

By initializing the model without present-day topography, we aim to look at the effect of internal forces related to the density and thickness configuration of the overriding plate layers. In models S4a and S4b, we allow for the topography to evolve with and without plate velocities (model S4a-b, Figure 3.6i-j). S4a

exhibits a strain rate distribution similar to S1 (cf. Figure 3.6a), but with higher strain localization at the trench and in the orogen on top of the flat-slab (Figure 3.7, +25 and 38%). In S4b, although no horizontal velocity is prescribed, the strain rate is higher in the orogen on top of the flat slab (+30%) and lower elsewhere. To investigate the effect of topography on the strain distribution, we ran two alternative models inhibiting topographic growth, with and without plate velocities (models S4b-c; Figure 3.6j-l). In the model with plate velocities (S4c) the strain rate is higher at the trench and the orogen on top of the flat-slab (+128 and 101%) and is more diffuse and lower in the foreland of the shallow and steep subduction domains (-23% and -36%). Without plate velocities (S4d), the strain rate only localizes in a narrow corridor along the orogen and otherwise decreases elsewhere.

3.4.2.4 Velocity boundary conditions (S5a-d)

Varying the prescribed boundary velocity allows us to determine the contribution of each plate to the intensity of strain localization in the overriding plate. In model S5a (Figure 3.6m), where velocities are only prescribed to the overriding plate (1cm yr-1; Figure 3.6m), the intensity of the deformation in the foreland is lower by 58 to 83% in all domains compared to model S1 (Figure 3.7) because the deformation slightly localizes at the trench in specific places. In model S5b, where the overriding plate is not advancing towards the trench, the deformation decreases everywhere by 15 to 30%, likely because the strain efficiently localizes in the orogen and the foreland (Figure 3.6n). Models S5c and S5d (Figure 3.6n-o) show that a in deformation intensity similar to the reference model can be reached if the total convergence velocity is applied to either the lower or the upper plate. Overall, high convergence rate controls the intensity of the deformation and its localization. In these models, the contribution of the subducting plate velocity seems more important than that of the overriding plate, although a high overriding plate velocity (S5d) can lead to similar deformation intensities as in the reference model. The overriding plate strain rate distribution does not depend on which side we prescribe the velocity. Both models that prescribe velocity from the west with the subducting plate (S5c) or from the east with the overriding plate (S5d) show similar structures and patterns.

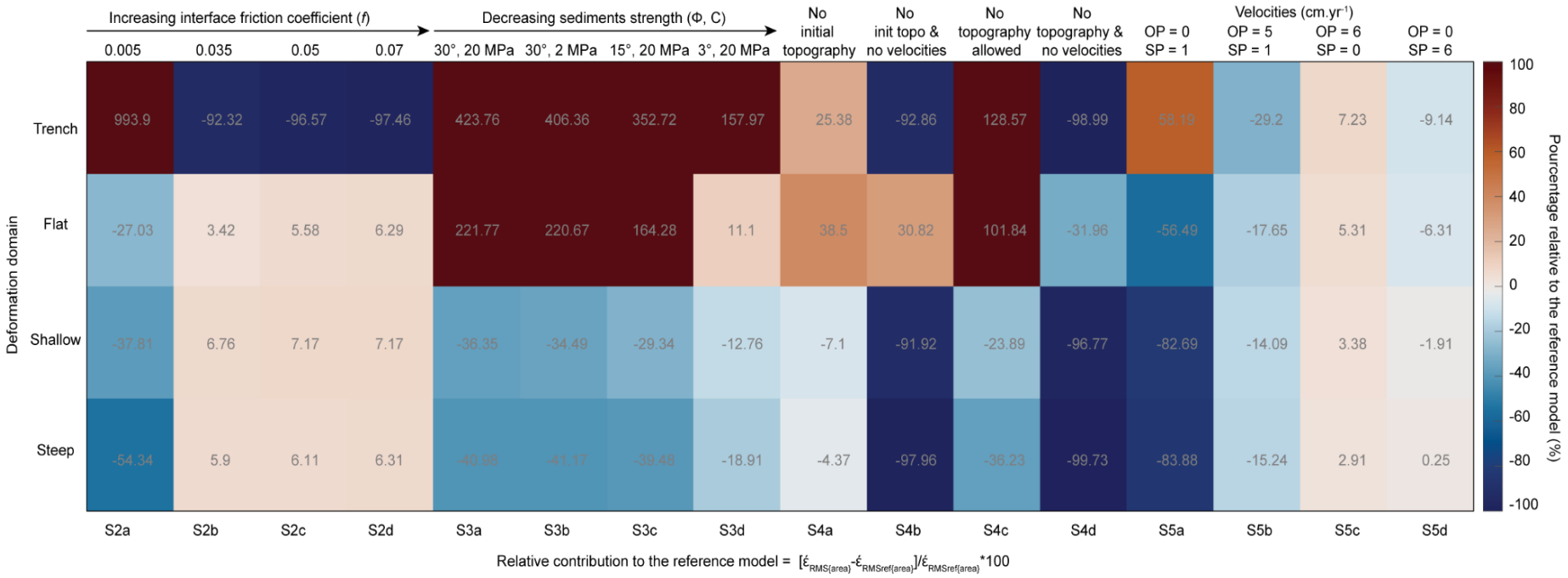

Figure 3.7 Relative surface strain rate difference between the reference and the model variants. Relative change of strain rate in percentage $[\dot{\varepsilon}\mathrm{RMS(area)} - \dot{\varepsilon}\mathrm{RMSref(area)}] \,/\, \dot{\varepsilon}\mathrm{RMSref(area)} * 100$ with respect to the reference model in each deformation domain for each model variant.

3.5 Discussion

To analyse the role of continental inheritance and oceanic plate geometry we assess the relative contribution of the overriding plate strength to strain localization along-strike-. We first compare the distribution of modelled strain rate patterns with the mapped structures (Section 3.5.1). Next, we discuss each tested key factor and how they affect the strength in our model, and their contribution to strain localization. We then discuss the role of shallow and deep structures (e.g. sediment strength, topography, and the thermal state and thickness of the lithosphere, section 3.5.2). Finally, we examine the effect of slab geometry (flat, shallow, and steep subduction) on the distribution and style of deformation in the foreland (section 3.5.3).

3.5.1 Correlation with mapped structures

Although we do not implement faults in the models explicitly, sediment deposition is partly associated with their activity. Mesozoic deposits are controlled by the extensional environment while reverse faults accumulate sediment at their footwalls. Therefore, sediment strength can strongly affect the location of deformation and reactivate shallow inherited faults, which explains why structures resulting from the reference model strain rate map show good spatial correlation with surface exposed faults (Fig4a-b, Moscoso & Mpodozis, 1988; García, 2001; Giambiagi et al., 2003; Broens & Pereira, 2005; Folguera & Zárate, 2011; Martino et al., 2016; Litvak et al., 2018; Martínez et al., 2017; Sánchez et al., 2017; Meeßen et al., 2018; Riesner et al., 2018; Olivar et al., 2018; Jensen, 2018; Melnick et al., 2020; Costa et al., 2020; Eisermann et al., 2021). In particular, the strain rate distribution in the reference model correlates with quaternary faults located at the front of the orogen in the foreland fold and thrust belts (e.g Malargue, San Rafael FTB), at the borders of the basins (e.g. Cuyo Baisn), and with the adjacent faults to the Sierras Pampeanas uplifted basement blocks. In some cases, Pre-Andean (inherited) structures have been reactivated that were associated to the amalgamation of Paleozoic crustal terranes at the western margin of Gondwana (Introcaso & Ruiz, 2001; Vietor & Echtler, 2006; Ortiz et al., 2021). For instance, the faults is the Desaguadero-Bermejo lineament (DBL) close to the Sierra Valle Fértil which borders the western Sierras Pampeanas (Figure 3.4b, Introcaso & Ruiz, 2001) is associated with the Ordovician collision of the Cuyania terrane against the Pampia terrane (Ramos, 2010). This strike-slip fault was reactivated during the neogene redistributing the sediment by splitting the Bermejo and Ischigualasto-Villa Unión Triassic basins (Introcaso & Ruiz, 2001). The model also predicts the reactivation of the Transbrasilian lineament (TBL), a major transpressive shear zone of Proterozoic age that borders the thicker mantle lithosphere of the Rio de la Plata Craton (Figure 3.4b, Cordani et al., 2013; Casquet et al., 2018). In contrast, the forearc is subjected to low deformation and acts as a rigid body (Tassara & Yáñez, 2003; Tassara, 2005; Hackney

et al., 2006), although previous studies have shown that the forearc experienced a certain degree of quaternary deformation (González et al., 2003; Melnick et al., 2006; Regard et al., 2010). The forearc mobility is controlled by the long-term weakening associated to the strain partitioning caused by the parallel plate convergence to the trench (Melnick et al., 2006; Rosenau et al., 2006; Eisermann et al., 2021) which is not considered by our model. Other regions showing low deformation are the foreland above the flat-slab segment (Figure 3.5a) and the back-arc in the steep-slab segment (Figure 3.5c). In the latter, most of the deformation is related to pre-Neogen structures (e.g.,Folguera & Zárate, 2009).

3.5.2 Upper-plate control on strain localization

The strength of the overriding plate controls the strain localization and is the result of the contributions of the frictional (brittle) and viscous (ductile) strength (Babeyko et al., 2006; Mouthereau, 2013; Jammes & Huismans, 2012; Liu et al., 2022). Several processes can weaken the plate and influence the localization of deformation. We distinguished between shallow and deep contributors, depending on their control on the frictional and viscous strength, respectively.

An important part of the stress is transmitted through the frictional regime (Figure 3.5), thus shallow contributors can significantly affect the strain localization through frictional weakening. The variations in frictional strength are related to the tectonic history, and are modulated by several features, including: the sediment strength relative to the underlying structures (Babeyko et al., 2006; Erdős et al., 2015; Mescua et al., 2016; Liu et al., 2022), the presence of inherited (Pre-Andean) faults and their orientation with respect to the convergence rate (Allmendinger et al., 1983; Kley, 1999; Kley & Monaldi, 2002) and the topography (Molnar & Tapponnier, 1975; Chen & Molnar, 1983; Stüwe, 2007; Mareschal & Jaupart, 2011; Liu et al., 2022). In turn, the deep contributors are those affecting the strength of the crust and the lithospheric mantle through variations in the temperature of these layers. The degree to which shallow and deep contributors interact and affect the strength of the overriding plate in the SCA is discussed in the following sections.

3.5.2.1 Shallow structures

Previous studies have shown the important role of the thickness and strength of sediments in shallow strain localization (Babeyko et al., 2006; Erdős et al., 2015; Mescua et al., 2016; Liu et al., 2022). In the Central Andes, the presence of mechanically weak and porous Palaeozoic sediments in the foreland spatially correlates with a change of deformational style from thin-skinned at latitudes of the Altiplano Plateau to thick-skinned deformation at latitudes of the Puna plateau (Allmendinger & Gubbels, 1996). Previous numerical models have shown that a low sediment friction coefficient (<0.05) promotes asymmetric deformation, a simple shear shortening and thin-skinned deformation style and that it is a

necessary condition to initiate foreland underthrusting at the latitudes of the Altiplano-Puna (Sobolev et al., 2006; Barrionuevo et al., 2021; Liu et al., 2022; Chapter 2). Additionally, Ibarra et al (2019) propose that deformation tends to localize within the areas with large lateral variations of crustal strength, such as the foreland where a thick sedimentary layer is present. Our results show that the distribution of sediments inherited from past tectonic events largely control the shallow strain localization (Figure 3.2d, Figure 3.6 and 3.7, S3a-c). Sediments tend to accumulate at the footwall of the faults or close to uplifted basement blocks. In addition, some of these depocenters were formed during Palaeozoic to early Mesozoic extensional phases, which could also have weakened the basement (Mescua et al., 2016). In our model, efficient simple shear shortening is favoured by the thick sedimentary layer of the foreland basin and as a result forms a detachment fault connecting plastic (brittle) and viscous strain rates in the upper and lower crust, respectively (Figure 3.5). When this connection is not possible, the shortening is accommodated by pure shear and the deformation distributes along multiple symmetrical faults (Figure 3.5). Model variations S3a-d show that weaker sediments are required to localize the deformation along specific discrete faults and structures (e.g., at the borders of the uplifted basement blocks or the Bermejo basin; Figure 3.6, S3c). Conversely, strong sediments (e.g. model S3a) with a small strength contrast with the upper crust lead to a broad diffuse shear zone in the foreland above the shallow slab segment (Figure 3.6e-h).

An additional factor that is proposed to exert a major control on strain localization is topography. In the orogen, the gravitational potential energy constitutes a resistive force to the orogenic growth (Molnar & Tapponnier, 1975; Chen & Molnar, 1983; Stüwe, 2007; Mareschal & Jaupart, 2011; Liu et al., 2022). If horizontal forces are not sufficient to overcome the stress exerted by the orogenic topography, the stress migrates laterally to the front of the orogen and the strain localizes in the foreland. This effect is demonstrated in Model S4c (Figure 3.6k), where no topography is allowed to grow, thus the deformation is less efficiently transmitted and localized in the weak areas of the foreland. Topography can also exert an indirect effect on deformation localization: the uplifted foreland basement blocks are bounded by faults and adjacent sediment depocenters, which promotes the localization of deformation as discussed previously in this section. In the alternative models without initial topography (Model S4a, Figure 3.6i) or where no topography is allowed to grow (Model S4c, Figure 3.6k), the removal of the orogenic load helps the strain to localize in the orogen. Additionally, the models without prescribed velocities (Models S4b, Figs. 6j and l) indicate that a low portion of the strain rate in the northern orogen in the model could result from some dynamic effect of the flowing mantle asthenosphere.

3.5.2.2 Effect of deep inherited structures.

The viscous strength of the continental crust and mantle lithosphere strongly depends on their inherited thickness and on their thermal state because of the strong dependence of viscosity on the temperature (Sippel et al., 2017; Anikiev et al., 2020; Ibarra et al., 2021; Rodriguez Piceda et al., 2022b). In the orogen, higher temperatures decrease the depth of the brittle-ductile transition favouring viscous deformation and crustal flow which may facilitate the connection with the plastically deforming foreland sediments, ultimately promoting simple shear deformation (Liu et al., 2022). Additionally, for a orogenic crust of more than 60 km thick, simple shear is almost always the preferred mode of foreland deformation (Liu et al., 2022). In contrast, a cold rigid lithosphere can act as an indenter by transmitting horizontal stress to its front, localizing the deformation at the transition between strong and weak domains (Calignano et al., 2015; Tesauro et al., 2015; Rodriguez Piceda, Scheck-Wenderoth, Bott, et al., 2022).

The lithospheric thermal field in the SCA is the result of the contributions from the compositional and thickness configuration of the lithospheric layers and the lithospheric basal heat flow (Rodriguez Piceda et al., 2022). The crustal thermal field mainly depends on the volumetric heat capacity of the radiogenic upper crust, whereas the thermal field of the mantle is strongly perturbed by the cooling effect of the subducting slab, which changes as a function of the slab dip and geometry (Rodriguez Piceda et al., 2022). In the northern part of the orogen, the effect of the thick felsic radiogenic crust overprints the cooling effect of the flat slab (Rodriguez Piceda et al., 2022). Therefore, the northern part of the orogen would be expected to actively deform, which contradicts our model results and the lack of observed seismicity in the area (ISC catalog, Rodriguez Piceda et al., 2022b; Figure SB.2). To explain this apparent contradiction (i.e. no deformation of the upper plate in this area), an additional mechanism must be invoked (further discussed in Section 3.5.3, Controls of the lower plate). Conversely, the lithosphere in the northern foreland is characterized by a thinner radiogenic upper crust which does not overprint the cooling effect of the flat-slab, thus resulting in a colder and stronger lithosphere. This strengthening allows for an efficient stress transmission from the oceanic plate to the continental plate between western and eastern domain above the flat slab segment. Additionally, that the strong thick cratonic domain (Figure 3.2f) allows for an efficient transmission of stress to the west. Consequently, the deformation localizes at the eastern edge of the broken foreland where the effects of forces applied from the subducted plate and the cratonic part of the continental plate meet (Figure 3.5a). Finally, the deformation is intensified by the overlying weak sediments.

Other deep lithospheric processes, such as eclogitization of the crust and delamination of the lithospheric mantle, are not considered in our models but could also weaken the overriding plate and facilitate strain localization (Babeyko et al., 2006; Sobolev et al., 2006; Chapter 2). However, in the southern central Andes, there is no evidence of delamination and extensive eclogitization below the

Western Sierras Pampeanas and Precordillera (Alvarado et al., 2007, 2009; Ammirati et al., 2013; 2015; 2018; Gilbert et al., 2006b; Marot et al., 2014). Thick warm orogenic crust (>~45 km) can also be subjected to intracrustal convection and partial melting, further weakening the overriding plate (Babeyko et al., 2006). However, such thickness values are only reached at flat slab latitudes (Assumpção, 2013; Rodriguez Piceda et al., 2021) where the lack of volcanism between ~27°S - 33°S (Figure 3.1) indicates a decrease in the lithospheric basal heat flux during the last ~6 Ma (Barazangi & Isacks, 1976; Isacks et al., 1982; Jordan et al., 1983; Kay et al., 1987; 1991; Jordan et al., 1993; Ramos et al., 2002a; Ramos & Folguera, 2009; Rodriguez Piceda et al., 2022), preventing partial melting and crustal convection in the southern Central Andes.

3.5.3 Lower-plate control on strain localization

In the SCA, the role of the flat-slab on the stress regime and the localization of deformation in the upper plate is strongly debated (Jordan et al., 1983; M. A. Gutscher et al., 2000; Folguera et al., 2009; M.-A. Gutscher, 2018; Horton, 2018; Martinod et al., 2020). In the classical view, steep subduction is associated with upper-plate extension and back-arc spreading, while low-angle subduction is related to upper-plate compression and shortening (Barazangi & Isacks, 1976; Ramos & Folguera, 2009; Horton, 2018). Eastward compression is driven by basal shear stress exerted by the underlying flat-slab (Gutscher et al., 2000). Additionally, the passage of the flat-slab scrapes the continental lithospheric mantle, weakening the overriding plate mechanically ('bulldozed mantle-keel' model, Liu & Currie, 2016; Gutscher, 2018; Axen et al., 2018) and thermally by exposing the remaining lithosphere to the warmer asthenosphere (Isacks, 1988). More recent studies, however, have emphasized that the stress regime of the overriding plate is more so determined by the velocity difference between the overriding plate and the trench than by the subduction angle (Lallemand et al., 2008; Faccenna et al., 2017, 2021, Chapter 2). The velocity of trench retreat can be perturbed by a rapid change in the subduction angle, which can be caused by the interaction between the slab and the mantle transition zone (Čížková & Bina, 2013; Cerpa et al., 2015; Briaud et al., 2020; Chapter 2). The absolute motion of the South American plate prescribed in model S1 is known to be the driving force of the Andean orogeny (Sobolev and Babeyko, 2005; Husson et al., 2008; Martinod et al., 2010), nevertheless at shorter geological time-scale model variants (S5b-d), illustrate that a similar strain rate than model S1 can be reached given a similar convergence rate value (Figure 3.6 and 3.7). In our short simulations, the subduction angle of the slab controls the distribution of strain localization in the upper plate. The flat slab propagates the stress eastward causing the shortening to take place in front of the flat slab, as proposed by the 'bulldozed mantle-keel' models ('slab bulldozing', Gutscher, 2018; Axen et al., 2018). Strain localization could be favoured by large crustal-scale inherited structures such as the Transbrasilian lineament in the SCA. The horizontal stress applied by the continental

plate is also more efficiently driven through the thicker and stronger cratonic domain (Figure 3.5). Our results predict almost no deformation in the upper plate overlying the flat-slab segment (28°S-32°S). We suggest that this is the result of the upper plate strengthening at these latitudes due to the cooling (as discussed in section 3.5.2.2) produced by the underplated oceanic slab at the base of the continental lithosphere. The idea that the upper plate is preserved from the deformation on top of the flat slab segment is also supported by the decrease in shortening in the Precordillera at ~9Ma at 30°S following the arrival of the Juan Fernandez Ridge at 12 Ma (Yáñez et al., 2001; Allmendinger & Judge, 2014; Bello-González et al., 2018). Moreover, little seismic activity is observed in the upper plate on the top of the flat slab (Figure SB.2). The colder subduction interface along the flat slab segment (Figure 3.5a) also contributes to an increase in the coupling between the plates and can locally reach more than 35 MPa of shear stress (Figure SB.4). The low temperatures of the subduction interface combined with the low frictional strength of the SCA could deepen the BDT to 100 km depth (Figure 3.5a). The average modelled shear stress at the subduction interface also indicates a higher coupling within flat slab domains compared to steeper domains. The comparison with the average shear stress at the plate interface by Lamb & Davis (2003; Figure SB.4) shows that our reference model (f=0.015) may underestimate the friction at the flat slab interface, whereas model S2d (f=0.07) may overestimate it. Further, the shear stress decreases towards the south, which is supported by the increased thickness of the trench-fill sediments.

As opposed to the flat slab segment, deformation in the steep slab segment (36°S-40°S) localizes along the front of the orogen, which shows that deformation cannot be efficiently propagated to the eastern domain if the slab is steeply dipping. Alternatively, the transition between the steep and flat slab geometry results in the formation of an intermediary shallow segment (32°S-36°S). Above this segment a large crustal shear zone develops in the broken foreland that results from the offset of strain localization between the flat and steep slab. Deformation takes place over multiple faults that border the uplifted basement of the Sierras Pampeanas (Figure 3.5d), and the strain localization along these faults is enhanced by the presence of weak sediments (Models S2, Figure 3.6a-d). From a dynamic point of view, we suggest that the shallowing of the slab produces a crustal contraction prior to the slab flattening in response to a large transpressive shear zone in the southern Sierras Pampeanas. The deformation could be accommodated by strike-slip deformation at the borders of the uplifted basement blocks as well as their rotation, we call this mechanism “flat-slab conveyor” (Chapter 5).

Contributors classification			Conceptual strength profile of the lithosphere	Effect on strain localization
Overriding plate	Shallow (~surface to ~10 km depth)	Topography	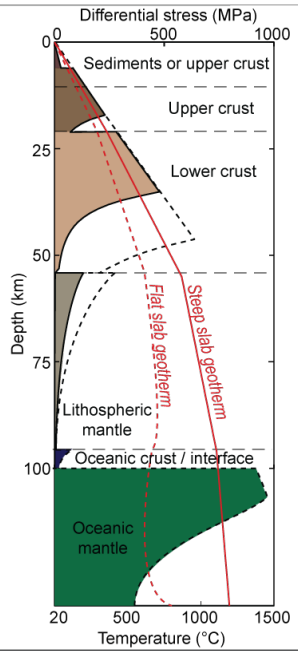	The GPE/topo prevents internal deformation of the orogen and promotes stress transmission to the foreland.
		Sediments / inherited faults		Weak sedimentary basins undergo deformation on their margins, which is often associated with displacement of weak faults and increased accommodation space.
	Intermediate (~10 to 60 km)	Crustal thickness		Thick, warm orogenic crust leads to a shallower BDT and favors simple shear shortening of the Foreland Fault and the Thurst belt.
				Thick lower crust in the forest and foreland promote viscous strengthening, allowing stress to be transmitted eastward.
				The composition and boundaries of the terranes favour strain localization
	Deep (~60 to 150 km)	Lithospheric mantle thickness		The thickening of the cratonic domain favors viscous strenghtening allowing the transmission of stresses to the west.
Subduction Interace		Frictional strength of the subduction interface		The strength of the interface allows stresses to be transmitted from the oceanic plate to the overriding plate and the deformation to propagate to the east.
Subducting plate		Temperature of the oceanic plate		The oceanic plate cools the dominant plate and strengthens it.
		Underplating of the oceanic plate		The underplating of the mechanically strong oceanic plate strengthens the lithosphere and contributes to the propagation of the deformation eastward.

North ---------- dominant contribution ---------- South

Table 3.3 Summary of the main contributing factors to strain localization in the Southern Central Andes indicates a switch from deep to shallow from North to South.

3.6 Conclusions

Using 3D data-driven geodynamic subduction modelling, we discuss the relative contribution of the subducting plate geometry and of the shallow and deep inherited structures of the overriding plate on strain localization in the SCA. The results of this study provide new insights in understanding the present-day interactions between the Pampean flat slab and the South American plate. The flat slab controls upper-plate deformation in the northern part of the SCA by strengthening the upper-plate lithosphere and by cooling down of the overriding plate through underplating. It preserves the upper-plate above the sub-horizontal segment of the oceanic plate from being deformed. As a consequence, the deformation propagates to the eastern edge of the flat slab by the bulldozing effect, and it is accommodated in the eastern broken foreland, where the slab is already dipping steeply.

The inherited structures in the overriding plate contribute to the strain localization in multiple different ways. (i) The sediment distribution works as a proxy for the distribution of major faults because depocenters usually form at their foot walls. Weaker sediments, and therefore weaker faults, significantly intensify deformation in the shallow slab segments. (ii) Older faults, such as the TBL located in the transition to the cratonic domain with thicker lithosphere, may be reactivated and localize the deformation as it occurs in the eastern Sierras Pampeanas. (iii) The localization of deformation in the forearc may be controlled by strain partitioning and long-term strain weakening. (iv) The crustal thickness may control the temperature of the crust due to the contribution of radiogenic heating, thus affecting the BDT depth. For a thicker crust the BDT is shallower, which promotes the development of deep seated asymmetric decollement and simple shear shortening in FTB. Meanwhile, the deeper BDT in the Sierras Pampeanas promotes the development of multiple symmetric faults and pure shear shortening. (v) The surface topography may also play a significant role in strain localization within the orogen by transmitting the horizontal stress to the foreland. Overall, the decreasing dip angle of the oceanic plate to the south allows the connection of the Eastern Pampeanas ranges in the North (e.g Sierra Cordoba, Sierra Grande) to the foreland fold and thrust belts in the South (e.g San Rafael and Malargue FTB). This connection can be achieved by a diffuse shear zone or facilitated by the intermediary of a possible "en-échelon" structure to diffuse crustal scale shear zone. The geometry of these structures correlates with the observed change of the foreland deformation style from thin- to thick-skinned, from the North to the South, respectively.

Chapter 4 Conveyor effect from precursory crustal contraction foreshadows the arrival of the Pampean flat-slab

4.1 Abstract

The southern Central Andes (29°S-39°S) is a key area to better understand the mechanisms of non-collisional mountain building associated with changes in oceanic plate dip geometry and the interaction between the oceanic and continental plates. The orogen experienced an increase of shortening during the last 35 Ma which is coeval with the southward migration of a flat subduction segment and the passage of a bathymetric anomaly known as the Juan Fernandez Ridge. Based on data-driven geodynamic numerical modelling, we use the present-day plate configuration to assess the role of the flat-slab on the deformation of the overriding plate. The resulting deformation field suggests that the shallowing of the oceanic slab controlled the onset of the compression at ~10 Ma before the arrival of the ridge leading to the formation of a ~370-km-wide transpressive shear zone at the transition between the flat (27°S - 31°S) and the steep slab segments (south of 33°S). The contraction of the crust is accommodated by the dextral rotation of micro-crustal Sierras Pampeanas basement blocks and strike-slip deformation at their borders (i.e., thick-skinned foreland deformation).

4.2 Introduction

Deformation styles of the foreland Fold and Trust Belt (FTB) are generally classified into two end-member models: thin-skinned type (Chapple, 1978; Davis et al., 1983), where deformation propagates through the development of thrust sheets in the sedimentary cover, and thick-skinned type, where deep faults develop in the crystalline crust by exhuming the underlying basement blocks (Coward, 1983). Numerous FTBs along active margins, such as along the Eastern Pacific Coast, show spatial and temporal variations in the style of deformation. For instance, during the Laramide orogeny, the foreland style changes from thin-skinned to thick-skinned causing the growth of the Rocky Mountains at 80 Ma (Saleeby, 2003; Erslev & Koenig, 2009). This transition is attributed to the flattening and bulldozing effects of the Farallon oceanic plate associated to the subduction of the buoyant Shatzky Plateau (Axen et al., 2018). Nevertheless, the effect of the lateral variation of the geometry of the subducting plate due to its shallowing on deformation styles remains poorly understood. The broken foreland of the Sierras Pampeanas in the southern Central Andes (SCA, 29°S-39°S, Figure 4.1a) is considered a present-day analogue of the Laramide foreland. Its formation has been attributed to the interaction between the horizontal subduction of the oceanic Nazca plate and the continental South American plate during the Neogene associated to the subduction of the Juan Fernández Ridge (JFR), which is currently situated at

the southern edge of the Pampean flat-slab (Gutscher, 2002; Mahlburg Kay & Mpodozis, 2002; Ramos et al., 2002; Jones et al., 2016); Figure 4.1a). The flat-slab segment transitions to a steeper subduction segments at 32°S, (Barazangi & Isacks, 1976; Isacks, 1988; Jordan et al., 1983). Plate reconstructions suggest that the JFR and the flat-slab have moved southward from 21°S (i.e Atliplano plateau) at ~25 Ma to their present-day position at 33°S (Figure 4.1b, Yáñez et al., 2001; Bello-González et al., 2018). The passage of the flat-slab correlates with the cessation of the volcanic activity (Barazangi & Isacks, 1976; Jordan et al., 1993; Ramos et al., 2002; SM Kay, 2002; Ramos & Folguera, 2009). In this context, the present-day plate configuration of the SCA can be considered a snapshot of the evolution of the South American plate margin since the Oligocene, thus it can be used to analyse the effect of the oceanic plate angle in the variations of upper-plate deformation style through time.

This contribution addresses the question "How does the foreland deformation evolve spatially and temporally with the arrival of a flat-slab?" To that end, we developed a three-dimensional numerical geodynamic data-driven model of the SCA which integrates the present-day structural, density and thermal fields of the lithosphere (Rodriguez Piceda et al., 2021, 2022) to simulate strain rate localization, together with the deformation and stress fields. Based on our modelling results, we propose that the contraction of the crust causes regional transpression and differential crustal block rotations within the Sierras Pampeanas, which results in the transition from thin- to thick-skinned foreland deformation (Figure 4.1c). This compression in the Sierras Pampeanas occurs during the shallowing of the oceanic plate which precedes the onset of the flat-slab by ~10 Ma, which is consistent with the timing of the geological events (see Regional setting of the Southern Andes for details). Furthermore, we suggest that these processes may have also conditioned the shortening along the Andean Plateau between 35 and 25 Ma and the Laramide Orogeny between 80 and 50 Ma, thus having profound implications on our understanding of the evolution of the foreland deformation at active margins along the Eastern Circum-Pacific Belt.

4.3 Regional setting of the southern Central Andes

The Pampean Flat-slab is situated at the transition between the Central and Southern Central Andes, which is characterized by a difference in the magnitude of shortening (~250 km at 23°S to less than 70 km at 27°S,Oncken, 2006-2012). Between 27°S and 33°S, the foreland deformation extend to the East and transitions from thin-skinned in the Precordillera FTB to thick-skinned expressed by isolated uplifted basement blocks in the Northern Sierras Pampeanas (Figure 4.1a; Jordan, 1984; Jordan & Allmendinger, 1986; Kay & Abbruzzi, 1996; Ramos et al., 2002). Between 33°S and 36°S, the deformation localize in front of the orogeny and deform by a mixed thin and thick-skinned yet locally involving basement blocks (Figure 4.1a; e.g. San Rafael Block, Manceda & Figueroa, 1995; Giambiagi et al., 2012; Fuentes, 2016). Between

33°S and 36°S, the foreland fully deformed by thin-skinned along the Cerrilladas Pedemontanas FTB (Figure 4.1a).

The tectonic history of the Sierras Pampeanas is intimately linked to the shallowing of the oceanic plate (Figure 4.1b, Ramos et al., 2002; V. A. Ramos & Folguera, 2009). At 30°S, Pre-Neogene normal faults are reactivated at ~21 Ma, marking the switch from extensional to compressional deformation (Figure 4.1c, Giambiagi et al., 2012; Martino et al., 2016, Ramos et al., 2002; Horton, 2018). The Precordillera registers three main deformational phases during the Neogen (Figure 4.1d, Allmendinger & Judge, 2014): a low deformational phase at ~20-13 Ma (with a shortening rate of 1-5 mm/yr), a high deformational phase at 12-9 Ma (the shortening rate increases to ~20 mm/yr), followed by a low deformational phase until present day (the shortening rate decreases to ~5 mm/yr). This last phase correlates with the onset of the flat-slab, marked by the arrival of the JFR at those latitudes (Figure 4.1b). Meanwhile the deformation migrated to the east from the Frontal Cordillera to the Sierras Pampeanas and switched from thinned to thick-skinned (Figure 4.1c), whereas the volcanism ceased at ~6 Ma. A major uplift phase of the Sierras Pampeanas blocks occur in the last ~5 Ma (Figure 4.1b, Jordan, 1984; Jordan & Allmendinger, 1986; Kay & Abbruzzi, 1996; Cristallini & Ramos, 2000; Ramos et al., 2002). The time spanned between the onset of the compression and the arrival of the flat-slab (~8 to 10 Ma), led some authors to propose alternative mechanisms controlling the deformation, including the reactivation of crustal inherited structures (Giambiagi et al., 2012; Walcek & Hoke, 2012; Levina et al., 2014; Suriano et al., 2017; Lossada et al., 2017) or the anchoring of the oceanic slab at the transition zone (Zapata et al., 2020).

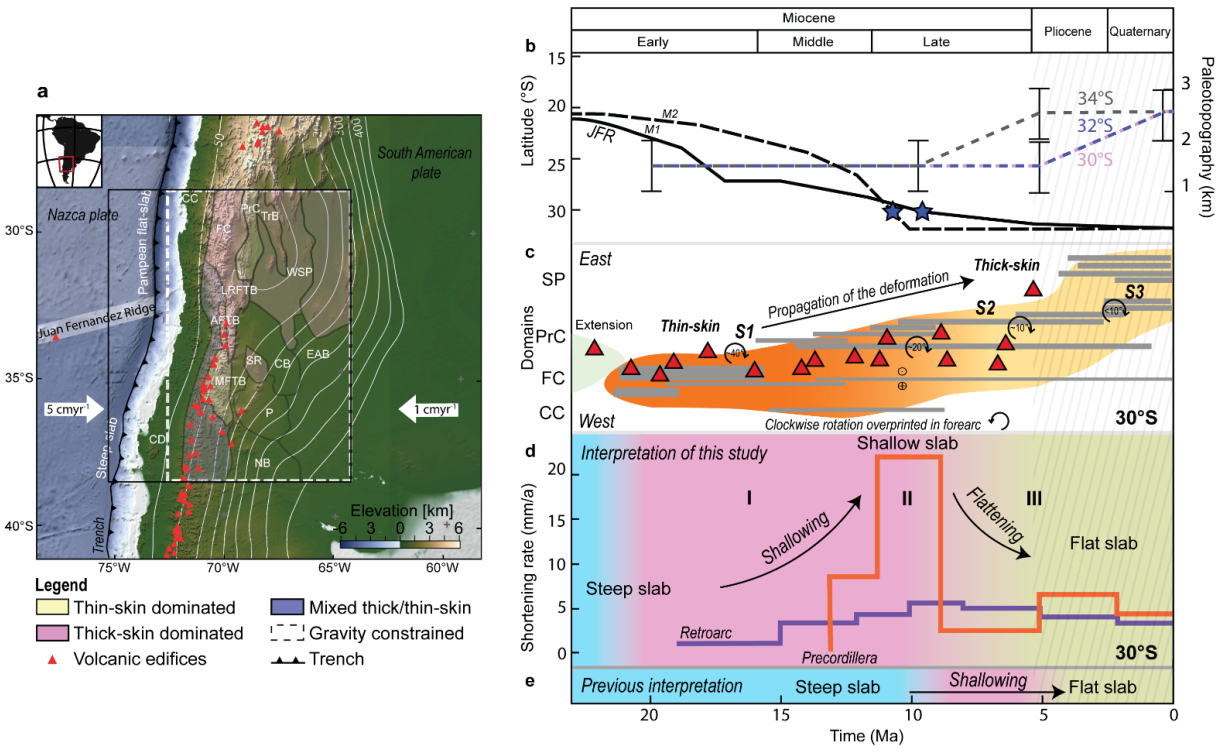

Figure 4.1 Summary of the geological events in Sierras Pampeanas. Regional setting of the southern Central Andes. **a** Topography and bathymetry from ETOPO-1 digital elevation model (Amante & Eakins, 2009) overlain with location of the most important morphotectonic provinces. The black rectangle denotes study area. The white dashed rectangle shows the extent of the gravity-constrained structural model (Rodriguez Piceda et al., 2021). The track of the Juan Fernandez Ridge (thick white line, Yáñez et al., 2001) and the depth contours of the subducting Nazca slab (white, Hayes et al., 2018) are also shown. Oceanic and continental plate velocities are indicated by white arrows (Sdrolias & Müller, 2006; Becker et al., 2015a). Abbreviations of main morphotectonic provinces: CB: Cuyo basin, CC: Coastal Cordillera, CP: Cerrilladas Pedemontanas, ESP: Eastern Sierras Pampeanas, NB: Neuquén basin; P: Payenia, PC: Principal Cordillera (LRFTB= La Ramada fold-thrust belt, AFTB: Aconcagua fold-thrust belt, MFTB: Malargüe fold-thust belt), FC: Frontal Cordillera, FA: forearc, PrC: Precordillera, SR: San Rafael Block, TrB: Triassic basins, WSP/SP: Western Sierras Pampeanas. **b** Evolution of paleo-topography; left y-axis: Position of the Juan Fernandez Ridge (JFR) at the trench in latitude in time (M1 : Bello-González et al., 2018, and M2 : Yáñez et al., 2001). The blue star indicates the time at which the ridge reaches 30°S. Right y-axis: paleotopographic evolution of the Precordillera at 30°S-32°S and Frontal Cordillera 34°S (Walcek & Hoke, 2012; Hoke et al., 2014; Schildgen & Hoke, 2018). **c** Deformational events at 30°S (grey bars, modified from Quiero et al., 2022). Red to yellow and green field indicates periods of shortening and extension and their areal extent. Red to yellow indicates the change from thin to thick-skinned foreland deformation (Ramos et al., 2002). Rotation symbols indicate crustal rotation based on paleomagnetic data (Japas et al., 2016), red triangles indicate volcanic events events (Trumbull et al., 2006; Litvak et al., 2018; Quiero et al., 2022). S1, S2, S3 hold for identified stages of propagation of the deformation to the east. **d** Shortening rate in Precordillera (orange, Allmendinger & Judge, 2014) and in retroarc (purple, Mardones et al., 2021; Quiero et al., 2022) at 30°S. Roman numerals I - III indicate main phases of deformation. **d-e** Color gradient in the background indicates the state of the slab geometry interpreted from this study and from previous studies (i.e., Ramos et al., 2002; Horton, 2018). Oblique gray lines in the background in **a**, **b**, **c** indicate time of cessation of the volcanism.

4.4 Modelling results

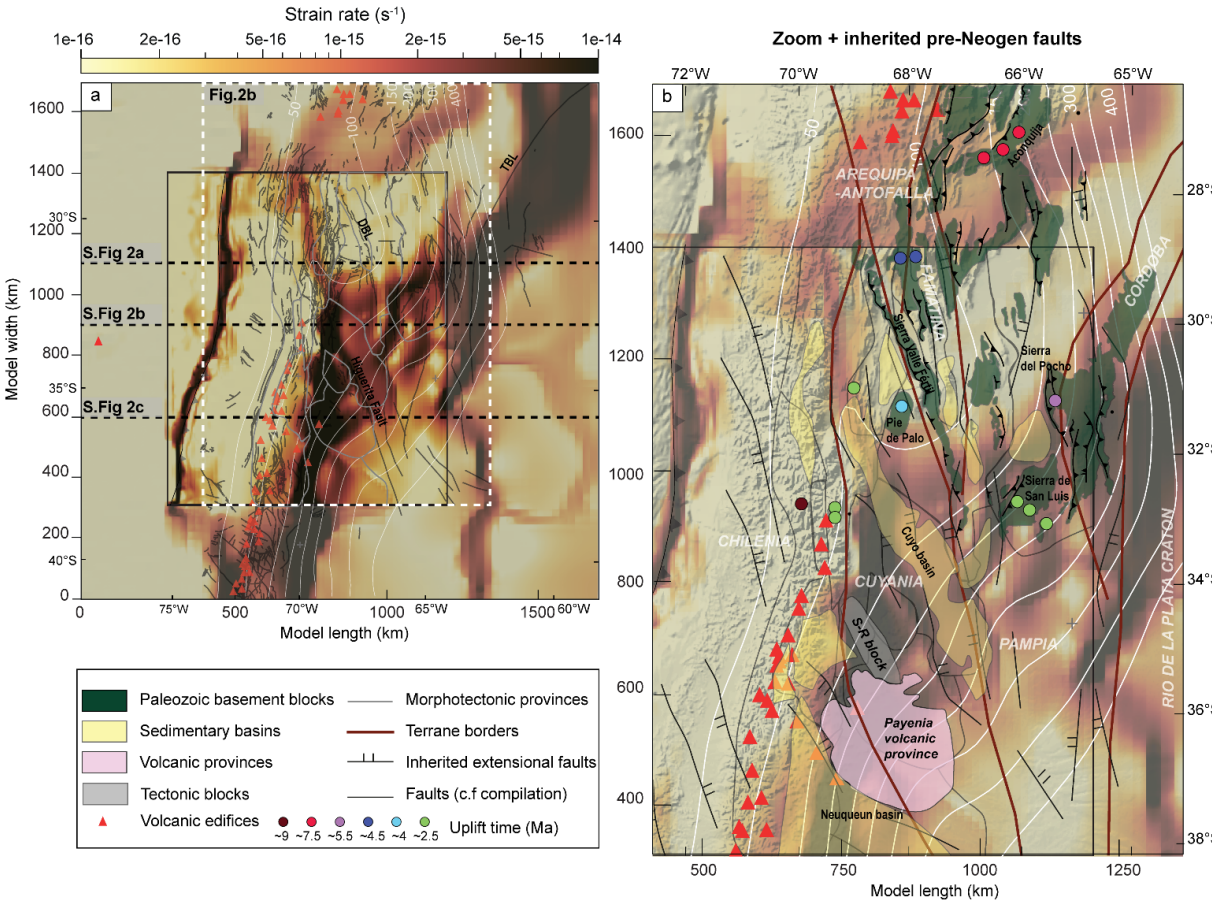

Figure 4.2 Modelled surface strain rate of the Sierras Pampeanas (Chapter 5). Modelled surface strain rate. **a** strain rate distribution of the SCA. **b**. Close-up of the Sierras Pampeanas. Overlain in a and b are the faults (black lines, Figure SB.5), the borders of the morphotectonic provinces (grey lines) and the contours of the top slab (Hayes et al., 2018). b also shows the main geological features (basement blocks, sedimentary basins and volcanic provinces), inherited pre-Neogene extensional faults (black lines), terrane borders (brown lines, Ramos et al., 2014; Wimpenny, 2022), active volcanic edifices (red triangles) and location of age-contrained uplift (Table B.S1).

The model indicates a complex interaction between three along-strike segments where deformation appears to be focused (4.2a): (i) a western segment (75°W to 73°W), located at the plate boundary, due to the decoupling of both plates; (ii) a central segment (73°W to 70°W), corresponding to the main front of the orogen and comprised of foreland fold-and-thrust belts (FTB , e.g., Neuquen, Malargue); this sector shows a decrease in the intensity of the deformation on top of the flat-slab; and (iii) an eastern segment (60°W to 65°W), where deformation localizes to the east of the flat-slab and extends to the south, following the deformed margins of the inferred position of the Rio de la Plata craton (Hamza & Vieira, 2012). This region includes the Transbrasilian lineament (TBL), a major transpressive shear zone of

Proterozoic age that borders the thicker mantle lithosphere of the Rio de la Plata Craton (Figure SB.5, Cordani et al., 2013; Casquet et al., 2018) and is associated with the amalgamation of the Cordoba and Pampia terranes to the craton during the formation of Gondwana (Fairhead & Maus, 2003; Ramos, 2010). The strain also localizes in the realm of other structural provinces, such as the Cuyo sedimentary basin, which is aligned with the orientation of inherited Triassic extensional structures (Lopez-Gamundi, 2010, Figure 4.2b). At the northern edge of the Cuyania terrane, localized deformation is aligned with the southern extent of the Desaguadero-Bermejo lineament (DBL, Introcaso & Ruiz, 2001); this lineament is the southward continuation of the Sierra Valle Fértil fault which borders the western Sierras Pampeanas and constitutes the eastern limit of the Cuyana terrane which was amalgamated with the Pampia terrane during the Ordovician (Ramos et al., 2004, 2010). At the southern limit of the Cuyo basin the strain rate localizes over the Higuerita Fault and also reflects the geometry of the San Rafael block and the Cerradillas Pedemontanas farther south. The forearc is subjected to reduced deformation, likely acting as a rigid body (Tassara & Yáñez, 2003; Tassara et al., 2006; Hackney et al., 2006).

The central and eastern segments interact over an extended shear zone between ~32 and 36°S (~600 km to 1000 km model width). South of it, deformation strongly localizes over a main structure, where the plastic strain rate connects in depth with the viscous strain rate (Babeyko & Sobolev, 2005, Figure 3.5) leading to the development of a deep-seated shear zone. The central segment deformation pattern is representative of thin-skinned foreland deformation with the formation of a major décollement in the FTB. Within the extended shear zone, the development of multiple “faults” indicates pure shear shortening of the upper crust, with the depth of these faults limited by the depth of the brittle-ductile transition (BDT) (Figure 3.5). This shortening mode is representative of a thick-skinned foreland deformation style. Overall, there is a switch of shortening mode from the South to North, from simple shear to pure-shear. The extended shear zone constitutes a large transpressive shear zone that accommodates regional shortening by the development of multiple en-echelon shear zones bordering the more rigid basement blocks of the Sierras Pampeanas, which are indicated by their shallower BDT (Figure 3.5). North of the extended shear zone, above the flat-slab, reduced deformation takes place at the eastern edge of the flat-slab, but not within the weak and warm orogen (Figure 3.5). The cooling effect of the flat-slab and the underplating of the slab may strengthen the lithosphere. Stresses generated by the motion of the continental plate do not affect the top of the shallow slab and are rather accommodated at its eastern limit (Figure 4.3a-b). Additionally, the lower plate exerts a shear force which is transmitted farther eastward along the shallow subduction interface (Figure 4.3c) causing the migration of deformation. This is well-expressed on the E-W sections of the velocity field shown for the flat, transitional, and steep slab segments (Vxx, Figure 4.3a-b).

Strike-slip deformation is predicted at the borders of the Sierras Pampeanas basement blocks, with an increased magnitude towards the flat-slab segment (Figure 4.3d). Importantly, since no parallel component of convergence is prescribed in the model, upper-plate deformation does not result from strain partitioning of oblique subduction, but from the curved geometry of the lower plate resulting from the gradual northward shallowing of the Nazca plate. A north-south-oriented section of the east-west velocity field indicates a ~370-km-wide transition zone with decreasing velocity southwards (Velocity X in latitudinal section, Figure 4.3b). This decrease is associated with the apparent rotation of the velocity field (Figure 4.3c). To isolate this signal, we corrected the east-west velocity from the plate motion and calculated its vorticity (Figure SB.6), which indicates that strong rotational motion may occur likely due to shearing in strongly deformed areas where widespread rotation affects the transition zone. From the vorticity and assuming a constant rotation, we quantify the angle of rotation for the ultimate ~6 Ma, which corresponds to the time interval during which the flattening of the slab was fully achieved, as inferred from the timing of the cessation of volcanism in the flat-slab (Figure 4.1). The results provide an approximate angle of rotation assuming constant rotation (Figure 4.3c). The model predicts a rotation of ~15-30° for the entire transition zone (Figure 4.3c), with differential rotations of the Sierras Pampeanas basement blocks. The rotation increases along the shear zone northward and becomes more pronounced in the flat-slab area.

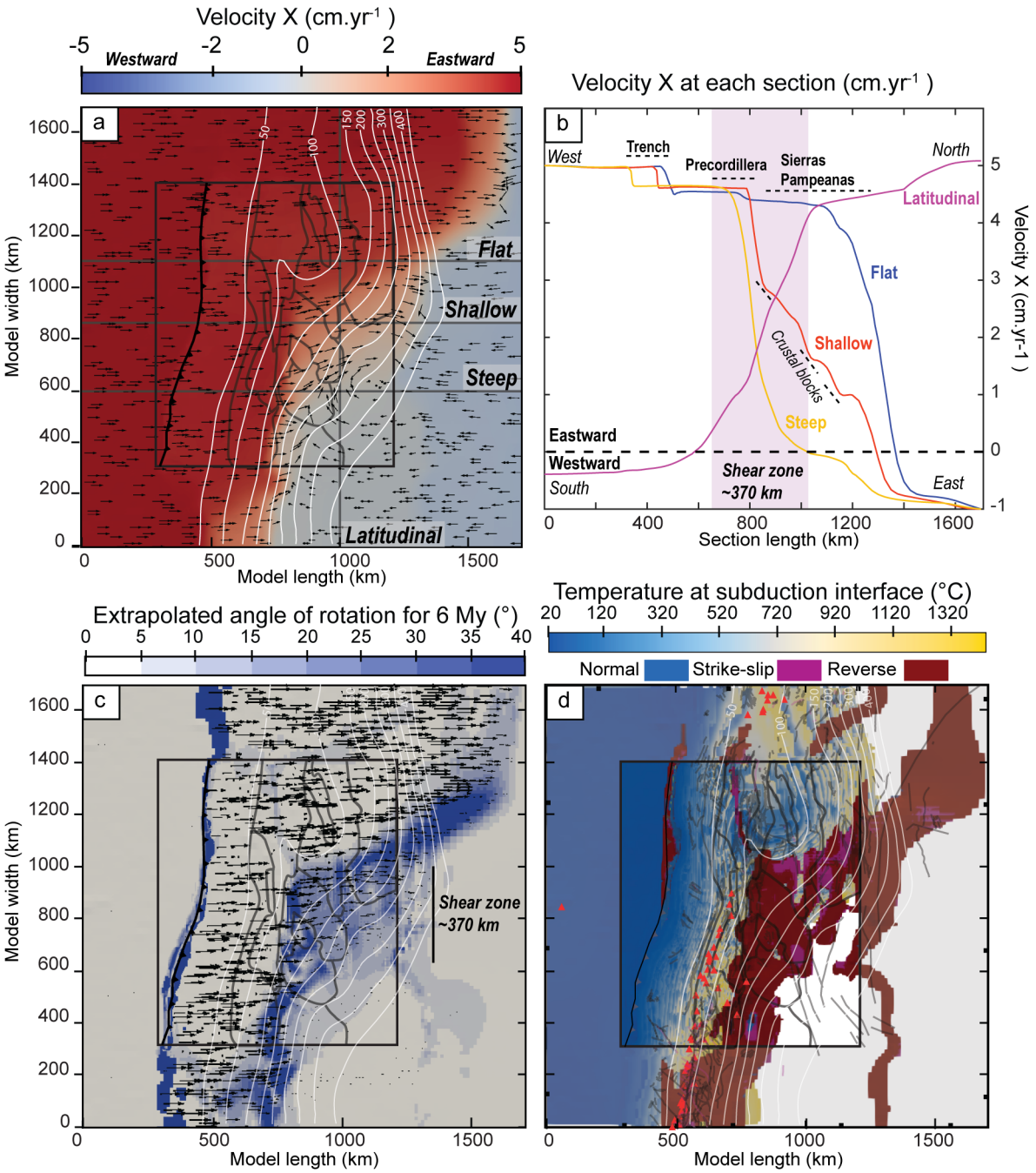

Figure 4.3 Velocity, rotation and deformation of the shear zone. **a** orientation of the East-West velocity (Vxx), velocity field 10 km depth without correction of net plate velocity. Overlain are location of 2D sections shown in **b**. **b** E-W velocity field along 2D sections with location shown in **a**. **c** Extrapolated angle of rotation over 6 Ma. **d** Type of modelled dominant deformation overlain to temperature at the subduction interface **b and c** Superposed velocity vector indicates the orientation of the velocity field corrected from the net velocity of the plate; vector size indicates relative magnitude with respect to the plates after correction. Flat-slab velocity propagates farther into the realm of the continent (Figure 4.3a-b). Within the transition zone the eastward velocity drops faster

with the localization of the deformation at the border of crustal basement blocks (Figure 4.3b). **a, c** and **d** are also overlain by the depth contours of the top of the slab(Hayes et al., 2018)

4.5 Discussion

Our model shows that significant compressional deformation in the upper plate can take place farther south of the ridge-trench intersection due to the shallowing of the slab also resulting in a switch between thin and thick-skinned foreland deformation style. Thus extending the initial period for which the shallowing is thought to have affected the deformation processes in the Sierras Pampeanas. These results enable us to revise the interpretation behind the timing of the most relevant Neogene geological events in relationship to the shallowing of the slab.

4.5.1 Timing and interpretation of tectono-magmatic events: model prediction versus observation

Onset of compressional deformation. Our model indicates that deformation within the transition zone results from the shallowing of the slab and involves a region with a length of more than ~370 km from the position of the JFR to the south. Using this distance and assuming a trench-parallel convergence rate of ~4 cm/yr at ~20 Ma (Sdrolias & Müller, 2006), the time span between the onset of deformation within the transition zone and the arrival of the ridge can be calculated (370 km / 4 cm.yr-1 = ~9.2 Ma). Since the ridge arrived at ~12 Ma at 30°S, the onset of compressional deformation due to shallowing of the slab should be ~21.2 Ma; this is consistent with the changeover from extension to shortening in this region. The southward-migrating slab thus acts as a conveyor of upper-plate crustal deformation, with an increase in the intensity of deformation foreshadowing its arrival.

Propagation of deformation. In the scenario described above the shallowing of the plate is expressed by the eastward propagation of deformation and volcanic activity. Structural reconstructions (Ramos et al., 2002) and compressional deformation at 30°S (Quiero et al., 2022, Figure 4.1c) suggest furthermore that the propagation of deformation from the Frontal Cordillera to the Precordillera had already started between ~20 Ma and ~16 Ma and accelerated until ~11 Ma (stage I). From ~11 to ~6 Ma the locus of deformation stagnated (Stage II) and at ~ 5Ma the deformation jumped to the eastern Sierras Pampeanas (stage III). Similarly, our model predicts the propagation of deformation in the same manner. We infer from our modelling that the shallowing of the slab and the evolution of the shear zone could explain the timing of the first increase of the propagation rate before ~12 Ma. In this context, the jump of deformation toward the eastern Sierras Pampeanas during the last ~5 Ma could be related to a bulldozing effect after completion of the flat-slab (e.g., Gutscher, 2018; Axen et al., 2018). Although very simplified, in such a

bulldozing scenario the shear forces exerted by the subducting plate would be transmitted through the subduction interface toward the front of the flat-slab segment, which in turn results in less deformation of the upper plate above the flat-slab. We propose that the jump of the deformation (Stage III) is preceded by a period of stagnation of the deformation (Stage II) caused by the change of stress transmission to the east between shallowing and bulldozing.

Evolution of shortening rate. At 30 °S, the Precordillera is characterized by three Neogene deformation phases (Figure 4.1d, Allmendinger & Judge, 2014) : a phase of gentle deformation between ~20 and 13Ma (1-5 mm/yr, phase 1), followed by an increase of the shortening rate and phase of more pronounced deformation between ~12 and 9 Ma (~20 mm/yr, phase 2), and finally, a fast reduction of the shortening rate to a more gentle deformation phase until the present-day (~5 mm/yr, phase 3). Geological data show that the shortening rate in the retroarc increases until ~9 Ma (~5mm/yr, Phase 1 and 2) and slightly decreases again until the present-day (~3-4 mm/yr, phase 3). Phase 3 is coeval with the onset of stagnating deformation (stage II) and the flattening of the slab following the arrival of the ridge (Ramos et al., 2002). Our model also predicts a reduction of shortening above the flat segment at ~30°S. In addition to the bulldozing effect coupled with the eastward transmission of deformation, the lithosphere is strengthened because of the underplating of the cold and mechanically strong oceanic lithosphere and concomitant cooling of the upper plate, thus preventing the efficient localization of deformation. However, because the depth of the brittle-ductile transition beneath the orogen does not significantly change between the flat and steep-subduction segments (Figure 3.5a), we conclude that the cooling effect of the flat-slab is a secondary process with regards to the strengthening of the lithosphere.

Uplift of the Sierras Pampeanas. Despite the arrival of the ridge at ~12 Ma, the volcanic activity continued until ~6Ma (Kay & Mpodozis, 2002; Jones et al., 2016). The cessation of the volcanism, was followed by an important phase of uplift of the retroarc in the last ~5 Ma (Walcek & Hoke, 2012; Hoke et al., 2014) and the Sierras Pampeanas basement block ~5.5-4.7 Ma (e.g Sierra del Pocho at ~31°S, (Ramos et al., 2002) which is not linked to a significant increase of the intensity of the shortening rate. We propose that their uplift is a consequence of the underplating of the flat-slab segment. The trend shows that the age of the uplift of the basement blocks becomes younger to the south and to the east (e.g San Louis block at ~33°S, uplift initiated ~2 Ma ago, Ramos et al., 2002).

Shallowing versus flattening. Our model results indicate a changeover in the mechanism that transmits stresses from the subducting plate to the upper plate between steep (35°W to 41°W, 0-600 km model width), shallow (32°W to 35°W , 600-1000 km model width), and flat (27°W to 32°W , 1000-1400 km model width) subduction segments, which is reflected in the geological history of the Sierras Pampeanas at ~30°S. We differentiate the transition from steep to shallow slab (“Shallowing”, ~21 to

12Ma, Stage 1 and Phase 1 and 2) to the transition from shallow to flat-slab ("Flattening",~11 to 5Ma, Stage 2 and Phase 3). During phases of slab shallowing, the available geological data and our model results suggest an increase in shortening rate and accelerated propagation of deformation toward the eastern foreland, whereas during flattening a reduction of the shortening rate and stagnation of the propagation of deformation occurs.

Cessation of volcanism. At present-day, ~80 to 85% of the transition zone is covered by active volcanic edifices, which indicates that the cessation of volcanism occurs while the slab is not yet fully flat. Since the transition zone is the surface expression of the shallow slab, a region with a length of ~55 to 75 km (~20 to 15%) at the southern margin of the flat-slab segment is volcanically inactive. Using an average parallel convergence rate of ~4cm/yr between ~10 to 5 Ma (Sdrolias & Müller, 2006), it can be inferred that that volcanism should shut off ~1.3 to 1.8 Ma (e.g, 55 km / 4 cm/yr) before the arrival of the flat-slab segment or before flattening has been completed. Thus, defining the flat subduction domain by absent volcanism may lead to mis- interpretations of mechanisms responsible for the spatiotemporal characteristics of deformation.

4.5.2 Transpressional system and deformation styles

Foreland transpression caused by shallowing. The footprint of strike-slip deformation in the Sierras Pampeanas has been overlooked over the years, despite structural evidence of diffuse deformation at the borders of the exhumed basement blocks (Introcaso & Ruiz, 2001; Gutiérrez et al., 2017; Giambiagi et al., 2017; Costa et al., 2019). Moreover, strike-slip focal mechanisms in the southern part of Sierras Pampeanas were reported (Alvarado, 2005; Richardson et al., 2012; Ammirati et al., 2015). Paleomagnetic studies have identified crustal rotations within a transpressional zone in the Northern Sierras Pampeanas (27°S-30°S; Aubry et al., 1996) at the transition with the Puna Plateau that was attributed to the difference of shortening magnitude. Additionally, the collision of the JFR ridge would have led to new rotations at 28°S-33°S (Japas & Ré, 2012; Japas et al., 2016a). Alternatively, we propose that the transpression results from the offset between the deformed segment at flat- slab latitudes, where deformation is transmitted eastward by bulldozing in the eastern Sierras Pampeanas, and the deformed segment in front of the orogen at steep-slab latitudes. The interaction between segments is controlled by the progressive shallowing of the oceanic plate which results in an oblique stress transmission (Vxx, Figure 4.3a). In this zone of interaction, the deformation localizes over "en-echelon" crustal scale structures that accommodate a differential dextral rotation of the Sierras Pampeanas rigid basement blocks (Figure SB.6, Figure 4.3c) delimited by strike-slip faults at their borders (Figure 4.3d). The rotation angle of ~20°-30° calculated in the transition zone represent the minimum rotation expected caused by the southwards migration of the flat-slab segment at 30°S where the shallowing was effective ~9.2 My before the arrival

of the ridge at ~ 12 Ma. Based on the model results and the timing of the rotation (Figure 4.1c), we propose that the Miocene-Pliocene rotations of crustal blocks (Aubry et al., 1996; Japas & Ré, 2012; Japas et al., 2016) recorded by paleomagnetic data could have been partially induced by the shallowing of the slab before the arrival of the ridge. At ~30°S, deformation propagates to the retroarc and crustal rotation increases from ~20 - 10 Ma (c.f. Shallowing) before decreasing until present day (Flattening). Additionally, Japas & Ré (2012) proposed that with the arrival of the ridge the shoreline bends and underwgoes forearc dextral rotations prior to the arrival of the ridge that are overprinted by sinistral rotation after its passage.

Deformation style. The change of foreland deformation style is another key characteristic of the Sierras Pampeanas tectonic history. At flat-slab latitudes (27°- 32°W) the deformation takes place by thick-skinned, intensively involving the foreland basement. At shallow slab (32°-35°W) the deformation is a mixt between thin-skinned of the FTB and thick-skinned of the Sierras Pampeanas. At steep-slab latitudes (35°-40°W) the deformation is dominated by the thin-skinned of the FTB. Previous studies have suggested that the flat-slab exerts a control on the foreland deformation style by propagating the deformation to the east and reactivating inherited back-arc normal to reverse faults inducing thick-skinned (Ramos et al., 2002). At 33°S, thin-skinned deformation was overprinted by thick-skin deformation at ~8.6 Ma (Ramos et al., 2002). Our model also indicates a progressive change of shortening mode from North to South between pure shear and simple shear (Figure 3.5) that reflects the present day thin and thick-skinned deformation style in foreland, respectively. We interpret these results in light of the previous mechanism described earlier in the discussion. In the north, localized pure shear shortening occurs in the eastern Sierras Pampeanas as the results of the “bulldozing” of the flat-slab. At the shear zone, a mix between simple shear of the FTB and distributed pure shear shortening over multiple faults in the Sierras Pampeanas take place as the results of the shallowing of the slab and the progressive strengthening of the overriding plate. In the south, simple shear shortening of the FTB takes place as the shallowing is not sufficient yet to propagate the deformation to the east. At lithospheric scale, thick-skinned deformation style appears as a contraction of the crust in order to accommodate the transpressional deformation arising for the curved shallowing of the oceanic plate foreshadowing the arrival of the Flat-slab segment (Figure 4.3d). By consequence, an extended diffuse ductile shear zone forms in which shallow pre-inherited faults associated to the deposition of weak sediments are more likely to be reactivated and to localize the deformation such at the border of the basement blocks.

Implications for regional deformation of the Central Andes. Lastly, we discuss the role of the flat-slab acting as a “conveyor” into the broader picture of the formation of the Central Andes. At the southern front of the migrating flat-slab, the shallowing of the oceanic plate causes the congestion of the upper

plate resulting in its transpression. The thin-skinned deformation propagates from the FTB to the east over multiple faults (i.e thick-skinned) because of the contraction of the crust. Rotation of crustal blocks bordered by strike-slip deformation occurs, likely enhanced by the reactivation of inherited faults. The arrival of the ridge is followed by the flattening of the slab, the decrease of the rotation and the cessation of the volcanic activity. The deformation propagates to the eastern edge of the flat-slab by bulldozing while the upper plate on top of the flat-slab segment is preserved from being deformed. The flat-slab scraps and weakens the lithospheric mantle (Liu & Currie, 2016). Once the oceanic plate steepens back, possible sinistral rotation would overprint the previous dextral rotation. Since the gradient of the oceanic plate steepening at the North is less important than in the south, we would expect less rotations. The steepening would also be associated with mantle removal, thermal weakening and trench hindering that would contribute to efficiently weaken and then shorten the upper plate (Isacks, 1988; Pons et al., 2022). As a results of the passage of the flat-slab the angle of the oceanic plate remains relatively shallow, therefore a buckling instability could formed under the weight of the long oceanic segment in the upper mantle (Ribe et al., 2007) resulting to the trench hindering of the plate (Pons et al., 2022) which would further contribute to the development of the present-day elevation of the Central Andes (Capitanio et al., 2010; Lee & King, 2011; Cerpa et al., 2015; Pons et al., 2022) .

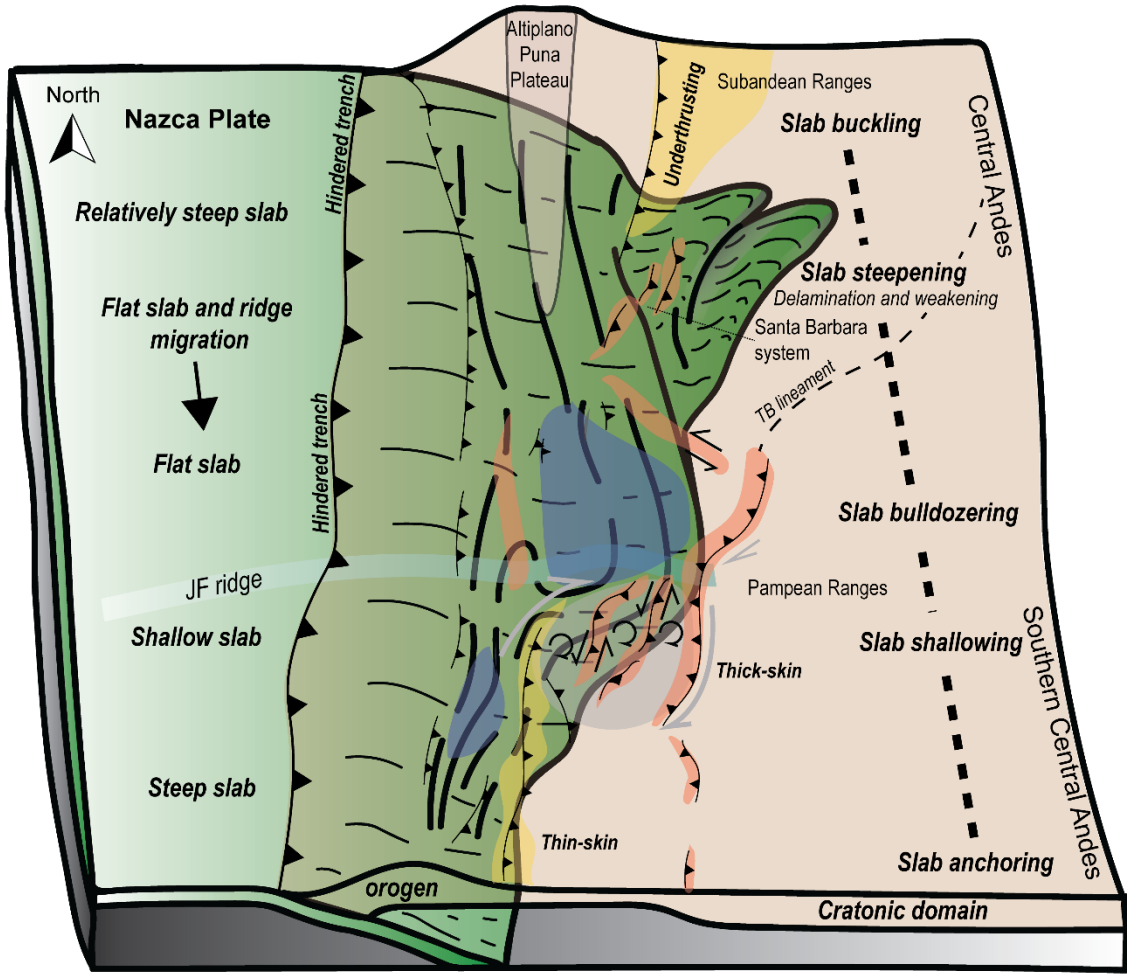

Figure 4.4 Conceptual figure of the role of the slab geometry in the foreland deformation of the Central Andes. Yellow and red areas indicate the thin and thick-skinned deformation. Blue indicates a cold continental lithosphere mantle. Green indicates the oceanic plate. JF is for Juan Fernandez hotspots ridge.

Comparison with the Laramide orogeny

It is currently not possible to construct a model of the older Laramide orogeny at the same resolution as the SCA, which is a current analogue. In the light of these new results, we discuss the evolution of Laramide structures. The Laramide orogeny is similar in its tectonic structures to the southern Central Andes (Figure 4.5). The reconstruction of the oceanic Shatsky Plateau in association with the shallow Farallon Plate starting around 80 Ma is related to the onset of deformation and transpressional dextral thick-skinned foreland deformation at 70 Ma (Axen et al., 2018), associated to the uplift of the eastern basement blocks at the margin of the oceanic plateau. After 10 Ma, the deformation migrated north orthogonally to the front of the Farallon flat-slab, the bulldozing uplifted the northern basement blocks at 60 Ma. The nature of this transition is similar to the shallowing and flattening happening in our model of the SCA. Volcanic provinces are also distributed along the margin of the Shatsky Plateau and could be

related to the steepening of the flat-slab. Furthermore, relatively minor deformation occurred on the top of the flat plate (Saleeby, 2003), similar to the strengthening of the lithosphere in our model, and finally the passage of the flat plate led to the thinning of the continental mantle lithosphere and the uplift of the Colorado Plateau.

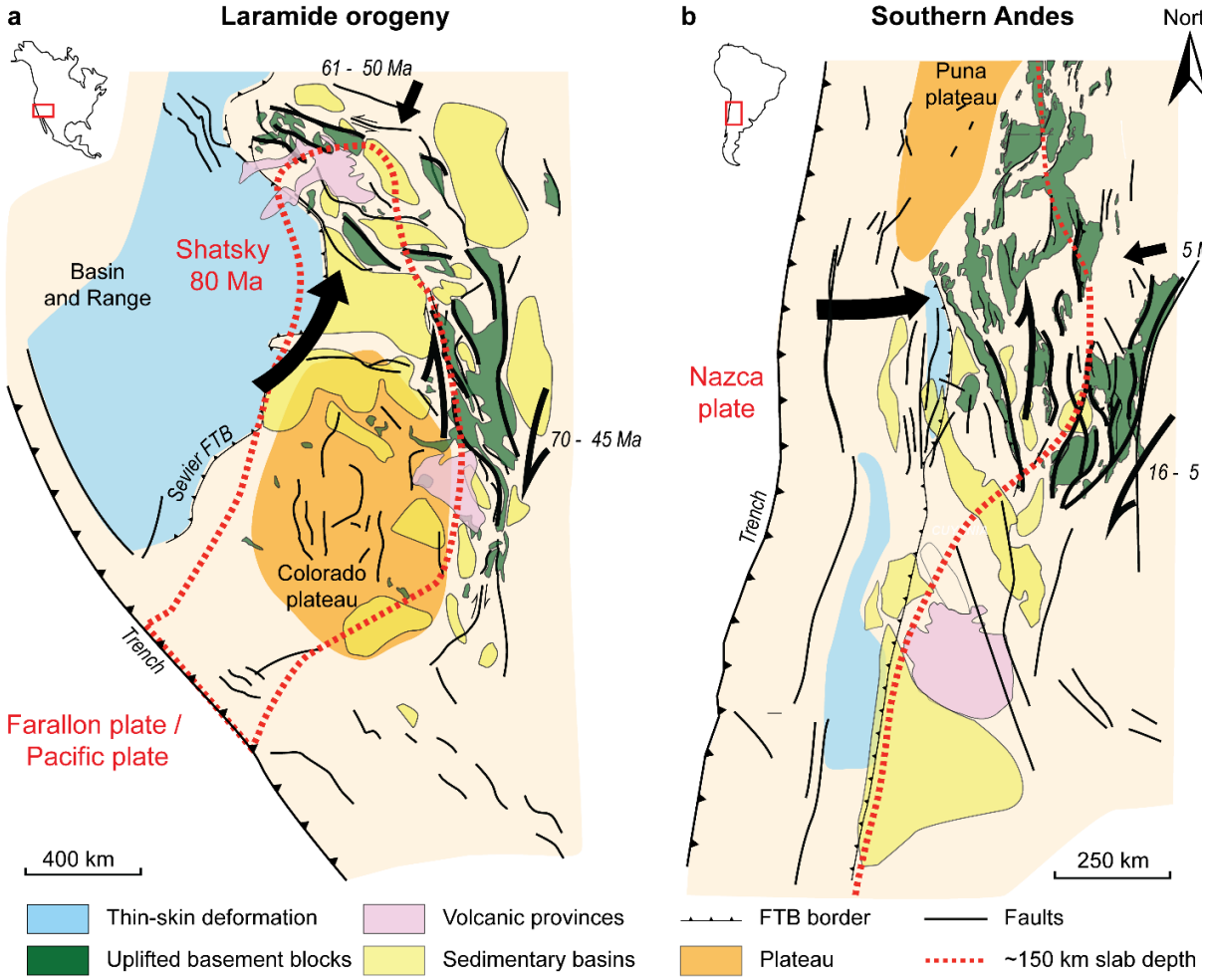

Figure 4.5 Comparison between the main structures of the Southern Andes and the Laramide orogeny (modified from Saleeby, 2003; Erslev & Koenig, 2009; Axen et al., 2018). Arrows indicate the direction of convergence between the Farallon plate and the North American plate at 80 Ma ago (Axen et al., 2018) and present-day velocity direction for the Southern Andes. Light brown indicates the continental domain.

Chapter 5 Discussion

In this discussion, I put into perspective the results described in the above chapters of this thesis in order to answer the main question driving this work: "What is the nature of the tectonic shortening in the Central Andes? ". This chapter is subdivided in three sections, each aiming at answering one of the three questions posed in the introduction, which all together comprise the main question listed above:

(I) What controls the variability of the shortening rate in Central Andes?

(II) What is the effect of inherited structures within the continent on strain localization?

(III) What is/was the role of the Pampean flat-slab on strain localization and in the formation of the Andes?

5.1 Buckling and steepening of the slab together with the weakening of the upper plate controls the variability of the shortening rate in Central Andes

The 2D geodynamic model presented in Chapter 2 showcase the mechanism responsible for the observed variability of the shortening rate in the central Andes (Oncken et al., 2006; 2012). The onset of the foreland underthrusting and thin-skinned deformation of the foreland is estimated at 10 Ma. Most of the shortening took place during 2 pulsatile phases in the last 15 Ma: the first one between 15 and 7 Ma and the second between 5 and 2 Ma.

The shortening rate of the overriding plate results from differences in velocity between the overriding plate velocity and the trench retreat (Faccena et al., 2007, Lallemand et al., 2008). Our hypothesis was that, although the overriding provides a driving force in trench retreat (Schepers et al., 2017), trench migration is also affected by the deep subduction dynamics, resulting in periods in of hindered trench retreat.

While most modelling studies focussed on either the dynamics of subduction (Schellart et al., 2017, Faccenna et al., 2017) or on the overriding plate strength and deformation (Sobolev et al., 2006, Gerbaut et al., 2009, Ibarra et al., 2019, Liu et al., 2021), few models have attempted to reconcile both aspects (Cerpa et al., 2014, Briaud et al., 2020, Boutoux et al., 2021). In this study, we have coupled subduction dynamics and overriding plate deformation by integrating the main constituents proposed in the literature that allow for the dynamic weakening of the overriding plate (e.g. eclogitization, fast weakening of foreland sediments) and for the stress transfer between the plates (e.g., free surface, realistic friction

at the subduction interface). Overall, I showed that subduction dynamics are strongly affected by the absolute trenchward motion of the overriding plate (V_{OP}) which forces the trench to retreat at different rate (V_T). From the relationship between Vop and Vt, we can distinguish 3 different regimes (regimes 1-3, Figure 2.8): (i) An **anchoring** regime, where V_{OP} is >> Vt and the overriding plate is significantly shortened (Figure 2.4j and SA.9): (ii) a **transient** regime of buckling and steepening in which the ratio between V_T and V_{OP} alternates between positive and negative values. During steepening, Vt<Vop, thus the overriding plates is subjected to shortening. Conversely, when Vt>Vop during slab shallowing, the overriding plate might be subjected to extension (Figure 2.4a and 2.9). (iii) A **piling** regime, where V_T is equivalent to V_{OP} and the overriding plate is in a neutral state (Figure 2.4i and SA.9).

The observed decrease in velocity of the South American plate from 3cm yr^{-1} to 1cm yr^{-1} in the last 40 Ma likely indicates an evolution from anchoring (40 Ma) to buckling and steepening (over the last 20 Ma) and may evolve to piling in the future. Converse to what is proposed by Faccenna et al (2017), slab anchoring alone overestimates the shortening rates over the last 15 Ma compared to the observations and does not reproduce the variability in shortening rate (Figure 2.4i,j and SA.9, Chapter 2, section 2.5.2.2). On the contrary, considering only slab folding and piling in the mantle transition zone results in an underestimation of the magnitude and variability of the shortening rate. Finally, the slab steepening that occurs in the transient regime during each buckling cycle is able to reproduce the pulses in the shortening rate over the last 15 Ma. In this regime, when the slab steepens, the trench is hindered and resists the forced trench retreat from the overriding plate, causing the increase of the shortening rate. This proposed new mechanism is consistent with multiple observations, including plate velocity from paleomagnetism, shortening rate and uplift timing (Quiero et al., 2022; Oncken et al., 2006-20012; Garzione et al., 2017). Furthermore, slab steepening phases in the model match the periodic increase in volcanic/ignimbritic activity (Trumbull et al., 2006). These periods of increase were initially interpreted as an increase in the heat flow at the base of the lithosphere as a result of the continental mantle delamination. I show that continental delamination is a consequence of slab steepening and the hindering of the trench. Moreover, slab steepening results in more vigorous flow in the mantle wedge which brings warm material to shallower depths. Finally, when the trench is hindered and the continental mantle is delaminated, underthrusting is facilitated.

The subduction zone in the central Andes is characterized by a high interplate friction coefficient, which prevents the plate to roll back because it is forced to drag with it the entire overriding plate. Therefore, the amount of trench retreat in the models of Chapter 2 is mostly controlled by the overriding plate velocity. However, most present day subduction zones are characterized by roll-back of the subducting plate and of the trench (Vt>>Vop: e.g. Thyrrenian, Egean). These subduction zones are often subjected to back-arc extension (Faccena et al., 2007, Lallemand et al., 2008). In this case, I conceptualize 3

additional scenarios: (regimes 4-6, Figure 5.1): (iv) a sinking regime, where the oceanic plate subducts directly into the lower mantle. In this regime the slab would be steeply dipping and the subduction velocity (Vsp) high, which could increase the flow in the mantle wedge and contribute to the erosion of the sublithospheric mantle by convective thinning, and mechanical and thermal weakening of the back-arc (Erdős et al., 2021). Once the overriding plate has weakened sufficiently, the oceanic plate roll-back would likely increases and drags the arc with it; (v) a regime of a buckling and penetrating slab, where the oceanic plate may stagnate temporarily at the transition between the upper and lower mantle before penetrating the latter, which may cause variations in the subduction angle of the plate in the mantle wedge. Therefore, as in the previous regime, the mantle flow in the wedge may becomes temporarily more active and weaken the back-arc, which could lead to multiple pulses of extension in the continental plate. (vi) A stagnating regime where the oceanic plate stagnates at the mantle transition zone and the oceanic plate is able to rollback steadily. The mantle flow in the wedge would become less vigorous than regimes (iv) and (v), which could lead to slower back-arc spreading. I conceptualize the different processes associated with two different subduction style (regime 2 and 6, Figure 6.1). Future modelling work is needed test these scenarios.

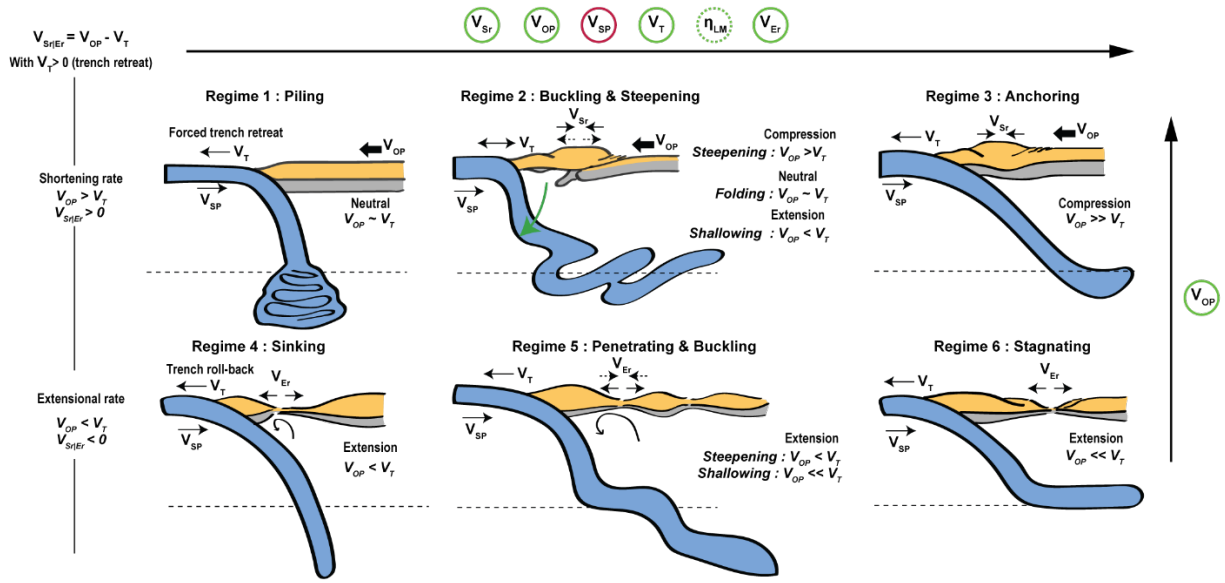

Figure 5.1 Regimes of subduction dynamics and associated overriding plate deformation regime. Regimes 1-3 results from the performed subduction model in Chapter 2 whereas regimes 4-6 are conceptualized for future modelling study. Green circle indicates increase and red indicate decrease.

5.2 Inherited structures facilities the localization of the deformation at different scales

One of the most hotly debated topics in geodynamics and tectonics is the degree to which continental inheritance controls the location and style of deformation. Reactivation of inherited structures in the

Sierras Pampeanas has been proposed in the southern central Andes to explain how compressional deformation took place away from the trench ~10 Ma before the arrival of the flat-slab (Ramos et al., 2009), as well as the reason for the transition between a thin and thick-skinned foreland deformation style. From a field perspective, inherited structures exist at all levels and are a complex issue. Geodynamic modelling allows us to upscale the problem to get a global view on inherited structures, as well as to quantify their relative contribution to the localization of deformation. I have developed 3D geodynamic data-driven models that includes the geometry of the subducted Nazca plate and the lithospheric structures of the South American plate (Rodriguez Piceda, 2020-2022) to investigate the relative effect of the flat-slab and of present-day continental inheritance on the localization of deformation. A similar approach was previously used to investigate the effect of lithospheric inheritance on the evolution of the Ethiopian rift system (Glerum et al., 2020) and on the Central Andes foreland style of deformation (Ibarra et al., 2019). I learned that the localization of deformation is largely controlled by the geometry of the oceanic plate. Where the slab is flat, the lithosphere is strengthened and the deformation on top is reduced. As expected, deformation occurs at the front of the slab like previously proposed by the bulldozed mantle-keel model (Gutscher et al., 2000). Inherited crustal structures contribute to the localization of the deformation, in particular sedimentary depocenters correlate with inherited faults that tend to be reactivated (Bense et al., 2013; Ortiz et al., 2021). More surprisingly, I discovered that a large transpressive shear zone of ~400x400 km, resulting from crustal contraction, may develop on the southern edge of the flat segment. Depending on the strength of the inherited faults and foreland sediments, the contraction can yield to a diffuse shear zone or to the localization of the deformation over strike slip faults boarding the Sierras Pampeanas blocks, if they are strong or weak, respectively. In the latter case, we observe a switch from simple shear shortening in a steep domain to pure shear shortening and the development of an “en-echelon” crustal shear zone bordering the uplifted basement blocks of the Sierras Pampeanas. This shear zone is analogous to the transition between a thin-skinned and thick-skinned foreland deformation style. Classically, only the flat-slab is considered to explain this transition. From our model, I propose that the transition occurs prior the arrival of the flat-slab, which is also supported by geological evidence (Ramos et al., 2002-2009; Chapter 4, section 4.5.1).

5.3 The role of the Pampean on the continental strain localization and in the formation of the Central Andes

By using the previous 3D geodynamic data-driven model of the Southern Central Andes (i.e. Chapter 3), we have learned that the contraction of the crust yields to a large transpressive zone of ~400 km length and width that forms at the southern edge of the flat-slab. Since we know the average absolute velocity of the oceanic plate parallel to the trench between 22 and 12 Ma (~4 cm/yr, Sdrolias et al., 2006),

which is assumed to be equivalent to the average velocity of the southward migration of the flat-slab between the time of the onset of the compressional deformation (~22 Ma at 30°S) and the time of the arrival of the flat-slab in Sierras Pampeanas (~12 Ma at 30°S), we can calculate that the onset of the transpressive zone should happens ~10 Ma before the arrival of the flat-slab (400km or 4 cm/yr) at ~12 Ma. Thus, matching the timing of the onset of compressional deformation. I conclude that the shallowing of the slab is a sufficient mechanism to explain the initiation of the compressional deformation 10 Ma prior to the arrival of the flat-slab at 30 °S. From my model, we can predict that the crustal contraction of Sierras Pampeanas could result in a large dextral rotational field >10 ° in some places during these 10 Ma and potentially higher at the border of the uplifted blocks. Data from the Precordillera show an increase of the vertical axis of rotation and an increasing number of strike-slip faults between ~21 and 12 Ma (Japas et al., 2012), but we lack data in the Central and eastern Sierras Pampeanas to properly investigate the cause. This model could be tested by the acquisition of new paleomagnetic data and an estimation of the vertical axis of rotation. In brief, we called this new mechanism"flat-slab conveyor", and consider the crustal contraction from 22 to 12 Ma being caused by the flat-slab shallowing. . The Sierras Pampeanas is a present-day analog of the Rocky Mountains formed during the Laramide orogeny. We propose that they could have been in a similar situation ~80 to 70 Ma ago, and be the result of a change of deformation style between thin and thick-skinned before and during transpression respectively, caused by crustal contraction during the shallowing of the oceanic plate.

5.4 A summary of the Pampean flat-slab and its interaction with the South American plate

Overall, we can combine what we learned from the 2D model of the Central Andes and 3D model of the Southern Central Andes to draw a conceptual picture of the role of the Pampean flat-slab and its interaction with the South American continental plate. The effect of the passage of the flat-slab in the Central Andes can be characterized by 3 stages: (i) slab shallowing (Figure 5.2a), (ii) slab flattening (Figure 5.2b) and (iii) slab steepening (Figure 5.2c). During the shallowing of the slab, the the oceanic plate geometry becomes curved (e.g. in SCA at ~100km depth), therefore the shallowing is more advanced in the North than in the South. Consequently, the horizontal stress is transmitted closer to the trench in the North than in the South. This difference leads to the formation of a transpressive field and the contraction of the crust, which is expressed ~10 My prior to the flattening of the slab in the Sierras Pampeanas at 30 °S, we call this mechanism "flat-slab conveyor". At this stage, the shortening rate increases, deformation migrates eastward, and strike-slip faults may develop locally. The volcanic activity is still active, and regional scale dextral rotation is predicted from the model. When the slab is flat, the volcanic activity shuts off and the shear stress is now transmitted through the subduction interface to the hinge of the eastern hinge of the flat segment. Additionally, the slab scrapes and bulldozes the continental mantle

keel. At the surface, the deformation is now localized at the eastern edge of the flat-slab segment, while it decreases on top of the flat segment because of the strengthening of the overriding plate. At this time deformation is dominated by thrust faults. After the passage of the flat-slab, the slab steepens. The continental mantle is partially removed and dragged down by the sinking plate. The continental lithosphere thermally weakens due to the increase in the thermal flux at its base (Isacks, 1988; Silva & Kay, 2018), which is expressed at the surface by the increasing volcanic and ignimbritic activity (Trumbull et al., 2006). The deformation migrates back towards the trench as the hinge of the flat segment rolls back. Potentially, the mantle wedge gets blocked by the delaminated continental lithospheric mantle, which could temporarily increase the plate coupling (Sobolev et al., 2005) and block the trench as the slab steepens. Finally, the additional length of the slab in the upper mantle following the passage of the flat-slab could contribute to initiating a buckling instability due to the critical length of the slab in the upper mantle (Ribe et al., 2007), thus triggering the collapse of the slab on itself.

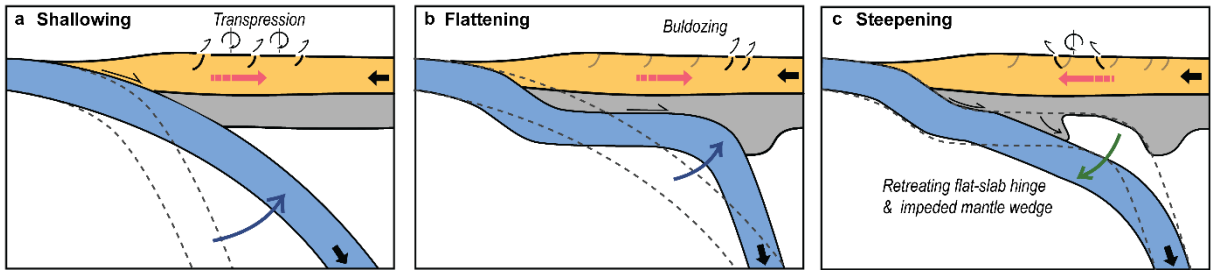

Figure 5.2 Slab stages and associated upper-plate deformation mechanisms. **a**. Slab shallowing and transpression caused by "flat-slab conveyor". **b**. Slab flattening and bulldozing. **c** Slab steepening, mantle wedge corner blocked. Blue, orange and grey indicate the oceanic plate, crust and continental mantle lithosphere, respectively. The black filled arrows indicate the direction of plate motion. Red arrows indicate the direction of deformation migration. The blue and green arrows indicate the shallowing and steepening of the slab dip.

5.5 Additional & future work

In this section, I discuss three possible perspectives for future work in modelling the interaction between the subduction of the Nazca oceanic plate and the South American continental plate. First, the 2D geodynamic model could be used to run alternative models at Puna latitudes for which the geometry of the upper plate and the timing of the passage of the flat-slab segment vary, thus affecting the strength of the lithosphere differently than at Alitplano latitudes. The delamination of the lithosphere under the Puna plateau at present-day (Figure 5.3a; Sobolev et al., 2006; Heit et al., 2008) is similar to the delamination seen in our reference model at 12.7 Ma (Figure 5.3b; chapter 2, section 2.5.1.1) and coincides with the timing when the flat-slab leaves the Puna at ~12 Ma (Ramos et al., 2009). Nevertheless,

the thick-skinned deformation of the Puna foreland likely indicates lower shortening magnitude than at the Altiplano foreland (Oncken et al., 2006-2016, Sobolev et al., 2006; Liu et al., 2021). This difference in shortening could be accommodated by the formation of diffuse or localized strike-slip deformation between Altiplano and Puna lattitudes which could be resolved by extending our long-term geodynamic model to 3D.

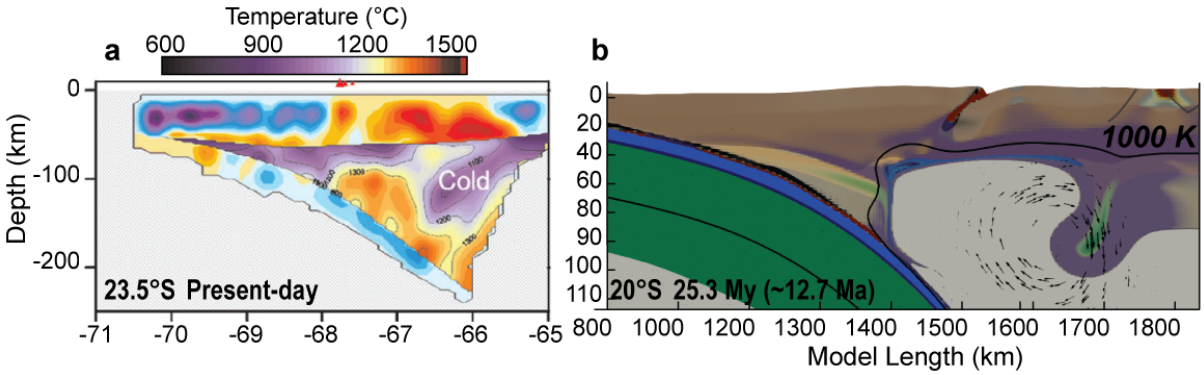

Figure 5.3 Lithosphere delamination comparison at Puna latitude between tomographic image (modified from Sobolev et al., 2006; Heit et al., 2008) at present-day and our reference model (chapter 2) at 12.7Ma.

Second, future studies should examine the effect of surface process in subduction modelling, specifically applied to the Andes from two different perspectives using the ASPECT - FastScape coupling (Neuharth et al., 2021): (i) The effects of erosion and sediment transport to the trench to investigate the role of trench-filled sediments on the coupling at the subduction interface, similar the mechanism suggested by Lamb & Davis, (2003). (ii) Foreland erosion as the effect of the orographic barrier (Strecker et al., 2007). In an earlier model, Babeyko et al. (2006) showed with a 2D model that strong erosion weakens the foreland and promotes simple shear shortening. Figure 5.4 provides an example of how climatic process can affect the deformation style of the foreland in our subduction model. In this example, I have applied a bedrock river incision rate (K_f value in the Stream Power Law; e.g. Kooi and Beaumont, 1994) of 1e-6m²/yr to our reference model (M1, Chapter 2), which results in a faster transition from pure to simple shear. In addition, the westward velocity of the overriding plate is accommodated by the deformation, therefore the trench retreat decreases (Figure 5.4). Further work is needed to investigate the effect of surface processes.

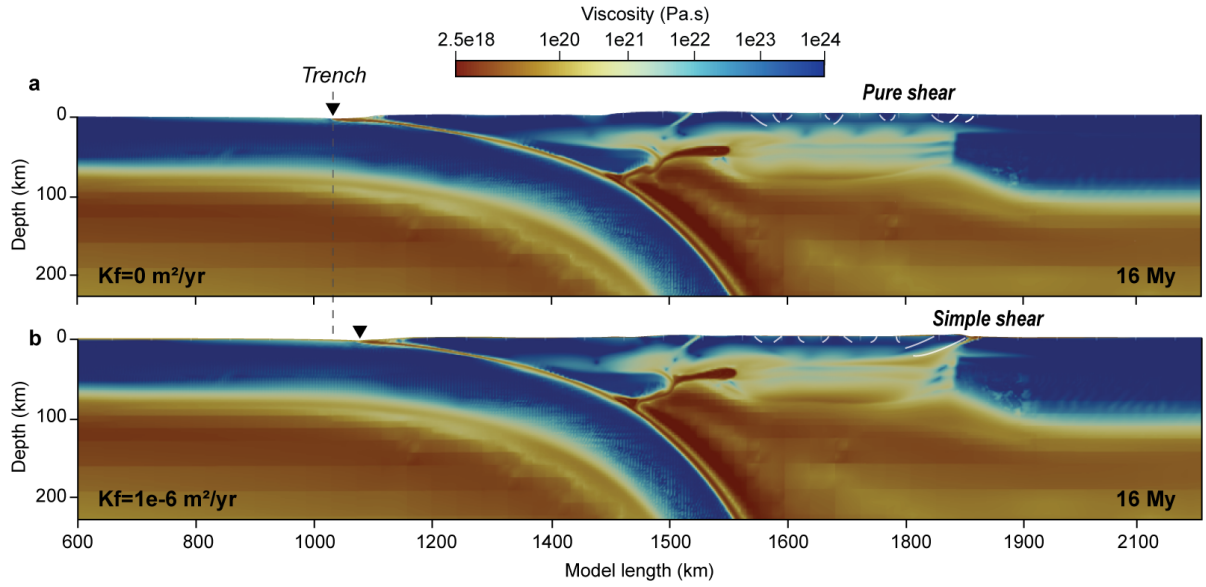

Figure 5.4 Effect of foreland erosion.**a** Reference model (M1, Chapter 2) with no erosion.**b** a model variant with a bedrock river incision rate of 1e-6 m²/yr. Dark triangles indicate the position of the trench.

Third, the recently published tomographic model of Portner et al., (2020) proposes that in the Central Andes the slab is stagnating near the transition to the lower mantle and then is penetrating it. The 2D generic model (chapter 2) suggests that the slab could fold while stagnating at the transition to the lower mantle. Nevertheless, I also discuss (chapter 2, section 2.5.3.2) the possibility of a slab avalanche to occur, which could likely lead to ~30 Ma cycles of plate convergence (Martinod et al., 2010; Lee & King, 2011). We propose a different interpretation of the tomography image of Portner et al (2020; Figure 5.5 & Figure 6.1) that shows slab avalanche induced break-off and folding at the mantle transition zone. In our modelling approach we have considered a standard viscosity profile for the mantle transition zone and lower mantle based on Steinberger & Calderwood, (2006). Čížková & Bina (2013) showed that slab buckling and stagnation at the mantle transition zone is sensitive to many parameters such as the friction at the slab interface, slab strength, viscosity of the surrounding mantle, and the Clapeyron slopes of the major olivine phase transitions. They demonstrate that all these parameters can affect the magnitude of trench retreat. Therefore, the study of slab avalanche in the context of the Chilean Nazca plate will require a comprehensive sensitivity analysis of these parameters. I suggest that future models should study the role of a slab avalanche on plate interactions. Finally, one could build a 3D generic numerical model of the southward migration of the flat-slab from the Altiplano to the Sierras Pampeanas to investigate the effect of “flat-slab conveyor” using different rheological parameters for the continental lithosphere.

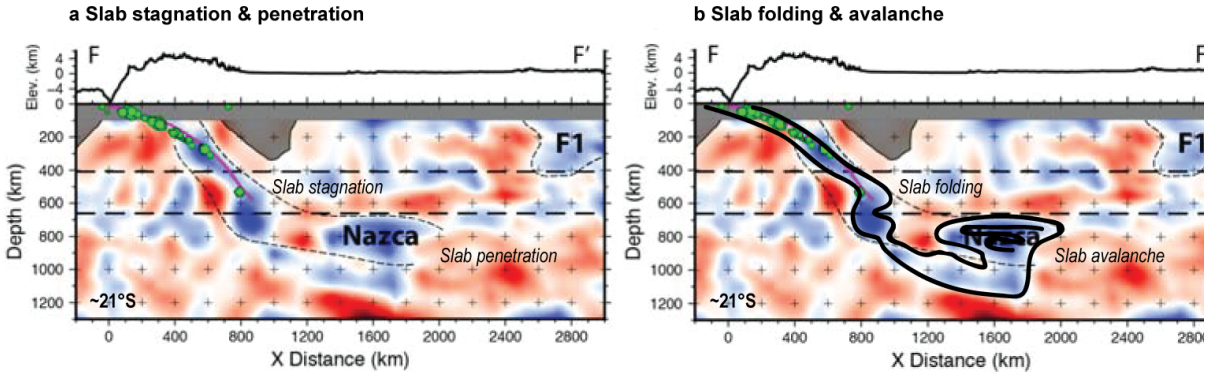

Figure 5.5 Interpretation of a tomographic image at 21°S modified from Portner et al., (2020). **a** Tomographic interpretation from Portner et al., (2020), the slab is stagnating and penetrating the lower mantle. **b** My tomographic interpretation, the slab is folding and avalanching.

Chapter 6 Conclusions

Using both generic (Chapter 2) and data-driven (Chapter 3-4) geodynamic modelling approaches, I aimed at bridging the gap between numerical models and geological and geophysical data. In this thesis I characterize “what is the nature of the tectonic shortening in the Central Andes over time and space?” The answer to this question resides in the complex interactions between the dynamics of the Nazca plate and the overriding plate. The main results of this work are summarized below and follow the chapter order:

1. In the Central Andes, because of the high coupling between the Nazca and South American plates, trench retreat is mostly forced by the westward motion of the overriding plate. The velocity of the overriding plate and, therefore, of the trench retreat controls the subduction dynamics regime. I propose 3 different regimes as a function of the decreasing velocity of the overriding plate: anchoring, buckling and steepening, and piling.
2. The pulsatile shortening rate of the Central Andes in the last 15 Ma can be explained by the buckling and the steepening of the Nazca oceanic plate at the mantle transition zone. When the slab steepens, the trench retreat caused by the overriding South American plate moving westwards is hindered, causing the continental plate to “collide” against the trench and to induce shortening within the overriding plate. The shortening rate is equal to the difference between the velocity of the overriding plate and the velocity of the trench retreat. The steepening mechanism of the slab during each buckling cycle explains many geological observations, including the temporal variability and magnitude of shortening in the Central Andes, the pulsatile increase of volcanic activity and of plate convergence rate, the timing of topographic growth and the timing of the onset of foreland underthrusting.
3. The passage of the flat-slab in the Central Andes is a key process that likely scraped part of the sublithospheric continental mantle, triggering a chain of events. These include: (i) the delamination of the continent during shortening, which further weakened the continental plate, (ii) An eastward migration of deformation, and (iii) the underthusting of the Brazilian cratonic shield.
4. My high resolution models confirm that a number of previously proposed factors in the literature are important in enhancing interplate coupling and the dynamic weakening of the upper plate, and as such contribute to successfully modelling the observed tectonic shortening in the Central Andes. These factors include a high interplate friction coefficient (f=0.035 to 0.07), eclogitization

of the lower crust to trigger delamination processes and a rapid weakening of foreland sediments to allow for foreland underthrusting.

5. The Pampean flat subduction contributes (by underplating and cooling) to a mechanical and thermal strengthening of the lithosphere above the flat-slab segment. This strengthening explains the lack of deformation observed in the area. Along the flat-slab, shear stress transmits deformation to the east. The deformation is then accommodated in the broken foreland at the eastern front of the flat-slab segment through bulldozing of the lithosphere mantle keel. As the slab segment becomes steeper to the south, plate strengthening becomes less important and deformation occurs closer to the orogenic front.
6. Over the flat-slab segment the horizontal stress from the slab is transmitted a larger distance over the overriding plate than above the steeper slab segment. This offset causes the formation of a large diffuse shear zone at the surface above the steeper segment due.
7. At the surface, deformation in the diffuse shear zone locally intensifies on pre-existing terrane boundaries and Mesozoic inverted faults. In this area, the degree of strain localization is controlled by the sediment strength. When the strength is low, strain localizes more efficiently near the Paleozoic basement blocks of the Sierras Pampeanas. This pattern of strain localization is similar to the transition from thin-skinned to thick-skinned deformation between the southern Sierras Pampeanas and the deformed foreland fold and thrust belt to the south.
8. In 3D, strain localization forms en-echelon strike-slip shear zones. This transpressive deformation is accommodated by differential dextral rotation of the basement blocks. The magnitude of the rotations is consistent with current paleomagnetic estimations, but further data, particularly in the central and eastern Sierras Pampeanas, is needed to fully evaluate the applicability on a larger scale. Nevertheless the rotational magnitude observed within the models is consistent with current paleomagnetic estimations in Precordillera.
9. This work provides a global picture of the interaction between the Pampean flat-slab subduction and the deformation of the South American continental margin by proposing a new mechanism called “flat-slab conveyor” that contributed to the formation of the Sierras Pampeanas. This mechanism additionally reconciles the timing of many geological events. From a dynamic point of view, the flat-slab segment acts as an indenter that is migrating southward. As a result, the deformation propagates not only to the eastern front, but also to the southern forefront of the flat-slab. In this case, when the slab is shallowing, it produces a transpressive field and a large crustal contraction. This field and contraction result in atransition from thin to thick skinned deformation. This new proposed mechanism, that I call “flat-slab conveyor,” explains the timing of the onset of compressive deformation and of the change in foreland deformation style 10 and 6 Ma before the arrival of the flat-slab, respectively.

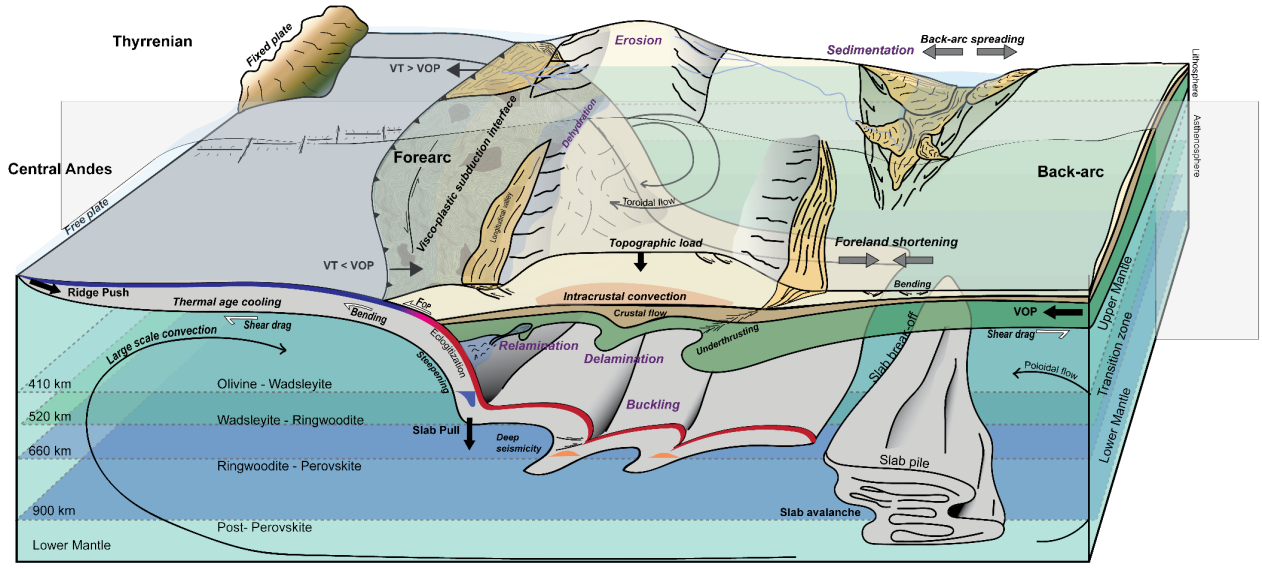

Figure 6.1 Summary of the processes and forces involved in 2 opposite styles of subduction, regime 2 (e.g Andean subdution style, in front) and regime 6 (e.g Thyrrenian subduction style, behind). Dark filled arrows are indicating the driving forces, White filled arrows and dark filled arrows indicate the resistive and driving forces. Grey filled arrows indicate foreland deformation and other arrows indicate motion of the mantle and trench.

Appendix A Central Andes

A.1 Description of the movies

In all movies, Black arrows are velocity vectors indicating the flowing direction. Coloured layers indicate the compositional fields to which are superposed different fields. Green field indicates active eclogite transformation, back field indicates the plastic strain accumulation, Red field indicates the strain rate and purple field indicates the viscous strain rate. White line isotherms are for 400°C, 800°C, 1300°C, and 1500°C.

Movies are temporarily available at this link: https://nextcloud.gfz-potsdam.de/s/yad5b3oKFRNKbQn

Movie S1, model 1 (Reference model). Animation showing the evolution of the horizontal stress for the model of reference.

Movie S2, model 1b (Reference model). Animation of the evolution of the model of reference.

Movie S3, model 2a. Animation of the evolution of the model variant with a friction at the interface of 0.015.

Movie S4, model 2b. Animation of the evolution of the model variant with a friction at the interface of 0.035.

Movie S5, model 2c. Animation of the evolution of the model variant with a friction at the interface of 0.06.

Movie S6, model 3. Animation of the evolution of the model without eclogitization of the lower crust.

Movie S7, model 4. Animation of the evolution of the model with an increase of thermal conductivity for the crust when T>1000K.

Movie S8, model 5a. Animation of the evolution of the model variant with a foreland sediments internal friction angle of 10° and Cohesion 20 MPa.

Movie S9, model 5b. Animation of the evolution of the model variant with a foreland sediments internal friction angle of 30° and Cohesion 20 MPa.

Movie S10, model 6a. Animation of the evolution of the model variant with an overriding plate velocity of ~1cm/yr.

Movie S11, model 6b. Animation of the evolution of the model variant with an overriding plate velocity of ~4cm/yr.

Movie S12, model 7. Animation of the evolution of the model without flat-slab.

A.2 Model set-up of the flat-slab (M1-6)

Subduction interface. Our models use a visco-plastic subduction interface based on the weakest quartzite rheological flow law from Ranalli (1997). This rheology was shown to be efficient in modelling a quartz-dominated "melange" at the interface (Sobolev et al., 2006; Muldashev & Sobolev, 2020).

Rheology. (Table A.S1) The oceanic plate is composed of an 8 km oceanic crust (3000 kg/m³) divided into 5 km of weak wet quartzite (Ranalli, 1997) and 3 km of mafic diabase (Mackwell et al., 1998). The oceanic mantle consists of 73 km of dry olivine (Hirth & Kohlstedt, 2004), and is compositionally lighter than the asthenosphere (ρAsthenosphere - 20 kg/m³). The lithosphere is given an initial dip of ~15° to facilitate the initial flat-slab stage (Van Hunen et al., 2004; Huangfu et al., 2016; Liu & Currie, 2016; Dai et al., 2020). A 12 km thick "ridge" (2800 kg/m³) of weak quartz (Ranalli, 1997) is placed along the dipping subduction interface to aid in subduction initialization.

The geometry and length of the continent are based on a structural reconstruction and a volume conservation at 30 Ma (Armijo et al., 2015; Sobolev et al., 2006) that have been calibrated to have an ~850 km long continent when the model is restarted after the initialization phase. In the orogenic domain, the upper crust (2800 kg/m³) is a 33 km thick layer of wet quartzite (Gleason & Tullis, 1995) and the lower crust (3000 kg/m³) is a 12 km thick layer of diabase (Mackwell et al., 1998). The continental mantle (3280 kg/m³) is wet olivine (Hirth & Kohlstedt, 2004) and 45 km thick. In the cold forearc the continental mantle thickens to 65 km. In the foreland, sediments (2670 kg/m³) are 5 km thick (Gleason & Tullis, 1995). The upper crust and the lower crust are 12 and 10 km thick, respectively. The depleted Brazilian cratonic shield (3240 kg/m³) is considered dry olivine (Hirth & Kohlstedt, 2004) and extends to a depth of 130 km. The foreland is thicker than the orogenic domain and therefore colder (Sobolev et al., 2006; Ibarra & Prezzi, 2019; Ibarra et al., 2019).

To simulate the rheology of the hydrated mantle wedge in the upper mantle, we use wet olivine laws for dislocation and diffusion (Hirth & Kohlstedt, 2004) (3300 kg/m³). Asthenospheric densities for the transition zone and the lower mantle are recalculated so that the final density after considering the pressure and temperature matches the PREM model (Figure S5d, Dziewonski & Anderson, 1981). We assigned constant viscosity for the transition zone (410-520 km ~6.75e20 Pa.s and 520-660 km ~1.05e21 Pa.s, Figure SA.5b) and the lower mantle (~7.5e21 Pa.s) based on the Steinberger & Calderwood (2006) viscosity profile.

The model utilizes an analytical phase function to simulate smooth phase transitions.

$$Phase\ fraction\ = \frac{1}{2}\left(1 + tanh\left(\frac{\Delta P}{\Delta Po}\right)\right), \quad (A.1)$$

with $\Delta P = \mathrm{P} - \mathrm{Ptransition} - \lambda(\mathrm{T} - \mathrm{Ttransition})$. ΔPo is the pressure difference over the width of the phase transition. Ptransition and Ttransition are the pressure and temperature of transition (Table A.S1).

λ is the Clapeyron slope. Tanh is the hyperbolic tangent. The phase function changes from 0 to 1 when the phase transition is fully completed. The main phase transitions were consider for the mantle are the Olivine-Wadsleyite at 410 km depth (Clapeyron slope, λ, of 2 MPa/K), Wadsleyite-Ringwoodite at 520 km (λ =3.5 MPa/K) and Post-spinel at 660 km (λ = -0.5 MPa/K; Quinteros & Sobolev, 2013). Gabbro-eclogite transition (+450 kg/m³) is completed at pressures of ~1.9 GPa (~60 km depth) and 800°C for the oceanic crust and ~1.2 GPa (~40 km depth) and 700°C for the lower crust (e.g. Green colour gradient in figures 2.4 and 2.6, Babeyko et al., 2006; Sobolev & Babeyko, 1994; Sobolev et al., 2006). Coesite-Stishovite phase transition also takes place at a pressure of ~9 GPa (~270 km depth) (Faccenda & Dal Zilio, 2017).

Initialization. Our goal is to investigate the temporal variation of the overriding plate shortening starting from flat subduction. For that reason, we do not allow plastic strain to accumulate during initialization. To initiate the flat-slab, we prescribed a ~400 km long plateau domain that corresponds to the dipping part of the slab, in which we split the 73 km oceanic lithosphere into 43.8 km of depleted "Harzburgite" (3233 kg/m³) and 29.2 km of "Lherzolite" (3300 kg/m³; Arredondo & Billen, 2017). This gives an average density of ~3260 kg/m³. Additionally, during initialization there is no eclogitization in the "ridge".

We pushed the oceanic plate at 7 cm/yr, similar to the absolute orthogonal velocity of the Nazca plate at ~35 Ma, and we pushed the overriding plate at 2 cm/yr (Sdrolias & Müller, 2006). The left asthenosphere boundary is open whereas the right and the bottom are set to free slip to avoid any "artificial mantle wind" that could arise from pressure perturbations. During initialization, we use a fully viscous interface to achieve flat subduction without any significant deformation inthe overriding plate. We set the minimum viscosity to 1e20 Pa.s for the first 1 My in order to dampen the high velocities that could arise from isostatic rebound. After 1 My the minimum viscosity is switched to 1e19 Pa.s. The interface viscosity is set to 5e19 Pa.s as this gives the minimum coupling strength required for flat subduction. As the slab warms, the oceanic crust eclogitized and its tip steepens, the initialization stops when the slab tip reaches 300 km depth. This depth is necessary for the Eclogite-Stishovite phase transition to be complete, which increases the slab pull during the free subduction and allows to generate subducting velocity similar in amplitude to the data after initialization (Figure SA.2, Quinteros & Sobolev, 2013). Furthermore, this depth is also consistent with the depth at which slab break-off and tearing can occur in a weak slab (Billen & Hirth 2007) and in a flat subduction due to the buoyancy contrast between the flat and steep segments (Schellart et al., 2021). For instance, such tears and break-off may have affected the Pampean flat-slab at ~10 Ma (Gao et al., 2021).

When the model is restarted after the flat subduction phase, the interface is set to include visco-plastic deformation. The "ridge" density is set to 3000kg/m³ to prevent relamination of the continent. Eclogitization of the "ridge" through the phase function only operates when the temperatures exceed a blocking temperature of 700°C (Sobolev & Babeyko, 1994; Babeyko et al., 2006) . The minimum viscosity is set to 2.5e18 Pa.s. The "Harzburgite" and "Lherzolite" density are changed to represent normal oceanic mantle (ρAsthenosphere - 20 kg/m³), and the left boundary is fully open.

Data acquisition and processing. Shortening for the main orogenic domain is aquired by tracking the extremities of the upper crust at the surface, from the trench to the sediments in the foreland. Underthrusting is obtained by tracking the difference between the eastern extremity of the orogenic domain and the western extremity of the craton. Next, to find the shortening rate we divided the total shortening by the timestep. To be comparable to the geological shortening rate that has a temporal resolution between 1 to 5 My (Oncken et al., 2006-2012) we smoothed the solution using a 5 My moving average filter. The position of the trench corresponds to the lowest point of the topography. We determine the position of the trench using the minimum topography in the model, and then determine the velocity by dividing the change of position by the time step. The noise observed in the solution (e.g Figure 2.9) is caused by the difference of resolution at the trench; we applied a moving average filter of 200 ka to reduce it without losing the main signal. Note that we refer to the plastic strain rate and the viscous strain rate whereas they are the second invariant of the square root of the deviatoric strain rate in the plastic and viscous domain, respectively. The plastic strain refers to the integrated plastic strain rate over time and allows us to identify places that were already deformed and weakened.

A.3 Model set-up of the normal subduction (M7)

We run a simplified model of temperature-driven normal subduction (density of oceanic mantle and crust = density of asthenosphere). As with the reference model, we first initialize the subduction by pushing it to a depth of 300 km and then let it evolve. The minimum viscosity (4e19 Pa.s) is changed to a more realistic minimum viscosity (~2.5e18 Pa.s) after the restart. In addition, we used a constant viscosity at the interface of 3e19 Pa.s that produces a similar magnitude of subduction velocity with the velocity obtained from paleomagnetic reconstruction (Figure SA.10, Sdrolias & Müller, 2006; Quiero et al., 2022). The model is run for 30 Ma because we do not include the flat-slab and its steepening. The model predicts velocity pulses that decay in a manner similar to the velocity data (Figure SA.10d). Unlike the flat-slab models, there is no initial delamination or weakening of the overriding plate, highlighting the role of flat subduction (Figure SA.10b-c).

A.4 Supplementary figures

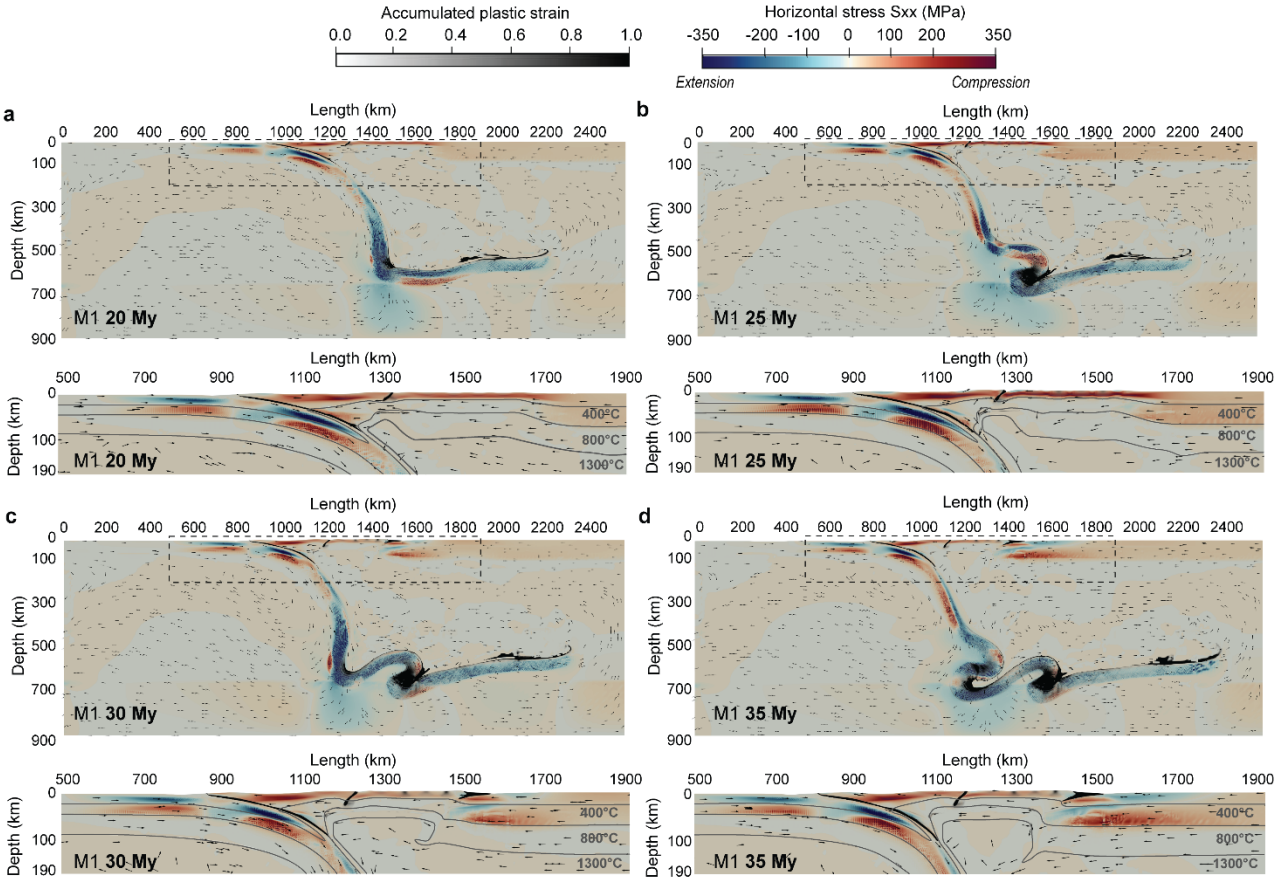

Figure SA.1 Horizontal stress evolution the model of reference M1. **a** 20 My. **b** 25 My. **c** 30 My. **d** 35 My. Grey line isotherms are for 400°C, 800°C, 1300°C.

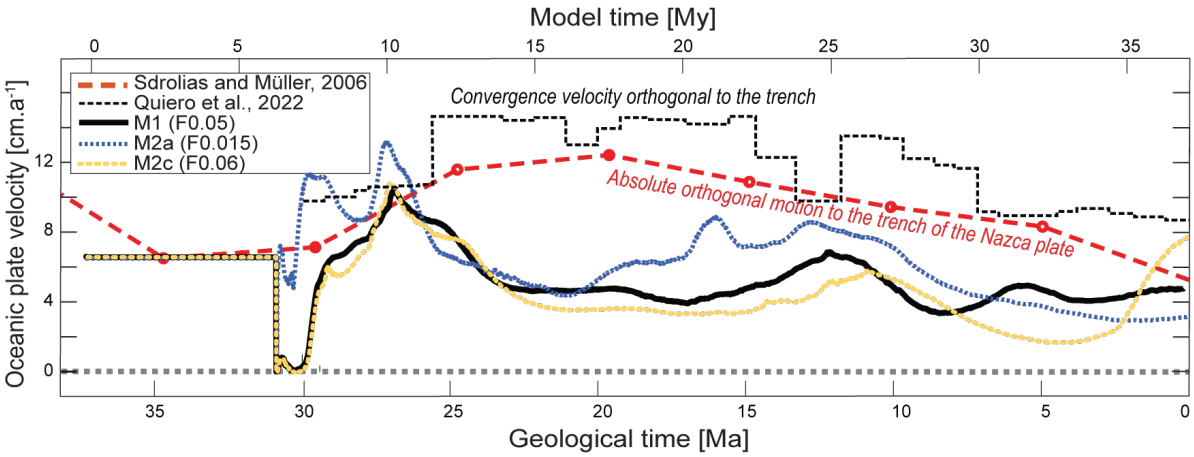

Figure SA.2 Effect of friction on the absolute velocity of the oceanic plate. Absolute velocity of the oceanic plate for **a** M1 Reference model. **b** M2a, which is the model with the lowest friction at the subduction interface. **c** M2c, which is the model with the highest friction at the subduction interface.

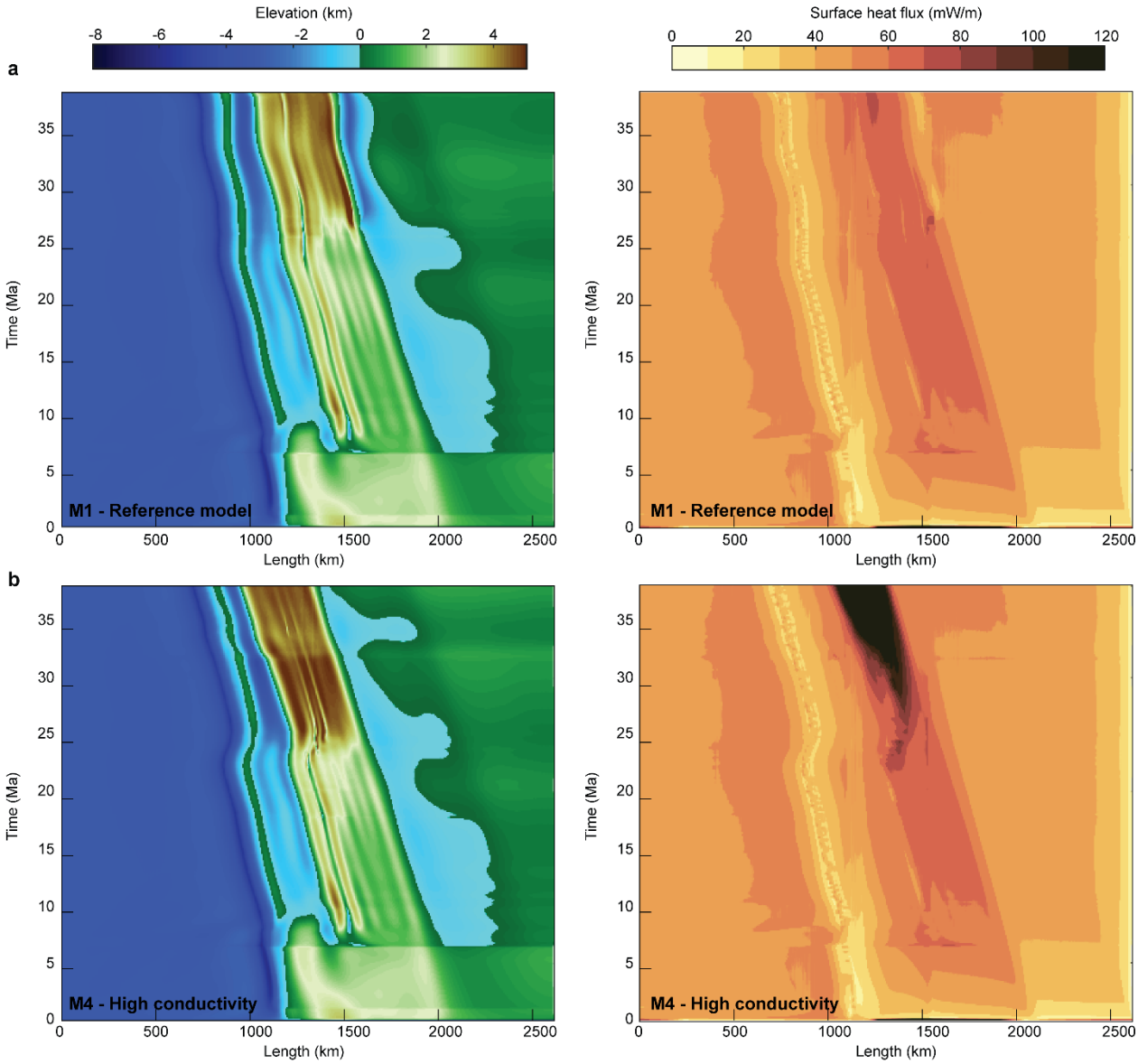

Figure SA.3 Topography and surface heat flux evolution comparison on the model variant 4. **a** Reference model. **b** model M4.

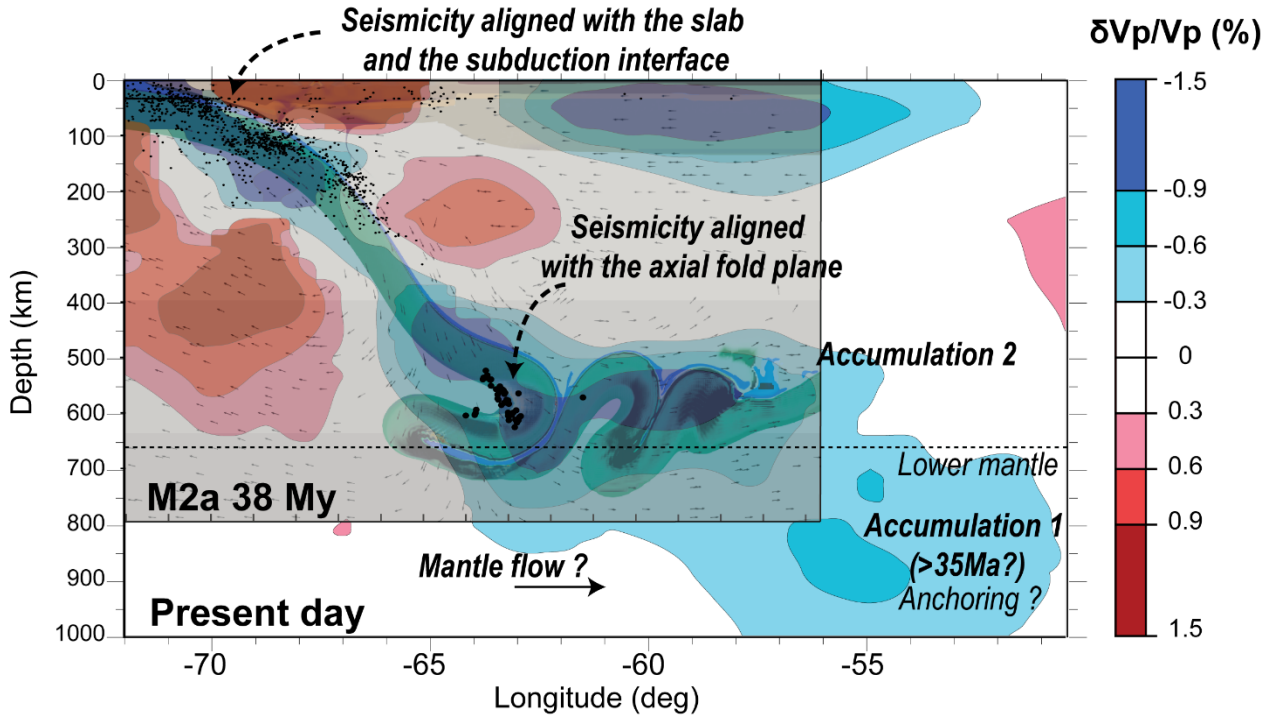

Figure SA.4 Comparison between model and tomographic image. Superposition of the best-fit model (M2a) with the tomographic image (Widiyantoro, 1997 and modified from Liu et al., (2003) at 21°S. Seismicity in the black dots aligns with the last folding event. The M3 model predicts a slab dip that fits the seismic tomography. The model is aligned with the current trench and rescaled to the size of the tomographic image. Two slab piles are identified, the first accumulation could be related to subduction > 35 Ma. In addition, eastward mantle flow could transport the pile eastward.

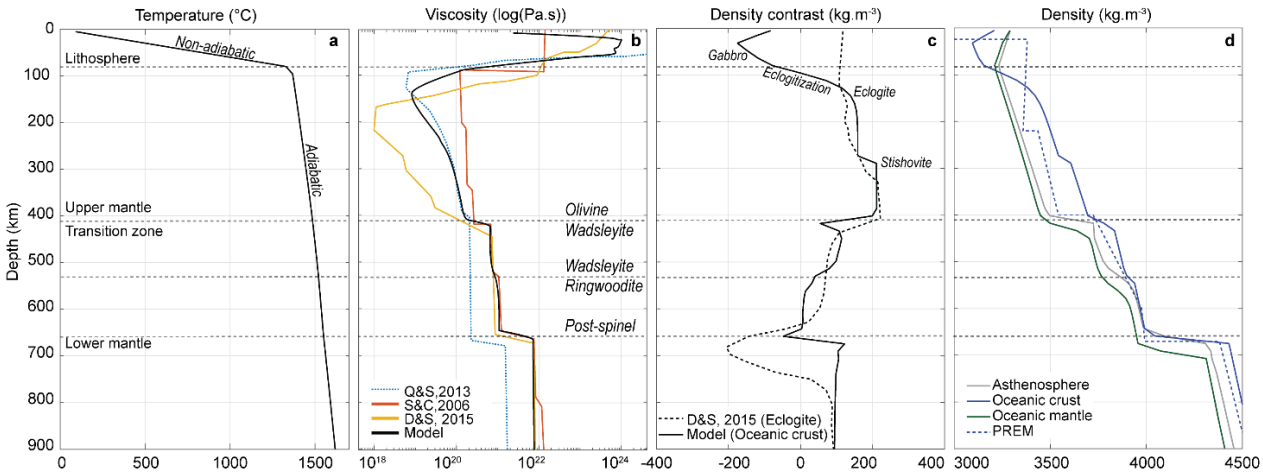

Figure SA.5 Indicative model profiles. **A** Initial temperature profile at 700 km model length. **B** Viscosity profile and comparison with the models of Quinteros & Sobolev (2013; Q&S,2013) and Dannberg & Sobolev

(2015; D&S,2015) as well as the reference viscosity profile of Steinberger & Calderwood (2006; S&C,2006). **C** Initial density contrast of the oceanic crust calculated by subtracting the asthenosphere density profile from that of the oceanic crust in d and comparison with D&S,2015. **D** Initial density profiles of the asthenosphere, oceanic crust and oceanic mantle lithosphere.

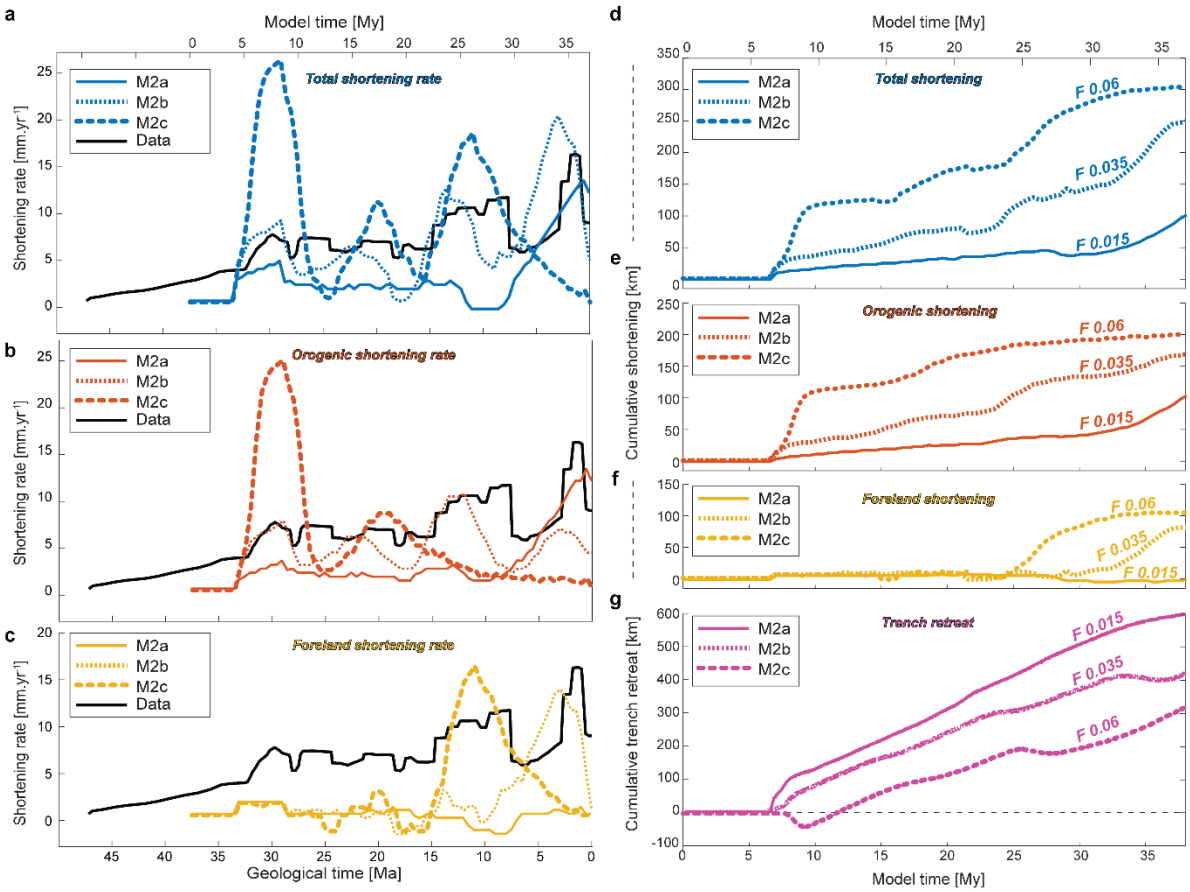

Figure SA.6 Shortening data for model variants M2a-c. **a, b, c** Total, orogenic and foreland shortening rate, respectively. **d, b, e** Total, orogenic and foreland cumulative shortening, respectively. **g** Cumulative trench retreat.

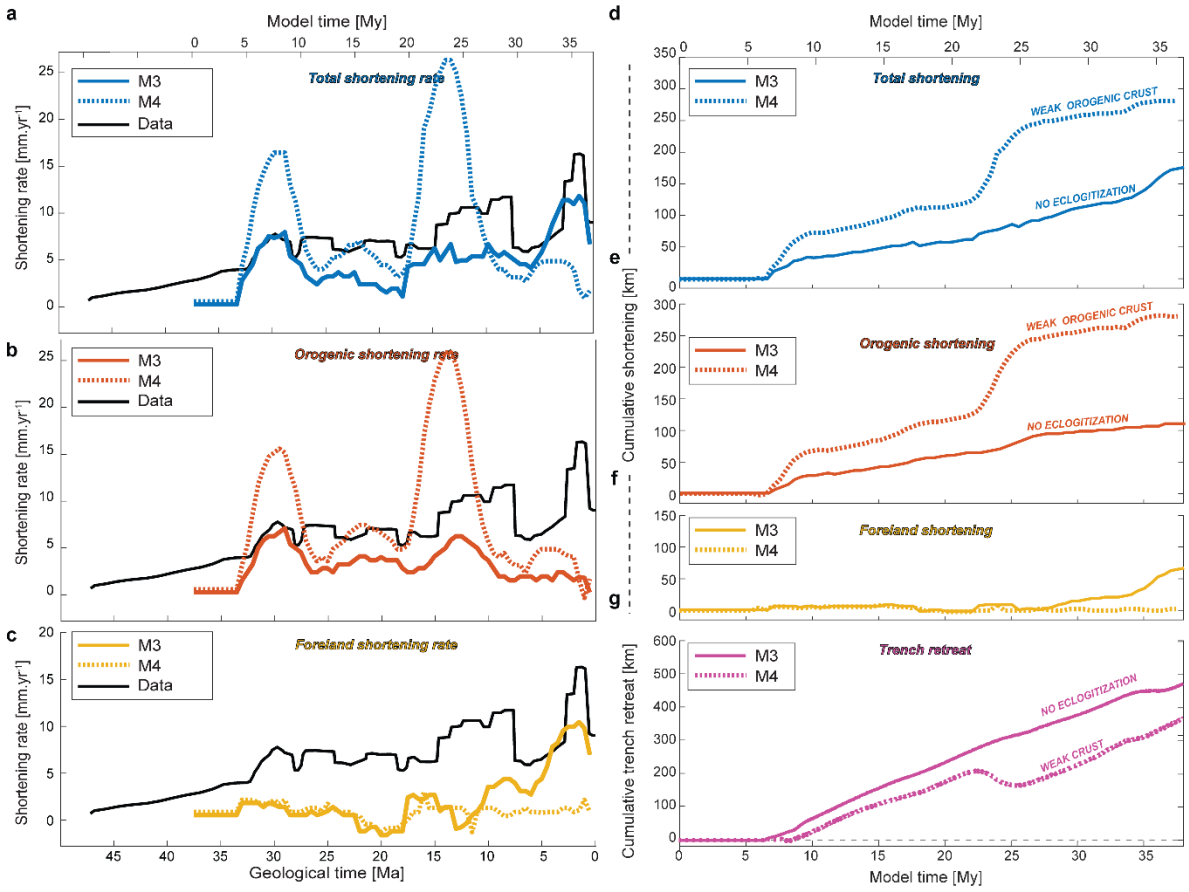

Figure SA.7 Shortening data for model variants M3 and M4. **a, b, c** Total, orogenic and foreland shortening rate, respectively. **d, b, e** Total, orogenic and foreland cumulative shortening, respectively. **g** Cumulative trench retreat.

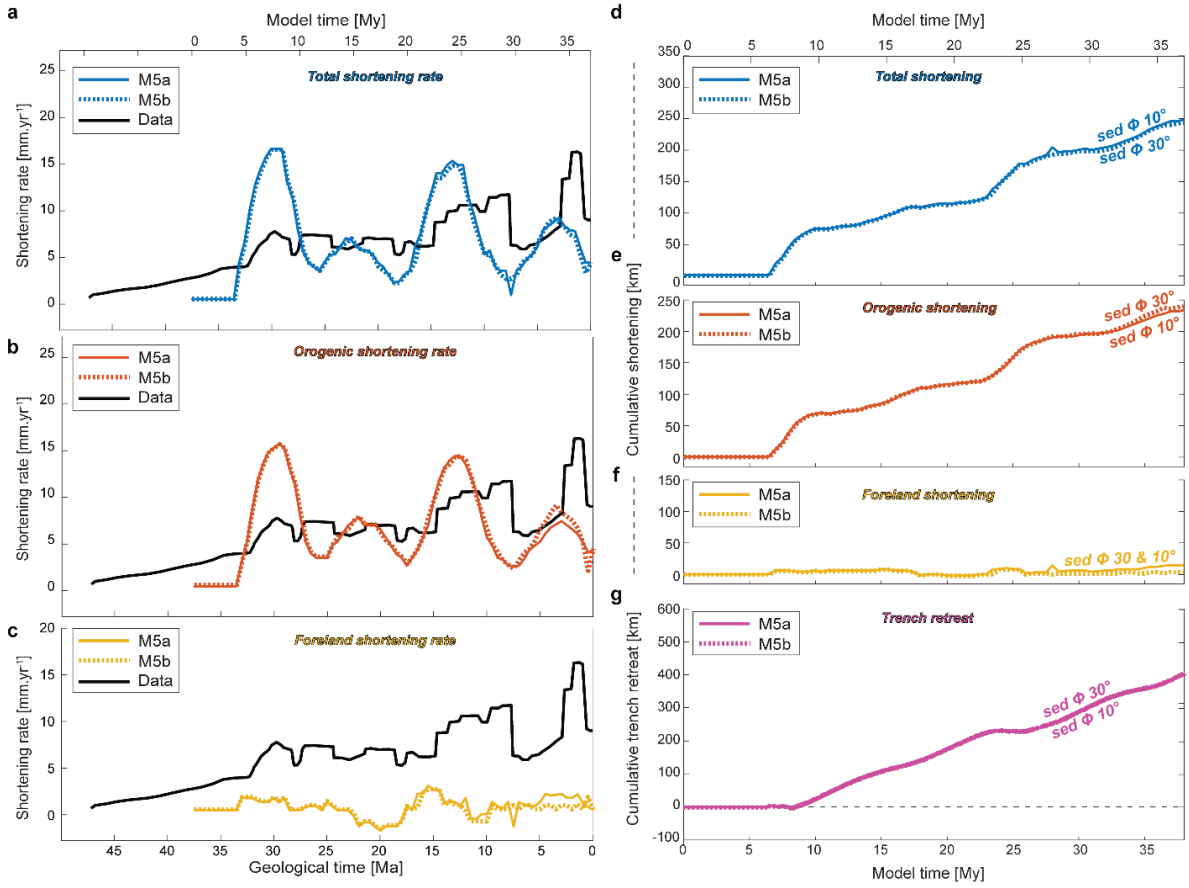

Figure SA.8 Shortening data for model variants M5a-b. **a, b, c** Total, orogenic and foreland shortening rate, respectively. **d, b, e** Total, orogenic and foreland cumulative shortening, respectively. **g** Cumulative trench retreat.

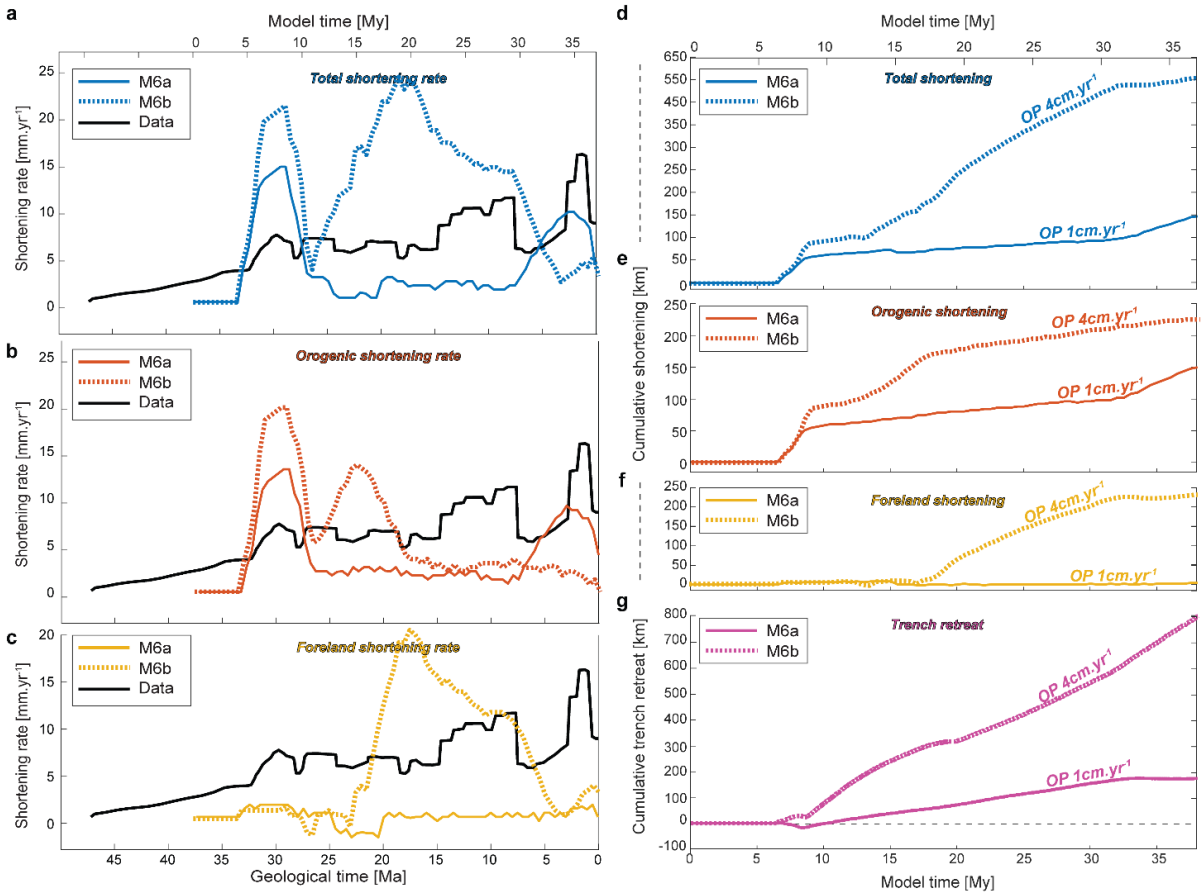

Figure SA.9 Shortening data for model variants M6a-b. **a, b, c** Total, orogenic and foreland shortening rate, respectively. **d, b, e** Total, orogenic and foreland cumulative shortening, respectively. **g** Cumulative trench retreat.

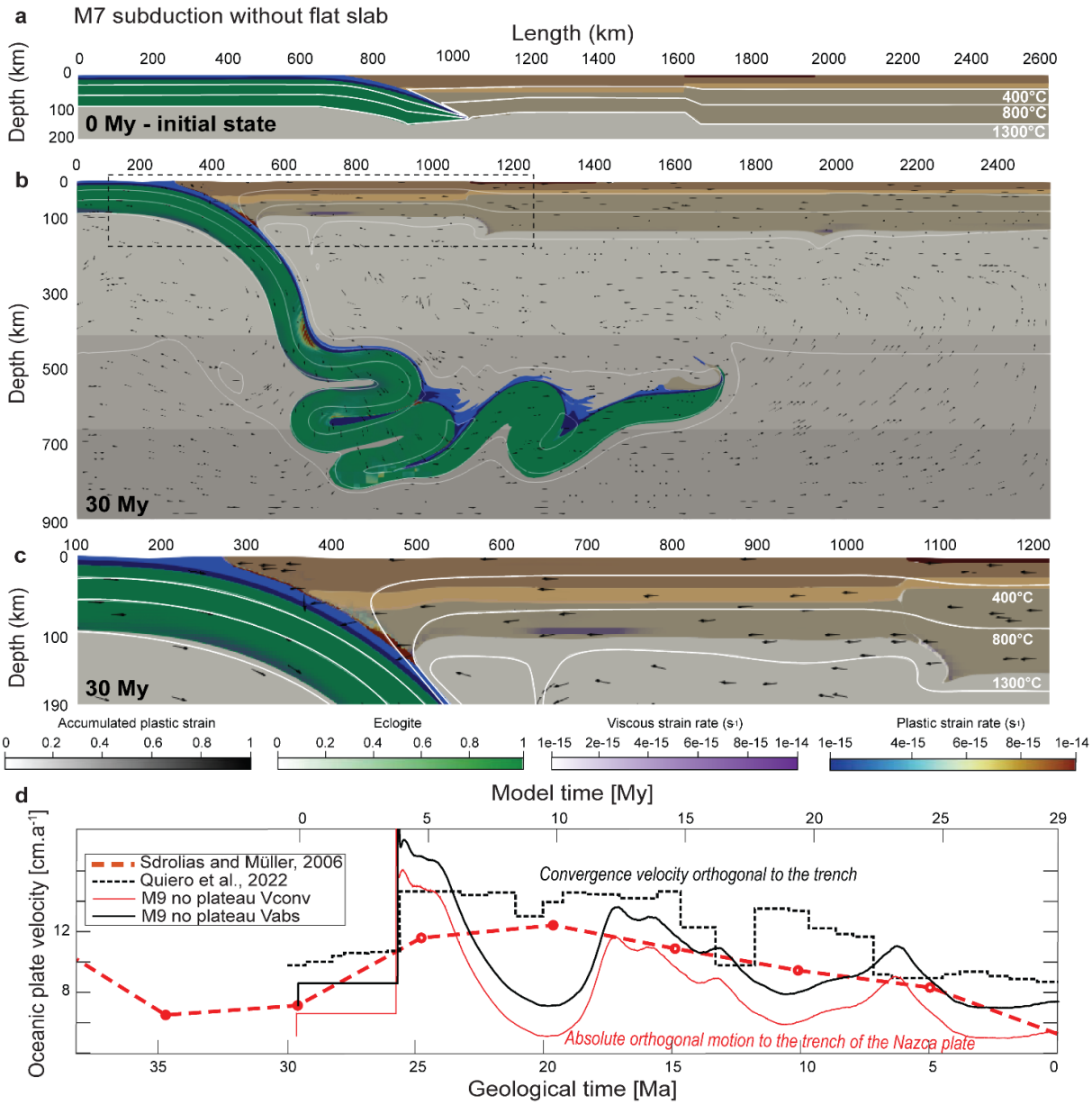

Figure SA.10 Normal subduction model M7 and absolute motion. **a** Initial state. **b** Model after 30 Ma. **c** Zoom in on the overriding plate. **d** Velocity comparison between the model and the velocity model from Sdrolias and Müller (2006) for the absolute orthogonal motion of the Nazca plate to the trench and Quiero et al., (2022) for convergence velocity orthogonal to the trench.

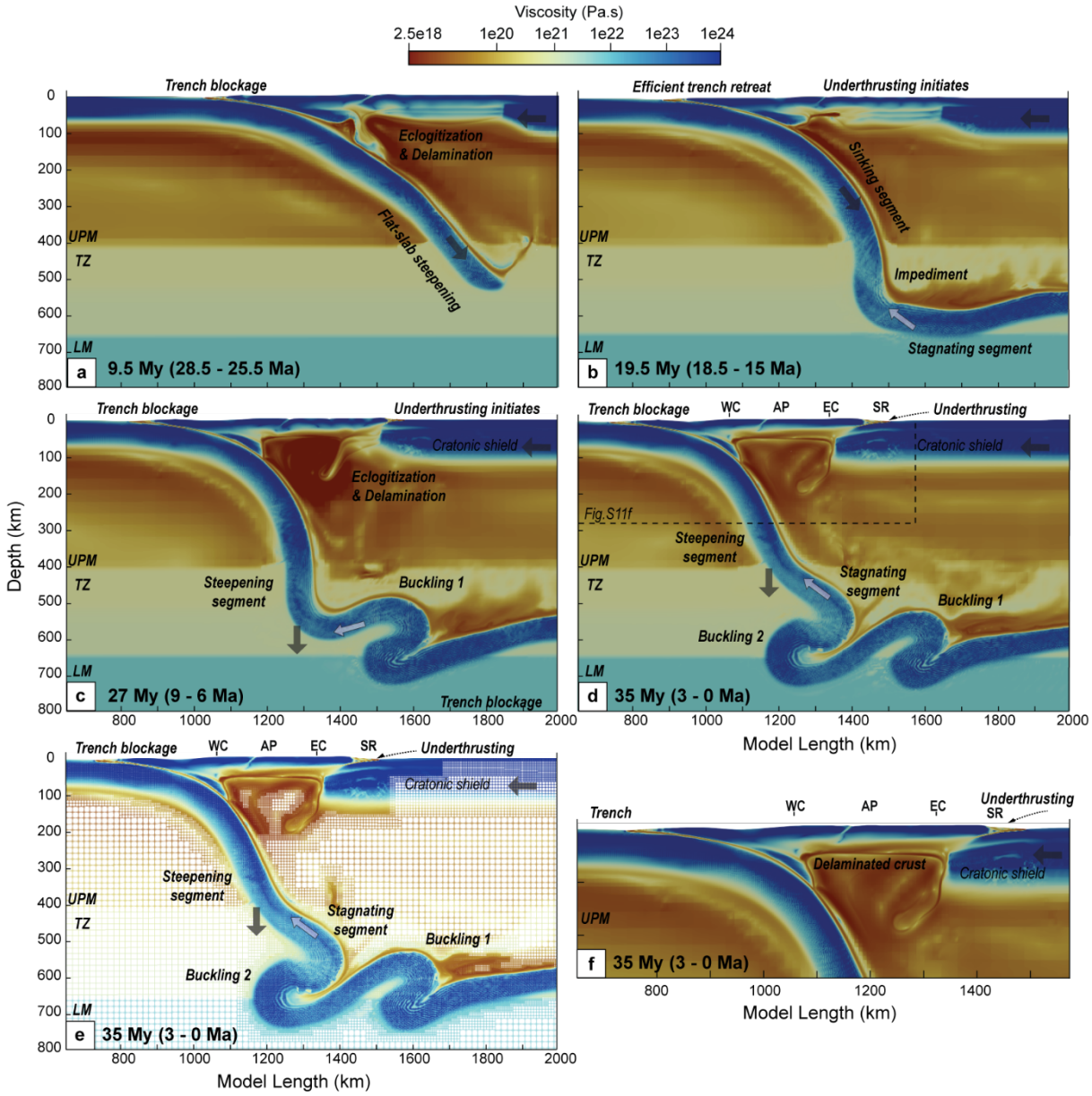

Figure SA.11 Viscosity field of the reference model. Evolution of the subduction model M1 (Figure 2.3) seen with the viscosity field. UPM, TZ and LM are the upper mantle, transition zone and lower mantle, respectively. Other acronyms defined in Figure 2.1. The small dark arrows indicate the direction of the velocity vectors. Bold arrows indicate the direction of the plate motion and white arrows indicate the direction of the main resistive forces due to slab stagnation in the transition zone. **a** The steepening of the slab is associated with the continental lithospheric mantle removal. **b** The slab freely sinks and flattens at lower mantle transition. **c** The slab buckles, the continent delaminates, the deformation migrates eastward and the foreland underthrusts. **d** The slab buckles a second time and the foreland underthrusts. **e** Model refinement at 35 My. **f** Focus on the upper plate at 35 My.

A.5 **Table of model properties**

Table SA.1 Model parameters (Chapter 2).Bd and Bn, Ed and En, Vd and Vn are for the pre-exponential factor, the energy of activation and the volume of activation for diffusion and dislocation creep, respectively. Pw is the pressure width, T is the temperature, and λ is for Clapeyron slope. SC2006 is for Steiberger and Calderwood, 2006 viscosity profile of reference. HK2003 is for Hirth & Kohlstedt, 2003. Mk1998 is for Mackwell et al., 1998. GT1998 is for Gleason & Tullis, 1995. R1997 is for Ranalli, 1997.

		Asthenosphere (AST)											
		Upper Mantle	Transition Zone		Lower mantle	Oceanic plate			Continental plate				
	Units	(< 410 km)	(410-520km)	(520-660km)	(>660km)	Ridge / Weak Gabbro	Gabbro	Lithomantle	Craton	Sediments	JpperCrust	LowerCrust	Lithomantle
Sources for rheology	/	HK2003	SC2006			R1997	Mk1998	HK2003		GT1995		Mk1998	HK2003
Rocks	/	Dry olivine				Wet quartzite	Columbia diabase	Dry olivine		Wet quartzite		Maryland diabase	Wet olivine
Grainsize	m	1e-3				1e-3	1e-3	1e-3		1e-3		1e-3	1e-3
Creep pre-exponential factor Bd / Bn	$Pa^{-ndiff/ndisl}$. s-1	1e-9 / 8.49e-15				- / 2.25e-17	- / 1.37e-25	2.25e-15 / 2.96e-16		- / 8.57e-28		- / 7.13e-18	1e-9 / 2.96e-14
Grain size exponents	mm	0	η = 1e20.83 Pa.s	η = 1e21.03 Pa.s	η = 1e21.87 Pa.s	-	-	3		-		-	0
Activation energies Ed / En	kJ/mol	335 / 540				- / 154	- / 488	375 / 535		- / 223		- / 345	335 / 515
Activation volume Vd / Vn	m^3/mol	4.8e-6 / 12e-6				- / 0	- / 0	10e-6 / 14e-6		- / 0		- / 0	4.8e-6 / 14e-6
Stress exponents	n	3.5				2.3	4.7	3.5		4		3	3.5
Friction angle	degree	30				2	30	0	30	30 -> 3	30 -> 6	30 -> 6	30 ->6
Cohesions	MPa	40				1	40	500	40	20 -> 0.2	20	40 -> 20	40 -> 20
Plastic strain weakening interval	none	-				0 - 0.3	0 - 0.3	-	-	0 - 0.5	0 - 1.5	0 - 1.5	0 - 1.5
Thermal conductivity	W/K/m	3.3				2.5	2.5	3.3	3.2	2.2	2.5	2.6	3.3
Densities at 0 / 60 /270 / 410 / 520 /660 km depth	kg/m^3	3300	3612	3760	4171	3000 / +450/+50 / +162 / +148 / +476		AST -20	3240 / AST -20	2670	2800	3000 / +450/+50 / +162 / +148 / +571	AST -20
Gabbro-eclogite (60 km) λ 1e6 Pa/K	Pw /T (Pa/K)	-	-	-	-	1.2e9/1073	1.2e9/1073	-	-	-	-	0.66e9/973	-
Coesite-Stishovite (270 km) λ 3e6 Pa/K	Pw /T (Pa/K)	-	-	-	-	9e9/1760	9e9/1760	-	-	-	-	9e9/1760	-
Olivine-Wadsleyite (410 km) λ 2e6 Pa/K	Pw /T (Pa/K)	0.08e9/1810	-	-	-	0.16e9/1810	0.16e9/1810	0.41e9/1810	0.41e9/1810	-	-	0.16e9/1810	0.41e9/1810
Wadsleyite - Ringwoodite (510 km) λ 3.5e6 Pa/K	Pw /T (Pa/K)	0.8e9/1870	0.8e9/1870	-	-	0.16e9/1870	0.8e9/1870	0.8e9/1870	0.8e9/1870	-	-	0.16e9/1870	0.8e9/1870
Spinel-Perovskite (660km) λ -0.5e6 Pa/K	Pw /T (Pa/K)	0.16e9/1940	0.16e9/1940	0.16e9/1940	-	0.16e9/1940	0.16e9/1940	0.16e9/1940	0.16e9/1940	-	-	0.16e9/1940	0.16e9/1940
Addtionnal blocking temperature	K	-	-	-	-	Ridge : 973	-	-	-	-	-	-	-

Group	Name	Variation
Reference model	M1	-
Friction coefficient of the subduction interface (μ_{int})	M2a/b/c	μ_{int} = 0.015/0.035/0.06
Eclogitization	M3	No eclogitization of the lower crust
"Partial melting"	M4	Upper crust heat flow (1000x)
Foreland sediment strength (internal friction angle Φ and cohesion C)	M5a	Φ = 10° , C = 20 Mpa
	M5b	Φ = 30°, C = 20 MPa
Overriding plate velocity	M6a/b	OP vel = 1 / 4 cm.yr-1
Flat-slab (A.3, Figure SA.10)	M7	no flat-slab

Table SA.2 Summary of the models performed.

At 38 My	Orogenic shortening	Under-thrusting	Total shortening	Total trench retreat (~6.5My to 38 My)	Trench retreat after initialization	Total (Shortening + trench retreat)	Total westward overriding plate motion
M1	196	106	302	328	130 (at ~6.5 My)	760	760 (VOP = 2 cm/yr)
M2a	104	-2	102	528	130 (at ~6.5 My)	760	760 (VOP = 2 cm/yr)
M2b	168	80	248	382	130 (at ~6.5 My)	760	760 (VOP = 2 cm/yr)
M2c	200	104	304	326	130 (at ~6.5 My)	760	760 (VOP = 2 cm/yr)
M3	110	66	176	454	130 (at ~6.5 My)	760	760 (VOP = 2 cm/yr)
M4	282	2	284	346	130 (at ~6.5 My)	760	760 (VOP = 2 cm/yr)
M5a	234	14	248	382	130 (at ~6.5 My)	760	760 (VOP = 2 cm/yr)
M5b	240	4	244	386	130 (at ~6.5 My)	760	760 (VOP = 2 cm/yr)
M6a	150	4	154	161	130 (at ~6.5 My)	445	445 (VOP = 2 cm/yr until 6.5 My and then 1cm/yr)
M6b	222	227	449	811	130 (at ~6.5 My)	1390	1390 (VOP = 2 cm/yr until 6.5 My and then 4cm/yr)
M7 (at 29 My)	82	0	82	438 (~3My to 29 My)	60 (at ~3My)	580	580 (VOP = 2 cm/yr)

Table SA.3 Final measured total shortening and total trench retreat for each model. The unit is in kilometres. VOP stands for westward overriding plate velocity.

Appendix B Southern Central Andes

B.1 Checking model densities

One advantage of implementing the data-driven model of Rodriguez Piceda et al. (2021) into a geodynamic simulation is the possibility of testing the evolution of topography as a response to the imposed structural and density configuration. The thickness, geometry and density of the lithospheric layers were obtained by integration of geological and geophysical data and testing with the gravity field.

The biggest advantage of this approach is the possibility to verify the robustness of the lithosphere model and in particular the consistency of the structures and density. The structural layers were obtained by compiling and integrating 3D geological and geophysical data to constrain the thickness of the different lithospheric layers. Then, the densities were inferred with the gravity using an iterative forward modelling approach (Rodriguez Piceda et al, 2021). The residual gravity (Fig. SB.1d) obtained indicates a good fit between the lithospheric model and the gravity. Using the average temperature for each layer we recalculated their average reference density (Table. 3.1). Subsequently we ran a geodynamic model, without prescribing any velocity and let the model re-equilibrate. The topography is smoothed with a moving filter with a radius of ~50 km in order to avoid local strong topographic gradients. After 100ka, we calculate the residual topography by subtracting the model to the present-day topography (Fig. SB.1e). The residual topography indicates a consistency in the area covered by data. Whereas the modelled topography is underestimated on the eastern border (+1 km) and overestimated locally at the trench (-1km). The orogenic domain is close to the present-day topography and range between ($\pm$ 0.5 km). Variations on the east suggest that thickness of the layers may vary far from the orogen where new data are required.

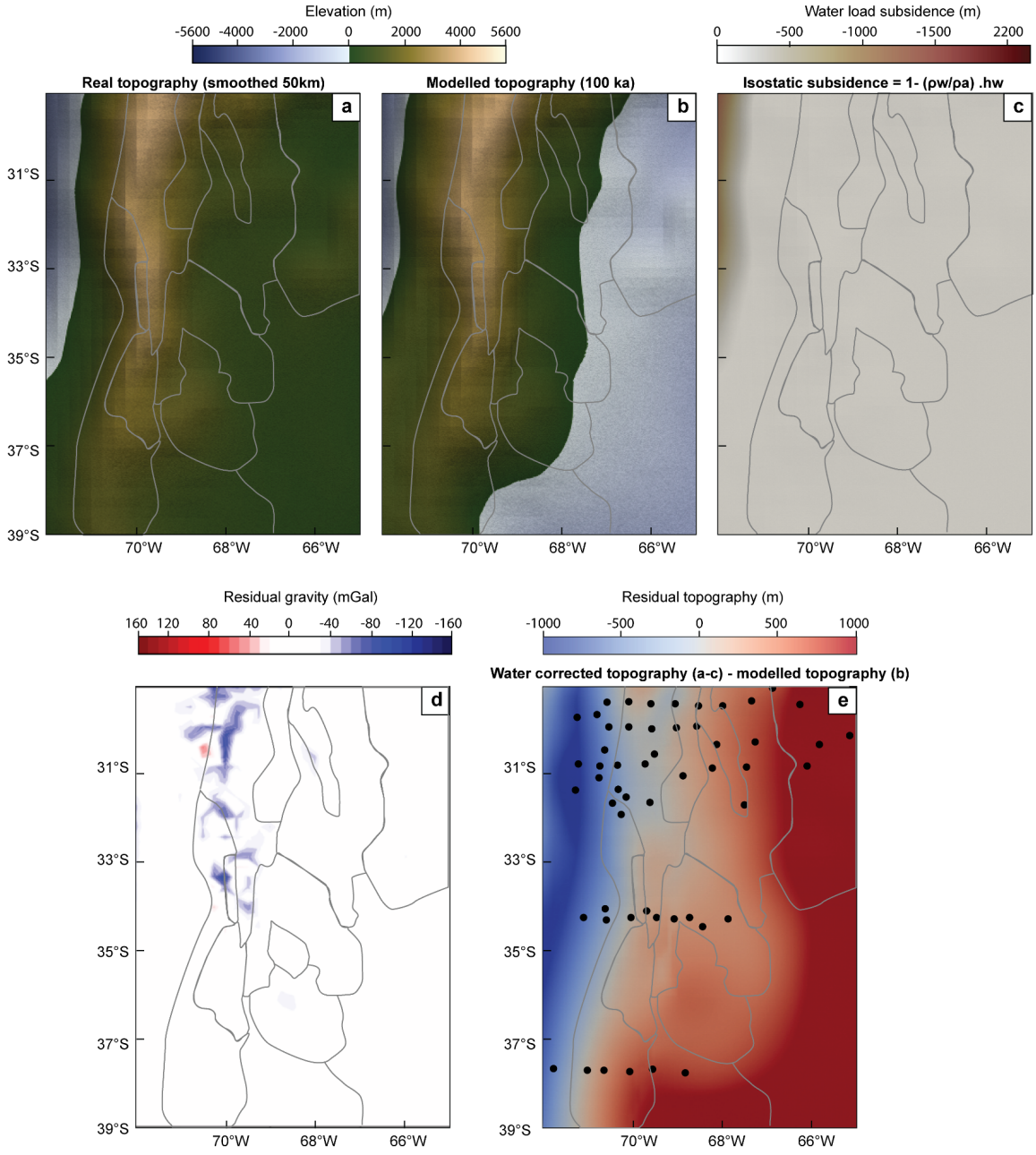

Figure SB.1 Comparison between the modelled and the real topography. **a** Real topography smoothed with a radial filter of 50 km. **b** Topography altered after 100 ky of model time. **c** Isostatic contribution of the sea water. **d** Residual gravity of the density model (modified from Rodriguez Piceda et al., 2021). **e** Residual topography. Black circles illustrate local data of the crustal thickness.

B.2 Supplementary figures

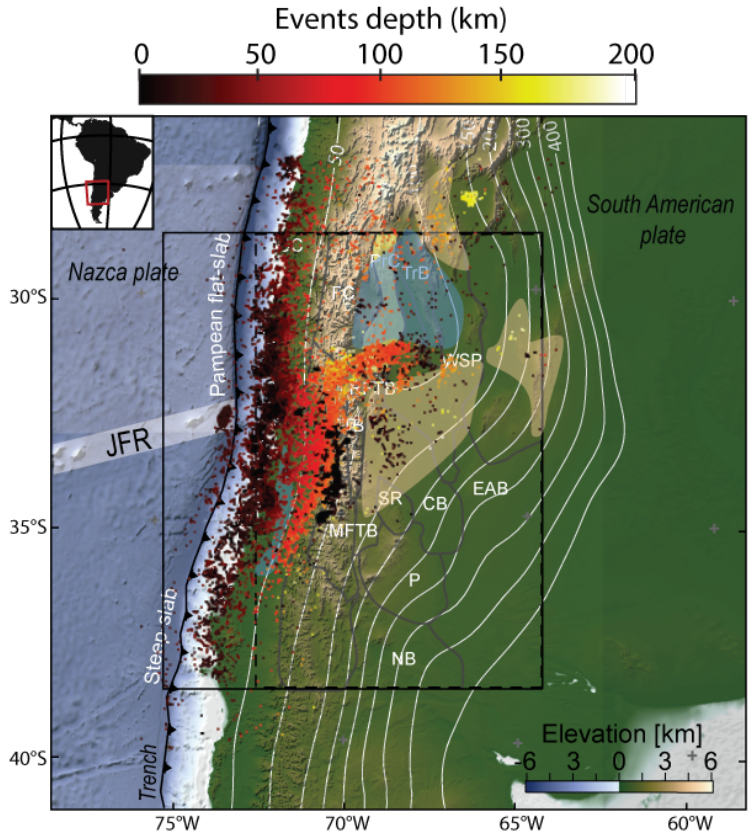

Figure SB.2 Distribution of seismic events in the Sierras Pampeanas (International Seismological Centre, 2021; Lentas et al., 2019). Few events are recorded on the top of the flat-slab (blue) compared to the East and South front and the South front (orange). JFR corresponds to the Juan Fernandez hotspot ridge. A greater density of events occurs in line with the eastern extension of the ridge. The other labels are defined in Figure 3.1.

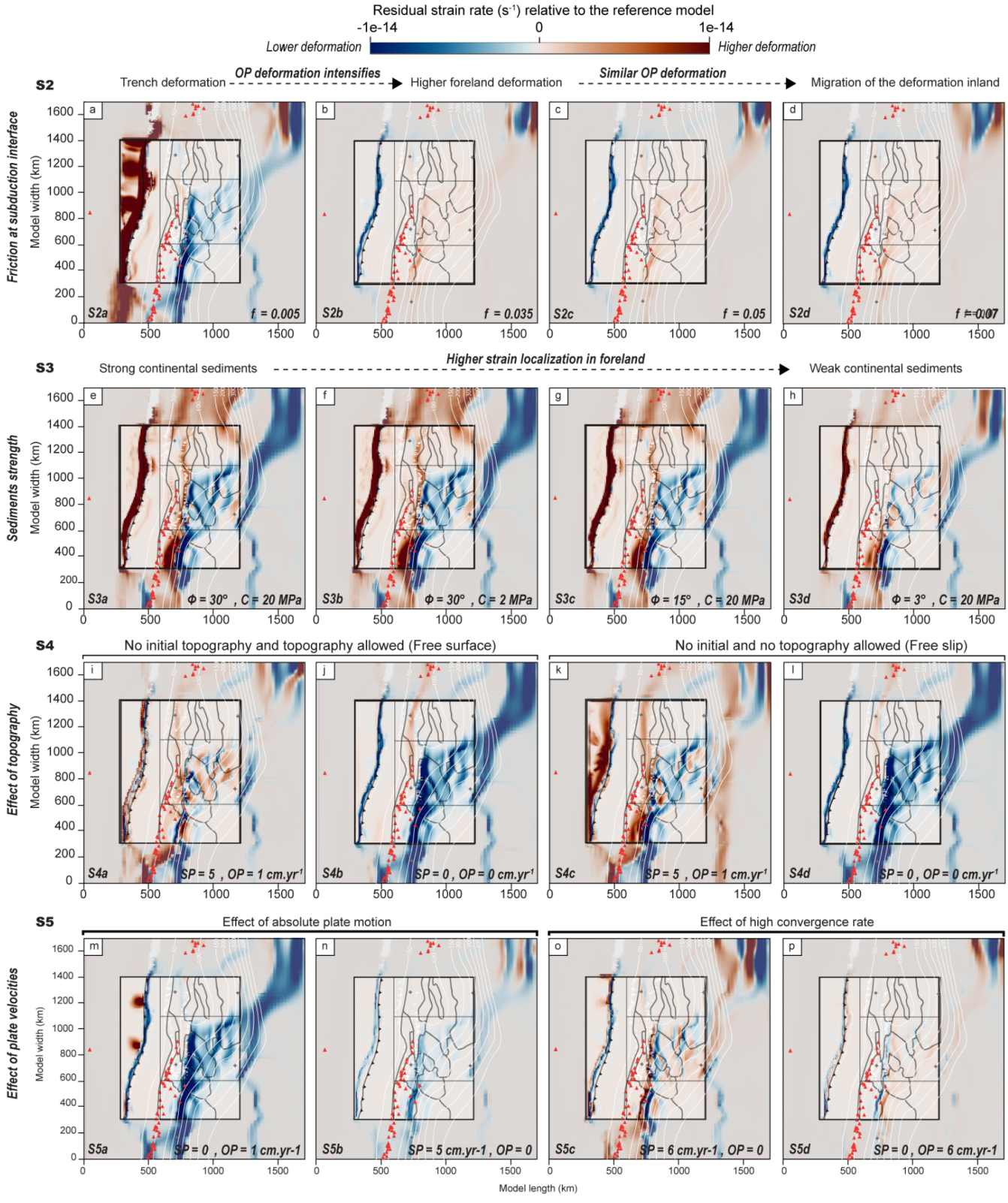

Figure SB.3 Residual obtained by subtracting the Reference model S1 to the model variants. Black squares indicate the deformational domains (e.g. Trench, flat subduction, shallow subduction and steep subduction). Blue color and red color indicate less or higher rate of deformation than in the reference model.

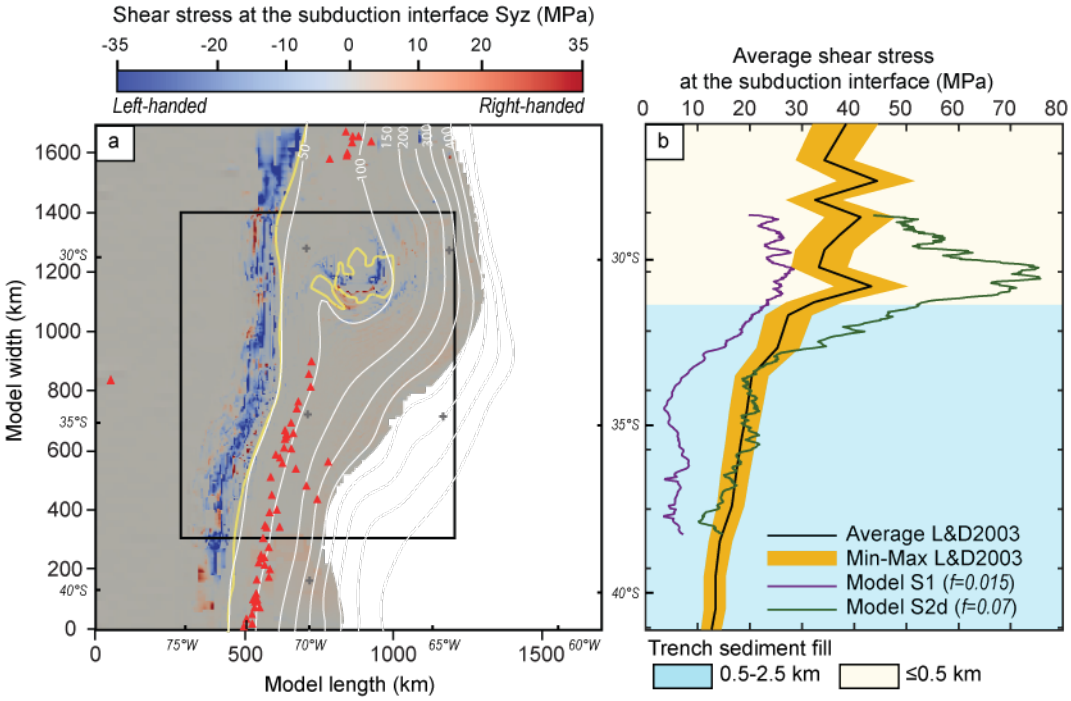

Figure SB.4 Shear stress at subduction interface**. a** The shear stress (Syz - pressure) from the reference model. Isobaths of the slab (in white) and volcanic edifices (red triangles) are represented. The yellow lines indicate the Brittle-Ductile-Transition. **b** Model shear stress (S1 and S2d) averaged at each latitude over an average plate interface depth of 120 km and compared to previous estimates by Lamb & Davis (L&D2003; 2003).

Ranges	Uplift Age (Ma)	References
Aconquija	7.6 - 6	Ramos et al., 2002
Famatina	4.5 – 4.19	Ramos et al., 2002
Pocho	5.5 - 4.7	Ramos et al., 2002
San Luis	2.6	Ramos et al., 2002
Sierra de Pie de Palo	onset ~6 – 4, main phase 4-2	Siame et al., 2015
Eastern Precordillera (31°S)	2	Ramos et al., 2002
Precordillera (33°S)	2.6 - present	Ramos et al., 2002
Frontal cordillera	9	Ramos et al., 2002

Table SB.1 Uplift age of the SCA used in figures 3.4 and 4.2

Table SB.2 Average Neogen vertical axis rotations from Japas et al., (2016) displayed in Figure 4.1c for the Precordillera at ~30°S indicates significant rotations before the arrival of the ridge and decrease during the flattening of the slab.

Japas et al., 2016	Western Precordillera	Central Precordillera	Eastern Precordillera
18 Ma	~40 °		
10 Ma	~20°	~10-20°	
2 Ma	<10 °	<10 °	<10 °

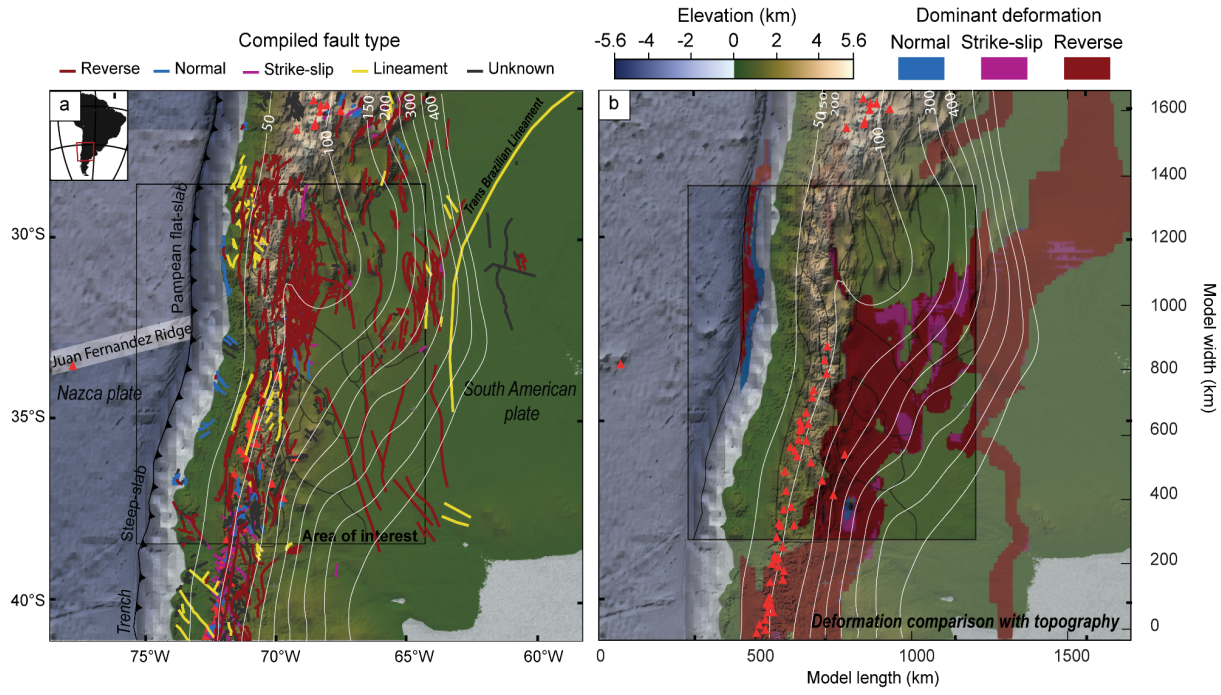

Figure SB.5 Deformation and faults type. **a** Compiled fault types (Moscoso & Mpodozis, 1988; García, 2001; Giambiagi et al., 2003; Broens & Pereira, 2005; Folguera & Zárate, 2011; Martino et al., 2016; Litvak et al., 2018; Martínez et al., 2017; Sánchez et al., 2017; Meeßen et al., 2018; Riesner et al., 2018; Olivar et al., 2018; Jensen, 2018; Melnick et al., 2020; Costa et al., 2020; Eisermann et al., 2021). **b** Modelled dominant deformation and present day topography.

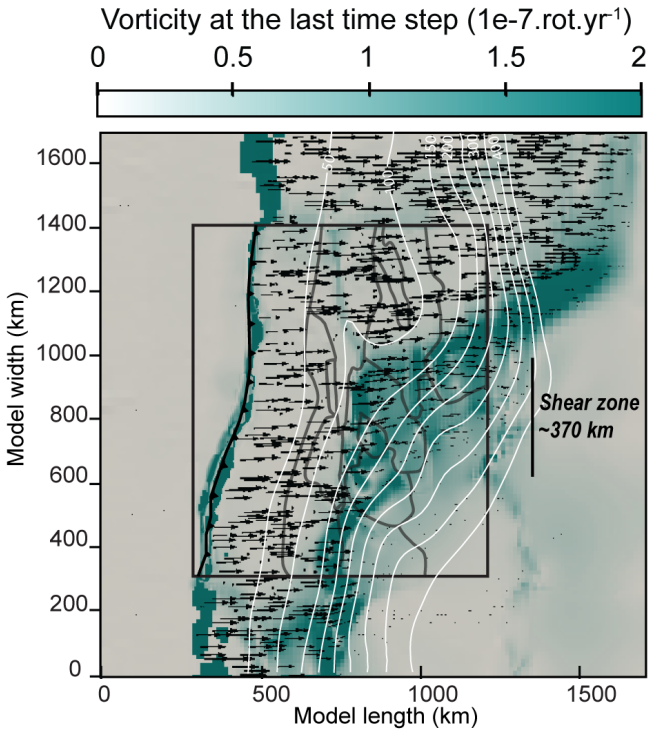

Figure SB.6 Vorticity at 250 kyr for the last time step. White line indicates the isobaths of the oceanic plate. Grey lines indicate the morphotectonic provinces and the black middle square the most refined area.

<u>Calculation step for the Angle of rotation Figure 4.3c (i.e. main text)</u>

The E-W velocity (xx) is first corrected from the net velocity of each plates, 5 cm/yr for the oceanic and 1cm/yr for the continental in order to only get the velocity resulting from the interaction between the plates.

The ***vorticity*** (rot.yr^{-1}) is obtained by calculating the curl of the velocity field. 6.1

$$\overrightarrow{\omega} = \nabla \, x \, \overrightarrow{u} \,, \tag{B.1}$$

$$\overrightarrow{\omega} = \left(\frac{\partial vz}{\partial y} - \frac{\partial vy}{\partial z} \quad \frac{\partial vx}{\partial z} - \frac{\partial vz}{\partial x} \quad \frac{\partial vy}{\partial x} - \frac{\partial vx}{\partial y} \right) , \tag{B.2}$$

The vorticity is twice the mean of the ***angular velocity*** (rad.yr^{-1}). Then,

$$\Omega = \frac{1}{2} * \overrightarrow{\omega} \,, \tag{B.3}$$

Inferred over a period of 6 million years, we can get the ***angle of rotation*** (degree °, Fig. 4.3c).

$$\Theta = \Omega * \frac{180}{\pi} * 6e6 \,, \tag{B.4}$$

Data and code availability

All input files to reproduce the results in Chapter 2 are available at https://doi.org/10.5880/GFZ.2.5.2022.001. The modified version of ASPECT (version 2.3.0-pre, dealii 9.2.0), including the implementation of new custom plugins needed to set up the model and handle prostocks, is available at https://github.com/Minerallo/aspect/tree/Paper_slab_buckling_Andes.

The input files to reproduce the results of Chapters 3 and 4 are not yet available but can be obtained by contacting me (Michaël Pons) or Dr. Constanza Rodriguez Piceda. The modified version of ASPECT (version 2.3.0-pre, dealii 9.2.0), including the implementation of new custom plugins needed for model set-up and prosthesis processing, is available at https://github.com/Minerallo/aspect/tree/GMS_model.

The original ASPECT code is open source and hosted on github https://github.com/geodynamics/aspect. The FASTSCAPE code is also available at https://github.com/fastscape-lem/fastscapelib-fortran. The figures in this thesis were created using Paraview and Illustrator. Colour scales are from Crameri, 2017 (10.5281/zenodo.5501399).

Acknowledgements

This dissertation was funded by the DeutscheForschungsgemeinschaft (DFG) and the Federal State of Brandenburg under the guidance of the International Research Training Group IGK2018 “SuRfAce processes, TEctonics and Georesources: The Andean foreland basin of Argentina” (STRATEGy DFG 373/34-1). The authors thank the Computational Infrastructure for Geodynamics (CIG, geodynamics.org), which is funded by the National Science Foundation under award EAR-0949446 and EAR-1550901, for supporting the development of ASPECT. The computations of this work were supported by the North-German Supercomputing Alliance (HLRN). I would like to thank the dissertation reviewers: Hanna Čížková and Eline le Breton as well as the committee members: Sascha Brune and Frank Krüger.

On a much personal note, this PhD has been a great adventure that I could not have accomplished without the support of many people whom I would like to thank.

First of all, I would like to thank the International StRATEGy Project for allowing me to live this wonderful adventure, the project has allowed me to develop both professionally and personally. In particular, I would like to thank Manfred Strecker, Verónica Torres Acosta, Gabriella Poïan, for their constant and multifaceted support. Through our travels, they have allowed me to discover Germany and its culture as well as Argentina, and the beautiful relationship that the two countries have developed over the past decades.

I would particularly like to thank my supervisor Stephan Sobolev for his working related advises and for his insatiable desire for science. I have learned with him that good work can take time but can be very satisfying in the end. Through our discussions, I learned a lot about all the complex concepts associated with geodynamic modelling and the functioning of the earth. His passion further fuelled my passion for geodynamics.

I would also like to express my appreciation to my colleagues with who I have spent the last 4 years of my life in particular to Sascha Brune, Andrey Babeyko, Bernard Steinberger, Uwe Lemgo, Daniela Kruse, Till Bruens, Anne glerum, Elodie Kendall, Boris Robert, Frank Zwaan, Zoltan Erdös, Marzie Baes, Ameha Atnafu Muluneh, Thilo Wrona, Charitra Jain, Poulamie Roy, Kai li, and Esther Lina Heckenbach who also helped with the German abstract of this thesis. I wish everyone to work in such a pleasant environment as the GFZ with such friendly colleagues. Going to work every day was a very pleasant experience. Discussion and debate at lunchtime were exciting.

I would especially like to thank my friend, colleague and former office mate Derek Neuharth, who was there from my first day, always ready to listen to my complaints and help me find solutions. He

was also a guide and an example to follow at work. With my supervisor, he introduced me to the world of geodynamic modelling. This thesis and the work carried out would not have reached this level without his contribution. He also proofread the English of this thesis.

I would also like to thank all of my friend, Michele Vallati, Roman Féal, Nikolaos Antonoglou, Camille Larroque, Sara Figueroa, Maxime Bernard, Matías Barrionuevo, Facundo Flores, the argentinian from the projects, and my distant friends Tonin Bechon, David Fuseau, Marco Papandrea, Thomas Lefebvre, Maxime Louwye, Mickael Boursier and those that I may not have cited here but still count. They not only improved my life in Potsdam, but many of them also during my studies at the university.

I could not forget to thank my partner Constanza Rodriguez Piceda, who has been present in many dimensions of this work. Without her half of this work would not have come to the same end. During the last 4 years, we shared our common passion for geodynamics. She was always there to support me and assert any wild new ideas I might have to get me back to reality. She brought to me a good balance between work and life.

Finally, I would like to thank some member of family for being there in difficult times and for supporting my choices, in particular, Elisabeth & Francis Chige, Annie Rallo & Christian Godin, Christelle & Jean-Michel Langlais, Jean-Luc Rallo & Isabelle Pons-Rallo, my father and her partner Jean-Philippe Pons and Nathalie Patenay, my grandmother Simone Constant.

This thesis, in the first place, would not have been possible without the moral support of my little sister Nelly Pons. We went through difficult times, but by helping each other we were able to move forward. She has been a great help in editing the final version this work. Finally, I dedicate this dissertation to the driving force along most of my life, she believed in my dreams and showed me the way, my mother, Isabelle Rallo, wherever you are.

References

Allmendinger, R. W., Ramos, V. A., Jordan, T. E., Palma, M., & Isacks, B. L. (1983). Paleogeography and Andean structural geometry, northwest Argentina. Tectonics, 2(1), 1-16. https://doi.org/10.1029/TC002i001p00001

Allmendinger, R. W., & Gubbels, T. (1996). Pure and simple shear plateau uplift, Altiplano-Puna, Argentina and Bolivia. Tectonophysics, 259(1-3 SPEC. ISS.), 1–13. https://doi.org/10.1016/0040-1951(96)00024-8

Allmendinger, R. W., Jordan, T. E., Kay, S. M., & Isacks, B. L. (1997). The evolution of the Altiplano-Puna plateau of the Central Andes. Annual Review of Earth and Planetary Sciences, 25, 139–174. https://doi.org/10.1146/ANNUREV.EARTH.25.1.139

Allmendinger, R. W., & Judge, P. A. (2014). The Argentine Precordillera : A foreland thrust belt proximal to the subducted plate. Geosphere, 10(6), 1203-1218. https://doi.org/10.1130/GES01062.1

Alvarado, P., S. B., G. Zandt. (2005). Crustal deformation in the south-central Andes backarc terranes as viewed from regional broad-band seismic waveform modelling. Geophys J Int, 163(2), 580-598. https://doi.org/10.1111/j.1365-246x.2005.02759.x

Alvarado, P., Beck, S., & Zandt, G. (2007). Crustal structure of the south-central Andes Cordillera and backarc region from regional waveform modeling. Geophysical Journal International, 170(2), 858-875. https://doi.org/10.1111/j.1365-246x.2007.03452.x

Alvarado, P., Barrientos, S., Saez, M., Astroza, M., & Beck, S. (2009). Source study and tectonic implications of the historic 1958 Las Melosas crustal earthquake, Chile, compared to earthquake damage. Physics of the Earth and Planetary Interiors, 175(1), 26-36. https://doi.org/10.1016/j.pepi.2008.03.015

Amante, C., & Eakins, B. (2009). ETOPO1 1 Arc-Minute Global Relief Model : Procedures, data sources and analysis. https://doi.org/10.7289/V5C8276M

Ammirati, J.-B., Alvarado, P., Perarnau, M., Saez, M., & Monsalvo, G. (2013). Crustal structure of the Central Precordillera of San Juan, Argentina (31°S) using teleseismic receiver functions. Journal of South American Earth Sciences, 46, 100-109. https://doi.org/10.1016/j.jsames.2013.05.007

Ammirati, J. B., Alvarado, P., & Beck, S. (2015). A lithospheric velocity model for the flat-slab region of Argentina from joint inversion of Rayleigh wave phase velocity dispersion and teleseismic receiver functions. Geophysical Journal International, 202(1), 224. https://doi.org/10.1093/gji/ggv140

Ammirati, J.-B., Venerdini, A., Alcacer, J. M., Alvarado, P., Miranda, S., & Gilbert, H. (2018). New insights on regional tectonics and basement composition beneath the eastern Sierras Pampeanas (Argentine back-arc region) from seismological and gravity data. Tectonophysics, 740-741, 42-52. https://doi.org/10.1016/j.tecto.2018.05.015

Anderson, R. B., Long, S. P., Horton, B. K., Thomson, S. N., Calle, A. Z., & Stockli, D. F. (2018). Orogenic wedge evolution of the central Andes, Bolivia (21 S): Implications for Cordilleran cyclicity. Tectonics, 37(10), 3577-3609.

Anikiev, D., Cacace, M., Bott, J., Gomez Dacal, M. L., & Scheck-Wenderoth, M. (2020). Influence of Lithosphere Rheology on Seismicity in an Intracontinental Rift : The Case of the Rhine Graben. Frontiers in Earth Science, 8, 492. https://doi.org/10.3389/feart.2020.592561

Aranda, N., & Assumpçao, M. (2013). Crustal thickness in the northern Andes from teleseismic pP and sS precursors. In 13th International Congress of the Brazilian Geophysical Society & EXPOGEF, Rio

de Janeiro, Brazil, 26?29 August 2013 (p. 1781-1785). Brazilian Geophysical Society. https://doi.org/10.1190/sbgf2013-366

Araneda, M., Asch, G., Bataille, K., Bohm, M., Bruhn, C., Giese, P., Lüth, S., Quezada, J., Rietbrock, A., & Wigger, P. (2003). A crustal model along 39° S from a seismic refraction profile-ISSA 2000. Revista geológica de Chile, 30(1), 83-101. http://dx.doi.org/10.4067/S0716-02082003000100006

Armijo, R., Lacassin, R., Coudurier-Curveur, A., & Carrizo, D. (2015). Coupled tectonic evolution of Andean orogeny and global climate. Earth-Science Reviews, 143, 1–35.

Arndt, J., Bartel, T., Scheuber, E., & Schilling, F. (1997). Thermal and rheological properties of granodioritic rocks from the Central Andes, North Chile. Tectonophysics, 271(1), 75–88. https://doi.org/10.1016/S0040-1951(96)00218-1

Arredondo, K. M., & Billen, M. I. (2016). The effects of phase transitions and compositional layering in two-dimensional kinematic models of subduction. Journal of Geodynamics, 100, 159–174. https://doi.org/10.1016/J.JOG.2016.05.009

Arredondo, K. M., & Billen, M. I. (2017). Coupled effects of phase transitions and rheology in 2-D dynamical models of subduction. Journal of Geophysical Research: Solid Earth, 122(7), 5813–5830. https://doi.org/10.1002/2017JB014374

Arriagada, C., Roperch, P., Mpodozis, C., & Cobbold, P. R. (2008). Paleogene building of the Bolivian Orocline : Tectonic restoration of the central Andes in 2-D map view. Tectonics, 27(6). https://doi.org/10.1029/2008TC002269

Assumpção, J. J., M. Feng, A. Tassara. (2013). Models of crustal thickness for South America from seismic refraction, receiver functions and surface wave tomography. Tectonophysics, 609, 82-96. https://doi.org/10.1016/j.tecto.2012.11.014

Aubry, L., Roperch, P., de Urreiztieta, M., Rossello, E., & Chauvin, A. (1996). Paleomagnetic study along the southeastern edge of the Altiplano - Puna Plateau : Neogene tectonic rotations. Journal of Geophysical Research: Solid Earth, 101(B8), 17883-17899. https://doi.org/10.1029/96JB00807

Axen, G. J., van Wijk, J. W., & Currie, C. A. (2018). Basal continental mantle lithosphere displaced by flat-slab subduction. Nature Geoscience, 11(12), Art. 12. https://doi.org/10.1038/s41561-018-0263-9

Babeyko, A. Y., & Sobolev, S. V. (2005). Quantifying different modes of the late Cenozoic shortening in the central Andes. Geology, 33(8), 621–624. https://doi.org/10.1130/G21126.1

Babeyko, A. Y., Sobolev, S. V., Trumbull, R. B., Oncken, O., & Lavier, L. L. (2002). Numerical models of crustal scale convection and partial melting beneath the Altiplano-Puna plateau. Earth and Planetary Science Letters, 199(3–4), 373–388. https://doi.org/10.1016/S0012-821X(02)00597-6

Babeyko, A. Y., Sobolev, S. V., Vietor, T., Oncken, O., & Trumbull, R. B. (2006). Numerical Study of Weakening Processes in the Central Andean Back-Arc. The Andes - Active Subduction Orogeny, 495–512. https://doi.org/10.1007/978-3-540-48684-8

Bangerth, W., Dannberg, J., Fraters, M., Gassmoeller, R., Glerum, A., Heister, T., & Naliboff, J. (2021). ASPECT v2.3.0. Zenodo. https://doi.org/10.5281/zenodo.5131909

Barazangi, M., & Isacks, B. L. (1976). Spatial distribution of earthquakes and subduction of the Nazca plate beneath South America. Geology, 4(11), 686–692. https://doi.org/10.1130/0091-7613(1976)4<686:SDOEAS>2.0.CO;2

Barazangi, M., & Isacks, B. L. (1979). Subduction of the Nazca plate beneath Peru : Evidence from spatial distribution of earthquakes. Geophysical Journal of the Royal Astronomical Society, 57(3), 537-555. https://doi.org/10.1111/j.1365-246X.1979.tb06778.x

Barrionuevo, M., Liu, S., Mescua, J., Yagupsky, D., Quinteros, J., Giambiagi, L., Sobolev, S. V., Piceda, C. R., & Strecker, M. R. (2021). The influence of variations in crustal composition and lithospheric strength on the evolution of deformation processes in the southern Central Andes : Insights from geodynamic models. International Journal of Earth Sciences 2021 110:7, 110(7), 2361-2384. https://doi.org/10.1007/S00531-021-01982-5

Beck, S. L., & Zandt, G. (2002). The nature of orogenic crust in the central Andes. Journal of Geophysical Research: Solid Earth, 107(B10), ESE 7-1-ESE 7-16. https://doi.org/10.1029/2000JB000124

Beck, S. L., Zandt, G., Ward, K. M., & Scire, A. (2015). Multiple styles and scales of lithospheric foundering beneath the Puna Plateau, central Andes. https://doi.org/10.1130/2015.1212(03)

Becker, T. W., & O'Connell, R. J. (2001). Predicting plate velocities with mantle circulation models. Geochemistry, Geophysics, Geosystems, 2(12).

Becker, T. W., Schaeffer, A. J., Lebedev, S., & Conrad, C. P. (2015). Toward a generalized plate motion reference frame. Geophysical Research Letters, 42(9), 3188–3196. https://doi.org/10.1002/2015GL063695

Bello-González, J. P., Contreras-Reyes, E., & Arriagada, C. (2018). Predicted path for hotspot tracks off South America since Paleocene times: Tectonic implications of ridge-trench collision along the Andean margin. Gondwana Research, 64, 216–234. https://doi.org/10.1016/j.gr.2018.07.008

Bense, F. A., Löbens, S., Dunkl, I., Wemmer, K., & Siegesmund, S. (2013). Is the exhumation of the Sierras Pampeanas only related to Neogene flat-slab subduction? Implications from a multi-thermochronological approach. Journal of South American Earth Sciences, 48, 123-144.

Bevis, M., Kendrick, E., Smalley Jr, R., Brooks, B., Allmendinger, R., & Isacks, B. (2001). On the strength of interplate coupling and the rate of back arc convergence in the central Andes: An analysis of the interseismic velocity field. Geochemistry, Geophysics, Geosystems, 2(11).

Billen, M. I., & Hirth, G. (2007). Rheologic controls on slab dynamics. Geochemistry, Geophysics, Geosystems, 8(8).

Billen, M. I. (2008). Modeling the dynamics of subducting slabs. Annual Review of Earth and Planetary Sciences, 36(1), 325-356.

Boschman, L. M. (2021). Andean mountain building since the Late Cretaceous: A paleoelevation reconstruction. Earth-Science Reviews, 103640.

Boutoux, A., Briaud, A., Faccenna, C., Ballato, P., Rossetti, F., & Blanc, E. (2021). Slab folding and surface deformation of the Iran mobile belt. Tectonics, 40(6), e2020TC006300.

Bovy, B. (2021). fastscape-lem/fastscape : Release v0.1.0beta3. Zenodo. https://doi.org/10.5281/zenodo.4435110

Braun, J., & Willett, S. D. (2013). A very efficient O (n), implicit and parallel method to solve the stream power equation governing fluvial incision and landscape evolution. Geomorphology, 180, 170-179.

Briaud, A., Agrusta, R., Faccenna, C., Funiciello, F., & van Hunen, J. (2020). Topographic Fingerprint of Deep Mantle Subduction. Journal of Geophysical Research: Solid Earth, 125(1), e2019JB017962. https://doi.org/10.1029/2019JB017962

Brizzi, S., van Zelst, I., Funiciello, F., Corbi, F., & van Dinther, Y. (2020). How Sediment Thickness Influences Subduction Dynamics and Seismicity. Journal of Geophysical Research: Solid Earth, 125(8), e2019JB018964. https://doi.org/10.1029/2019JB018964

Brocher, T. (2005). Empirical relations between elastic waves peeds and density in the Earth's crust. Bull Seismol Soc Am, 95(6), 2081-2092. https://doi.org/10.1785/0120050077

Broens, S., & Pereira, D. M. (2005). Evolución estructural de la zona de transición entre las fajas plegadas y corridas de Aconcagua y Malargüe Provincia de Mendoza. Revista de la Asociación Geológica Argentina, 60(4), 685-695.

Burchfiel, B. C., & DAVIS, G. A. (1976). Compression and crustal shortening in Andean-type orogenesis. Nature, 260(5553), 693-694.

Buiter, S. J., Govers, R., & Wortel, M. J. R. (2001). A modelling study of vertical surface displacements at convergent plate margins. Geophysical Journal International, 147(2), 415-427.

Calignano, E., Sokoutis, D., Willingshofer, E., Gueydan, F., & Cloetingh, S. (2015). Strain localization at the margins of strong lithospheric domains : Insights from analog models. Tectonics, 34(3), 396-412. https://doi.org/10.1002/2014TC003756

Capitanio, F. A., Morra, G., & Goes, S. (2007). Dynamic models of downgoing plate-buoyancy driven subduction: Subduction motions and energy dissipation. Earth and Planetary Science Letters, 262(1-2), 284-297.

Capitanio, F. A., Stegman, D. R., Moresi, L. N., & Sharples, W. (2010). Upper plate controls on deep subduction, trench migrations and deformations at convergent margins. Tectonophysics, 483(1-2), 80-92.

Capitanio, F. A., Faccenna, C., Zlotnik, S., & Stegman, D. R. (2011). Subduction dynamics and the origin of Andean orogeny and the Bolivian orocline. Nature, 480(7375), 83-86.

Casquet, C., Dahlquist, J. A., Verdecchia, S. O., Baldo, E. G., Galindo, C., Rapela, C. W., Pankhurst, R. J., Morales, M. M., Murra, J. A., & Mark Fanning, C. (2018). Review of the Cambrian Pampean orogeny of Argentina; a displaced orogen formerly attached to the Saldania Belt of South Africa? Earth-Science Reviews, 177, 209-225. https://doi.org/10.1016/j.earscirev.2017.11.013

Cermak, V., & Rybach, L. (1982). 4.1.1 Introductory remarks. In G. Angenheister (Éd.), Subvolume A: Vol. c (p. 305-310). Springer-Verlag. https://doi.org/10.1007/10201894_62

Cerpa, N. G., Hassani, R., Gerbault, M., & Prévost, J. H. (2014). A fictitious domain method for lithosphere-asthenosphere interaction: Application to periodic slab folding in the upper mantle. Geochemistry, Geophysics, Geosystems, 15(5), 1852-1877.

Cerpa, N. G., Araya, R., Gerbault, M., & Hassani, R. (2015). Relationship between slab dip and topography segmentation in an oblique subduction zone : Insights from numerical modeling. Geophysical Research Letters, 42(14), 5786-5795. https://doi.org/10.1002/2015GL064047

Chen, W.-P., & Molnar, P. (1983). Focal depths of intracontinental and intraplate earthquakes and their implications for the thermal and mechanical properties of the lithosphere. Journal of Geophysical Research: Solid Earth, 88(B5), 4183-4214. https://doi.org/10.1029/JB088iB05p04183

Chen, Y. W., Wu, J., & Suppe, J. (2019). Southward propagation of Nazca subduction along the Andes. Nature, 565(7740), 441–447. https://doi.org/10.1038/S41586-018-0860-1

Christensen, U. R., & Hofmann, A. W. (1994). Segregation of subducted oceanic crust in the convecting mantle. Journal of Geophysical Research: Solid Earth, 99(B10), 19867-19884.

Christensen, N. I., & Mooney, W. D. (1995). Seismic velocity structure and composition of the continental crust : A global view. Journal of Geophysical Research: Solid Earth, 100(B6), 9761-9788. https://doi.org/10.1029/95JB00259

Čížková, H., & Bina, C. R. (2013). Effects of mantle and subduction-interface rheologies on slab stagnation and trench rollback. Earth and Planetary Science Letters, 379, 95-103. https://doi.org/10.1016/j.epsl.2013.08.011

Conrad, C. P., & Hager, B. H. (1999). Effects of plate bending and fault strength at subduction zones on plate dynamics. Journal of Geophysical Research: Solid Earth, 104(B8), 17551-17571.

Contreras-Reyes, E., Grevemeyer, I., Flueh, E. R., & Reichert, C. (2008). Upper lithospheric structure of the subduction zone offshore of southern Arauco peninsula, Chile, at ∼38°S. Journal of Geophysical Research, 113(B7), B07303. https://doi.org/10.1029/2007JB005569

Cordani, U., Pimentel, M., Ganade, C., & Fuck, R. (2013). The significance of the Transbrasiliano-Kandi tectonic corridor for the amalgamation of West Gondwana. Brazilian Journal of Geology, 43, 583-597. https://doi.org/10.5327/Z2317-48892013000300012

Cosentino*, N. J., Aron, F., Crempien, J. G. F., & Jordan, T. E. (2018). Role of subducted sediments in plate interface dynamics as constrained by Andean forearc (paleo)topography. https://doi.org/10.1130/2018.2540(03)

Costa, C. H., Morla, P. N., Hauria, N. U., & Garro, H. E. (2019). The structural framework of an intermountain basin in the Pampean Ranges of Argentina; the Conlara depression. Journal of South American Earth Sciences, 96, 102387. https://doi.org/10.1016/j.jsames.2019.102387

Costa, C., Alvarado, A., Audemard, F., Audin, L., Benavente, C., Bezerra, F. H., Cembrano, J., González, G., López, M., Minaya, E., Santibañez, I., Garcia, J., Arcila, M., Pagani, M., Pérez, I., Delgado, F., Paolini, M., & Garro, H. (2020). Hazardous faults of South America; compilation and overview. Journal of South American Earth Sciences, 104, 102837. https://doi.org/10.1016/j.jsames.2020.102837

Cristallini, E. O., & Ramos, V. A. (2000). Thick-skinned and thin-skinned thrusting in the La Ramada fold and thrust belt. Tectonophysics, 317(3-4), 205-235. https://doi.org/10.1016/s0040-1951(99)00276-0

Dai, L., Wang, L., Lou, D., Li, Z.-H., Dong, H., Ma, F., Li, F., Li, S., & Yu, S. (2020). Slab Rollback Versus Delamination: Contrasting Fates of Flat-Slab Subduction and Implications for South China Evolution in the Mesozoic. Journal of Geophysical Research: Solid Earth, 125(4), e2019JB019164. https://doi.org/10.1029/2019JB019164

Dannberg, J., & Sobolev, S. V. (2015). Low-buoyancy thermochemical plumes resolve controversy of classical mantle plume concept. Nature communications, 6(1), 1-9.

Dávila, F. M., & Lithgow-Bertelloni, C. (2008). Dynamic topography during flat-slab subduction: a first approach in the south-central andes. In 7th International Symposium on Andean Geodynamics, Nice, Francia. CD.

Dávila, F. M., & Lithgow-Bertelloni, C. (2013). Dynamic topography in South America. Journal of South American Earth Sciences, 43, 127-144.

Decelles, P. G., Ducea, M. N., Kapp, P., & Zandt, G. (2009). Cyclicity in Cordilleran orogenic systems. Nature Geoscience, 2(4), 251–257. https://doi.org/10.1038/NGEO469

DeCelles, P. G., Zandt, G., Beck, S. L., Currie, C. A., Ducea, M. N., Kapp, P., ... & Schoenbohm, L. M. (2014). Cyclical orogenic processes in the Cenozoic central Andes. Geological Society of America Memoirs, 212, MWR212-22.

Del Papa, C., Hongn, F., Powell, J., Payrola, P., Do Campo, M., Strecker, M. R., Petrinovic, I., Schmitt, A. K., & Pereyra, R. (2013). Middle Eocene-Oligocene broken-foreland evolution in the Andean Calchaqui Valley, NW Argentina : Insights from stratigraphic, structural and provenance studies. Basin Research, 25(5), 574-593. https://doi.org/10.1111/BRE.12018

De Silva, S. L., & Kay, S. M. (2018). Turning up the heat: high-flux magmatism in the Central Andes. Elements: An International Magazine of Mineralogy, Geochemistry, and Petrology, 14(4), 245-250.

Dingwell, D. B., Hess, K.-U., & Knoche, R. (1996). Granite and granitic pegmatite melts: Volumes and viscosities. Earth and Environmental Science Transactions of The Royal Society of Edinburgh, 87(1–2), 65–72. https://doi.org/10.1017/S0263593300006489

Dziewonski, A. M., & Anderson, D. L. (1981). Preliminary reference Earth model. Physics of the Earth and Planetary Interiors, 25(4), 297–356. https://doi.org/10.1016/0031-9201(81)90046-7

Eisermann, J. O., Göllner, P. L., & Riller, U. (2021). Orogen-scale transpression accounts for GPS velocities and kinematic partitioning in the Southern Andes. Communications Earth & Environment, 2(1), 167. https://doi.org/10.1038/s43247-021-00241-4

Eisermann, J. O., Göllner, P. L., & Riller, U. (2021). Orogen-scale transpression accounts for GPS velocities and kinematic partitioning in the Southern Andes. Communications Earth & Environment, 2(1), 167. https://doi.org/10.1038/s43247-021-00241-4

Erdős, Z., Huismans, R. S., & van der Beek, P. (2015). First-order control of syntectonic sedimentation on crustal-scale structure of mountain belts. Journal of Geophysical Research: Solid Earth, 120(7), 5362-5377. https://doi.org/10.1002/2014JB011785

Erdős, Z., Huismans, R. S., Faccenna, C., & Wolf, S. G. (2021). The role of subduction interface and upper plate strength on back-arc extension: Application to Mediterranean back-arc basins. Tectonics, 40(8), e2021TC006795.

Erslev, E., & Koenig, N. (2009). Three-dimensional kinematics of Laramide, basement-involved Rocky Mountain deformation, USA : Insights from minor faults and GIS-enhanced structure maps. Geological Society of America Memoirs, 204, 125-150. https://doi.org/10.1130/2009.1204(06)

Espurt, N., Funiciello, F., Martinod, J., Guillaume, B., Regard, V., Faccenna, C., & Brusset, S. (2008). Flat subduction dynamics and deformation of the South American plate: Insights from analog modeling. Tectonics, 27(3).

Fuentes, B. H., D. Starck, A. Boll. (2016). Structure and tectonic evolution of hybrid thick- and thin-skinned systems in the Malargüe fold-thrust belt, Neuquén basin, Argentina. Geol Mag, 153(5-6), 1066-1084. https://doi.org/10.1017/s0016756816000583

Faccenda, M., & Dal Zilio, L. (2017). The role of solid–solid phase transitions in mantle convection. Lithos, 268–271, 198–224. https://doi.org/10.1016/j.lithos.2016.11.007

Faccenna, C., Heuret, A., Funiciello, F., Lallemand, S., & Becker, T. W. (2007). Predicting trench and plate motion from the dynamics of a strong slab. Earth and Planetary Science Letters, 257(1-2), 29-36.

Faccenna, C., Oncken, O., Holt, A. F., & Becker, T. W. (2017). Initiation of the Andean orogeny by lower mantle subduction. Earth and Planetary Science Letters, 463, 189–201. https://doi.org/10.1016/J.EPSL.2017.01.041

Faccenna, C., Becker, T. W., Holt, A. F., & Brun, J. P. (2021). Mountain building, mantle convection, and supercontinents : Holmes (1931) revisited. Earth and Planetary Science Letters, 564.

Fairhead, J. D., & Maus, S. (2003). CHAMP satellite and terrestrial magnetic data help define the tectonic model for South America and resolve the lingering problem of the pre-break-up fit of the South Atlantic Ocean. The Leading Edge, 22(8), 779-783. https://doi.org/10.1190/1.1605081

Fennell, L. M., Iannelli, S. B., Encinas, A., Naipauer, M., Valencia, V., & Folguera, A. (2019). Alternating contraction and extension in the Southern Central Andes (35°–37°S). American Journal of Science, 319(5), 381-429. https://doi.org/10.2475/05.2019.02

Folguera, A., & Zárate, M. (2009). La sedimentación neógena continental en el sectorextrandino de Argentina central. Revista de la Asociación Geológica Argentina, 64(4), 692-712.

Folguera, A., & Zárate, M. (2011). Neogene sedimentation in the Argentine foreland between 34 30'S and 41 S and its relation to the Andes evolution. Cenozoic Geology of the Central Andes of Argentina. SCS Publisher, Salta, 123-134.

Folguera, A., Naranjo, J. A., Orihashi, Y., Sumino, H., Nagao, K., Polanco, E., & Ramos, V. A. (2009). Retroarc volcanism in the northern San Rafael Block (34°-35°30'S), southern Central Andes : Occurrence, age, and tectonic setting. Journal of Volcanology and Geothermal Research, 186(3-4), 169-185. https://doi.org/10.1016/J.JVOLGEORES.2009.06.012

Fraters, M. (2014). Thermo-mechanically coupled subduction modelling with ASPECT. August. https://dspace.library.uu.nl/handle/1874/297347

Funiciello, F., Faccenna, C., Heuret, A., Lallemand, S., Di Giuseppe, E., & Becker, T. W. (2008). Trench migration, net rotation and slab-mantle coupling. Earth and Planetary Science Letters, 271(1–4), 233–240. https://doi.org/10.1016/J.EPSL.2008.04.006

Gans, C. R., Beck, S. L., Zandt, G., Gilbert, H., Alvarado, P., Anderson, M., & Linkimer, L. (2011). Continental and oceanic crustal structure of the Pampean flat-slab region, western Argentina, using receiver function analysis: new high-resolution results. Geophysical Journal International, 186(1), 45-58.

Gao, Y., Tilmann, F., van Herwaarden, D. P., Thrastarson, S., Fichtner, A., Heit, B., ... & Schurr, B. D. (2021). Full Waveform Inversion beneath the Central Andes: Insight into the dehydration of the Nazca slab and delamination of the back-arc lithosphere. Earth and Space Science Open Archive ESSOAr.

García, H. P. (2001). Basement-cored uplift deformation in the northern Sierras Pampeanas : Three-dimensional uplift structure, basement deformation, and regional analysis. https://repository.arizona.edu/handle/10150/280775

Garfunkel, Z., Anderson, C. A., & Schubert, G. (1986). Mantle circulation and the lateral migration of subducted slabs. Journal of Geophysical Research: Solid Earth, 91(B7), 7205-7223.

Garzione, C. N., Molnar, P., Libarkin, J. C., & MacFadden, B. J. (2006). Rapid late Miocene rise of the Bolivian Altiplano: Evidence for removal of mantle lithosphere. Earth and Planetary Science Letters, 241(3–4), 543–556. https://doi.org/10.1016/J.EPSL.2005.11.026

Garzione, C. N., Hoke, G. D., Libarkin, J. C., Withers, S., MacFadden, B., Eiler, J., Ghosh, P., & Mulch, A. (2008). Rise of the Andes. Science, 320(5881), 1304–1307. https://doi.org/10.1126/SCIENCE.1148615

Garzione, C. N., McQuarrie, N., Perez, N. D., Ehlers, T. A., Beck, S. L., Kar, N., Eichelberger, N., Chapman, A. D., Ward, K. M., Ducea, M. N., Lease, R. O., Poulsen, C. J., Wagner, L. S., Saylor, J. E., Zandt, G., & Horton, B. K. (2017). Tectonic Evolution of the Central Andean Plateau and Implications for the Growth of Plateaus. Annual Review of Earth and Planetary Sciences, 45(1), 529–559. https://doi.org/10.1146/annurev-earth-063016-020612

Gerbault, M., Cembrano, Mpodozis, J., Farias, C., & Pardo M, M. (2009). Continental Margin Deformation along the Andean Subduction zone: Thermomechanical Models. Physics of the Earth and Planetary Interiors, 177(3–4), 180. https://doi.org/10.1016/j.pepi.2009.09.001

Gerya, T. V., Fossati, D., Cantieni, C., & Seward, D. (2009). Dynamic effects of aseismic ridge subduction: numerical modelling. European Journal of Mineralogy, 21(3), 649-661.

Gerya, T. (2019). Introduction to Numerical Geodynamic Modelling (2nd ed.). Cambridge University Press. https://doi.org/10.1017/9781316534243

Giambiagi, L. B., Ramos, V. A., Godoy, E., Alvarez, P. P., & Orts, S. (2003). Cenozoic deformation and tectonic style of the Andes, between 33° and 34° south latitude. Tectonics, 22(4), n/a-n/a. https://doi.org/10.1029/2001TC001354

Giambiagi, L., Mescua, J., Bechis, F., Tassara, A., & Hoke, G. (2012). Thrust belts of the southern Central Andes : Along-strike variations in shortening, topography, crustal geometry, and denudation. Bulletin of the Geological Society of America, 124(7-8), 1339-1351. https://doi.org/10.1130/B30609.1

Giambiagi, L., Mescua, J., Heredia, N., Farías, P., García-Sansegundo, J., Fernández, C., Stier, C., Pérez, D., Bechis, F., Moreiras, M., & Lossada, A. (2014). Reactivation of Paleozoic structures during Cenozoic deformation in the Cordón del Plata and Southern Precordillera ranges (Mendoza, Argentina). Journal of Iberian Geology, 40(2). https://doi.org/10.5209/rev_JIGE.2014.v40.n2.45302

Giambiagi, L., Álvarez, P. P., Creixell, C., Mardonez, D., Murillo, I., Velásquez, R., Lossada, A., Suriano, J., Mescua, J., & Barrionuevo, M. (2017). Cenozoic Shift From Compression to Strike-Slip Stress Regime in the High Andes at 30°S, During the Shallowing of the Slab : Implications for the El Indio/Tambo Mineral District. Tectonics, 36(11), 2714-2735. https://doi.org/10.1002/2017TC004608

Giambiagi, L., Tassara, A., Echaurren, A., Julve, J., Quiroga, R., Barrionuevo, M., ... & Lothari, L. (2022). Crustal anatomy and evolution of a subduction-related orogenic system: Insights from the Southern Central Andes (22-35° S). Earth-Science Reviews, 104138.

Gilbert, H., Beck, S., & Zandt, G. (2006). Lithospheric and upper mantle structure of central Chile and Argentina. Geophysical Journal International, 165(1), 383-398. https://doi.org/10.1111/J.1365-246X.2006.02867.X

Gibert, G., Gerbault, M., Hassani, R., & Tric, E. (2012). Dependency of slab geometry on absolute velocities and conditions for cyclicity: insights from numerical modelling. Geophysical Journal International, 189(2), 747-760.

Gleason, G. C., & Tullis, J. (1995). A flow law for dislocation creep of quartz aggregates determined with the molten salt cell. Tectonophysics, 247(1–4), 1–23. https://doi.org/10.1016/0040-1951(95)00011-B

Glerum, A., Thieulot, C., Fraters, M., Blom, C., & Spakman, W. (2018). Nonlinear viscoplasticity in ASPECT: benchmarking and applications to subduction. Solid Earth, 9(2), 267-294.

Goes, S., Govers, R., & Vacher, P. (2000). Shallow mantle temperatures under Europe from P and S wave tomography. Journal of Geophysical Research: Solid Earth, 105(B5), 11153-11169. https://doi.org/10.1029/1999JB900300

Goetze, C., & Evans, B. (1979). Stress and temperature in the bending lithosphere as constrained by experimental rock mechanics. Geophysical Journal of the Royal Astronomical Society, 59(3), 463-478. https://doi.org/10.1111/J.1365-246X.1979.TB02567.X

González, G., Cembrano, J., Carrizo, D., Macci, A., & Schneider, H. (2003). The link between forearc tectonics and Pliocene–Quaternary deformation of the Coastal Cordillera, northern Chile. Journal of South American Earth Sciences, 16(5), 321-342. https://doi.org/10.1016/S0895-9811(03)00100-7

Gripp, A. E., & Gordon, R. G. (2002). Young tracks of hotspots and current plate velocities. Geophysical Journal International, 150(2), 321-361.

Gutiérrez, A. A., Mon, R., Sàbat, F., & Iaffa, D. N. (2017). Origin and Evolution of the Salinas Grandes and Salina De Ambargasta, Argentina. IOP Conference Series: Earth and Environmental Science, 95, 022036. https://doi.org/10.1088/1755-1315/95/2/022036

Gutscher, M. A., Spakman, W., Bijwaard, H., & Engdahl, E. R. (2000). Geodynamics of flat subduction : Seismicity and tomographic constraints from the Andean margin. Tectonics, 19(5), 814-833. https://doi.org/10.1029/1999TC001152

Gutscher, M. A. (2002). Andean subduction styles and their effect on thermal structure and interplate coupling. Journal of South American Earth Sciences, 15(1), 3-10. https://doi.org/10.1016/S0895-9811(02)00002-0

Gutscher, M.-A. (2018). Scraped by flat-slab subduction. Nature Geoscience, 11(12), 889 890. https://doi.org/10.1038/s41561-018-0264-8

Haberland, C., Rietbrock, A., Schurr, B., & Brasse, H. (2003). Coincident anomalies of seismic attenuation and electrical resistivity beneath the southern Bolivian Altiplano plateau. Geophysical Research Letters, 30(18), 1–4. https://doi.org/10.1029/2003GL017492

Hackney, R., Echtler, H., Franz, G., Götze, H.-J., Lucassen, F., Marchenko, D., Melnick, D., Meyer, U., Schmidt, S., Alasonati Tasarova, Z., Tassara, A., & Wienecke, S. (2006). The Segmented Overriding Plate and Coupling at the South-Central Chilean Margin (36–42°S) (p. 355-374). https://doi.org/10.1007/978-3-540-48684-8_17

Hamza, V. M., Dias, F. J. S. S., Gomes, A. J. L., & Terceros, Z. G. D. (2005). Numerical and functional representations of regional heat flow in South America. Physics of the Earth and Planetary Interiors, 152(4), 223–256. https://doi.org/10.1016/j.pepi.2005.04.009

Hamza, V. M., & Vieira, F. P. (2012). Global distribution of the lithosphere-asthenosphere boundary : A new look. Solid Earth, 3(2), 199-212. https://doi.org/10.5194/se-3-199-2012

Haschke, M. R., Scheuber, E., Günther, A., & Reutter, K. J. (2002). Evolutionary cycles during the Andean orogeny: repeated slab breakoff and flat subduction?. Terra nova, 14(1), 49-55.

Hasterok, D., & Chapman, D. (2011). Heat production and geotherms for the continental lithosphere. Earth and Planetary Science Letters, 307(1-2), 59-70. https://doi.org/10.1016/j.epsl.2011.04.034

Hayes, G. P., Moore, G. L., Portner, D. E., Hearne, M., Flamme, H., Furtney, M., & Smoczyk, G. M. (2018). Slab2, a comprehensive subduction zone geometry model. Science, 362(6410), 58-61. https://doi.org/10.1126/science.aat4723

He, L., Hu, S., Huang, S., Yang, W., Wang, J., Yuan, Y., & Yang, S. (2008). Heat flow study at the Chinese Continental Scientific Drilling site : Borehole temperature, thermal conductivity, and radiogenic heat production. Journal of Geophysical Research, 113(B2), B02404. https://doi.org/10.1029/2007JB004958

Heister, T., Dannberg, J., Gassmöller, R., & Bangerth, W. (2017). High accuracy mantle convection simulation through modern numerical methods—II: Realistic models and problems. Geophysical Journal International, 210(2), 833–851. https://doi.org/10.1093/GJI/GGX195

Hertgen, S., Yamato, P., Guillaume, B., Magni, V., Schliffke, N., & van Hunen, J. (2020). Influence of the thickness of the overriding plate on convergence zone dynamics. Geochemistry, Geophysics, Geosystems, 21(2), e2019GC008678.

Heuret, A., Funiciello, F., Faccenna, C., & Lallemand, S. (2007). Plate kinematics, slab shape and back-arc stress: a comparison between laboratory models and current subduction zones. Earth and Planetary Science Letters, 256(3-4), 473-483.

Heuret, A., Conrad, C. P., Funiciello, F., Lallemand, S., & Sandri, L. (2012). Relation between subduction megathrust earthquakes, trench sediment thickness and upper plate strain. Geophysical Research Letters, 39, L05304. https://doi.org/10.1029/2011GL050712

Hindle, D., Kley, J., Oncken, O., & Sobolev, S. (2005). Crustal balance and crustal flux from shortening estimates in the Central Andes. Earth and Planetary Science Letters, 230(1–2), 113–124. https://doi.org/10.1016/J.EPSL.2004.11.004

Hirth, G., & Kohlstedt, D. (2004). Rheology of the upper mantle and the mantle wedge: A view from the experimentalists. Geophysical Monograph Series, 138, 83–105. https://doi.org/10.1029/138GM06

Hoke, G. D., Giambiagi, L. B., Garzione, C. N., Mahoney, J. B., & Strecker, M. R. (2014). Neogene paleoelevation of intermontane basins in a narrow, compressional mountain range, southern Central Andes of Argentina. Earth and Planetary Science Letters, 406, 153-164. https://doi.org/10.1016/j.epsl.2014.08.032

Holt, A. F., Becker, T. W., & Buffett, B. A. (2015). Trench migration and overriding plate stress in dynamic subduction models. Geophysical Journal International, 201(1), 172–192. https://doi.org/10.1093/GJI/GGV011

Hongn, F., Papa, C. del, Powell, J., Petrinovic, I., Mon, R., & Deraco, V. (2007). Middle Eocene deformation and sedimentation in the Puna-Eastern Cordillera transition (23°-26°S) : Control by preexisting heterogeneities on the pattern of initial Andean shortening. Geology, 35(3), 271-274. https://doi.org/10.1130/G23189A.1

Horton, B. (2016). Andean stratigraphic record of the transition from backarc extension to orogenic shortening : A case study from the northern Neuquén Basin, Argentina. J. South Am. Earth Sci., 71, 17-40. https://doi.org/10.1016/j.jsames.2016.06.003

Horton, B. (2018). Tectonic regimes of the Central and Southern Andes: Responses to variations in plate coupling during subduction. Tectonics, 37(2), 402–429. https://doi.org/10.1002/2017tc004624

Horton, B. K. (2018). Sedimentary record of Andean mountain building. Earth-Science Reviews, 178, 279-309. https://doi.org/10.1016/J.EARSCIREV.2017.11.025

Horton, B. K., & Folguera, A. (2022). Chapter 1—Tectonic inheritance and structural styles in the Andean fold-thrust belt and foreland basin. In G. Zamora & A. Mora (Éds.), Andean Structural Styles (p. 3-28). Elsevier. https://doi.org/10.1016/B978-0-323-85175-6.00001-8

Hu, J., & Gurnis, M. (2020). Subduction Duration and Slab Dip. Geochemistry, Geophysics, Geosystems, 21(4), e2019GC008862. https://doi.org/10.1029/2019GC008862

Hu, J., Liu, L., & Gurnis, M. (2021). Southward expanding plate coupling due to variation in sediment subduction as a cause of Andean growth. Nature communications, 12(1), 1-9.

Huangfu, P., Wang, Y., Cawood, P. A., Li, Z. H., Fan, W., & Gerya, T. V. (2016). Thermo-mechanical controls of flat subduction: Insights from numerical modeling. Gondwana Research, 40(December), 170–183. https://doi.org/10.1016/j.gr.2016.08.012

Husson, L., Conrad, C. P., & Faccenna, C. (2008). Tethyan closure , Andean orogeny , and westward drift of the Paci fi c Basin. 271, 303-310. https://doi.org/10.1016/j.epsl.2008.04.022

Husson, L., Conrad, C. P., & Faccenna, C. (2012). Plate motions, Andean orogeny, and volcanism above the South Atlantic convection cell. Earth and Planetary Science Letters, 317–318, 126–135. https://doi.org/10.1016/j.epsl.2011.11.040

Husson, L. (2012). Trench migration and upper plate strain over a convecting mantle. Physics of the Earth and Planetary Interiors, 212, 32-43.

Ibarra, F., & Prezzi, C. B. (2019). The thermo-mechanical state of the andes in the altiplano-puna region: Insights from curie isotherm and effective elastic thickness determination. Revista de La Asociacion Geologica Argentina, 76(4), 352–362.

Ibarra, F., Liu, S., Meeßen, C., Prezzi, C. B., Bott, J., Scheck-Wenderoth, M., Sobolev, S., & Strecker, M. R. (2019). 3D data-derived lithospheric structure of the Central Andes and its implications for deformation: Insights from gravity and geodynamic modelling. Tectonophysics, 766(February), 453–468. https://doi.org/10.1016/j.tecto.2019.06.025

Ibarra, F., Meeßen, C., Liu, S., Prezzi, C., & Sippel, J. (2018). Density structure and rheology of northern Argentina : From the Central Andes to the foreland basin. 20(April), 16756-16756.

Ibarra, F., Prezzi, C. B., Bott, J., Scheck-Wenderoth, M., & Strecker, M. R. (2021). Distribution of Temperature and Strength in the Central Andean Lithosphere and Its Relationship to Seismicity and Active Deformation. Journal of Geophysical Research: Solid Earth, 126(5). https://doi.org/10.1029/2020JB021231

Introcaso, A., & Ruiz, F. (2001). Geophysical indicators of Neogene strike-slip faulting in the Desaguadero–Bermejo tectonic lineament (northwestern Argentina). Journal of South American Earth Sciences, 14(7), 655-663. https://doi.org/10.1016/S0895-9811(01)00057-8

Isacks, B., Jordan, T., Allmendinger, R., & Ramos, V. (1982). La segmentación tectónica de los Andes Centrales y su relación con la Placa de Nazca subductada. Congreso Latinoamericano de Geología, 5, 587-606.

Isacks, B. (1988). Uplift of the Central Andean Plateau and bending of the Bolivian Orocline. J Geophys Res, 93(B4), 3211. https://doi.org/10.1029/jb093ib04p03211

James, D. E., & Sacks, I. S. (1999). Cenozoic formation of the Central Andes: A geophysical perspective.

Jammes, S., & Huismans, R. S. (2012). Structural styles of mountain building : Controls of lithospheric rheologic stratification and extensional inheritance. Journal of Geophysical Research: Solid Earth, 117(B10). https://doi.org/10.1029/2012JB009376

Japas, M. S., & Ré, G. H. (2012). Neogene tectonic block rotations and margin curvature at the Pampean flat-slab segment (28o-33o SL, Argentina). Geoacta, 37(1), 01-04.

Japas, M. S., Ré, G. H., Oriolo, S., & Vilas, J. F. (2016). Basement-involved deformation overprinting thin-skinned deformation in the Pampean flat-slab segment of the southern Central Andes, Argentina. Geological Magazine, 153(5-6), 1042-1065. https://doi.org/10.1017/S001675681600056X

Japas, M. S., Ré, G. H., Oriolo, S., & Vilas, J. F. (2016). Palaeomagnetic data from the Precordillera fold and thrust belt constraining Neogene foreland evolution of the Pampean flat-slab segment (Central Andes, Argentina). Geological Society, London, Special Publications, 425(1), 81-105. https://doi.org/10.1144/SP425.9

Jensen, E. (2018). Efectos de fluidos hidrotermales en el desarrollo de fallas : Petrografía y propiedades mecánicas [PhD Dissertation, Universidad Católica del Norte]. https://doi.org/10.13140/RG.2.2.34341.35049

Jones, R. E., Kirstein, L. A., Kasemann, S. A., Litvak, V. D., Poma, S., Alonso, R. N., & Hinton, R. (2016). The role of changing geodynamics in the progressive contamination of Late Cretaceous to Late Miocene arc magmas in the southern Central Andes. Lithos, 262, 169-191.

Jordan, T. E., Isacks, B. L., Ramos, V. A., & Allmendinger, R. W. (1983). Mountain building in the central Andes. Episodes, 1983(3), 20-26. https://doi.org/10.18814/EPIIUGS/1983/V6I3/005

Jordan, T. E., Ramos, V. A. ,. Allmendinger, R. W. ,. &. Isacks, B. L. (1984). Andean tectonics related to geometry of subducted Nazca plate : Discussion and reply : Reply. July, 877 880. https://doi.org/10.1130/0016-7606(1984)95<877

Jordan, T. E., & Allmendinger, R. W. (1986). The Sierras Pampeanas of Argentina : A modern analogue of Rocky Mountain foreland deformation. American Journal of Science, 286(10), 737-764. https://doi.org/10.2475/AJS.286.10.737

Jordan, T. E., Allmendinger, R. W., Damanti, J. F., & Drake, R. E. (1993). Chronology of motion in a complete thrust belt : The Precordillera, 30-31°S, Andes Mountains. Journal of Geology, 101(2), 135-156. https://doi.org/10.1086/648213

Kay, S. M., Maksaev, V., Moscoso, R., Mpodozis, C., & Nasi, C. (1987). Probing the evolving Andean Lithosphere : Mid-Late Tertiary magmatism in Chile (29°–30°30'S) over the modern zone of subhorizontal subduction. Journal of Geophysical Research: Solid Earth, 92(B7), 6173-6189. https://doi.org/10.1029/JB092iB07p06173

Kay, S. M. (1991). Magma source variations for mid-late Tertiary magmatic rocks associated with a shallowing subduction zone and a thickening crust in the central Andes (28 to 33°S). pecial Paper of the Geological Society of America, 265, 113-137. http://dx.doi.org/10.1130/SPE265-p113

Kay, R. W., & Kay, M. S. (1993). Delamination and delamination magmatism. Tectonophysics, 219(1–3), 177–189. https://doi.org/10.1016/0040-1951(93)90295-U

Kay, S. M., & Abbruzzi, J. M. (1996). Magmatic evidence for Neogene lithospheric evolution of the central Andean « flat-slab » between 30°S and 32°S. Tectonophysics, 259(1-3 SPEC. ISS.), 15-28. https://doi.org/10.1016/0040-1951(96)00032-7

Kay, S. M., & Mpodozis, C. (2002). Magmatism as a probe to the Neogene shallowing of the Nazca plate beneath the modern Chilean flat-slab. Journal of South American Earth Sciences, 15(1), 39-57.

Kay, S. M., Godoy, E., & Kurtz, A. (2005). Episodic arc migration, crustal thickening, subduction erosion, and magmatism in the south-central Andes. Bulletin of the Geological Society of America, 117(1-2), 67-88. https://doi.org/10.1130/B25431.1

Kay, S. M., & Coira, B. L. (2009). Shallowing and steepening subduction zones, continental lithospheric loss, magmatism, and crustal flow under the Central Andean Altiplano-Puna Plateau.

Kincaid, C., & Olson, P. (1987). An experimental study of subduction and slab migration. Journal of Geophysical Research: Solid Earth, 92(B13), 13832-13840.

Kley, J. (1996). Transition from basement-involved to thin-skinned thrusting in the Cordillera Oriental of southern Bolivia. Tectonics, 15(4), 763-775. https://doi.org/10.1029/95TC03868Kley, J. (1999). Geologic and geometric constraints on a kinematic model of the Bolivian orocline. Journal of South American Earth Sciences, 12(2), 221-235. https://doi.org/10.1016/S0895-9811(99)00015-2

Kley, J., & Monaldi, C. R. (1998). Tectonic shortening and crustal thickness in the Central Andes: How good is the correlation?. Geology, 26(8), 723-726.

Kley, J., Monaldi, C. R., & Salfity, J. A. (1999). Along-strike segmentation of the Andean foreland: Causes and consequences. Tectonophysics, 301(1–2), 75–94. https://doi.org/10.1016/S0040-1951(98)90223-2

Kley, J., & Monaldi, C. R. (2002a). Tectonic inversion in the Santa Barbara System of the central Andean foreland thrust belt, northwestern Argentina. Tectonics, 21(6), 11-1-11-18. https://doi.org/10.1029/2002TC902003

Klotz, J., Abolghasem, A., Khazaradze, G., Heinze, B., Vietor, T., Hackney, R., ... & Perdomo, R. (2006). Long-term signals in the present-day deformation field of the Central and Southern Andes and constraints on the viscosity of the Earth's upper mantle. In The Andes (pp. 65-89). Springer, Berlin, Heidelberg.

Kooi, H., & Beaumont, C. (1994). Escarpment evolution on high-elevation rifted margins: Insights derived from a surface processes model that combines diffusion, advection, and reaction. Journal of Geophysical Research: Solid Earth, 99(B6), 12191-12209.

Kronbichler, M., Heister, T., & Bangerth, W. (2012). High accuracy mantle convection simulation through modern numerical methods. Geophysical Journal International, 191(1), 12–29. https://doi.org/10.1111/J.1365-246X.2012.05609.X

Lallemand, S., Heuret, A., & Boutelier, D. (2005). On the relationships between slab dip, back-arc stress, upper plate absolute motion, and crustal nature in subduction zones. Geochemistry, Geophysics, Geosystems, 6(9). https://doi.org/10.1029/2005GC000917

Lallemand, S., Heuret, A., Faccenna, C., & Funiciello, F. (2008). Subduction dynamics as revealed by trench migration. Tectonics, 27(3). https://doi.org/10.1029/2007TC002212

Lamb, S., & Davis, P. (2003). Cenozoic climate change as a possible cause for the rise of the Andes. Nature, 425(6960), 792–797. https://doi.org/10.1038/NATURE02049

Lee, C., & King, S. (2011). Dynamic buckling of subducting slabs reconciles geological and geophysical observations. https://doi.org/10.1016/J.EPSL.2011.10.033

Leier, A., McQuarrie, N., Garzione, C., & Eiler, J. (2013). Stable isotope evidence for multiple pulses of rapid surface uplift in the Central Andes, Bolivia. Earth and Planetary Science Letters, 371–372, 49–58. https://doi.org/10.1016/j.epsl.2013.04.025

Lentas, K., Di Giacomo, D., Harris, J., and Storchak, D. A. (2019). The ISC Bulletin as a comprehensive source of earthquake source mechanisms, Earth Syst. Sci. Data, 11, 565-578, doi: https://doi.org/10.5194/essd-11-565-2019

Levina, M., Horton, B. K., Fuentes, F., & Stockli, D. F. (2014). Cenozoic sedimentation and exhumation of the foreland basin system preserved in the Precordillera thrust belt (31-32°S), southern central Andes, Argentina. Tectonics, 33(9), 1659-1680. https://doi.org/10.1002/2013TC003424

Litvak, V. D., Poma, S., Jones, R. E., Fernández Paz, L., Iannelli, S. B., Spagnuolo, M., Kirstein, L. A., Folguera, A., & Ramos, V. A. (2018). The Late Paleogene to Neogene Volcanic Arc in the Southern Central Andes (28°–37° S). 503-536. https://doi.org/10.1007/978-3-319-67774-3_20

Liu, K. H., Gao, S. S., Silver, P. G., & Zhang, Y. (2003). Mantle layering across central South America. Journal of Geophysical Research: Solid Earth, 108(B11).

Liu, S., & Currie, C. A. (2016). Farallon plate dynamics prior to the Laramide orogeny: Numerical models of flat subduction. Tectonophysics, 666, 33-47.

Liu, S., Sobolev, S. V., Babeyko, A. Y., & Pons, M. (2022). Controls of the Foreland Deformation Pattern in the Orogen-Foreland Shortening System : Constraints From High-Resolution Geodynamic Models. Tectonics, 41(2). https://doi.org/10.1029/2021TC007121

Lopez-Gamundi, O. (2010). Sedimentation styles and variability of organic matter types in the Triassic, non-marine half-grabens of west Argentina : Implications for petroleum systems in rift basins. Petroleum Geoscience - PETROL GEOSCI, 16, 267-272. https://doi.org/10.1144/1354-079309-912

Lossada, A., Giambiagi, L., Hoke, G., AU, & Suriano, J. (2017). Cenozoic Uplift and Exhumation of the Frontal Cordillera Between 30° and 35° S and the Influence of the Subduction Dynamics in the Flat-slab Subduction Context, South Central Andes. https://doi.org/10.1007/978-3-319-67774-3_16

Lyu, T., Zhu, Z., & Wu, B. (2019). Subducting slab morphology and mantle transition zone upwelling in double-slab subduction models with inward-dipping directions. Geophysical Journal International, 218(3), 2089-2105.

Mackwell, S. J., Zimmerman, M. E., & Kohlstedt, D. L. (1998). High-temperature deformation of dry diabase with application to tectonics on Venus. Journal of Geophysical Research: Solid Earth, 103(1), 975–984. https://doi.org/10.1029/97JB02671

Mahlburg Kay, S., & Mpodozis, C. (2002). Magmatism as a probe to the Neogene shallowing of the Nazca plate beneath the modern Chilean flat-slab. Journal of South American Earth Sciences, 15(1), 39-57. https://doi.org/10.1016/S0895-9811(02)00005-6

Maloney, K. T., Clarke, G. L., Klepeis, K. A., & Quevedo, L. (2013). The Late Jurassic to present evolution of the Andean margin: Drivers and the geological record. Tectonics, 32(5), 1049–1065. https://doi.org/10.1002/TECT.20067

Manceda, R., & Figueroa, D. (1995). Inversion of the Mesozoic Neuquén rift in the Malargüe fold and thrust belt, Mendoza, Argentina.

Manea, V., & Gurnis, M. (2007). Subduction zone evolution and low viscosity wedges and channels. Earth and Planetary Science Letters, 264(1-2), 22-45.

Manea, V. C., Pérez-Gussinyé, M., & Manea, M. (2012). Chilean flat-slab subduction controlled by overriding plate thickness and trench rollback. Geology, 40(1), 35-38.

Manea, V. C., Manea, M., Ferrari, L., Orozco-Esquivel, T., Valenzuela, R. W., Husker, A., & Kostoglodov, V. (2017). A review of the geodynamic evolution of flat-slab subduction in Mexico, Peru, and Chile. Tectonophysics, 695, 27-52.

Mardones, V., Peña, M., Pairoa, S., Ammirati, J. B., & Leisen, M. (2021). Architecture, Kinematics, and Tectonic Evolution of the Principal Cordillera of the Andes in Central Chile (∼33.5°S) : Insights From Detrital Zircon U-Pb Geochronology and Seismotectonics Implications. Tectonics, 40(7). https://doi.org/10.1029/2020TC006499

Mareschal, J.-C., & Jaupart, C. (2011). Energy Budget of the Earth. In H. K. Gupta (Éd.), Encyclopedia of Solid Earth Geophysics (p. 285-291). Springer Netherlands. https://doi.org/10.1007/978-90-481-8702-7_64

Marot, M., Monfret, T., Gerbault, M., Nolet, G., Ranalli, G., & Pardo, M. (2014). Flat versus normal subduction zones: A comparison based on 3-D regional traveltime tomography and petrological modelling of central Chile and western Argentina (29°–35°S). Geophysical increase in mantle viscosity. Nature Geoscience, 8(4), 311–314. https://doi.org/10.1038/ngeo2393

Marquardt, H., & Miyagi, L. (2015). Slab stagnation in the shallow lower mantle linked to an Letters, 299(3–4), 299–309.

Martínez, F., Parra, M., Arriagada, C., Mora, A., Bascuñan, S., & Peña, M. (2017). Late Cretaceous to Cenozoic deformation and exhumation of the Chilean Frontal Cordillera (28°–29°S), Central Andes. Journal of Geodynamics, 111, 31-42. https://doi.org/10.1016/j.jog.2017.08.004

Martino, R. D., Guereschi, A. B., & Montero, A. C. (2016). Reactivation, inversion and basement faulting and thrusting in the Sierras Pampeanas of Córdoba (Argentina) during Andean flat-slab deformation. Geological Magazine, 153(5-6), 962-991. https://doi.org/10.1017/S0016756816000339

Martinod, J., Gérault, M., Husson, L., & Regard, V. (2020). Widening of the Andes: An interplay between subduction dynamics and crustal wedge tectonics. Earth-Science Reviews, 204, 103170.

Martinod, J., Husson, L., Roperch, P., Guillaume, B., & Espurt, N. (2010). Horizontal subduction zones, convergence velocity and the building of the Andes. Earth and Planetary Science Journal International, 199(3), 1633–1654. https://doi.org/10.1093/gji/ggu355

McKenzie, D. P. (1968). The influence of the boundary conditions and rotation on convection in the earth's mantle. Geophysical Journal International, 15(5), 457-500.

McKenzie, D. P. (1969). Speculations on the consequences and causes of plate motions. Geophysical Journal International, 18(1), 1-32.

McKenzie, D., & Bickle, M. J. (1988). The Volume and Composition of Melt Generated by Extension of the Lithosphere. Journal of Petrology, 29(3), 625–679. https://doi.org/10.1093/petrology/29.3.625

Meeßen, C., Sippel, J., Scheck-Wenderoth, M., Heine, C., & Strecker, M. R. (2018). Crustal Structure of the Andean Foreland in Northern Argentina : Results From Data-Integrative Three-Dimensional Density Modeling. Journal of Geophysical Research: Solid Earth, 123(2), 1875-1903. https://doi.org/10.1002/2017JB014296

Melnick, D., & Echtler, H. P. (2006). Inversion of forearc basins in south-central Chile caused by rapid glacial age trench fill. Geology, 34(9), 709-712.

Melnick, D., Charlet, F., Echtler, H. P., & De Batist, M. (2006). Incipient axial collapse of the Main Cordillera and strain partitioning gradient between the central and Patagonian Andes, Lago Laja, Chile. Tectonics, 25(5). https://doi.org/10.1029/2005TC001918

Melnick, D., Maldonado, V., & Contreras, M. (2020). Database of active and potentially-active continental faults in Chile at 1:25,000 scale. PANGAEA. https://doi.org/10.1594/PANGAEA.922241

Mescua, J. F., Giambiagi, L. B., Tassara, A., Gimenez, M., & Ramos, V. A. (2014). Influence of pre-Andean history over Cenozoic foreland deformation : Structural styles in the Malargüe fold-and-thrust belt at 35 S, Andes of Argentina. Geosphere, 10(3), 585-609. https://doi.org/10.1130/GES00939.1

Mescua, J. F., Giambiagi, L., Barrionuevo, M., Tassara, A., Mardonez, D., Mazzitelli, M., & Lossada, A. (2016). Basement composition and basin geometry controls on upper-crustal deformation in the Southern Central Andes (30-36°S). Geological Magazine, 153(5-6), 945-961. https://doi.org/10.1017/S0016756816000364

Molnar, P., & Tapponnier, P. (1975). Cenozoic Tectonics of Asia : Effects of a Continental Collision. Science, 189(4201), 419-426. https://doi.org/10.1126/science.189.4201.419

Montgomery, D. R., Balco, G., & Willett, S. D. (2001). Climate, tectonics, and the morphology of the Andes. Geology, 29(7), 579-582.

Mora, A., Gaona, T., Kley, J., Montoya, D., Parra, M., Quiroz, L. I., ... & Strecker, M. R. (2009). The role of inherited extensional fault segmentation and linkage in contractional orogenesis: A reconstruction of Lower Cretaceous inverted rift basins in the Eastern Cordillera of Colombia. Basin Research, 21(1), 111-137.

Moscoso, R., & Mpodozis, C. (1988). Estilos estructurales en el norte chico del Chile (28-31 OS), regiones de Atacama y Coquimbo. Revista Geologica de Chile, 15(2), 151-166.

Mouthereau, E. B., AB Watts. (2013). Structure of orogenic belts controlled by lithosphere age. Nat Geosci, 6(9), 785-789. https://doi.org/10.1038/ngeo1902

Mpodozis, C., & Kay, S. M. (1990). Provincias magmáticas ácidas y evolución tectónica de Gondwana : Andes chilenos (28-31 S). Andean Geology, 17(2), 153-180. http://dx.doi.org/10.5027/andgeoV17n2-a03

Muldashev, I. A., & Sobolev, S. V. (2020). What Controls Maximum Magnitudes of Giant Subduction Earthquakes? Geochemistry, Geophysics, Geosystems, 21(9). https://doi.org/10.1029/2020GC009145

Murnaghan, F. D. (1944). The Compressibility of Media under Extreme Pressures. Proceedings of the National Academy of Sciences, 30(9), 244–247. https://doi.org/10.1073/pnas.30.9.244

Neuharth, D., Brune, S., Glerum, A., Heine, C., & Welford, J. K. (2021a). Formation of Continental Microplates Through Rift Linkage: Numerical Modeling and Its Application to the Flemish Cap and Sao Paulo Plateau. Geochemistry, Geophysics, Geosystems, 22(4), e2020GC009615-e2020GC009615. https://doi.org/10.1029/2020GC009615

Neuharth, D., Brune, S., Glerum, A. C., Morley, C. K., Yuan, X., & Braun, J. (2021b). Flexural strike-slip basins. https://eartharxiv.org/repository/view/2439/

O'Driscoll, L. J., Richards, M. A., & Humphreys, E. D. (2012). Nazca–South America interactions and the late Eocene–late Oligocene flat-slab episode in the central Andes. Tectonics, 31(2).

Olivar, J., Nacif, S., Fennell, L., & Folguera, A. (2018). Within plate seismicity analysis in the segment between the high Cordillera and the Precordillera of northern Mendoza (Southern Central Andes). Geodesy and Geodynamics, 9(1), 13-24. https://doi.org/10.1016/j.geog.2017.09.004

Oncken, O., Hindle, D., Kley, J., Elger, K., Victor, P., & Schemmann, K. (2006). Deformation of the Central Andean Upper Plate System—Facts, Fiction, and Constraints for Plateau Models. The Andes, 3–27. https://doi.org/10.1007/978-3-540-48684-8_1

Oncken, O., Boutelier, D., Dresen, G., & Schemmann, K. (2012). Strain accumulation controls failure of a plate boundary zone: Linking deformation of the Central Andes and lithosphere mechanics. Geochemistry, Geophysics, Geosystems, 13(12). https://doi.org/10.1029/2012GC004280

Ortiz, G., Stevens Goddard, A. L., Fosdick, J. C., Alvarado, P., Carrapa, B., & Cristofolini, E. (2021). Fault reactivation in the Sierras Pampeanas resolved across Andean extensional and compressional regimes using thermochronologic modeling. Journal of South American Earth Sciences, 112, 103533. https://doi.org/10.1016/j.jsames.2021.103533

Pérez-Gussinyé, M., Lowry, A. R., Phipps Morgan, J., & Tassara, A. (2008). Effective elastic thickness variations along the Andean margin and their relationship to subduction geometry. Geochemistry, Geophysics, Geosystems, 9(2).

Perkins, J. P., Ward, K. M., de Silva, S. L., Zandt, G., Beck, S. L., & Finnegan, N. J. (2016). Surface uplift in the Central Andes driven by growth of the Altiplano Puna Magma Body. Nature Communications, 7(1), 13185. https://doi.org/10.1038/ncomms13185

Pesicek, J. D., Engdahl, E. R., Thurber, C. H., DeShon, H. R., & Lange, D. (2012). Mantle subducting slab structure in the region of the 2010 M8.8 Maule earthquake (30-40°S), Chile : Mantle subducting slab structure in Chile. Geophysical Journal International, 191(1), 317-324. https://doi.org/10.1111/j.1365-246X.2012.05624.x

Pilger Jr, R. H. (1981). Plate reconstructions, aseismic ridges, and low-angle subduction beneath the Andes. Geological Society of America Bulletin, 92(7), 448-456.

Pilger, R. H. (1984). Cenozoic plate kinematics, subduction and magmatism: South American Andes. Journal of the Geological Society, 141(5), 793-802.

Pons, M., Sobolev, S., Liu, S., Neuharth, D. (2022): 2D geodynamic subduction model of the Central Andes. GFZ Data Services. https://doi.org/10.5880/GFZ.2.5.2022.001

Portner, D. E., Rodríguez, E. E., Beck, S., Zandt, G., Scire, A., Rocha, M. P., ... & Alvarado, P. (2020). Detailed structure of the subducted Nazca slab into the lower mantle derived from continent-scale teleseismic P wave tomography. Journal of Geophysical Research: Solid Earth, 125(5), e2019JB017884.

Quiero, F., Tassara, A., Iaffaldano, G., & Rabbia, O. (2022). Growth of Neogene Andes linked to changes in plate convergence using high-resolution kinematic models. Nature communications, 13(1), 1-9.

Quinteros, J., & Sobolev, S. V. (2013). Why has the Nazca plate slowed since the Neogene? Geology, 41(1), 31–34. https://doi.org/10.1130/G33497.1

Quinteros, J., Sobolev, S. V., & Popov, A. A. (2010). Viscosity in transition zone and lower mantle: Implications for slab penetration. Geophysical Research Letters, 37(9), n/a-n/a. https://doi.org/10.1029/2010GL043140

Ramos, V. A., & Scientific, N. (2002). Flat-slab subduction in the Andes. Journal of South American Earth Sciences, 15(1), 1-2. https://doi.org/10.1016/s0895-9811(02)00011-1

Ramos, V. A., Cristallini, E. O., & Pérez, D. J. (2002). The Pampean flat-slab of the Central Andes. Journal of South American Earth Sciences, 15(1), 59-78. https://doi.org/10.1016/S0895-9811(02)00006-8

Ramos, V., Cristallini, E., & Introcaso, A. (2004). The Andean thrust system latitudinal variations in structural styles and orogenic shortening. AAPG Spec Vol. Memoir, 82, 30-50.

Ramos, V. A., & Folguera, A. (2009). Andean flat-slab subduction through time. Geological Society

Ramos, V. A. (2009). Anatomy and global context of the Andes : Main geologic features and the Andean orogenic cycle. In S. M. Kay, V. A. Ramos, & W. R. Dickinson (Éds.), Backbone of the Americas : Shallow Subduction, Plateau Uplift, and Ridge and Terrane Collision (Vol. 204, p. 0). Geological Society of America. https://doi.org/10.1130/2009.1204(02)

Ramos, V. (2010). The Grenville-age basement of the Andes. J S Am Earth Sci, 29(1), 77-91. https://doi.org/10.1016/j.jsames.2009.09.004

Ramos, V. A., Litvak, V. D., Folguera, A., & Spagnuolo, M. (2014). An Andean tectonic cycle : From crustal thickening to extension in a thin crust (34°–37°SL). Geoscience Frontiers, 5(3), 351-367. https://doi.org/10.1016/j.gsf.2013.12.009

Ranalli, G. (1997). Rheology and deep tectonics. Annals of Geophysics, 40(3), 3. https://doi.org/10.4401/ag-3893

Regard, V., Saillard, M., Martinod, J., Audin, L., Carretier, S., Pedoja, K., Riquelme, R., Paredes, P., & Hérail, G. (2010). Renewed uplift of the Central Andes Forearc revealed by coastal evolution during the Quaternary. Earth and Planetary Science Letters, 297(1), 199-210. https://doi.org/10.1016/j.epsl.2010.06.020

Ribe, N. M., Stutzmann, E., Ren, Y., & Van Der Hilst, R. (2007). Buckling instabilities of subducted lithosphere beneath the transition zone. Earth and Planetary Science Letters, 254(1-2), 173-179.

Richardson, T., Gilbert, H., Anderson, M., & Ridgway, K. D. (2012). Seismicity within the actively deforming Eastern Sierras Pampeanas, Argentina. Geophysical Journal International, 188(2), 408-420. https://doi.org/10.1111/j.1365-246X.2011.05283.x

Riesner, M., Lacassin, R., Simoes, M., Carrizo, D., & Armijo, R. (2018). Revisiting the Crustal Structure and Kinematics of the Central Andes at 33.5°S : Implications for the Mechanics of Andean Mountain Building. Tectonics, 37(5), 1347-1375. https://doi.org/10.1002/2017TC004513

Rodriguez Piceda, C., Scheck Wenderoth, M., Gomez Dacal, M. L., Bott, J., Prezzi, C. B., & Strecker, M. R. (2021). Lithospheric density structure of the southern Central Andes constrained by 3D data-integrative gravity modelling. International Journal of Earth Sciences, 110(7), 2333-2359. https://doi.org/10.1007/S00531-020-01962-1

Rodriguez Piceda, C., Scheck-Wenderoth, M., Bott, J., Gomez Dacal, M. L., Cacace, M., Pons, M., Prezzi, C. B., & Strecker, M. R. (2022). Controls of the Lithospheric Thermal Field of an Ocean-Continent Subduction Zone : The Southern Central Andes. Lithosphere, 2022(1), 2237272. https://doi.org/10.2113/2022/2237272

Rodriguez Piceda, C., Scheck-Wenderoth, M., Cacace, M., Bott, J., & Strecker, M. R. (2022b). Long-Term Lithospheric Strength and Upper-Plate Seismicity in the Southern Central Andes, 29°–39°S. Geochemistry, Geophysics, Geosystems, 23(3), 22. https://doi.org/10.1029/2021GC010171

Rose, I., Buffett, B., & Heister, T. (2017). Stability and accuracy of free surface time integration in viscous flows. Physics of the Earth and Planetary Interiors, 262, 90–100. https://doi.org/10.1016/J.PEPI.2016.11.007

Rosenau, M., Melnick, D., & Echtler, H. (2006). Kinematic constraints on intra-arc shear and strain partitioning in the southern Andes between 38°S and 42°S latitude. Tectonics, 25(4). https://doi.org/10.1029/2005TC001943

Russo, R. M., & Silver, P. G. (1994). Trench-parallel flow beneath the Nazca plate from seismic anisotropy. Science, 263(5150), 1105-1111.

Russo, R. M., & Silver, P. G. (1996). Cordillera formation, mantle dynamics, and the Wilson cycle. Geology, 24, 511. https://doi.org/10.1130/0091-7613(1996)024<0511:CFMDAT>2.3.CO;2

Saleeby, J. (2003). Segmentation of the Laramide Slab—Evidence from the southern Sierra Nevada region. Geological Society of America Bulletin, 115, 655-668. https://doi.org/10.1130/0016-7606(2003)115<0655:SOTLSF>2.0.CO;2

Sánchez, M. A., Winocur, D., Álvarez, O., Folguera, A., & Martinez, M. P. (2017). Crustal structure of the high Andes in the North Pampean flat-slab segment from magnetic and gravity data. Journal of South American Earth Sciences, 73, 153-167. https://doi.org/10.1016/j.jsames.2016.12.007

Scarfi, L., & Barbieri, G. (2019). New insights on the tectonic structure of the Southern Central Andes – Western Argentina – from seismic tomography. Geology, Earth & Marine Sciences, 1(1). https://doi.org/10.31038/GEMS.2019113

Schaeffer, A., & Lebedev, S. (2013). Global shear speed structure of the upper mantle and transition zone. Geophysical Journal International, 194(1), 417-449.

Schellart, W. P., Freeman, J., Stegman, D. R., Moresi, L., & May, D. (2007). Evolution and diversity of subduction zones controlled by slab width. Nature, 446(7133), 308-311.

Schellart, W. P. (2017). Andean mountain building and magmatic arc migration driven by subduction-induced whole mantle flow. Nature communications, 8(1), 1-13.

Schellart, W. P. (2020). Control of Subduction Zone Age and Size on Flat-slab Subduction. Frontiers in Earth Science, 0, 26–26. https://doi.org/10.3389/FEART.2020.00026

Schellart, W. P., & Strak, V. (2021). Geodynamic models of short-lived, long-lived and periodic flat-slab subduction. Geophysical Journal International, 226(3), 1517–1541. https://doi.org/10.1093/gji/ggab126

Schepers, G., Van Hinsbergen, D. J. J., Spakman, W., Kosters, M. E., Boschman, L. M., & McQuarrie, N. (2017). South-American plate advance and forced Andean trench retreat as drivers for transient flat subduction episodes. Nature Communications, 8. https://doi.org/10.1038/NCOMMS15249

Schildgen, T. F., & Hoke, G. D. (2018). The Topographic Evolution of the Central Andes. Elements, 14(4), 231-236. https://doi.org/10.2138/gselements.14.4.231

Schilling, F. R., Trumbull, R. B., Brasse, H., Haberland, C., Asch, G., Bruhn, D., Mai, K., Haak, V., Giese, P., Muñoz, M., Ramelow, J., Rietbrock, A., Ricaldi, E., & Vietor, T. (2006). Partial Melting in the Central Andean Crust: A Review of Geophysical, Petrophysical, and Petrologic Evidence. In O. Oncken, G. Chong, G. Franz, P. Giese, H.-J. Götze, V. A. Ramos, M. R. Strecker, & P. Wigger (Eds.), The Andes: Active Subduction Orogeny (pp. 459–474). Springer. https://doi.org/10.1007/978-3-540-48684-8_22

Schurr, B., Asch, G., Rietbrock, A., Trumbull, R., & Haberland, C. (2003). Complex patterns of fluid and melt transport in the central Andean subduction zone revealed by attenuation tomography. Earth and Planetary Science Letters, 215(1–2), 105–119. https://doi.org/10.1016/S0012-821X(03)00441-2

Sdrolias, M., & Müller, R. D. (2006). Controls on back-arc basin formation. Geochemistry, Geophysics, Geosystems, 7(4). https://doi.org/10.1029/2005GC001090

Siame, L. L., Sébrier, M., Bellier, O., Bourlès, D., Costa, C., Ahumada, E. A., Gardini, C. E., & Cisneros, H. (2015). Active basement uplift of Sierra Pie de Palo (Northwestern Argentina) : Rates and inception from 10 Be cosmogenic nuclide concentrations: ACTIVE BASEMENT UPLIFT. Tectonics, 34(6), 1129-1153. https://doi.org/10.1002/2014TC003771

Silver, P. G., Russo, R. M., & Lithgow-Bertelloni, C. (1998). Coupling of South American and African plate motion and plate deformation. Science, 279(5347), 60-63.

Sippel, J., Meeßen, C., Cacace, M., Mechie, J., Fishwick, S., Heine, C., Scheck-Wenderoth, M., & Strecker, M. R. (2017). The Kenya rift revisited : Insights into lithospheric strength through data-driven 3-D gravity and thermal modelling. Solid Earth, 8(1), 45-81. https://doi.org/10.5194/se-8-45-2017

Sobolev, S. V., & Babeyko, A. Y. (1994). Modeling of mineralogical composition, density and elastic wave velocities in anhydrous magmatic rocks. Surveys in Geophysics, 15(5), 515–544. https://doi.org/10.1007/BF00690173

Sobolev, S. V., & Babeyko, A. Y. (2005). What drives orogeny in the Andes? Geology, 33(8), 617–620. https://doi.org/10.1130/G21557AR.1

Sobolev, S. V., Babeyko, A. Y., Koulakov, I., & Oncken, O. (2006). Mechanism of the Andean Orogeny: Insight from Numerical Modeling. The Andes, 513–535. https://doi.org/10.1007/978-3-540-48684-8_25

Stalder, N. F., Herman, F., Fellin, M. G., Coutand, I., Aguilar, G., Reiners, P. W., & Fox, M. (2020). The relationships between tectonics, climate and exhumation in the Central Andes (18–36 S): Evidence from low-temperature thermochronology. *Earth-Science Reviews*, *210*, 103276.

Stegman, D. R., Farrington, R., Capitanio, F. A., & Schellart, W. P. (2010). A regime diagram for subduction styles from 3-D numerical models of free subduction. Tectonophysics, 483(1-2), 29-45.

Steinberger, B., Sutherland, R., & O'connell, R. J. (2004). Prediction of Emperor-Hawaii seamount locations from a revised model of global plate motion and mantle flow. Nature, 430(6996), 167-173.

Steinberger, B., & Calderwood, A. R. (2006). Models of large-scale viscous flow in the Earth's mantle with constraints from mineral physics and surface observations. Geophysical Journal International, 167(3), 1461–1481. https://doi.org/10.1111/J.1365-246X.2006.03131.X

Stüwe, K. (2007). Geodynamics of the Lithosphere. Springer-Verlag Berlin Heidelberg.

Suriano, J., Mardonez, D., Mahoney, J. B., Mescua, J. F., Giambiagi, L. B., Kimbrough, D., & Lossada, A. (2017). Uplift sequence of the Andes at 30°S : Insights from sedimentology and U/Pb dating of synorogenic deposits. Journal of South American Earth Sciences, 75, 11-34. https://doi.org/10.1016/j.jsames.2017.01.004

Tan, E., Lavier, L. L., Van Avendonk, H. J. A., & Heuret, A. (2012). The role of frictional strength on plate coupling at the subduction interface. Geochemistry, Geophysics, Geosystems, 13(10). https://doi.org/10.1029/2012GC004214

Tassara, A. (2005). Interaction between the Nazca and South American plates and formation of the Altiplano–Puna plateau : Review of a flexural analysis along the Andean margin (15°–34°S). Andean Geodynamics:, 399(1), 39-57. https://doi.org/10.1016/j.tecto.2004.12.014

Tassara, A., & Yáñez, G. (2003). Relación entre el espesor elástico de la litosfera y la segmentación tectónica del margen andino (15-47°S). Revista geológica de Chile, 30(2), 159-186. https://doi.org/10.4067/S0716-02082003000200002

Tassara, A., Götze, H. J., Schmidt, S., & Hackney, R. (2006). Three-dimensional density model of the Nazca plate and the Andean continental margin. Journal of Geophysical Research: Solid Earth, 111(9). https://doi.org/10.1029/2005JB003976

Tesauro, M., Kaban, M. K., & Mooney, W. D. (2015). Variations of the lithospheric strength and elastic thickness in North America : Lithospheric Strength and Te variations. Geochemistry, Geophysics, Geosystems, 16(7), 2197-2220. https://doi.org/10.1002/2015GC005937

Trumbull, R., Riller, U., Oncken, O., Scheuber, E., Munier, K., & Hongn, F. (2006). The time-space distribution of Cenozoic volcanism in the south-central Andes : A new data compilation and some tectonic implications. The Andes - Active Subduction Orogeny, 29-43.

Turcotte, D. L., Schubert, G., (2002). Geodynamics (2nd ed). Cambridge University Press.

Turcotte, D.L. and Schubert, G. (2014) Geodynamics. Cambridge University Press, Cambridge, 848 p.

Uba, C. E., Kley, J., Strecker, M. R., & Schmitt, A. K. (2009). Unsteady evolution of the Bolivian Subandean thrust belt: The role of enhanced erosion and clastic wedge progradation. Earth and Planetary Science Letters, 281(3-4), 134-146.

Uliana, M. A., Arteaga, M. E., Legarreta, L., Cerdán, J. J., & Peroni, G. O. (1995). Inversion structures and hydrocarbon occurrence in Argentina. Geological Society, London, Special Publications, 88(1), 211-233. https://doi.org/10.1144/GSL.SP.1995.088.01.13

Van Hunen, J., van den Berg, A. P., & Vlaar, N. J. (2004). Various mechanisms to induce present-day shallow flat subduction and implications for the younger Earth: A numerical parameter study. Physics of the Earth and Planetary Interiors, 146(1–2), 179–194. https://doi.org/10.1016/J.PEPI.2003.07.027

Van Keken, P. E., Wada, I., Sime, N., & Abers, G. A. (2019). Thermal Structure of the Forearc in Subduction Zones : A Comparison of Methodologies. Geochemistry, Geophysics, Geosystems, 20(7), 3268-3288. https://doi.org/10.1029/2019GC008334

Vietor, T., & Echtler, H. (2006). Episodic Neogene Southward Growth of the Andean Subduction Orogen between 30°S and 40°S — Plate Motions, Mantle Flow, Climate, and Upper-Plate Structure. In O. Oncken, G. Chong, G. Franz, P. Giese, H.-J. Götze, V. A. Ramos, M. R. Strecker, & P. Wigger (Éds.), The Andes (p. 375-400). Springer Berlin Heidelberg. https://doi.org/10.1007/978-3-540-48684-8_18

Völker, D., Geersen, J., Contreras-Reyes, E., & Reichert, C. (2013). Sedimentary fill of the Chile Trench (32–46 S): volumetric distribution and causal factors. Journal of the Geological Society, 170(5), 723-736.

Von Huene, R., Corvalán, J., Flueh, E. R., Hinz, K., Korstgard, J., Ranero, C. R., & Weinrebe, W. (1997). Tectonic control of the subducting Juan Fernández Ridge on the Andean margin near Valparaiso, Chile. Tectonics, 16(3), 474-488.

Wada, I., & Wang, K. (2009). Common depth of slab-mantle decoupling : Reconciling diversity and uniformity of subduction zones. Geochemistry, Geophysics, Geosystems, 10(10). https://doi.org/10.1029/2009GC002570

Wagner, L. S., Beck, S., & Zandt, G. (2005). Upper mantle structure in the south central Chilean subduction zone (30° to 36°S). Journal of Geophysical Research: Solid Earth, 110(B1). https://doi.org/10.1029/2004JB003238

Walcek, A. A., & Hoke, G. D. (2012). Surface uplift and erosion of the southernmost Argentine Precordillera. Geomorphology. https://doi.org/10.1016/j.geomorph.2012.02.021

Wang, H., Currie, C. A., & DeCelles, P. G. (2021). Coupling Between Lithosphere Removal and Mantle Flow in the Central Andes. Geophysical Research Letters, 48(16), e2021GL095075. https://doi.org/10.1029/2021GL095075

Widiyantoro, S. (1997). Studies of seismic tomography on regional and global scale.

Wimpenny, S. (2022). Weak, Seismogenic Faults Inherited From Mesozoic Rifts Control Mountain Building in the Andean Foreland. Geochemistry, Geophysics, Geosystems, 23(3), e2021GC010270. https://doi.org/10.1029/2021GC010270

Wolf, S. G., & Huismans, R. S. (2019). Mountain building or Backarc extension in ocean-continent subduction systems: A function of backarc lithospheric strength and absolute plate velocities. Journal of Geophysical Research: Solid Earth, 124(7), 7461-7482.

Woods, M. T., & Okal, E. A. (1994). The structure of the Nazca ridge and Sala y Gomez seamount chain from the dispersion of Rayleigh waves. Geophysical Journal International, 117(1), 205-222.

Xu, Y., Shankland, T. J., Linhardt, S., Rubie, D. C., Langenhorst, F., & Klasinski, K. (2004). Thermal diffusivity and conductivity of olivine, wadsleyite and ringwoodite to 20 GPa and 1373 K. Physics of the Earth and Planetary Interiors, 143-144, 321-336. https://doi.org/10.1016/j.pepi.2004.03.005

Xue, K., Schellart, W. P., & Strak, V. (2022). Overriding plate deformation and topography during slab rollback and slab rollover: insights from subduction experiments. Tectonics, 41(2), e2021TC007089.

Yáñez, G. A., Ranero, C. R., Von Huene, R., & Díaz, J. (2001). Magnetic anomaly interpretation across the southern central Andes (32°-34°S): The role of the Juan Fernández Ridge in the late Tertiary evolution of the margin. Journal of Geophysical Research: Solid Earth, 106(B4), 6325–6345. https://doi.org/10.1029/2000JB900337

Yuan, X., Sobolev, S.V., and Kind, R., 2002, New data on Moho topography in the Central Andes and their geodynamic implications: Earth and Planetary Science Letters , v. 199p. 389-402.

Zapata, S., Sobel, E. R., Del Papa, C., & Glodny, J. (2020). Upper Plate Controls on the Formation of Broken Foreland Basins in the Andean Retroarc Between 26°S and 28°S : From Cretaceous Rifting to Paleogene and Miocene Broken Foreland Basins. Geochemistry, Geophysics, Geosystems, 21(7), e2019GC008876. https://doi.org/10.1029/2019GC008876